

ASTON UNIVERSITY

**Development of novel small-molecule
inhibitors of human tissue transglutaminase**

Ngoc Thi Anh Nguyen

Doctor of Philosophy

Aston University

March 2020

© Ngoc Thi Anh Nguyen, 2020

Ngoc Thi Anh Nguyen asserts her moral right to be identified as
the author of this thesis

This copy of the thesis has been supplied on condition that anyone who consults it is understood to recognise that its copyright rests with its author and that no quotation from the thesis and no information derived from it may be published without appropriate permission or acknowledgement.

Aston University

Development of small-molecule inhibitors of human tissue transglutaminase

Ngoc Thi Anh Nguyen

PhD

2020

Abstract

Tissue transglutaminase (TG2) is the most ubiquitous enzyme among Ca^{2+} -dependent crosslinking-protein enzyme family that catalyses the acyl-transfer reaction between the γ -carboxamide group of a peptide-bound glutamine and the ϵ -amino group of a peptide-bound lysine or a primary amine. The adventitious cross-linking related to unregulated TG2 activity has been implicated in various pathologies. This research focused on the development of both allosteric and irreversible TG2 inhibitors.

LDN27219, a published lead TG2 allosteric inhibitor, whose binding site was predicted by the previous computational modelling, was modified to develop potential allosteric inhibitors. Molecular dynamics (MD) simulations were applied for the complexes of the parent compound and newly designed compounds docked into the predicted allosteric site. Attempts were made to prepare the designed compounds from ethyl 4-oxo-5-phenyl-3H-thieno[2,3-d]pyrimidine-2-carboxylate derivatives. However, the key literature method failed to provide the desired esters. Many attempts were made and the optimised reaction conditions provided the pure desired products in 83% yield, followed by the discovery of novel methods to synthesise 5-phenyl-3H-thieno[2,3-d]pyrimidine-4-ones in up to 84% yields. Consequently, a set of potential allosteric inhibitors was prepared and screened *in vitro* against human TG2. The highest potency was seen in acylhydrazide derivatives, two of which are nearly two times more potent than the parent compound. In the MD simulations, the binding of the potent inhibitors were observed to stabilise the open conformation of TG2 but also enlarge the catalytic site's entrance and cause the moving of TRP241, which stabilises the enzyme-thiol intermediates, from the catalytic binding site.

Potential irreversible TG2 inhibitors were designed by modifications of the lead inhibitor developed by the Griffin group (Aston University) including attachment of a carboxyl group on the acrylamide warhead, shortening the aliphatic side chain length, inserting a phenyl ring between the piperazine ring and the acrylamide warhead and changing the whole scaffold structure. The parent and the designed compounds docked into the TG2 catalytic binding site were subjected to MD simulations. The affinity and potency of the ligands were predicted based on stability of the ligand into the catalytic site and the distance between the warhead electrophilic carbon and the catalytic cystein sulphur. A set of acrylamides with short side chains and (2Z)-4-amino-4-oxo-2-butenic acid derivatives were prepared and tested against human TG2. All the newly synthesised acrylamides are significantly less potent than the parent compound and the potency was halted by the attachment of the carboxyl on *cis* position of the acrylamide warhead.

Keywords: tissue transglutaminase, allosteric inhibitor, irreversible inhibitor, molecular dynamics simulation.

Acknowledgements

I would like to express my deepest gratitude to my main supervisor, Dr. Dan Rathbone, for his continuous encourage and advice during the course of this PhD research. Without his persistent help, the goal of this project would not have been achieved.

I wish to express my special thanks to Professor Martin Griffin, my associate supervisor and Dr. Vivian Wang, for their consistent support and guidance in biology and biochemistry.

Special thanks is extended to the Dr. Bill Fraser for always being willing and enthusiastic to assist in any way he could.

I would like to acknowledge the helpful assistance that provided by all the laboratory technicians.

I gratefully acknowledge the provision received towards my PhD from the School of Life and Health Sciences, Aston University. I am also grateful for the Foundation Grant received through the British Federation of Women Graduates.

The assistance in measuring high-resolution mass spectrometry of EPSRC National Mass Spectrometry Centre is gratefully acknowledged.

I wish to express our sincere gratitude to my family and my friends for their prayers, support and great love.

Table of Contents

ABSTRACT	2
ACKNOWLEDGEMENTS	3
TABLE OF CONTENTS	4
LIST OF TABLES	11
LIST OF SCHEMES	11
LIST OF FIGURES	13
1 GENERAL INTRODUCTION.....	22
1.1 Tissue transglutaminase	22
1.1.1 Physiological roles and disorders.....	22
1.1.2 Structural diversity	23
1.2 Biological assays for TG2 activity.....	26
1.2.1 Enzyme-coupled assay	26
1.2.2 Radioactive transamidation assay	26
1.2.3 Fluorescence transamidation assay	26
1.2.4 Absorbance-based assay	27
1.2.5 Fluorescence anisotropy assay	27
1.3 Kinetics of enzyme inhibition.....	27
1.4 TG2 inhibitors	29
1.4.1 Inhibitors competitive with amine substrates	29
1.4.2 Inhibitors competitive with acyl-donor substrates	30
1.4.3 Allosteric reversible inhibitors.....	32
1.4.4 Irreversible inhibitors.....	34

1.5	Computational techniques.....	58
1.5.1	Molecular dynamics simulations	58
1.5.2	Stages of MD simulations	61
1.5.3	Amber overview.....	61
1.5.4	Molecular docking	62
1.6	Aim and Objectives.....	63
2	GENERAL METHODOLOGY	65
2.1	Computational modelling.....	65
2.1.1	Programs	65
2.1.2	Molecular dynamics (MD) simulations	65
2.1.3	Visual inspection and analysis of MD trajectories.....	67
2.2	Synthetic chemistry experiments.....	68
2.3	Biological assays for screening the inhibitory effect.....	68
3	MOLECULAR DYNAMICS SIMULATIONS OF POTENTIAL ALLOSTERIC INHIBITORS OF TG2.....	70
3.1	MD trajectory of the parent compound.....	74
3.2	MD trajectory of compound 31	76
3.3	MD trajectories of compounds having a N,N-dimethyl ethyl amide side chain.....	78
3.3.1	MD trajectory of compound 32a.....	78
3.3.2	MD trajectory of compound 32b.....	79
3.3.3	MD trajectory of compound 32c.....	80
3.3.4	MD trajectory of compound 32d.....	82
3.4	MD trajectories of compounds having an N,N-dimethyl propyl amide side chain.....	82
3.4.1	MD trajectory of compound 33a.....	83
3.4.2	MD trajectory of compound 33b.....	84

3.4.3	MD trajectory of compound 33c.....	85
3.4.4	MD trajectory of compound 33d.....	86
3.5	MD trajectories of compounds having an amide side chain	88
3.5.1	MD trajectory of compound 34a.....	88
3.5.2	MD trajectory of compound 34b.....	90
3.5.3	MD trajectory of compound 34c.....	91
3.5.4	MD trajectory of compound 34d.....	91
3.5.5	MD trajectory of compound 34e.....	93
3.5.6	MD trajectory of compound 34f	95
3.5.7	MD trajectory of compound 34g.....	97
3.6	MD trajectories of compounds having a hydrazide side chain.....	98
3.6.1	MD trajectory of compound 35a.....	98
3.6.2	MD trajectory of compound 35b.....	99
3.6.3	MD trajectory of compound 35c.....	101
3.7	MD trajectories of compounds having an ethyl acetate side chain	103
3.7.1	MD trajectory of compound 36a.....	103
3.7.2	MD trajectory of compound 36b.....	103
3.7.3	MD trajectory of compound 36c.....	103
3.8	MD trajectories of the compounds having a carboxylate side chain.....	104
3.9	Conclusion	105
4	SYNTHESIS OF POTENTIAL ALLOSTERIC INHIBITORS OF TG2	107
4.1	Optimisation of conditions to synthesise the key ester	107
4.2	Synthesis of the target compounds from the esters 36a,b,c.....	111
4.3	Identification of compound 39a and its derivatives	112
4.4	Optimisation of conditions to synthesise 5-phenyl-3H-thieno[2,3-d]pyrimidine-4-ones (compounds 39a,b,c).....	114
4.5	Conclusion	115

4.6	Chemistry experimental procedures	116
5	MOLECULAR DYNAMICS SIMULATIONS OF POTENTIAL IRREVERSIBLE INHIBITORS OF TG2.....	134
5.1	MD trajectory of the lead irreversible inhibitor (compound 27).....	136
5.2	MD trajectories of compounds having the same scaffold as the lead compound 27.....	138
5.2.1	MD trajectory of compound 27a.....	138
5.2.2	MD trajectory of compound (E)-27b	140
5.2.3	MD trajectory of compound (Z)-27b	142
5.2.4	MD trajectory of compound (E)-27c	143
5.3	MD trajectories of compounds with a shorter side chain modified from compound 27.....	146
5.3.1	MD trajectory of compound 27e.....	146
5.3.2	MD trajectory of compound (Z)-27f.....	148
5.4	MD trajectories of compounds with a more rigid side chain modified from compound 27.....	149
5.4.1	MD trajectory of compound 27g.....	149
5.4.2	MD trajectory of compound (Z)-27h	151
5.5	MD trajectories of compounds with a more rigid side chain modified from compound 26.....	152
5.5.1	MD trajectory of compound 26a.....	152
5.5.2	MD trajectory of compound (Z)-26b	154
5.6	MD trajectories the rhodanine derivatives.....	156
5.6.1	MD trajectory of compound 40a.....	156
5.6.2	MD trajectory of compound 40b.....	157
5.7	MD trajectories of 1,2,4-triazole derivatives	160
5.7.1	MD trajectory of compound 41b.....	160
5.7.2	MD trajectory of compound 41a.....	162

5.8	Conclusion	164
6	SYNTHESIS OF POTENTIAL IRREVERSIBLE INHIBITORS OF TG2	166
6.1	Synthesis of the compounds modified from compound 27	168
6.1.1	Preparation of the scaffold of compound 27	168
6.1.2	Synthesis of compounds with a shorter side chain	169
6.1.3	Modification of the acrylamide warhead of compound 27	170
6.2	Synthesis of rhodanine derivatives	173
6.2.1	Preparation of the scaffold	173
6.2.2	Attachment of the acrylamide warhead	173
6.2.3	Attachment of the dimethylsulfonium ketone warhead	174
6.3	Synthesis of 1,2,4-triazole derivatives	176
6.3.1	Synthesis of pyridyl triazole scaffolds	176
6.3.2	Attachment of warheads on the pyridyl triazolyl aniline scaffolds	179
6.3.3	Attachment of a side chain on the pyridyl triazolyl anilide scaffolds.....	181
6.4	Conclusion	182
6.5	Chemistry experimental session	183
7	SCREENING POTENCY OF POTENTIAL INHIBITORS OF TG2.....	213
7.1	Method	213
7.1.1	Preparation of inhibitors	213
7.1.2	Data analysis	213
7.1.3	Protocol	213
7.2	Results and discussion	215
7.2.1	Potency of potential irreversible inhibitors of TG2	215
7.2.2	Potency of the potential allosteric inhibitors of TG2.....	218
7.2.3	Investigation of the inhibitory effect against rhTG2 of the most potent newly synthesised allosteric inhibitor in the presence of GTP.....	219
7.3	Conclusion	221

8	LONG MOLECULAR DYNAMICS SIMULATIONS OF TG2	
	ALLOSTERIC INHIBITORS	223
8.1	MD simulations applied for the whole TG2 structure.....	223
8.1.1	MD simulation of the empty TG2 (run 1).....	224
8.1.2	MD simulation of the compound having no inhibitory effect (run2)	227
8.1.3	MD simulation of TG2 docked potent inhibitors complexes.....	228
8.2	Repeated long MD simulations	238
8.2.1	Repeated long MD simulation of compound 35b – TG2 complex (run 6)...	238
8.2.2	Repeated long MD simulation of the compound having no inhibitory effect (run 7).....	240
8.3	Discussion.....	243
9	GENERAL DISCUSSION AND CONCLUSIONS	245
9.1	Structure-activity relationship of the newly synthesised allosteric inhibitors of TG2	245
9.2	Structure-activity relationships of the newly synthesised irreversible inhibitors of TG2.....	246
10	APPENDIX.....	248
11	REFERENCES.....	253

List of Abbreviations

AMBER	assisted model building with energy refinement
BOC or tBOC	tert-butyloxycarbonyl protective group
Cbz	benzyloxycarbonyl protective group
CDI	1'-carbonyldiimidazole
DON	6-diazo-5-oxo-norleucine
d	doublet
DCM	dichloromethane
dd	doublet of doublets
DIPEA	N,N-diisopropylethylamine
DMSO	dimethyl sulfoxide
dt	doublet of triplets
dtc	dithiothreitol
ECM	extracellular matrix
EDC	1-ethyl-3-(3-dimethylaminopropyl)carbodiimide
EDTA	ethylenediaminetetraacetic acid
Fmoc	9-fluorenylmethoxycarbonyl
GAFF	general amber force field
GOLD	genetic optimisation for ligand docking
GDP	guanosine diphosphate
GTP	guanosine triphosphate
HRMS	high resolution mass spectra
m	multiplet
MD	molecular dynamics
PDB	protein data bank
rhTG2	recombinant human tissue transglutaminase
RMSD	root-mean-squared-deviation
RMSF	root-mean-squared-fluctuation
s	singlet
t	triplet
td	triplet of doublets
TFA	trifluoroacetic acid
TGases	transglutaminases
TG2	human tissue transglutaminase
TLC	thin layer chromatography
tt	triplet of triplets
VMD	visual molecular dynamics

List of Tables

Table 3.1. List of potential allosteric inhibitors subjected to MD simulations.....	72
Table 4.1. Optimisation of conditions of the reactions to synthesise the key intermediate esters ethyl 4-oxo-5-phenyl-3H-thieno[2,3-d]pyrimidine-2-carboxylates (compounds 36a,b,c) from the commercially available ethyl 2-amino-4-phenyl-thiophene-3-carboxylate derivatives (compounds 38a,b,c).	110
Table 5.1. List of potential irreversible TG2 inhibitors applied for MD simulations...	135
Table 6.1. The target potential irreversible inhibitors attempted to synthesise.	167
Table 7.1. Inhibition data for the lead TG2 irreversible inhibitor (compound 27) and the newly synthesised irreversible TG2 inhibitors.	216
Table 7.2. Inhibition data for the lead allosteric TG2 inhibitor (compound 6) and the newly synthesised allosteric TG2 inhibitors.	219
Table 8.1. Ligands used for long MD simulations of TG2-ligand complexes.....	224
Table 10.1. Log [inhibitor] vs. %TG2 activity curves of irreversible inhibitors of TG2.	248
Table 10.2. Log [inhibitor] vs %TG2 activity curves of allosteric inhibitors of TG2 ..	250

List of Schemes

Scheme 1.1. Proposed inhibition mechanism of halomethyl ketones (Powers et al., 2002).	35
Scheme 1.2. Proposed TG2 inhibition mechanism of 3-halo-4,5-dihydroisoxazoles (Castelhano et al., 1988).	37
Scheme 1.3. Proposed inhibition mechanism of thioimidazolium methyl ketones (Freund et al., 1994).....	43
Scheme 1.4. Proposed inhibition mechanism of 1,2,4-thiadiazole inhibitors (Marrano et al., 2001).	44
Scheme 1.5. Proposed inhibition mechanism of vinyl sulfones and α,β -unsaturated carbonyl TG2 inhibitors (Powers et al., 2002).....	46
Scheme 1.6. Proposed inhibition mechanism of epoxides (Powers et al., 2002).....	54
Scheme 1.7. Proposed inhibition mechanism of diazomethyl ketones (Powers et al., 2002).	55

Scheme 4.1. A method to synthesise ethyl 4-oxo-5-phenyl-3H-thieno[2,3-d]pyrimidine-2-carboxylate (compound 36a) according to the key publication with a reported yield of 80% (Nara et al., 2017).	107
Scheme 4.2. Synthesis of the potential TG2 allosteric inhibitor target compounds from the key intermediate esters 36a,b,c	112
Scheme 4.3. A 3-step scheme to synthesise substituted thieno[2,3-d]pyrimidin-4(3H)-ones (compound 39a,b,c).	115
Scheme 6.1. Synthesis of the scaffold of compound 27	168
Scheme 6.2. Attachment of acrylamide and 4-amino-4-oxo-2-butenic acid warheads on the short amine 43	170
Scheme 6.3. Attachment of various electrophilic warheads on the the scaffold of compound 27	171
Scheme 6.4. Attempted synthesis of the (E)-isomer of compound 27b	172
Scheme 6.5. Synthesis of 3-amino-5-benzylidenerhodanine derivatives.	173
Scheme 6.6. Attempted attachment of the acrylamide warhead on 47b	173
Scheme 6.7. Attempted synthesis of the 2-bromo amide derivative from amine 47b . ..	174
Scheme 6.8. Synthesis of pyridyl triazoly aniline scaffolds.	176
Scheme 6.9. Possible interconverting keto-enol forms of 52a,b	178
Scheme 6.10. Synthesis of the acrylamide having a short scaffold (compound 41a)... ..	179
Scheme 6.11. Attempted synthesis of 2-bromoacetamide derivatives.....	179
Scheme 6.12. Synthesis of 2-chloroacetamide derivatives from anilines 54a,b	180
Scheme 6.13. The attachment of a BOC group on amine 54a	181

List of Figures

Figure 1.1. A ping-pong mechanism of TGase-catalyzed acyl transfer reaction.....	22
Figure 1.2. Overall crystal structures and simplified cartoons of TG2 in different conformations.	25
Figure 1.3. (a) The formation of product via a catalytic reaction between an enzyme and a substrate in the absence of any inhibitor. (b) The inhibition of a competitive inhibitor to a free enzyme. (c) The inhibition of a covalent and irreversible inhibitor at a specific binding site of an enzyme.	29
Figure 1.4. Common TG2 inhibitors competitive with amine substrates.	30
Figure 1.5. <i>Trans</i> -cinnamoyl derivatives as highly potent competitive TG2 inhibitors developed by the Keillor group (Pardin et al., 2008a; Pardin et al., 2008b).....	31
Figure 1.6. The lead competitive TG2 inhibitor achieved by modification the α,β -unsaturated carbonyl motif of the lead <i>trans</i> -cinnamoyl TG2 inhibitor (Apperley et al., 2016).	32
Figure 1.7. 3-Acylidene-2-oxoindole TG2 reversible inhibitors developed by Klöck and co-workers (Klöck et al., 2011).	33
Figure 1.8. Lead allosteric reversible inhibitors of TG2.....	34
Figure 1.9. Chloromethyl amide TG2 inhibitors developed by the Keillor group (Pardin et al., 2006).	36
Figure 1.10. Halomethyl carbonyl TG2 inhibitors developed by the Griffin group (Badarau et al., 2015).	36
Figure 1.11. A series of 3-bromo 4,5-dihydroisoxazoles based on a Cbz-Phe scaffold or a Cbz-Tyr scaffold synthesised by the Khosla group (Choi et al., 2005).	37
Figure 1.12. Lead 3-bromo-4,5-dihydroisoxazoles inhibitors of TG2 developed by the Khosla group (Choi et al., 2005; Watts et al., 2006).....	39
Figure 1.13. Initial dimethylsulfonium ketone TG2 inhibitors (Pliura et al., 1992).....	40
Figure 1.14. Dimethylsulfonium ketone TG2 inhibitors developed by the Griffin group (Griffin et al., 2008).	41
Figure 1.15. Dimethylsulfonium ketone TG2 inhibitors based on the piperazine scaffold developed by the Griffin group (Badarau et al., 2015).	42
Figure 1.16. The prototype compound of thioimidazolium methyl ketone TG2 inhibitors (Barsigian et al., 1991).....	42
Figure 1.17. Thioimidazolium methyl ketone TG2 inhibitors developed by the Griffin group (Badarau et al., 2013).....	44

Figure 1.18. 1,2,4-thiadiazole TG2 inhibitors developed by the Keillor group (Marrano et al., 2001).	45
Figure 1.19. α,β -unsaturated carbonyl derivatives based on the Cbz-Gln-Gly scaffold (de Macédo et al., 2002).....	47
Figure 1.20. Fluorescent Cbz-Lys-based acryloyl TG2 inhibitors developed by the Keillor group (Keillor et al., 2008).	48
Figure 1.21. Cbz-Phe-based acryloyl TG2 inhibitors developed by the Keillor group (Pardin et al., 2006).....	49
Figure 1.22. General structure of a large series of acrylamide TG2 inhibitors having structures based on Cbz-Lys scaffolds developed by the Keillor group (Akbar et al., 2017).	49
Figure 1.23. The two best acrylamide TG2 inhibitors developed by the Keillor group (Akbar et al., 2017).	50
Figure 1.24. Lead Michael acceptor TG2 inhibitors discovered by the CHDI Foundation (Prime et al., 2012a; Prime et al., 2012b).	51
Figure 1.25. Acrylamide and vinylsulfonamide TG2 inhibitors developed by the Griffin group (Badarau et al., 2015).....	52
Figure 1.26: The lead acrylamide TG2 inhibitor discovered by the Griffin group (Badarau et al., 2015).....	52
Figure 1.27: Dipeptide mimic maleimide TG2 inhibitors developed by the Keillor group (Pardin et al., 2006).....	53
Figure 1.28. Epoxide TG2 inhibitors developed by the Keillor group (de Macédo et al., 2002).	55
Figure 1.29. Diazomethyl ketone TG2 inhibitors developed by the Khosla group (Hausch et al., 2003).	56
Figure 1.30. Diazomethyl ketone TG2 inhibitors developed by Zedira GmbH (Schaertl et al., 2010).	57
Figure 1.31. Simplified flowchart describes general process of a typical MD simulation.	59
Figure 3.1. The predicted allosteric site used for docking purpose (yellow) and the GTP/GDP binding site (red) in the open (active) conformation of TG2.	70
Figure 3.2. Interactions between the parent allosteric inhibitor with nearby residues at the starting frame of the MD simulation.	74
Figure 3.3. Intramolecular and intermolecular hydrogen bonds of the acylhydrazide thioether side chain of the parent compound at various frames of 200 ns MD simulation.	75

Figure 3.4. Some hydrophobic interactions formed between the phenyl ring of compound 31 and TG2 during 200 ns MD simulation.	76
Figure 3.5. Position of compound 31 when it formed hydrogen bonds with LEU420 (A) and GLU452 (B), and distances between the relevant atoms of these hydrogen bonds.	77
Figure 3.6. RMSD (Å) of compound 31 in comparison to that of the parent compound.	78
Figure 3.7. (a) Interactions between compound 32a and TYR445; (b) distance between the ligand O (pyrimidine CO) and TYR445 H (backbone NH); (c) distance between the ligand H (pyrimidine NH) and O (backbone CO) of TYR445.	79
Figure 3.8. (a) An alkyl-alkyl interaction between LYS344 and compound 32b ; (b) distance between C (para CH ₃) of compound 32b and C (CH ₂ side chain) of LYS344.	80
Figure 3.9. (a) Interactions between ALA399 and compound 32c ; (b) distance between the ligand H27 and O of ALA399; (c) distance between the ligand O26 and H of ALA399.	81
Figure 3.10. (a) The ligand thieno[2,3-d]pyrimidine ring was clamped between PHE456 and ARG418; (b) interactions between the thieno[2,3-d]pyrimidine ring and nearby residues.	81
Figure 3.11. RMSD values for compounds 32a,b,c during 200 ns MD simulations.....	82
Figure 3.12. Hydrophobic interactions between the ligand phenyl head and the nearby residues.	83
Figure 3.13. Proposed distances of the hydrophobic interactions formed between the ligand phenyl ring and three residues of the hydrophobic pocket: ALA455, LYS444 and PHE394.	84
Figure 3.14. RMSD values of compound 33b during 200 ns MD simulation.....	84
Figure 3.15. (a) Hydrogen bond between compound 33b and ALA399 and (b) the distance between the relevant atoms of this hydrogen bond during 200 ns simulation..	85
Figure 3.16. (a) Interactions between TYR445 and compound 33c ; (b) distance between O26 of the ligand and H of TYR445 amino; (c) distance between H27 of the ligand and O of TYR445 carbonyl.	86
Figure 3.17. RMSD values of compound 33d during 200 ns MD simulation.....	87
Figure 3.18. (a) Interactions between the head of compound 33d and 2 residues ALA455 and PHE394; (b) Distance between ligand C15 and ALA455 CB; (c) Distance between the ligand C11 and the centre of the PHE394 phenyl ring; (d) Distance between the centres of the two phenyl rings of the ligand and PHE394.....	88
Figure 3.19. High occurrence hydrogen bonds between compound 34a and four residues including ALA399, LEU420, VAL422 and LYS444.	89

Figure 3.20. Distances between the relevant atoms of the hydrogen bonds between the ligand amide side chain and three residues including ALA399, LEU420 and VAL422.	89
Figure 3.21. RMSD values (Å) of compound 34a during 100 ns MD simulation.	90
Figure 3.22. (a) Hydrogen bonds between the amide tail of compound 34b and two residues ALA399 and VAL422; (b) Distance between the ligand amide carbonyl O and the VAL422 amino H; (b) Distance between the ligand amide amino H and the ALA399 carbonyl O.	91
Figure 3.23. (a) Hydrogen bonds between the head of compound 34d and two residues LYS380 and TYR445; (b) distances between the relevant atoms.	92
Figure 3.24. RMSD values (Å) of compound 34d during 100 ns MD simulation.	93
Figure 3.25. (a,b) Positions of the hydroxyl group of compound 34e when it formed hydrogen bonds with TYR443 and LYS380, respectively; (c) distances between the relevant atoms of these hydrogen bonds.	94
Figure 3.26. (a) Hydrogen bonds between compound 34e and TYR445; (b) Distance between O26 and H of TYR445, distance between H27 and O of TYR445 and RMSD values.	95
Figure 3.27. RMSD values (Å) of compounds 34e during 100 ns MD simulation.	95
Figure 3.28. Hydrogen bonds between compound 34f and TYR445 and distances between the relevant atoms of these hydrogen bonds during 100 MD simulation.	96
Figure 3.29. The hydrogen bond between the side chain of compound 34f and GLU447 (a); the hydrophobic interactions between the phenyl head of compound 34f and nearby residues.	97
Figure 3.30. RMSD values (Å) of compounds 34a,f during 100 ns MD simulation.	97
Figure 3.31. RMSD values (Å) of compounds 34a,g during 100 ns MD simulation.	98
Figure 3.32. (a,b) Hydrogen bonds between compound 35a and two residues ASN398 and ALA399; (c) distance between the relevant atoms of these hydrogen bonds.	99
Figure 3.33. (a) Hydrogen bond between compound 35b and ASN398; (b) Distances between the relevant atoms.	100
Figure 3.34. (a) Hydrophobic interactions between the head of compound 35b and LYS444 and PHE394; (b) distance between the carbon atom of LYS444 and the central of the phenyl ring of the ligand; (c) distance between the ligand para-methyl carbon and the central of the phenyl ring of PHE394.	101
Figure 3.35. Hydrogen bonds between compound 35c and two residues ALA399 and LEU420 and distances of the relevant atoms of the bonds.	102

Figure 3.36. (a) Hydrogen bonds between compound 36c and two residues ASN398 and ALA399; (b) distances between the relevant atoms of these hydrogen bonds.	103
Figure 3.37. (a) Hydrophobic interactions between the head of the ligand and two residues ALA455 and ALA459; (b) distance between the carbon atom of the para-methyl and two methyl carbon atoms of ALA459 and ALA455.	104
Figure 3.38. RMSD values (Å) of compounds 37a,b,c during 100 ns MD simulations.	105
Figure 4.1. General structure of the potential TG2 allosteric inhibitor target compounds.	107
Figure 4.2. Structure of 5-phenyl-3H-thieno[2,3-d]pyrimidine-4-one and its derivatives (compounds 39a,b,c)	113
Figure 5.1. Interactions between the lead TG2 irreversible inhibitor and the enzyme catalytic binding site in the starting frame of the MD simulation.	136
Figure 5.2. Positions of compound 27 in the catalytic binding site in the first frame (a) and in the last frame (b) of 200 ns MD simulation.	137
Figure 5.3. Hydrogen bonds between compound 27 and two residues ASN333 and PHE334 and the distances between the relevant atoms during the first 15.2 ns MD simulation.	137
Figure 5.4. Distance between the electrophilic warhead carbon of compound 27 and the CYS277 sulphur during the period the warhead was retained in the catalytic tunnel (a) and the position of the ligand and CYS277 when the distance was the shortest (b). ...	138
Figure 5.5. Position of compound 27a at the first frame (a) and at the last frame (b) of 200 ns MD simulation.	138
Figure 5.6. Hydrogen bonds between compound 27a and four residues ASN333, PHE334, GLN276 and CYS277 and the distances between the relevant atoms.	139
Figure 5.7. Distance between the warhead electrophilic carbon of compound 27a and CYS277 sulphur atom during 200 ns MD simulation (a) and the position of compound 27a and CYS277 when the distance was the shortest (b).	140
Figure 5.8. Position of compound (E)- 27b at the beginning (a) and at the end (b) of 200 ns MD simulation.	140
Figure 5.9. Hydrogen bonds between compound (E)- 27b and three residues ASN333, PHE334 and CYS336 (a) and the distances between the relevant atoms (b).	141
Figure 5.10. Distance between the warhead of compound (E)- 27b and CYS277 sulphur atom during the period the warhead was maintained in the catalytic tunnel (a) and positions of compound (E)- 27b and CYS277 when the distance was the shortest (b).	142

- Figure 5.11. Distance between the warhead electrophilic carbon of compound (**Z**)-**27b** and CYS277 sulphur atom during 200 ns MD simulation (a) and positions of compound (**Z**)-**27b** and CYS277 when distance was the lowest (b). 142
- Figure 5.12. Position of compound (**Z**)-**27b** at a frame when the hydrogen bond was formed between the ligand carboxylate and the imidazole amino of protonated HIS335 (a) and the distance between the relevant atoms during 200 ns MD simulation (b). 143
- Figure 5.13. Position of compound (**E**)-**27c** in the first frame (a) and in the last frame (b) of 200 ns MD simulation. 144
- Figure 5.14. (a) Hydrogen bonds between compound (**E**)-**27d** and three residues GLN169, ASN333 and PHE334; (b) distance between O the ligand carboxylate CO and H of GLN169 side chain NH; (c) distances between relevant atoms of the hydrogen bonds between the ligand CO and the NH groups of two residues PHE334 and ASN333; (d) Distance between H of the ligand acrylamide NH and O of PHE334 CO. 145
- Figure 5.15. The distance between the warhead electrophilic carbon of compound (**E**)-**27c** and CYS277 sulphur atom during 200 ns MD simulation (a) and the position of this compound and CYS277 when the distance was the shortest (b). 146
- Figure 5.16. Positions of compound **27e** at the first frame and at a frame when the naphthalene ring relocated to the outside of the catalytic tunnel. 146
- Figure 5.17. Interactions between compound **27e** and three residues ASN333, PHE334 and CYS336 (a) and distances between the relevant atoms of these hydrogen bonds during the first 107.0 ns MD simulation. 147
- Figure 5.18. Distances between the warhead electrophilic carbon of compound **27e** and sulphur atoms of CYS336 and CYS277 during the period the warhead was retained in the catalytic tunnel (a) and positions of the ligand when these distances were the lowest, respectively (b,c). 148
- Figure 5.19. The distance between the warhead electrophilic carbon of compound (**Z**)-**27f** and CYS277 sulphur atom during 200 ns MD simulation. 149
- Figure 5.20. RMSD values of compound **27g** and the distance between the warhead electrophilic carbon and CYS277 sulphur atom during 200 ns MD simulation. 150
- Figure 5.21. Hydrogen bonds between compound **27g** and two residues CYS277 and PHE334 (a) and distances of the relevant atoms during the first 28.5 ns MD simulation (b). 150
- Figure 5.22. Distance between the warhead electrophilic carbon of compound **27g** and CYS277 sulphur atom during the first 28.5 ns MD simulation (a) and the position of this compound when the distance was the shortest (b). 151
- Figure 5.23. The distance between the warhead electrophilic carbon of compound (**Z**)-**27h** and CYS277 sulphur atom during 200 ns MD simulation. 152

Figure 5.24. Hydrogen bonds between compound 26a and two residues ASN333 and PHE334 (a) and distances of the related atoms during the first 17.3 ns MD simulation.	153
Figure 5.25. Positions of compound 26a in the first (a) and the last frame (b) of 200 ns MD simulation.	153
Figure 5.26. The distance between the warhead electrophilic carbon of compound 26a and CYS277 sulphur atom during the first 17.3 ns MD simulation (a) and the position of this compound when the distance was the shortest (b).	154
Figure 5.27. Hydrogen bonds between compound (Z)- 26b and three residues GLN276, TRP278 and PHE334 (a) and distances of the relevant atoms during the first 9.4 ns of the MD simulation.	155
Figure 5.28. The distance between the warhead electrophilic carbon of compound (Z)- 26b and CYS277 sulphur atom during the first 9.4 ns MD simulation (a) and the position of this compound when the distance was the shortest (b).	155
Figure 5.29. The hydrogen bond between compound 40a and residue ASN333 when the ligand warhead was held in the catalytic tunnel (a) and when it relocated to the outside of the tunnel (b).	156
Figure 5.30. RMSD values of compound 40a , the distance between the O carbonyl warhead and the H amine backbone of ASN333 and the distance between the warhead electrophilic carbon and CYS277 sulphur atom during 120 ns MD simulation.	157
Figure 5.31. Pi-pi stacked interactions between the naphthalene ring of compound 40b and two residues TRP241 and TRP332 during 200 ns MD simulation.	158
Figure 5.32. Hydrogen bonds between compound 40b and two residues ASN229 and ARG240 (a), the distance between H atom of ASN229 side chain amino and the O atom of the ligand acrylamide carbonyl (b) and the distance between the H atom of ARG240 backbone amino and the ligand sulphur (C=S) during 200 ns MD simulation.	159
Figure 5.33. The distance between the warhead electrophilic carbon of compound 40b and CYS277 sulphur atom (a) and the position of this compound at the shortest distance (b).	160
Figure 5.34. The position of compound 41b (a) and interactions between this compound and the protein (b) in the first frame of the MD simulation.	160
Figure 5.35. Hydrogen bonds between compound 41b and two residues GLN276 and CYS277 (a) and distances of these bonds during 19.0 ns MD simulation.	161
Figure 5.36. The distance between the warhead electrophilic carbon of compound 41b and CYS277 sulphur atom during the first 18.5 ns MD simulation (a) and the position of this compound at the shortest distance (b).	161
Figure 5.37. (a) RMSD values of compound 41a and the distance between the warhead electrophilic carbon and CYS277 sulphur atom during 200 ns MD simulation; (b) The	

distance between the warhead electrophilic carbon and CYS277 sulphur atom during the first 17.9 ns MD simulation.	163
Figure 5.38. A hydrogen bond between compound 41a and GLN276 (a) and the distance between H atom of the ligand acrylamide NH and the O atom of the side chain CO of GLN276 (b) in the first 17.9 ns MD simulation.	164
Figure 6.1. ¹ H NMR spectra of compound 52a taken at room temperature (upper) and at 60 °C (lower).	177
Figure 6.2. ¹ H NMR spectra of compound 52b taken at room temperature (upper) and at 60 °C (lower).	178
Figure 7.1. Log [inhibitor]-%TG2 activity curves of compound 35b with and without addition of GTP.	221
Figure 8.1. RMSF values of empty TG2 during 800 ns MD simulation.	225
Figure 8.2. Conformations of TG2 in the first cluster (blue), cluster 3 (yellow) and the final cluster (red) in run 1.	225
Figure 8.3. Positions of CYS277, TRP241, TRP332 and two loops (coloured in purple and blue) residing in front of the proposed acyl-acceptor entrance (A) and the residues forming hydrogen bonds between these loops (B).	226
Figure 8.4. Distances between the relevant atoms of the hydrogen bonds between SER328 and two residues PRO361 and GLN362 during 800 ns MD simulation of the empty TG2.	227
Figure 8.5. RMSD values of compound 32a during 300 ns MD simulation.	228
Figure 8.6. Conformations of TG2 in the first (blue) and the final (red) cluster of 700 ns MD simulation of the parent allosteric inhibitor – TG2 complex.	229
Figure 8.7. RMSF values of the empty TG2 and TG2 under the binding of the parent allosteric inhibitor during 700 ns MD simulation.	229
Figure 8.8. A hydrogen bond between the parent allosteric inhibitor and residue ALA399 and the distance between the relevant atoms.	230
Figure 8.9. Conformations of TG2 under the binding of compound 35c in the first (blue) and the final (red) cluster during 800 ns MD simulation.	230
Figure 8.10. RMSF values of the empty TG2 and TG2 under the binding of compound 35c during 800 ns MD simulation.	231
Figure 8.11. Hydrogen bonds between compound 35c and two residues ALA399 and ASP400.	232
Figure 8.12. Distances between the relevant atoms of the hydrogen bonds formed between compound 35c and two residues ALA399 and ASP400.	232

Figure 8.13. RMSD (Å) of the parent compound, compounds 35b and 35c during the MD simulations.....	233
Figure 8.14. Conformations of TG2 under the binding of compound 35b in the first (blue) and the final (red) cluster.....	233
Figure 8.15. RMSF values of the empty TG2 and TG2 under the binding of compound 35b during 800 ns MD simulation.	234
Figure 8.16. Hydrogen bonds between compound 35b and ASP400 and the distances between the relevant atoms.	234
Figure 8.17. RMSD (Å) of TG2 backbone atoms during run 1 (a), 3 (b), 5 (c) and 4 (d).	235
Figure 8.18. Differences between RMSF values of the empty TG2 and TG2 under the binding of the potent inhibitors 35b,c	236
Figure 8.19. Relevant hydrogen bonds formed between the allosteric inhibitor 35b , residue ASP400 of the predicted allosteric site, residue ASP573 and residue SER328 of the catalytic site.....	237
Figure 8.20. Distances between the sulphur atom of CYS277 and hydro (indole NH) of TRP241 during MD simulation of the empty TG2 (red) and TG2 under the binding of compound 35b (blue).	238
Figure 8.21. Differences between RMSF values of empty TG2 and TG2 under the binding of 35b in the repeated MD simulation.	239
Figure 8.22. Hydrogen bonds between compound 35b and two residues ASN398 and ASP399 and the distances between the relevant atoms during the repeated 800 ns MD simulation.....	239
Figure 8.23. (a) Hydrogen bonds formed between compound 35b and ASP400; (b) distance between CYS277 sulphur and TRP241 indole NH (H) and the distances between the atoms relevant to the hydrogen bonds formed between the ligand and ASP400 during the period TRP241 moved towards to the outside of the catalytic binding site.....	240
Figure 8.24. Distances between the relevant atoms of the hydrogen bonds formed between the two loops residing in front of the catalytic binding site during 800 ns MD simulation of compound 32a – TG2 complex.	241
Figure 8.25. Differences between RMSF values of the empty TG2 and TG2 under the binding of 32a in the repeated MD simulation.	241
Figure 8.26. (a) Position of compound 32a when it formed hydrogen bonds with TYR445 (the loop containing ASN398, ALA399 and ASP400 is coloured in yellow) (b) the hydrogen bonds between the ligand and TYR445.	242
Figure 8.27. Distances between atoms related to the hydrogen bonds formed between compound 32a and residue TYR445.	242

1 General Introduction

1.1 Tissue transglutaminase

1.1.1 Physiological roles and disorders

Transglutaminases (TGases) are calcium dependent enzymes that catalyse the cross-linking of proteins by mediating an acyl-transfer reaction between the gamma carboxamide group of a peptide-bound glutamine residue and the epsilon amino group of a peptide-bound lysine or a primary amine (Griffin et al., 2002). The TGases-mediated acyl transfer reaction is known as a ping-pong mechanism that includes the reversible acylation of an active-site cysteine residue and the release of one equivalent of ammonia to give an acyl-enzyme intermediate. If an amine acyl acceptor substrate is present, the acyl-enzyme intermediate reacts with the amine and releases the transamidation product with the free enzyme. In the absence of a free amine, the acyl-enzyme intermediate undergoes hydrolysis, resulting in hydrolytic deamidation with the formation of a free enzyme, which returns to the catalytic cycle. The catalytic cycle is summarised in Figure 1.1.

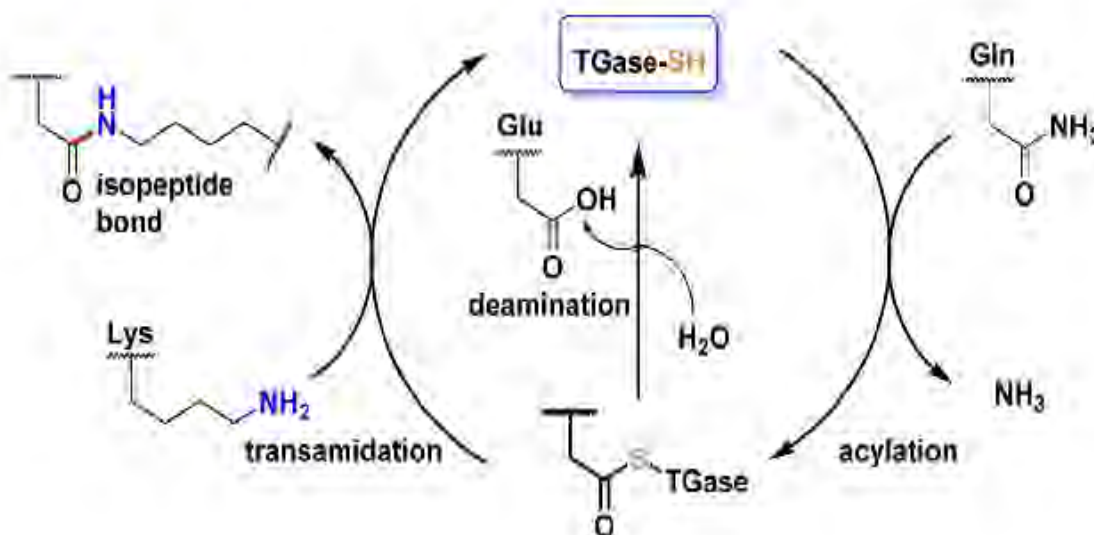


Figure 1.1. A ping-pong mechanism of TGase-catalyzed acyl transfer reaction.

Reproduced (open access) from (Song et al., 2017).

Tissue transglutaminase (TG2) is possibly the most ubiquitous member among eight catalytically active TGases including TG1, TG3, and TG5, which are mainly expressed

in epithelial tissue; TG4, which is expressed in the prostate gland; factor XIIIa (FXIIIa), which is expressed in the blood; TG6 which is expressed in the testis, lungs, and brain; TG7, which is prominently distributed in the testis and lungs (Odi and Coussons, 2014). TG2 has been proved to be involved in number of biological roles and pathological disorders. Catalyzing the cross-linking of the extracellular matrix is possibly the most essential biological role of TG2, however, under stress, the over expression of TG2 has been indicated to be involved in various types of fibrosis (Olsen et al., 2011) and atherosclerosis (Lai et al., 2007). TG2 has been proposed as a novel target for the treatment of pulmonary fibrosis (Olsen et al., 2014), liver fibrosis (Daneshpour et al., 2011), chronic kidney disease (Scarpellini et al., 2014) and cardiac fibrosis (Wang et al., 2018). Additionally, TG2-mediated cross-linking has been implicated in contributing to the pathogenesis of many neurodegenerative disorders, including Alzheimer's, Parkinson's, and Huntington's diseases (Kim et al., 2002; Ruan and Johnson, 2007; Aronin, 1999) and in diseases related to neurotransmitter release. TG2 has also been indicated to play a pathogenesis role in cancer, in which the increased cellular level of TG2 promotes to the development of drug resistance and metastatic phenotype in various cancer cell types such as that of pancreatic cancer (Verma et al., 2007), ovarian cancer cells (Hwang et al., 2008; Satpathy et al., 2007), breast cancer (Mangala et al., 2007), glioblastoma and malignant melanoma (Fok et al., 2006). The over-expression of TG2 was pointed out in the contribution of cancer cell migration and invasion (Kumar et al., 2014). More recently, TG2 has also been considered as a novel therapeutic target for the prevention and treatment of castration-resistant prostate cancer (Han et al., 2014). However, the best-understood pathology of TG2 is probably celiac disease, which is an immune-mediated disease activated by the ingestion of gliadin and of other toxic prolamines in genetically susceptible individuals. TG2 is a target autoantigen and its deamidation reaction of glutamine-rich gliadin peptides enhance the immunostimulatory effect of gluten (Di Sabatino et al., 2012).

1.1.2 Structural diversity

Full-length human TG2 embraces 687 amino acids that are distributed in four separate domains: the N-terminal β -sandwich domain, the catalytic domain containing a CYS277–HIS335–ASP358 catalytic triad, and two C-terminal β -barrel domains. Between the catalytic core and the first β -barrel there is a cleft where a unique GTP-binding site is located (Liu et al., 2002). The catalytic CYS277 is located near a

threonine residue (THR360) at the edge of a hydrophobic tunnel bridged by two tryptophan residues (TRP241 and TRP332) on separate loops in the active site (Pinkas et al., 2007). The enzymatic activity of TG2 was proved to require the presence of the N-terminal β -sandwich domain and the catalytic domain but not the C-terminal β -barrel domains (Iismaa et al., 1997).

TG2 has been pointed out in various structural studies to undergo an extraordinarily large conformational change upon activation. Ca^{2+} activates TG2 by promoting an extended structure (open form) in which the active site is exposed to the substrates. The binding of a gluten peptide mimetic irreversible inhibitor (Ac-Pro-Gln-Pro-DON-Leu-Pro-Tyr-NH₂) also promoted an open form of TG2 (Pinkas et al., 2007). In contrast, guanosine-5'-triphosphate (GTP), guanosine diphosphate (GDP), and adenosine triphosphate (ATP) inactivate TG2 by inducing a compact conformation (closed form) in which the active site is buried by two C-terminal β -barrels and the extended conformational change is blocked by a hydrogen bond formed between Cys277 and Tyr516 (Liu et al., 2002; Jang et al., 2014). The crystal structures of the open and closed form of TG2 under the binding of GDP and the gluten peptide mimetic irreversible inhibitor, respectively, are described in Figure 1.2. The PDB file of the TG2's active form (code 2Q3Z) achieved in the study of Pinkas and co-workers (Pinkas et al., 2007) was used in computational modelling work in this project.

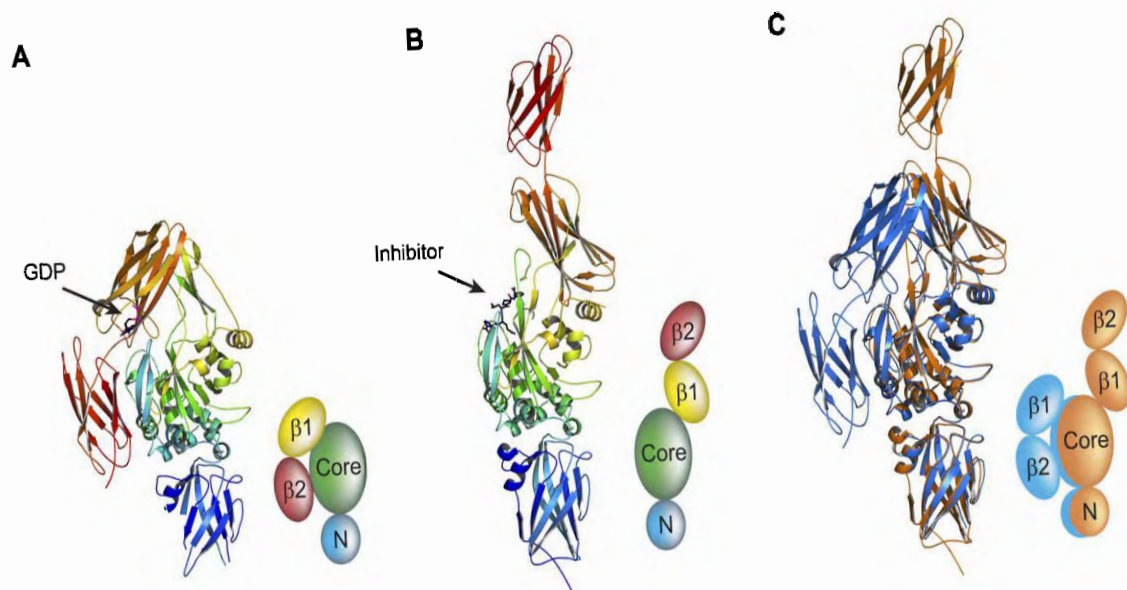


Figure 1.2. Overall crystal structures and simplified cartoons of TG2 in different conformations.

(A) GDP-bound closed conformation, (B) irreversible inhibitor Ac-Pro-Gln-Pro-DON-Leu-Pro-Tyr-NH₂-bound open conformation and (C) superimposed structures of the GDP-bound structure and the inhibitor-bound structure.

(A and B) The N-terminal β -sandwich (N) is coloured in blue, the catalytic core domain (Core) in green, and the C-terminal β -barrels ($\beta 1$ and $\beta 2$) in yellow and red, respectively. (C) The GDP-bound structure is coloured in blue and the inhibitor-bound structure in gold.

Reproduced (open access) from (Pinkas et al., 2007).

TG2 was primarily found in the cytosol where its transamidase activity is normally silent owing to the low concentration of Ca^{2+} allowing GTP/GDP to act as allosteric inhibitors by inducing a closed conformation (Begg et al., 2006). However, under chemical and physical injuries and circumstances in which concentration of Ca^{2+} is increased, the closed conformation of TG2 is transformed rapidly into the active form for transamidase activity. In the extracellular space, where concentration of GTP/GDP is low and concentration of Ca^{2+} is high, TG2 should be in the active form. However, it was observed that under normal physiological conditions, most TG2 in the extracellular matrix is in the inactive form and is only transiently activated upon certain types of inflammation and cell injury (Siegel et al., 2008). It was indicated that the activity of extracellular TG2 is regulated by the isomerization of disulfide bonds within its tertiary structure (Stamnaes et al., 2010).

1.2 Biological assays for TG2 activity

1.2.1 Enzyme-coupled assay

There are two-step reactions in this assay technique. Firstly, 1 equiv of ammonia is released by the transamidation reaction of TG2 on its glutamine substrate, N-benzyloxycarbonyl-L-glutaminyglycine (Cbz-Gln-Gly). This released ammonia will be used by a glutamate dehydrogenase (GDH) coupled reaction where GDH catalyzes the reductive amination of α -ketoglutarate (α -KG) to produce a glutamate following the consumption of a hydride donor, nicotinamide adenine dinucleotide (NADH). The amount of NADH was detected by monitoring its absorbance at 340 nm to indirectly measure TG2 activity (Day and Keillor, 1999).

1.2.2 Radioactive transamidation assay

This assay technique is based on the TG2-catalysed crosslinking reaction between a radioactive amine substrate ($[^3\text{H}]$ or $[1,4\text{-}^{14}\text{C}]$ putrescine) and a glutamine-containing protein substrate (N,N-dimethylatedcasein or succinylated casein) in a buffer system. The reaction is terminated by the addition of trichloroacetic acid and a scintillation counter is used to quantify the radioactivity after adding scintillation fluid (Schaertl et al., 2010; Lee et al., 2013).

1.2.3 Fluorescence transamidation assay

Case and coworkers developed a fluorescence assay technique in which TG2 activity is measured by the covalent incorporation of fluorescent Lys derivative (N-Boc-Lys-NH-CH₂-CH₂-NH-dansyl; KXD) into NMC. The product formed by the TGase-catalyzed covalent coupling of KXD and NMC generates a shift in intensity and wavelength of fluorescence of the dansyl group. Therefore, kinetic measurement is possible during the reaction with excitation at 330 nm and emission at 530 nm (Case et al., 2005a).

The Keillor group reported a fluorescence transamidation assay using a fluorogenic substrate 4- (N-carbobenzoxy-L-phenylalanyl-amino)butyric acid coumarin-7-yl ester (ZFBC) (Gillet et al., 2005). This assay is based on the hydrolysis or transamidation reactions catalysed by TG2 following the release of the 7-hydroxycoumarin, which can be monitored by the increase of fluorescence with excitation at 330 nm and emission at 460 nm. Recently, a new fluorogenic substrate

bearing 7-hydroxy-4-methylcoumarin (7-HMC), Z-Glu-(HMC)-Gly-OH, was developed by the same group to improve this fluorescence assay technique (Wodtke et al., 2016).

The Keillor group also developed a direct discontinuous fluorometric transamidation assay based on the formation of a biotin-fluorophore conjugate, using a fluorescent, high affinity gamma-glutamyl donor substrate and a biotinylated amine as a gamma-glutamyl acceptor substrate. The consequent conjugate is fixed on streptavidin-coated beads and excess substrate is washed away. The transamidation activity of TG2 is measured by fluorescence measurement. (Gnaccarini et al., 2009)

1.2.4 Absorbance-based assay

A direct and continuous absorbance assay technique for determining TG2 activity by using N,N-dimethyl-1,4-phenylenediamine (DMPDA) as a gamma-glutamyl acceptor substrate and Cbz-Gln-Gly as a typical peptide gamma-glutamyl donor substrate was developed by de Macedo et al. The transamidation activity of TGase can be determined continuously following the increase in absorbance at 278 nm of the consequent anilide substituted with a strong electron-donating group (de Macedo et al., 2000).

1.2.5 Fluorescence anisotropy assay

This recent reported assay technique detected the fluorescence anisotropy caused by cross-linking of a fluorescently labeled TG2 substrate peptide to a larger acceptor protein through transamidation (Kenniston et al., 2013). Briefly, a fluorescein-labeled glutamine donor peptide (FL-PepT26) is used as a substrate for conjugation with a bovine serum albumin (BSA), a large protein containing numerous surface-exposed lysines. The resulting crosslinking product of the transamidation reaction between the donor peptide FL-PepT26 and the acceptor BSA causes a greater modification in fluorescence anisotropy.

1.3 Kinetics of enzyme inhibition

The formation of product via a catalytic reaction in the absence of any inhibitor consists of 2 steps as shown in Figure 1.3a. The rate of forming the product is approximated by Michaelis-Menten kinetics:

$$V(t) = \frac{dP}{dt} = \frac{V_{max} \times [S]}{K_m + [S]}$$

where $V(t)$ is the velocity of product (P) formation at any given time t , V_{max} is the maximal velocity of product formation, $[S]$ is the concentration of the substrate at time t , and K_m is the concentration of the substrate at which the product is formed at half of the maximal velocity (Krippendorff et al., 2009).

In the presence of a competitive inhibitor, which may form a complex with the free enzyme, the inhibition process is described in Figure 1.3b. The maximal velocity of product formation (V_{max}) is not altered over time while the rate of product formation at time t (V_t) is decreased. The chemical parameter used to evaluate the potency of a competitive inhibitor is the specificity constant K_i/K_m in which $K_i = k_{-1}/k_1$ indicates the dissociation constant of the inhibitor-enzyme complex (Krippendorff et al., 2009).

The inhibition of a covalent and irreversible inhibitor at a specific binding site of an enzyme occurs in two steps as showed in Figure 1.3c. First, the inhibitor binds to the active site to form a reversible protein-inhibitor complex ($E \cdot I$). The potency of this first step is defined by the binding constant K_I , which denotes the concentration of the inhibitor required for half of the maximum potential rate of covalent bond formation. In the second step, the inhibitor attacks the active site and forms a covalent protein-inhibitor complex ($E-I$). When the entire enzyme exists in the reversible complex with the inhibitor ($E \cdot I$) and no free enzyme remains (E), the observed rate of inactivation is the k_{inact} . The k_{inact} is a first-order rate constant describing the maximum potential rate of covalent bond formation. Collectively, the efficiency of a covalent and irreversible inhibitor is defined by the ratio k_{inact}/K_I (Strelow, 2017).

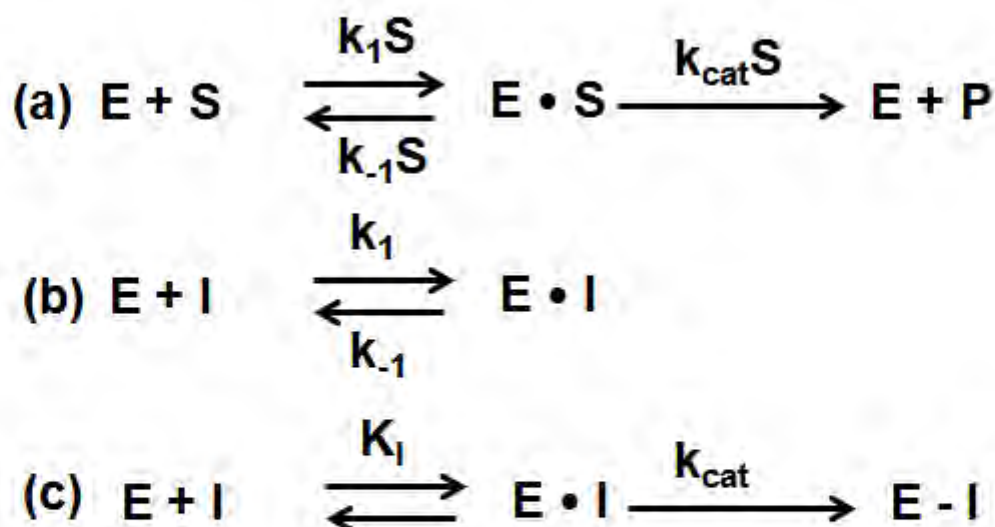


Figure 1.3. (a) The formation of product via a catalytic reaction between an enzyme and a substrate in the absence of any inhibitor. (b) The inhibition of a competitive inhibitor to a free enzyme. (c) The inhibition of a covalent and irreversible inhibitor at a specific binding site of an enzyme.

1.4 TG2 inhibitors

As a result of the acknowledged roles of TG2 in human pathogenesis, there has been a substantial interest in developing inhibitors of this enzyme for therapeutic treatment of various diseases. Until now, TG2 inhibitors have been generally classified in two distinct subclasses namely reversible (competitive or non-competitive) and irreversible inhibitors depending on the mechanism of inactivating the enzyme transamidation activity.

1.4.1 Inhibitors competitive with amine substrates

The inhibitors of this class block TG2 activity by competing with natural amine substrates such as peptide-bound lysine in the reaction to form an isopeptide bond. Putrescine, cystamine and cadaverine derivatives (Figure 1.4) are the most popular inhibitors among competitive amine inhibitors.

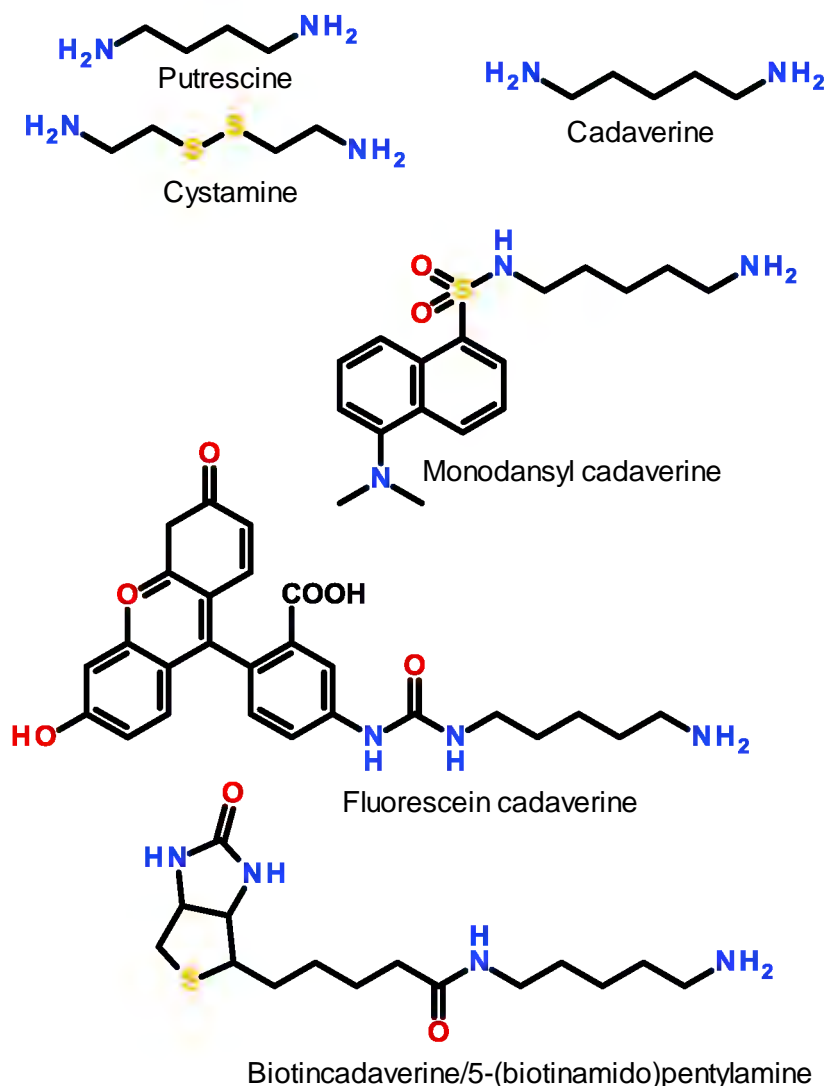


Figure 1.4. Common TG2 inhibitors competitive with amine substrates.

1.4.2 Inhibitors competitive with acyl-donor substrates

In 2008, a series of *trans*-cinnamoyl derivatives was prepared and tested against guinea pig liver transglutaminase by the Keillor group (Pardin et al., 2008a). Among the synthesised compounds, substituted cinnamoyl benzotriazolyl amides and 3-substituted cinnamoyl pyridines were acknowledged as the most potent inhibitors. Both of these subclasses expressed reversible inhibition and are competitive with acyl donor substrates of TG2 in kinetic assays. For the first subclass, the cinnamoyl alkene and the amide bond were proved to be essential for their potency. The most potent inhibitor (compound **1** Figure 1.5) in this subclass has an IC₅₀ value of 18 ± 1 μ M. Within the second subclass, the presence of nitrogen atom in the azachalcones and the attachment of p-nitro group on the cinnamoyl aromatic ring were demonstrated to favour inhibition.

The most potent inhibitor in this subclass (compound **2** Figure 1.5) has an IC_{50} value of $21 \pm 1 \mu M$.

Following this work, the same group further synthesised a new series of 15 cinnamoyl triazole derivatives and tested against guinea-pig liver transglutaminase in the same method (Pardin et al., 2008b). 4-Nitrocinnamoyltriazoles were demonstrated to be potent TG2 inhibitors by competition with acyl-donor substrates and compound **3** (Figure 1.5) is the most potent inhibitor in this class with an IC_{50} value of $2.1 \pm 0.3 \mu M$.

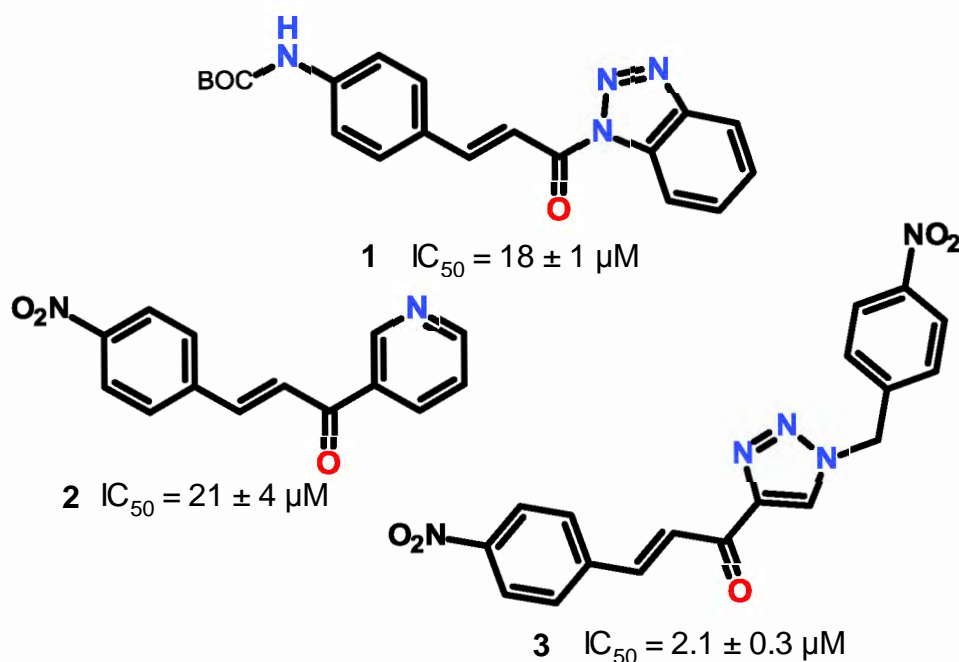


Figure 1.5. *Trans*-cinnamoyl derivatives as highly potent competitive TG2 inhibitors developed by the Keillor group (Pardin et al., 2008a; Pardin et al., 2008b).

Most recently, the same group (Apperley et al., 2016) suggested that the electrophilic α,β -unsaturated carbonyl in the developed *trans*-cinnamoyl derivatives may encounter a Michael addition with nucleophiles such as glutathione, a tripeptide thiol with a millimolar range of intracellular concentration. This reaction may result in a loss of potency *in vivo* because the alkene structure was proved to be vital for the potency of this class. Therefore, some modifications were made to the electrophilic moiety of compound **3** to decrease its reactivity toward glutathione. The synthesised compounds were tested against guinea pig liver transglutaminase using the same method as previously. Firstly, an alkyl group was added to the β -position of the $C=C$ double bond of the cinnamoyl moiety in order to increase steric hindrance and consequently reduce the electrophilic activity of the α,β -unsaturated carbonyl. Secondly, the α,β -unsaturated

carbonyl motif was modified to two three membered rings such as a cyclopropane to mimic the C=C double bond or an epoxide to mimic the carbonyl. The α,β -double bond of compound **3** was also incorporated into a heteroaromatic ring. Nonetheless, all that modifications significantly reduced the potency. The C=C double bond was then modified to a triple bond. That alteration provided a considerable increase in potency, with compound **4** (Figure 1.6) being a competitive inhibitor with IC_{50} value of $0.79 \pm 0.05 \mu\text{M}$ and K_i of $0.42 \pm 0.05 \mu\text{M}$. However, compound **4** is still reactive toward glutathione. The electrophilic alkene was replaced by a second triazole group. The resulting compounds showed a significant increase in resistance to nucleophilic attack by glutathione but their affinity is lower in comparison to the parent compound **3**.

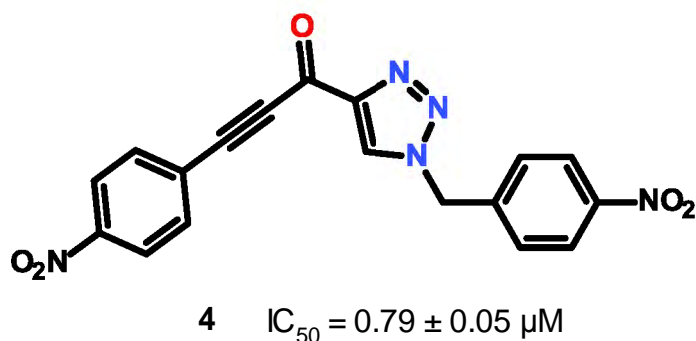


Figure 1.6. The lead competitive TG2 inhibitor achieved by modification the α,β -unsaturated carbonyl motif of the lead *trans*-cinnamoyl TG2 inhibitor (Apperley et al., 2016).

1.4.3 Allosteric reversible inhibitors

This class of TG2 inhibitors inhibits the enzyme activity by binding to an allosteric site and obstructing the access of substrates to the active site without covalently modifying the enzyme. Guanine nucleotides such as GTP and GDP, which promote the closed, catalytically inactive form of the enzyme, are examples of allosteric, reversible TG2 inhibitors (Lai et al., 1998). TG2 activity is also reversibly inhibited by the binding of the divalent metal ion Zn^{2+} that competes with Ca^{2+} for metal binding sites in the protein (Lorand and Conrad, 1984; Aeschlimann and Paulsson, 1994).

A series of 3-acylidene-2-oxoindoles (Figure 1.7a) was developed and evaluated against human TG2 using a glutamate dehydrogenase coupled deamidation assay with Cbz-Gln-Gly as the acyl donor substrate by Klöck and co-workers. The development of this class was based on the structure of isatin (indoline-2,3-dione) whose analogs have been

generally used as reversible inhibitors of Cys-dependent proteases. The 4-chloro analogue (compound **5** Figure 1.7b) exhibited the highest potency, with an IC_{50} value of 1.5 μ M. It was also observed that replacing the methyl group on the ketone moiety of compound **5** with an aromatic ring such as phenyl, substituted phenyl, pyridinyl and substituted pyridinyl groups provided a new set of TG2 inhibitors with similar IC_{50} values (Klöck et al., 2011).

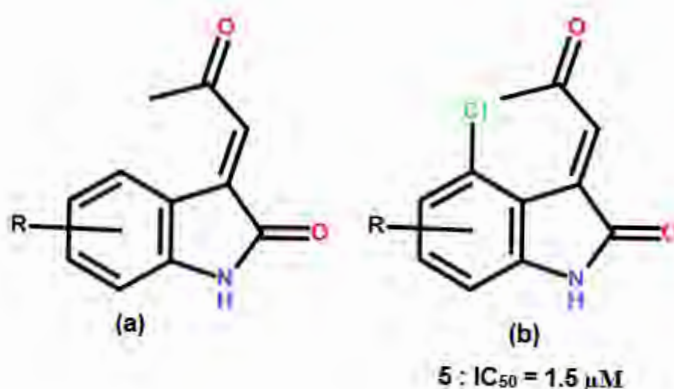


Figure 1.7. 3-Acylidene-2-oxoindole TG2 reversible inhibitors developed by Klöck and co-workers (Klöck et al., 2011).

A class of allosteric, reversible inhibitors with thieno[2,3-d]pyrimidin-4-one acylhydrazide backbones was discovered by screening a library of 110,000 compounds for TG2 inhibitors. The potency of this class was evaluated using a fluorescence-based assay that measured TG2 catalyzed incorporation of the dansylated Lys derivative into the protein substrate N,N-dimethylated-casein (Case et al., 2005a). Compound **LDN-27219** (compound **6** Figure 1.8) was identified to be the most potent inhibitor in this class with IC_{50} value of $0.6 \pm 0.1 \mu M$ against human TG2 (Duval et al., 2005). It was also indicated that **LDN-27219** is a slow-binding inhibitor and mutually exclusive with GTP. In addition, it was observed to be non-competitive inhibition with the protein substrate N,N-dimethylated-casein but competitive inhibition with GLN-containing tetrapeptides. The dependence of the potency and kinetics on the substrates suggested different binding of this inhibitor to multiple conformational states of TG2 (Case and Stein, 2007).

Kim et al discovered 2-(phenylethynyl)-3-(2-(pyrrolidin-1-yl) ethoxy) quinoxaline (compound **7** Figure 1.8) as the lead competitive inhibitor of TG2 after screening 1,000 structurally druggable heterocyclic compound libraries. The compound has an IC_{50}

value of 16.4 μM when being tested against guinea pig liver TG2 using a radioactive transamidation assay technique to measure the incorporation of $[1,4\text{-}^{14}\text{C}]$ putrescine into succinylated casein (Lee et al., 2013). The potency of compound **7** is increased approximately two fold when altering the quinoxaline ring to pyrido[2,3-*b*]pyrazine ring to make compound **8** (Figure 1.8) (Ku et al., 2014). The modification of the quinoxaline ring of compound **7** to thieno[3,4-*b*]pyrazine ring following various alterations on the phenyl ring as well as changing the 2-cyclopentylethoxy to optimize the novel core skeleton. Compound **9** (Figure 1.8) is the most potent allosteric TG2 inhibitor with an IC_{50} value approximately four times lower than its parent compound (Kim et al., 2014). Most recently, by using fluorescence techniques and a mass analysis approach the same group proved compound **8** allosterically binds to the N-terminus of TG2 around residues 81–116 and its binding inactivates TG2 activity through acceleration of non-covalent self-polymerization of TG2 via conformational change (Kim et al., 2018).

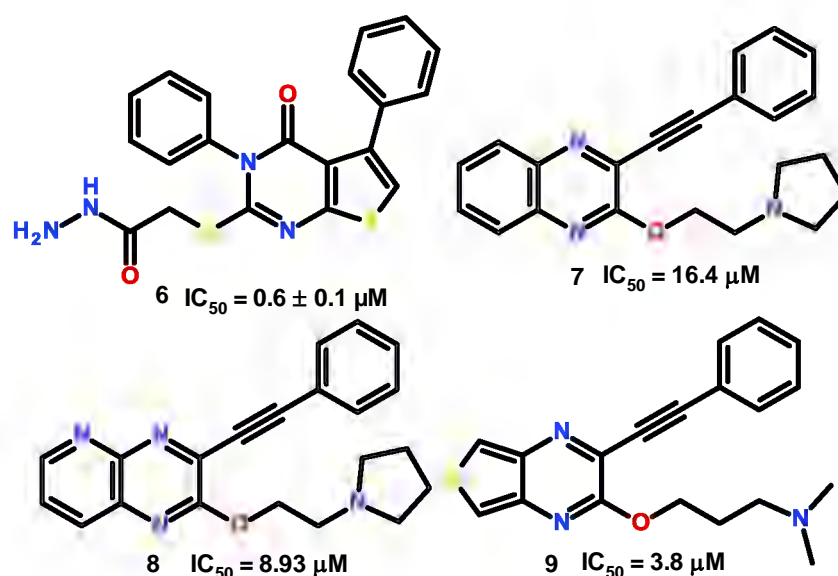


Figure 1.8. Lead allosteric reversible inhibitors of TG2.

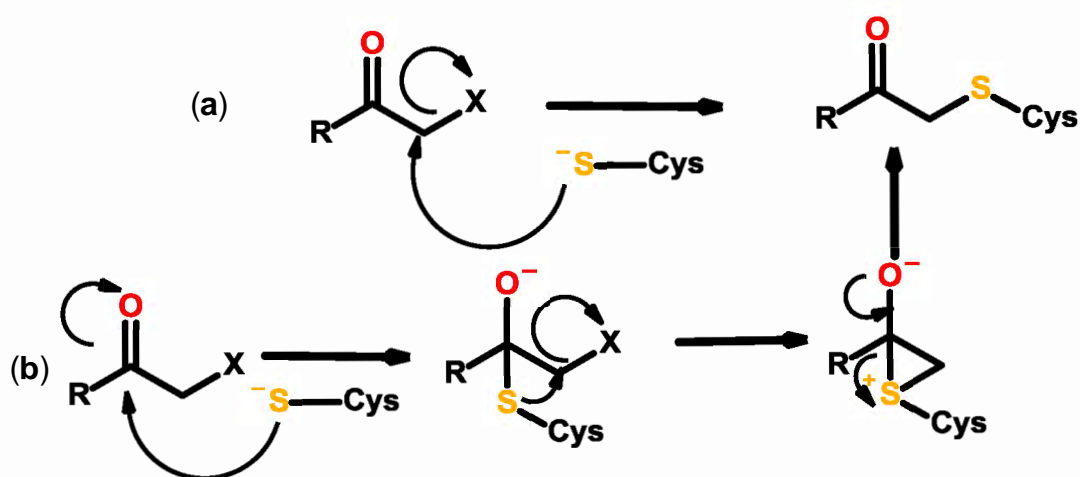
1.4.4 Irreversible inhibitors

Irreversible inhibitors contain an electrophilic functional group called a ‘warhead’ that blocks the enzyme activity by forming a covalent bond with the nucleophilic sulphur atom of catalytic CYS277 of the enzyme. This is the most widely developed category among TG2 inhibitors. The major research organizations involved include Griffin’s group (Aston University), Keillor’s group (University of Ottawa), Zedira, CHDI Foundation, Khosla’s group (Stanford University), and Kim’s group (National Cancer

Center Korea). Some of the most potent TG2 irreversible inhibitors sorted by the class of warhead are presented hereafter.

1.4.4.1 Halomethyl carbonyl derivatives

X-ray crystal structural data showed that the halomethyl ketones alkylated the active site cysteine residue to form a thioether bond. Therefore, the covalent thioether adduct was assumed to be produced by a direct displacement of the halide group by the thiolate anion or via forming of a thiohemiketal and a three-membered sulfonium intermediates before giving the final product (Scheme 1.1) (Powers et al., 2002).



Scheme 1.1. Proposed inhibition mechanism of halomethyl ketones (Powers et al., 2002).

Iodoacetamide is the structurally simplest irreversible inhibitor of thiol-dependent enzymes such as cysteine protease and also the first irreversible inhibitor tested against TG2 (Folk and Cole, 1966). The iodide moiety can be easily displaced by the nucleophilic active site thiol to form a relatively stable thioether bond. Iodoacetamide showed high potency on TGase purified from guinea pig liver with an efficiency constant $k_{\text{inact}}/K_I = 1.2 \times 10^7 \text{ M}^{-1} \text{ min}^{-1}$ (Folk et al., 1968).

In 2006, the Keillor group synthesised a series of chloromethyl ketones based on the simple Cbz-Phe dipeptide scaffold (Figure 1.9). The synthesised compounds were tested against the recombinant guinea pig liver TGase using a continuous chromogenic assay technique. The affinity for TG2 of the chloromethyl amide compounds is 2 orders of magnitude higher than that of iodoacetamide. In addition, it is affected by the length of

the Cbz-Phe-spacer-electrophile: the longer the spacer, the more efficient the inhibitors are (Pardin et al., 2006).

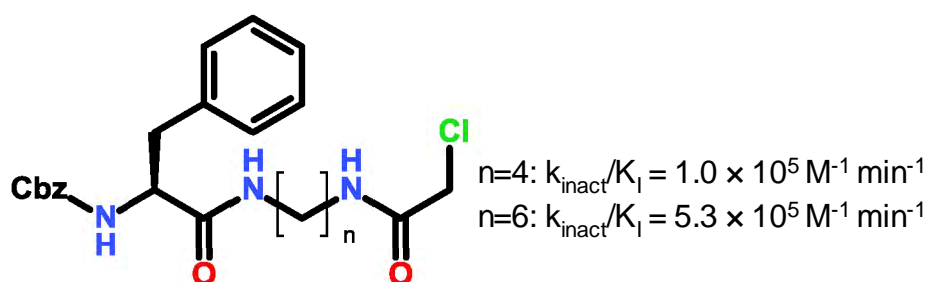


Figure 1.9. Chloromethyl amide TG2 inhibitors developed by the Keillor group (Pardin et al., 2006).

More recently, a series of halomethyl carbonyl derivatives with scaffolds containing a piperazine ring incorporating a carbamate (various-sized aromatic carbamates or tertbutyl carbamates) was synthesised by the Griffin group (Figure 1.10). The synthesised derivatives were tested against recombinant purified human TG2 using an enzyme sorbent assay technique to measure the covalent incorporation of biotinyl-5-pentylamine into N,N-dimethylcasein. These inhibitors expressed excellent potency with IC_{50} values in low nanomolar range. However, their high cellular toxicity profile due to the halide precursors, especially the more reactive bromides, prevented them from further pharmacological research (Badarau et al., 2015).

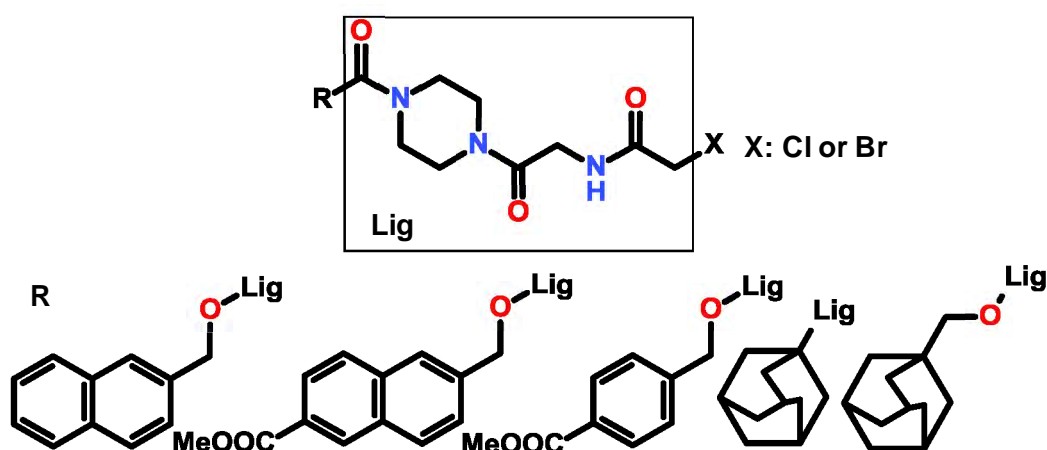
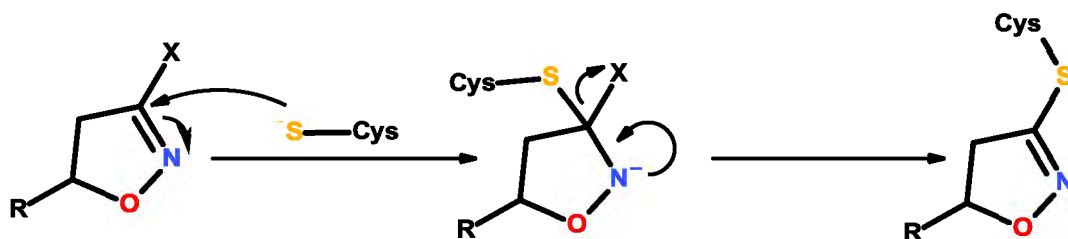


Figure 1.10. Halomethyl carbonyl TG2 inhibitors developed by the Griffin group (Badarau et al., 2015).

1.4.4.2 3-Halo-4,5-dihydroisoxazoles

It was proposed that the nucleophilic thiol of the catalytic cysteine residue covalently attacks 3-halo-4,5-dihydroisoxazole inhibitors on the electrophilic imino-halogen site of the dihydroisoxazole ring, then the halogen (X) is displaced to form an iminothioether adduct (Scheme 1.2) (Castelhano et al., 1988).



Scheme 1.2. Proposed TG2 inhibition mechanism of 3-halo-4,5-dihydroisoxazoles (Castelhano et al., 1988).

This series of TG2 inhibitors was designed as analogs of acivicin, a natural product Gln isostere known as a cysteine-dependent enzyme inhibitor. A large series of 3-bromo 4,5-dihydroisoxazoles based on a Cbz-Phe scaffold or the analogous Cbz-Tyr scaffold (Figure 1.11) was synthesised by the Khosla group (Choi et al., 2005) and was tested against recombinant human TG2 by using GDP-coupled assay (Yuan et al., 2007). Structure-activity studies pointed out that the hydrophobic aromatic groups on the side chain of the central amino acid and on its N-terminal protecting group play vital roles in their potency. Evidently, substitution of the small acetyl group with a bulky Cbz group on the side chain of the central amino acid or on its N-terminal protecting group made a noticeable increase in their potency.

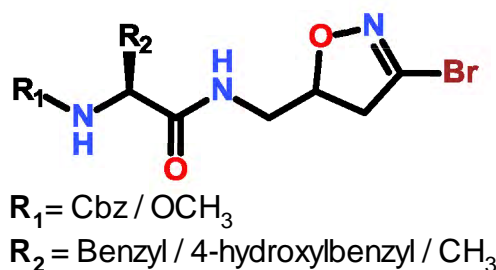


Figure 1.11. A series of 3-bromo 4,5-dihydroisoxazoles based on a Cbz-Phe scaffold or a Cbz-Tyr scaffold synthesised by the Khosla group (Choi et al., 2005).

The replacement of the benzyl group at the N-terminal and the central amino acid by dioxobenzothiophenyl and a tryptophan derivative, respectively, provided the most potent inhibitor (compound **10** Figure 1.12) for this category with $k_{\text{inact}}/K_{\text{I}} = 6.8 \times 10^3 \text{ M}^{-1} \text{ min}^{-1}$. However, its metabolic instability due to the reaction with glutathione made it an inappropriate candidate for *in vivo* investigations. Compound **KCC009** (compound **11** Figure 1.12) is less potent than compound **10** but it expressed good oral bioavailability and efficient extracellular TG2 inhibition in small intestinal tissue with low toxicity (Choi et al., 2005).

This class of TG2 inhibitors was further proved to form a covalent bond with catalytic Cys277 of the enzyme. The potency of this series was identified to be significantly increased by several factors including heteroatom-containing amino acid side chains, hydrogen bond acceptors in the N-carbamate moieties, and (S-) stereochemistry at the 5- position of the dihydroisoxazole pharmacophore. Additionally, the replacement of the phenol side chain of **KCC009** with a 5-fluoroindole group and the substitution of the Cbz group with a quinolyl carbamate provided a highly potent inhibitor (compound **12** Figure 1.12) with $k_{\text{inact}}/K_{\text{I}} = 5.7 \times 10^5 \text{ min}^{-1} \text{ M}^{-1}$ (Watts et al., 2006).

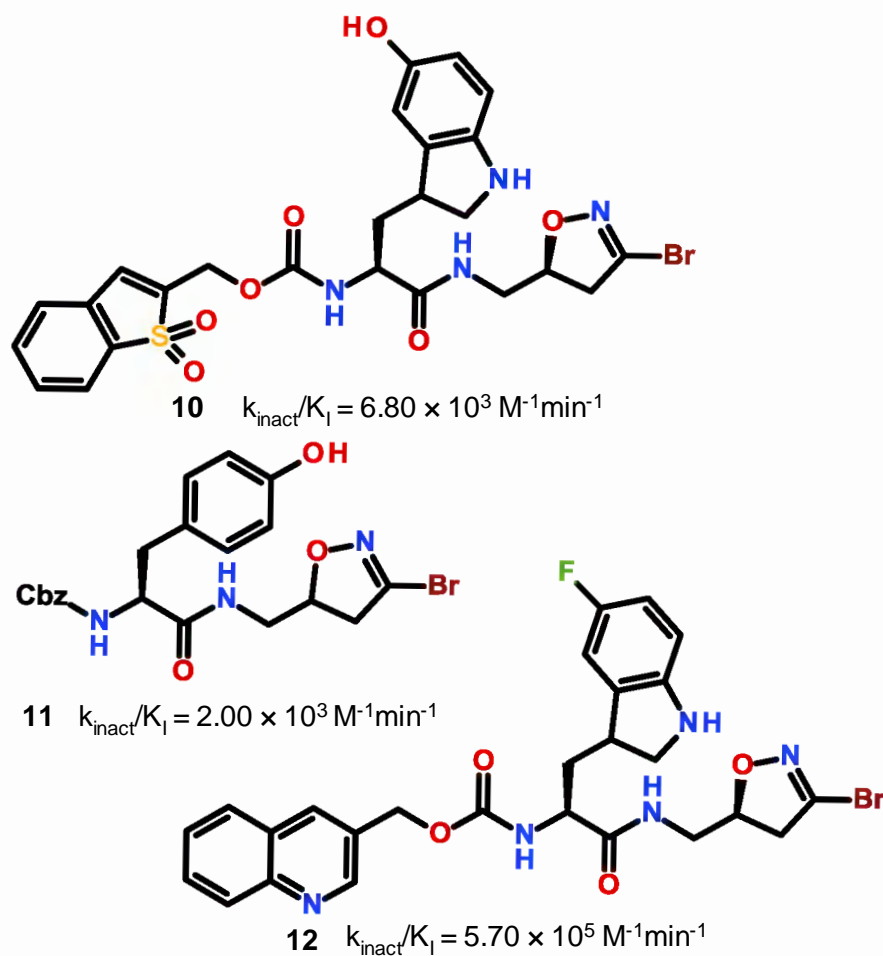


Figure 1.12. Lead 3-bromo-4,5-dihydroisoxazoles inhibitors of TG2 developed by the Khosla group (Choi et al., 2005; Watts et al., 2006).

1.4.4.3 Sulfonium methyl ketones

The initial general structure of this class includes a dimethyl sulfonium warhead incorporating a Cbz-Phe scaffold as $\text{Cbz-Phe-NH}(\text{CH}_2)_n\text{COCH}_2\text{S}^+(\text{CH}_3)_2$, $n > 2$ (Pliura et al., 1992). The potency of these compounds on TG2 was indicated to be significantly affected by the length of the $(\text{CH}_2)_n$ -spacer moiety (Figure 1.13). Particularly, a gamma aminobutyric acid spacer ($n = 3$) provided the most efficient inhibitor against TG2 in this class with $k_{\text{inact}}/K_{\text{I}} = 2.95 \times 10^4 \text{ min}^{-1} \text{ M}^{-1}$.

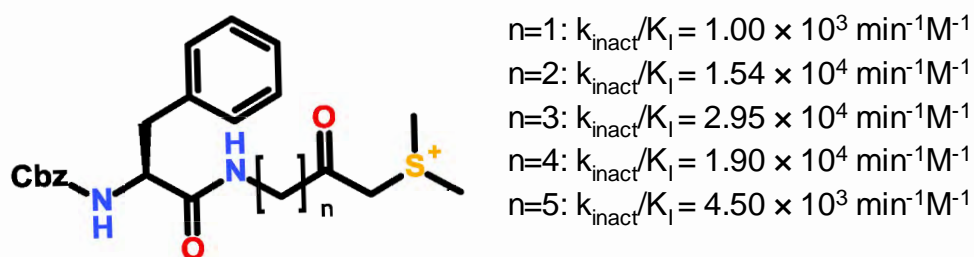


Figure 1.13. Initial dimethylsulfonium ketone TG2 inhibitors (Pliura et al., 1992).

The Griffin group developed a set of sulfonium-based TG2 inhibitors bearing an extra carboxyl group to improve the aqueous solubility (Figure 1.14a) (Griffin et al., 2008). The potency of these inhibitors was evaluated by an enzyme linked sorbent assay technique against either against guinea pig liver TG2 or recombinant human TG2. In agreement with the work of Pliura and coworkers, it concluded that among carbamate analogues attached on the N-terminus, Cbz is the optimal structure to provide highly potent inhibitors within this class. A set of compounds with N-terminal Cbz carbamate and various amino acids including proline, glycine and phenylalanine in the central scaffold have similar potency (IC_{50} ranged from 5 to 10 μM). Among them, compound **13** (Figure 1.14b) expressed no sign of cell toxicity, no animal toxicity up to 120 days and successfully reduced kidney fibrosis and scarring by up to 85% with a significant increase in kidney function (Huang et al., 2009) (Johnson et al., 2007).

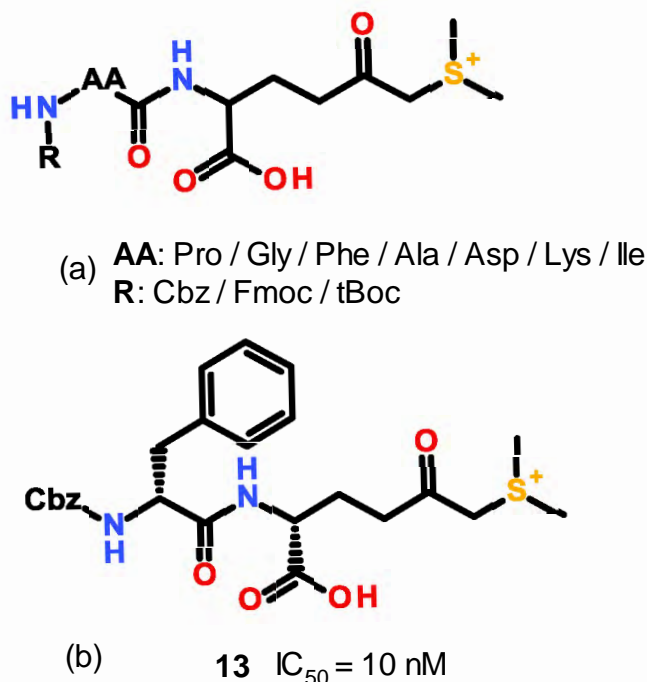


Figure 1.14. Dimethylsulfonium ketone TG2 inhibitors developed by the Griffin group (Griffin et al., 2008).

The same group then developed a new series of TG2 inhibitors based on the structure of compound **13** (Figure 1.14b) while modification of the central amino acid region to a piperazine ring and substitution of the carbamate region to a bulky adamantyl ring, aromatic carbamates or tertbutyl carbamates (Figure 1.15a) (Badarau et al., 2015). This class of inhibitors expressed high potency against recombinant purified human TG2 with lower nanomolar range in IC₅₀ values. The most potent compound (compound **14** Figure 1.15b) containing a tertbutyl carbamate had IC₅₀ value of 0.273 μ M. Modification of compound **14** by attaching a dansyl fluorescent tag into the central piperazine scaffold provided a comparable inhibitor with 0.380 μ M in IC₅₀ and $k_{\text{inact}}/K_{\text{I}} = 5.8 \times 10^3 \text{ min}^{-1}\text{M}^{-1}$ (compound **15** Figure 1.15c). This compound was selective over TG1, TG3, TG6, and Factor XIIIa (FXIIIa) in addition to good toxicity profile and high microsomal stability.

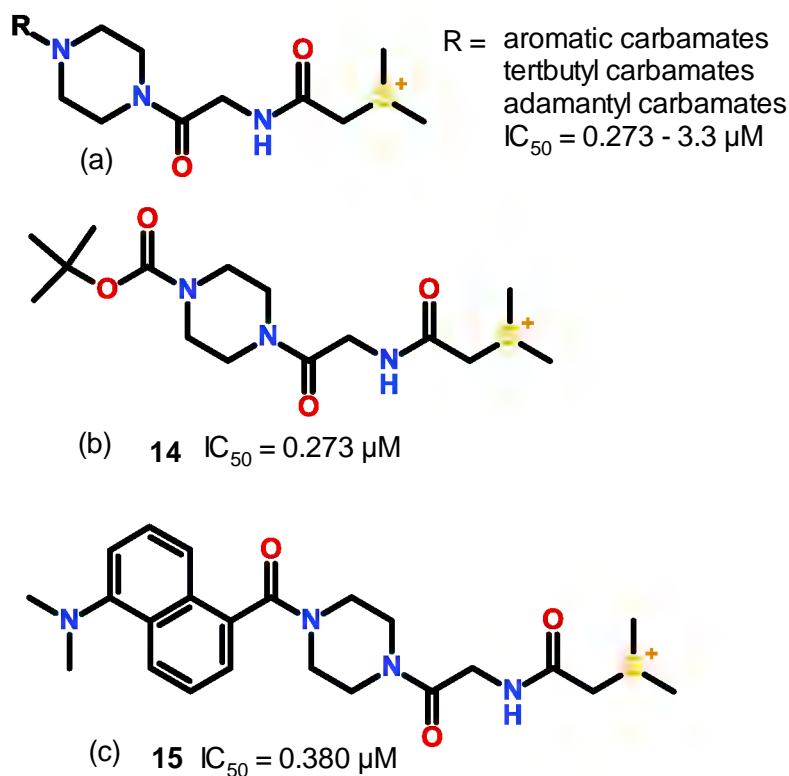


Figure 1.15. Dimethylsulfonium ketone TG2 inhibitors based on the piperazine scaffold developed by the Griffin group (Badarau et al., 2015).

1.4.4.4 Thioimidazolium methyl ketones

In the 1990s, Merck Sharp & Dohme discovered compound **L682777** (compound **16** Figure 1.16) as a prototype compound of this class with IC_{50} value of $0.2 \mu M$ for inhibition of the incorporation of $[^{14}C]$ putrescine into hepatocyte (Barsigian et al., 1991).

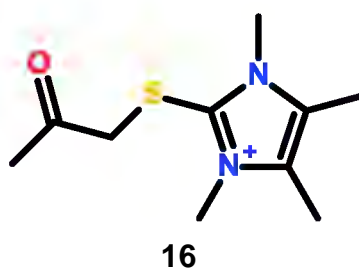
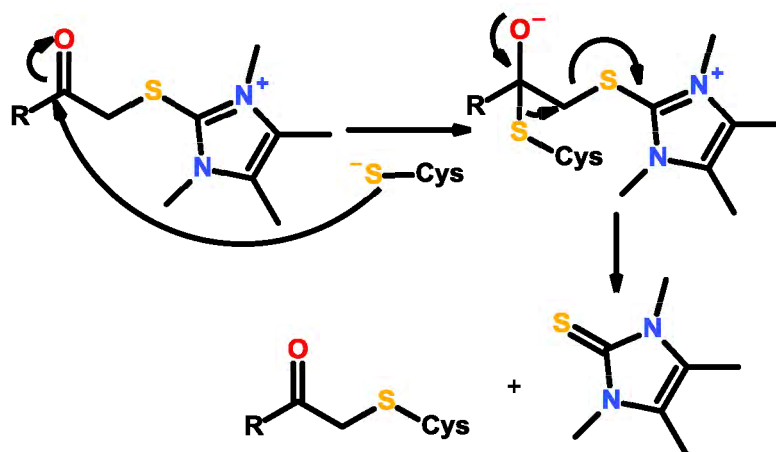


Figure 1.16. The prototype compound of thioimidazolium methyl ketone TG2 inhibitors (Barsigian et al., 1991).

The inhibition mechanism of this class was proposed to be the nucleophilic thiolate of the active site cystein residue attacking the carbonyl group then the thione is released following the acetylation of the cysteine (Scheme 1.3) (Freund et al., 1994).



Scheme 1.3. Proposed inhibition mechanism of thioimidazolium methyl ketones (Freund et al., 1994).

In the same Griffin group's study as described previously (Griffin et al., 2008), the substitution of the sulfonium methyl ketone warhead of compound **13** with tetramethylimidazolium provided a highly potent TG2 inhibitor (compound **17**) with IC_{50} value of $3 \pm 1 \mu M$ (Figure 1.17a). Compound **17** then became the parent compound to design a new series of TG2 inhibitors by alteration of the substituents on the imidazolium nitrogens and changing the amino acid in the central scaffold (Figure 1.17b). It pointed out that these compounds are exceptionally sensitive to the alteration of the substituents on the imidazolium nitrogens. Indeed, passing from the methyl group to an ethyl substituent or even increasing only one nitrogen substituent's size halved the potency. However, the compounds with modifications of substituents on carbon positions of imidazolium scaffold maintained a good inhibition range. The alkylsulfonium series also had the similar reduction in their potency when attaching bulky groups on the imidazolium nitrogens. Preliminary docking studies in this research suggested a bent conformation for the imidazolium family in the warhead region when they bind to the active site of TG2 (Badarau et al., 2013).

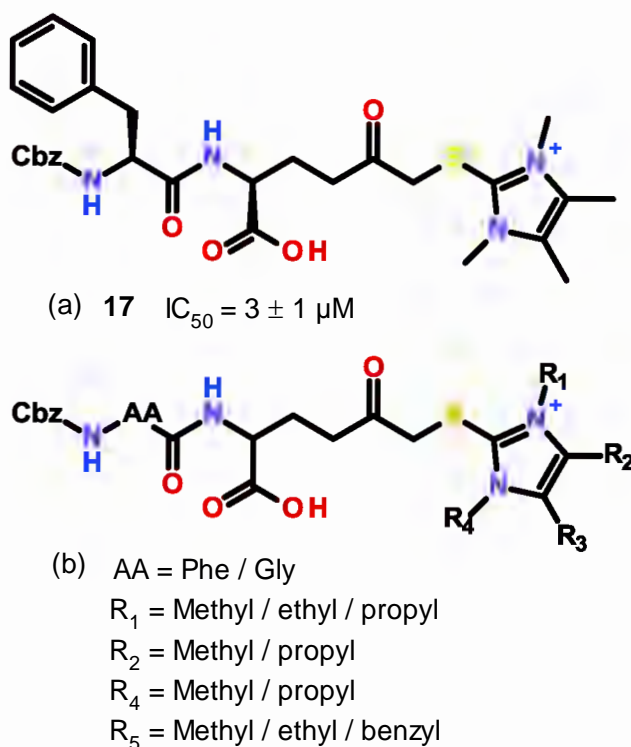
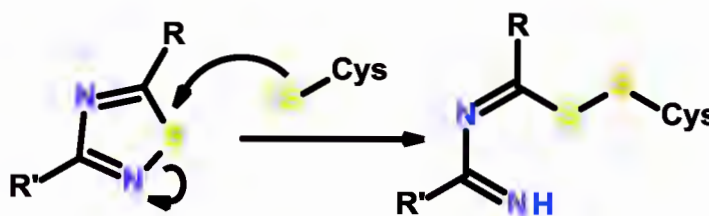


Figure 1.17. Thioimidazolium methyl ketone TG2 inhibitors developed by the Griffin group (Badarau et al., 2013).

1.4.4.5 1,2,4-Thiadiazoles

The TG2 enzymatic inhibition mechanism of this class was proposed to occur by the formation of a disulfide bond upon the opening of the thiadiazole ring (Scheme 1.4) (Marrano et al., 2001). This proposal was based on previous evidence showing that 1,2,4-thiadiazoles are susceptible to nucleophilic attack at sulphur followed by ring opening (Franz and Dhingra, 1984).



Scheme 1.4. Proposed inhibition mechanism of 1,2,4-thiadiazole inhibitors (Marrano et al., 2001).

Based on the Cbz-Glu-Gly scaffold but modifying the length of the side chain spacer as well as the sequence of the peptide backbone, a series of 1,2,4-thiadiazole derivatives was developed by the Keillor group (Marrano et al., 2001). The synthesised compounds were tested against guinea pig TG2 using an absorbance assay (de Macedo et al., 2000). Six of the 14 synthesised thiadiazole peptides in this work showed significant irreversible inhibitory activity with inactivation rate constants varying between 0.33 and $0.89 \mu\text{M}^{-1} \text{min}^{-1}$ (Figure 1.18). It can be clearly seen that in the series of 3-methoxy-1,2,4-thiadiazole inhibitors, modification of the length of the side chain caused little effect on their potency. In addition, no distinctive effect was observed when passing 3-methoxy to 3-methyl thiadiazole or when changing the amine to an amide side chain linkage.

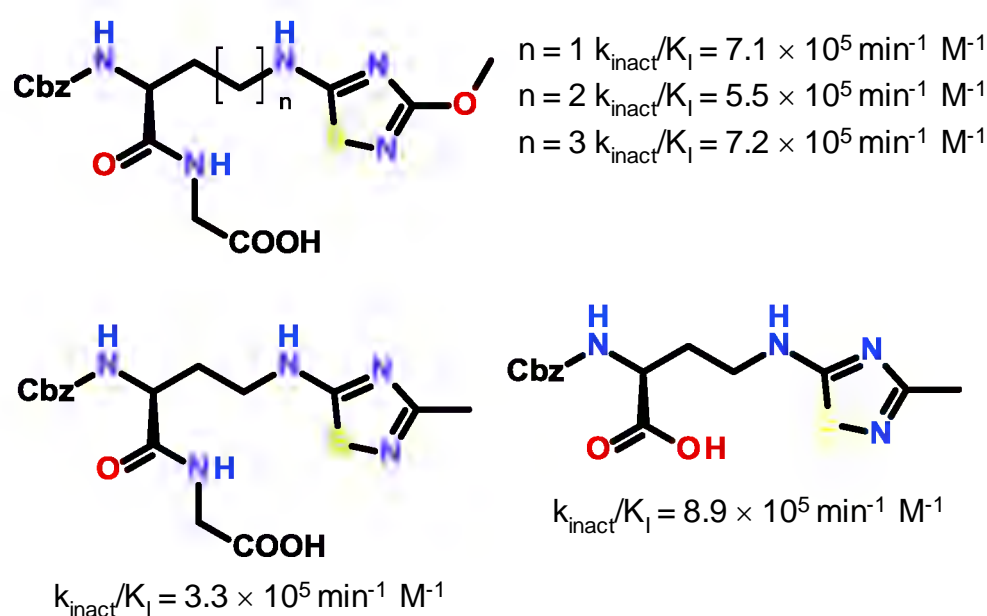
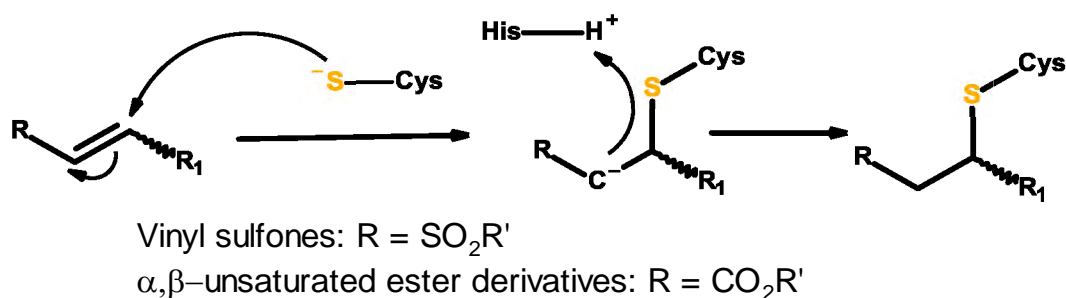


Figure 1.18. 1,2,4-thiadiazole TG2 inhibitors developed by the Keillor group (Marrano et al., 2001).

1.4.4.6 Michael acceptors

Michael acceptors were established to be specific for cysteine proteases (Powers et al., 2002) and some have been used in human clinical trials for rhinovirus infection and cancer treatment (Hayden et al., 2003; Carmi et al., 2011). Vinyl sulfones, α,β -unsaturated carbonyl derivatives, and maleimides are among the most common Michael acceptor warheads that have been applied in the development of irreversible inhibitors of TG2. Vinyl sulfones and α,β -unsaturated carbonyl derivatives inhibit cysteine proteases via a Michael addition with an attack of the active site cysteine on the β

carbon followed by protonation of the α -carbon to form a thioether derivative (Scheme 1.5) (Powers et al., 2002).



Scheme 1.5. Proposed inhibition mechanism of vinyl sulfones and α,β -unsaturated carbonyl TG2 inhibitors (Powers et al., 2002).

The Keillor group synthesised a series of α,β -unsaturated carbonyl derivatives based on the Cbz-Gln-Gly scaffold (de Macédo et al., 2002). The length of the side chain and the sequence of the peptide backbone were modified (Figure 1.19). The potency of the synthesised compounds was evaluated against purified guinea pig liver TG2, using a direct and continuous absorbance assay (Marrano et al., 2001). All the inhibitors showed excellent potency with $k_{\text{inact}}/K_{\text{I}}$ values around $10^6 \text{ min}^{-1}\text{M}^{-1}$. The affinity of the inhibitors generally increased proportionally with the length of the side chains. Indeed, the highest potency among three developed derivatives was accomplished when the scaffold was Cbz-Lys(Acr)-Gly (compound **18** Figure 1.19).

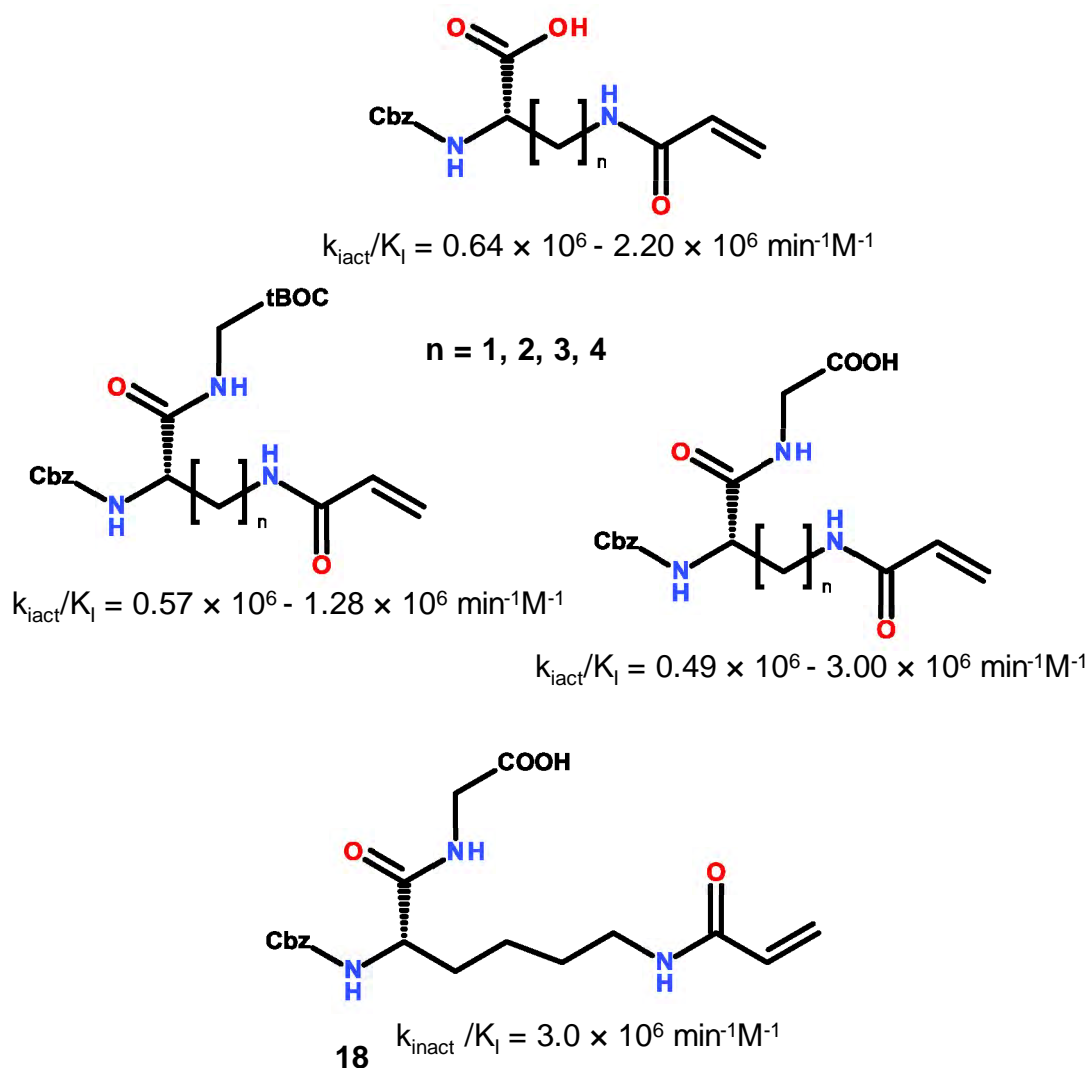


Figure 1.19. α,β -unsaturated carbonyl derivatives based on the Cbz-Gln-Gly scaffold (de Macédo et al., 2002).

From the optimal scaffold Cbz-Lys(Acr)-Gly, the same group further developed a new series by lengthening the spacer and linking a dansyl group into this scaffold (Figure 1.20). However, the modified compounds (compound **19** and **20** Figure 1.20) have lower affinities and that result in a decrease of roughly two orders of magnitude in $k_{\text{iact}}/K_{\text{I}}$ values compared to the parent compound (Keillor et al., 2008).

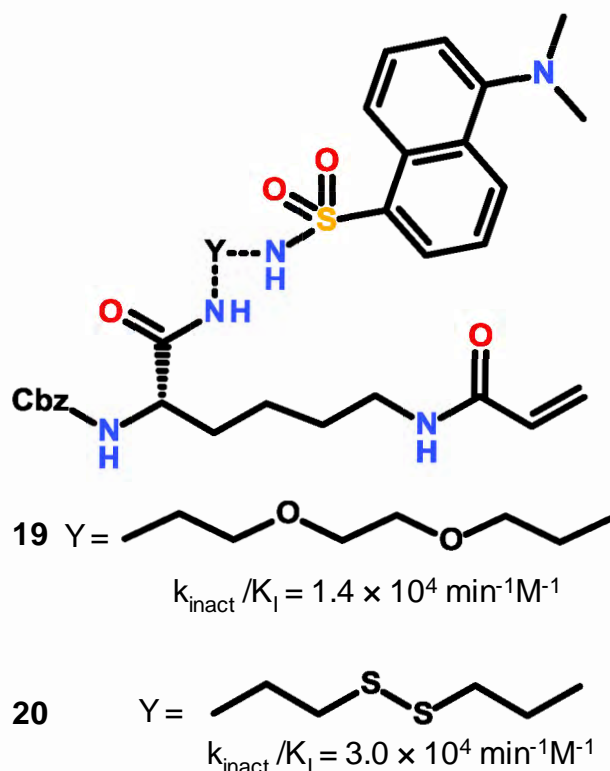


Figure 1.20. Fluorescent Cbz-Lys-based acryloyl TG2 inhibitors developed by the Keillor group (Keillor et al., 2008).

Other series of α,β -unsaturated carbonyl derivatives, in which the acryloyl group was incorporated into the Cbz-Phe scaffold, was developed by the Keillor group (Figure 1.21). The synthesised compounds were evaluated against recombinant guinea pig liver TG2 using continuous chromogenic or fluorogenic activity assays (Pardin et al., 2006). This class of TG2 inhibitors expresses reasonable potency with nearly eightfold more active than the analogous chloromethyl ketone derivatives (Figure 1.9) described in the same study. However, the potency of these compounds is roughly an order of magnitude lower than the acryloyl compounds based on the Cbz-Glu-Gly scaffold shown in Figure 1.19.

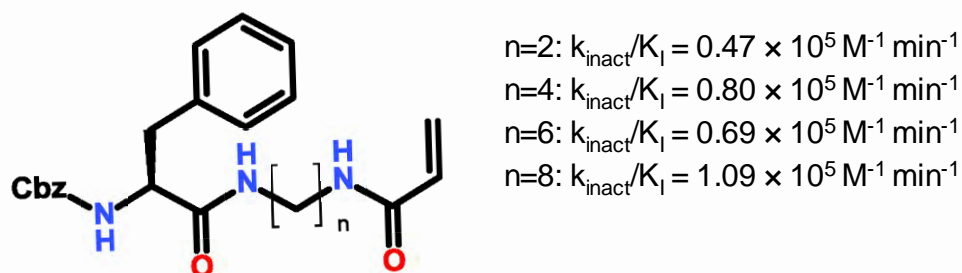


Figure 1.21. Cbz-Phe-based acryloyl TG2 inhibitors developed by the Keillor group (Pardin et al., 2006).

Most recently, the same group tested the lead developed inhibitors (compound **19** and **20**) against human TG2 using a colorimetric assay. The affinity and the reaction efficiency for human TG2 of compound **19** was 2 orders of magnitude worse in comparison to the results achieved when being tested against guinea pig liver TG2. In contrast, compound **20** showed a significant increase in the rate constant (k_{inact}) following a 5-fold increase in the overall efficiency (k_{inact}/K_I). Therefore, a large series of acrylamide compounds whose structures are based on Cbz-Lys scaffolds while varying the side chain length, the peptide backbone spacer, and the C-terminal R group was synthesised (Figure 1.22) (Akbar et al., 2017).

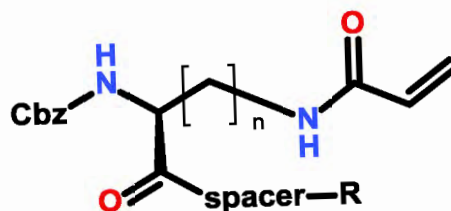


Figure 1.22. General structure of a large series of acrylamide TG2 inhibitors having structures based on Cbz-Lys scaffolds developed by the Keillor group (Akbar et al., 2017).

The first series was developed by modification the length of compound **20**. It was observed that reducing the spacer length from eight atoms in **20** to the distance associated with a two-methylene spacer but in the form of the more rigid piperazine ring provided the best inhibitor with $k_{\text{inact}}/K_I = 1.07 \times 10^5 \text{ min}^{-1} \text{ M}^{-1}$. This compound then became the parent compound to develop a new series containing the dansyl piperazine but modifying the length of the side chains bearing the acrylamide warhead. In consistency with previous studies, the results showed that reducing the number of

methylene units of the side chain less than 4 had deleterious effects on the potency. Another set of derivatives was developed from compound **20** by replacing the N,N-dimethyl naphthyl group with various aromatic and aliphatic functional groups. The kinetic data concluded that the cyclohexyl, isopropyl, ethyl, and methyl sulfonamides all gave comparable inhibition values to those of the aromatic derivatives. The results also showed that replacement of the C terminal sulfonamide group with a carboxamide functional group provided higher inhibition efficiency. Indeed, the aromatic derivatives with a carboxamide functional group expressed at least a 2-fold increase in the overall inhibition efficiency compared to their sulfonamide counterparts. When considering affinity, efficiency, and physicochemical properties it was concluded that compounds **21** and **22** (Figure 1.23) are the best leads among the developed derivatives. Compound **21** also was indicated being high selective over TG1, TG3a, TG6, and FXIIIa. Interestingly, these two lead compounds were proved to block GTP binding nearly completely (Akbar et al., 2017).

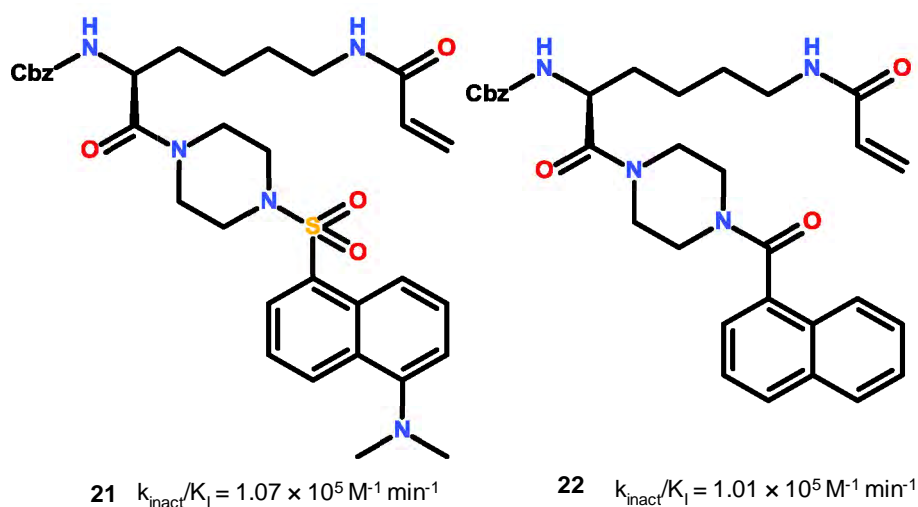


Figure 1.23. The two best acrylamide TG2 inhibitors developed by the Keillor group (Akbar et al., 2017).

The CHDI foundation used high-throughput screening to identify promising hits for TG2 inhibitors and synthesised a wide range of derivatives including phenylacrylamides, sulfonamide-bearing phenylacrylamides, sulfonamidopiperazine and heterocyclic acrylamides. Then, their activity and selectivity were evaluated by incubation for 30 min with 8 mM N,N-dimethylated casein (NMC) and 16 mM α-N-Boc-Lys-NHCH₂CH₂NH-dansyl (KXD, acyl-acceptor substrate). Among these series, compound **23** (Figure 1.24) is the most potent and selective inhibitor, with IC₅₀ of 10

nM against TG2 and showed 18, 84, 340, and >8000-fold selectivity against FXIIIa, TG6, TG1, and TG3, respectively (Prime et al., 2012a). Nonetheless, compound **23** suffered from low stability in plasma (mouse plasma $t_{1/2}$ = 3.5 h), thus, it was further modified by replacing the problematic anilide by a more robust alkylamide. Later, two newer compounds, **24** and **25** (Figure 1.24) were reported to be less potent than compound **23** but had greater plasma stability (mouse plasma $t_{1/2}$ >24 h) and resistance to (25 mM) glutathione conjugation over a period of 120 h *in vitro* (Prime et al., 2012b).

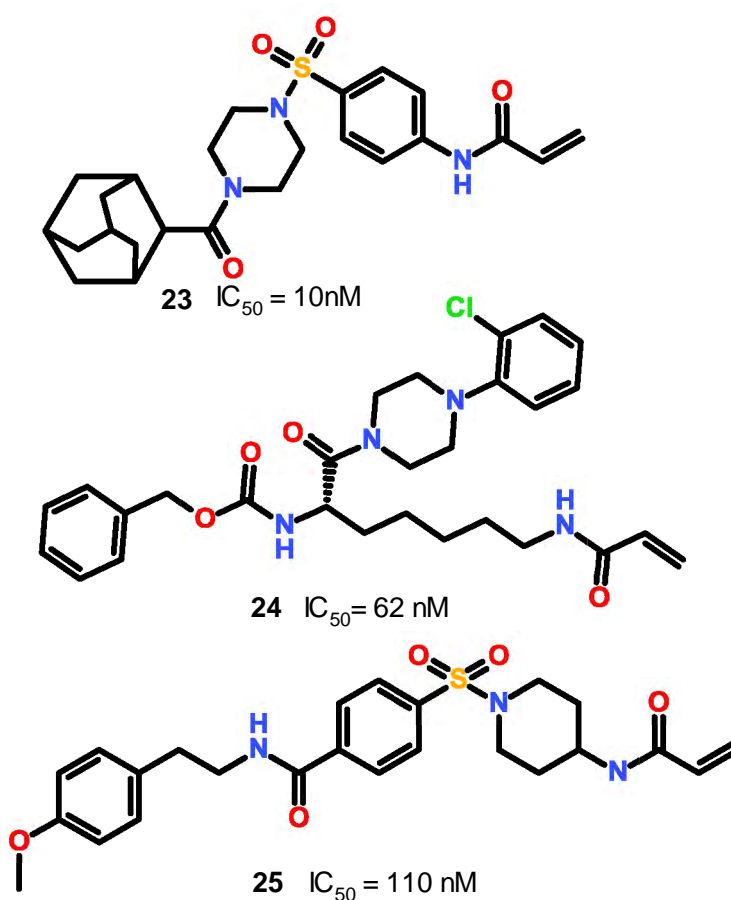


Figure 1.24. Lead Michael acceptor TG2 inhibitors discovered by the CHDI Foundation (Prime et al., 2012a; Prime et al., 2012b).

The Griffin group synthesised a series of acrylamides and vinylsulfonamides based on scaffolds containing a piperazine ring (Figure 1.25). The carbamate region was modified by introducing various-sized aromatic carbamates and tertbutyl carbamates. The synthesised compounds were tested against human TG2 using enzyme sorbent assay technique as described previously. These compounds displayed excellent

potencies with IC_{50} values varied in the lower micromolar range and compound **26** (Figure 1.25) was the most potent among them with IC_{50} of 0.125 μ M.

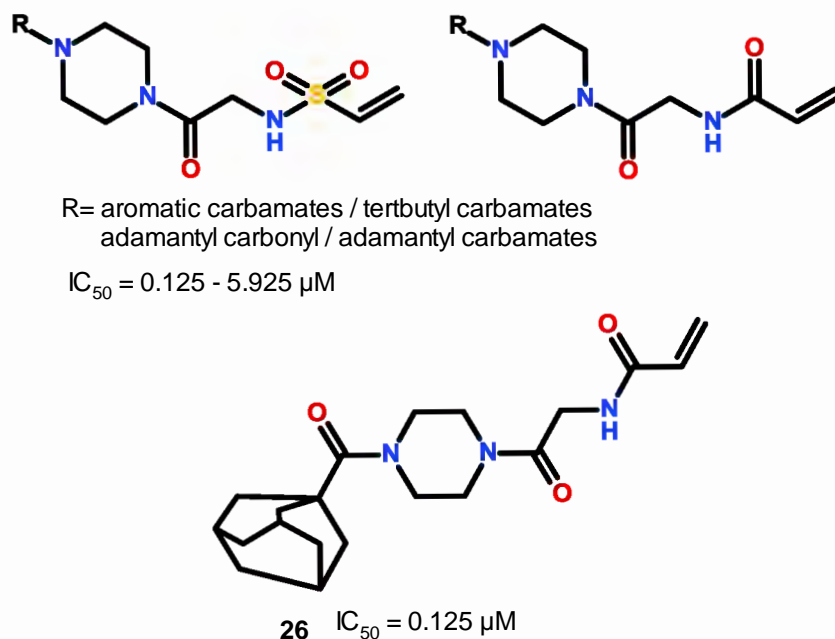


Figure 1.25. Acrylamide and vinylsulfonamide TG2 inhibitors developed by the Griffin group (Badarau et al., 2015).

Attachment of a dansyl fluorescent tag to the central piperazine scaffold provided compound **27** (Figure 1.26) with an exceptional potency and a high selectivity for TG2 with IC_{50} = 6.1 nM, 5 μ M, 20 μ M, 25 μ M and >100 μ M against TG2, TG6, TG3, TG1, and FXIII, respectively. The results from the glutamate dehydrogenase coupled assay indicated compound **27** is a highly potent TG2 inhibitor with k_{inact}/K_I value of $2.98 \times 10^5 \text{ min}^{-1} \text{ M}^{-1}$.

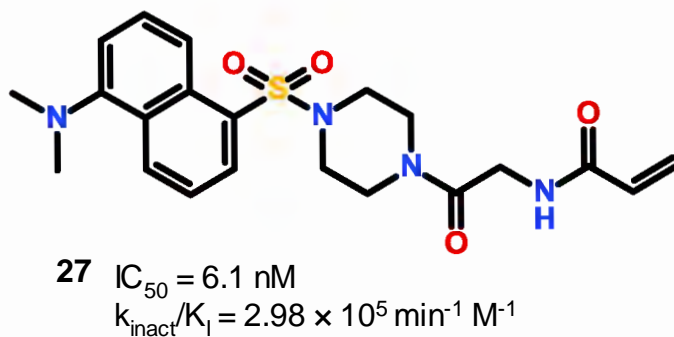


Figure 1.26: The lead acrylamide TG2 inhibitor discovered by the Griffin group (Badarau et al., 2015).

In the category of Michael acceptors, together with acrylamide derivatives, the Keillor group also prepared a series of inhibitors bearing a maleimide warhead. Initially, the maleimide active group was attached on the Cbz-Phe scaffold (Figure 1.27a) and the resulting compound was tested against recombinant guinea pig liver TGase. However, its low solubility and relatively high inhibition constant ($K_I > 160 \mu\text{M}$) prevented its kinetic parameters to be measured precisely (Pardin et al., 2006). Later, the same group synthesised a new set of maleimides based on peptidic scaffolds similar to Cbz-Gln-Gly (Figure 1.27b) (Halim et al., 2007). The synthesised compounds were tested against recombinant guinea pig liver TG2. Compounds with 4 methylene units of the side chain have the highest efficiency. Nonetheless, in comparison to a series of acrylamide inhibitors with the same scaffolds, the maleimide derivatives are 3 to 4 order of magnitude less potent. That result was consistent with the sterically constrained environment of the active site tunnel of TG2 (Chica et al., 2004), which may prevent the accommodation of the greater volume of the cyclic maleimide group.

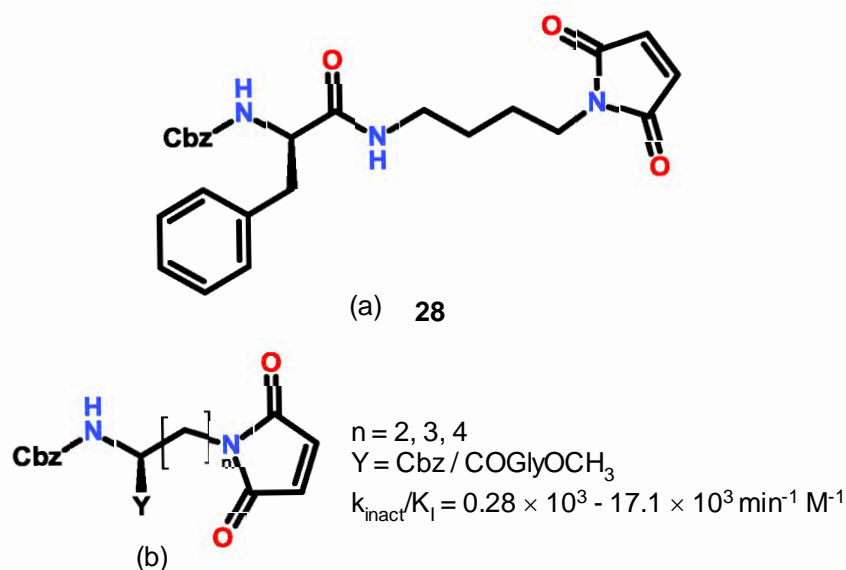
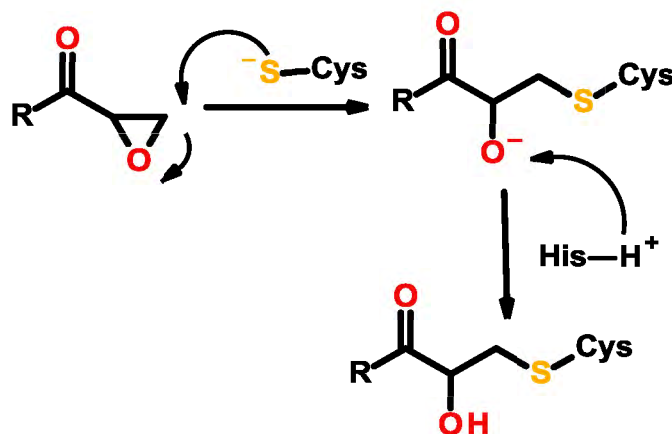


Figure 1.27: Dipeptide mimic maleimide TG2 inhibitors developed by the Keillor group (Pardin et al., 2006).

1.4.4.7 Epoxides

The proposed mechanism of inhibition for epoxides with the cysteine active site residue of TG2 is shown in Scheme 1.6.



Scheme 1.6. Proposed inhibition mechanism of epoxides (Powers et al., 2002).

In the same research as described previously (de Macédo et al., 2002), the authors attached an α,β -epoxyketone active functional group on the Cbz-Glu-Gly scaffold instead of the Michael acceptor warheads to develop a new set of TG2 inhibitors (Figure 1.28). The resulting series was evaluated against purified guinea pig liver TG2, using a transamidation assay (Marrano et al., 2001). All synthesised epoxides showed excellent efficacy on TG2 with $k_{\text{inact}}/K_{\text{I}}$ values were between 0.42×10^6 to $2.03 \times 10^6 \text{ min}^{-1}\text{M}^{-1}$. However, this class had higher K_{I} values than the corresponding analogous with Michael acceptors. The steric effect of the additional volume of the epoxide ring in the narrow active site tunnel was suggested to be the main reason leading to the lower affinity.

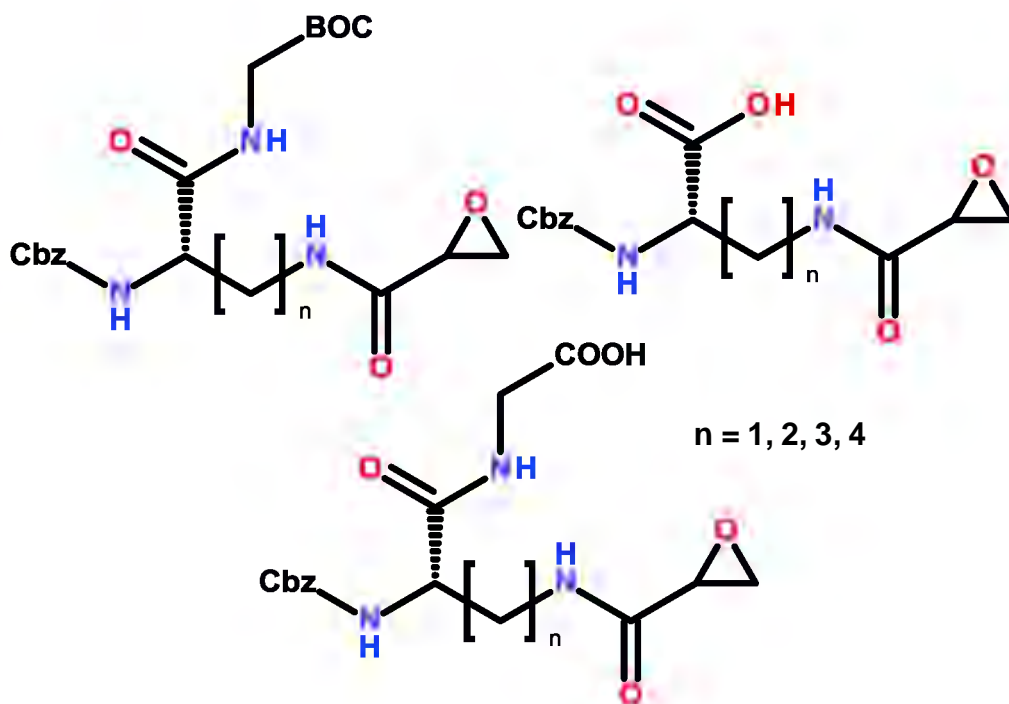
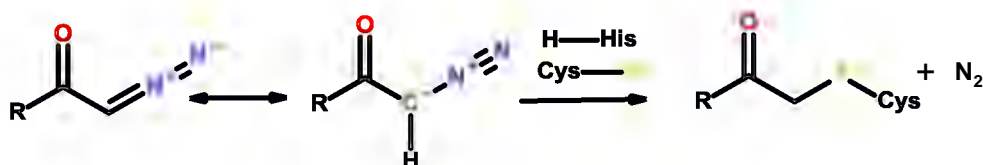


Figure 1.28. Epoxide TG2 inhibitors developed by the Keillor group (de Macédo et al., 2002).

1.4.4.8 Diazomethyl ketones

This class has been known as highly efficient inhibitors of cysteine proteases (Shaw, 1994). The inhibition mechanism of diazomethyl ketones is not yet completely understood. It was proposed to be involved the transfer of a proton from HIS335 to the methylene carbon of the inhibitor with the loss of N_2 and alkylation of CYS277 (Scheme 1.7). It is also assumed that the active site cysteine attacks the carbonyl group of the inhibitor to give a tetrahedral intermediate, which then transfers to the stable thioether derivative (Powers et al., 2002).



Scheme 1.7. Proposed inhibition mechanism of diazomethyl ketones (Powers et al., 2002).

The Khosla group (Hausch et al., 2003) discovered a naturally occurring glutamine isostere, 6-diazo-5-oxo-norleucine (DON) having an inhibitory effect against human

TG2 although it has very poor affinity ($K_I = 130$ nM). The group then developed a new series of TG2 inhibitors by incorporation of the DON residue into various peptide scaffolds (Figure 1.29). The substitution of a reactive glutamine in a high affinity peptide sequence derived from gluten peptide (Ac-Pro-Gln-Pro-Gln-Leu-Pro-Tyr-NH₂, reactive glutamine highlighted) with DON residue provided a new inhibitor with a substantial increase in the affinity and the efficiency. The efficiency is increased with the affinity suggested a proper binding of DON into the active site of TG2 while the peptide backbone binds into the donor substrate binding site. All the synthesised compounds in this research was tested against recombinant human TG2 using the coupled enzyme activity assay.

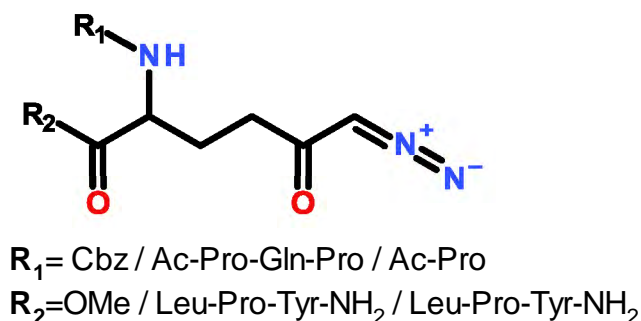
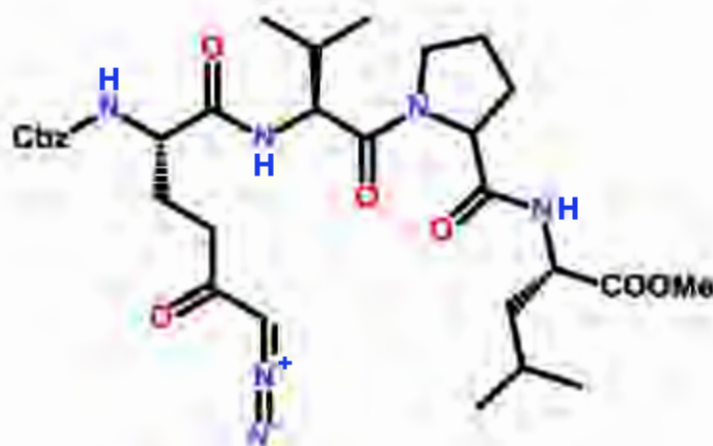


Figure 1.29. Diazomethyl ketone TG2 inhibitors developed by the Khosla group (Hausch et al., 2003).

Zedira GmbH also synthesised two derivatives with a DON moiety attached on a peptide scaffold (compound **29** and **30** Figure 1.30) (Schaertl et al., 2010). These compounds are different on the amine protecting group and the aminoacid backbone. Compounds **29** and **30** have a Cbz and a Boc protecting group at the N terminal position, respectively. Amino acid backbones are the following: Cbz-DON-Val-Pro-LeuOMe for **29**, and Boc-DON-Gln-Ile-ValOMe for **30**. Both derivatives were tested against human TG2 using a fluorescent assay technique that is based on transglutaminase-mediated incorporation of a dansylated lysine into casein. The IC₅₀ values of compound **29** and **30** are 0.02 μM and 0.3 μM , respectively.



29 $IC_{50} = 0.02 \mu M$



30 $IC_{50} = 0.3 \mu M$

Figure 1.30. Diazomethyl ketone TG2 inhibitors developed by Zedira GmbH (Schaertl et al., 2010).

Some derivatives of effectively irreversible TG2 inhibitors have been presented herein having different scaffolds and warheads with varied levels of success. Several research groups have currently explored many classes of the warhead such as Michael acceptors, and 3-halo-4,5-dihydroisoxazoles, which have efficiency constants over $10^6 \text{ M}^{-1} \text{ min}^{-1}$ or inhibition constants in the low nanomolar range. A few irreversible inhibitors have expressed high efficacy and good bioavailability in cell culture and animal models. However, limitations in *in vitro* ADME properties and toxicity have been the challenges for many lead compounds. Therefore, the development of irreversible TG2 inhibitors to become drugs still requires many attempts from the research community.

1.5 Computational techniques

1.5.1 Molecular dynamics simulations

The binding of a small molecule (a ligand) into a target macromolecule (a receptor) is a very dynamic process that involves interactions between the ligand and the receptor in constant motion and may induce various conformational changes of the receptor. X-ray crystallography is the main experimental technique to elucidate the molecular structures of macromolecules. However, this technique can only provide a static snapshot of a fully functional state. Nuclear magnetic resonance (NMR) spectroscopy provides access to the flexibility of protein structures by revealing an ensemble of conformations but it remains challenging and time consuming for large protein complexes. Molecular dynamics (MD) simulation is a technique based on Newtonian physics to simulate atomic motions by using simple approximations. MD simulations provide valuable insights into ligand-receptor motion. Therefore, it plays an essential role in drug discovery. (Durrant and McCammon, 2011; Mortier et al., 2015)

The general process of performing an MD simulation includes 4 main steps as described in Figure 1.31. First, an initial atomic model of a ligand-receptor complex is prepared from NMR, crystallographic, or homology-modeling data. The forces acting on each of the system atoms consists of so-called bonded terms and nonbonded terms. Bonded terms indicate the energy related to covalently bound atoms including chemical bonds, atomic angles and dihedral angles (that is, the angle between the 2 planes defining 4 successively bound atoms). Non-bonded terms describe forces arising from the interactions between each atom pair that is not connected by a covalent bond and these terms include van der Waals interactions and electrostatic interactions. Van der Waals forces represent attraction or repulsion between uncharged non-bonded atoms while electrostatic interactions describe attractive and repulsive forces between electrically charged non-bonded atoms. (Durrant and McCammon, 2011)

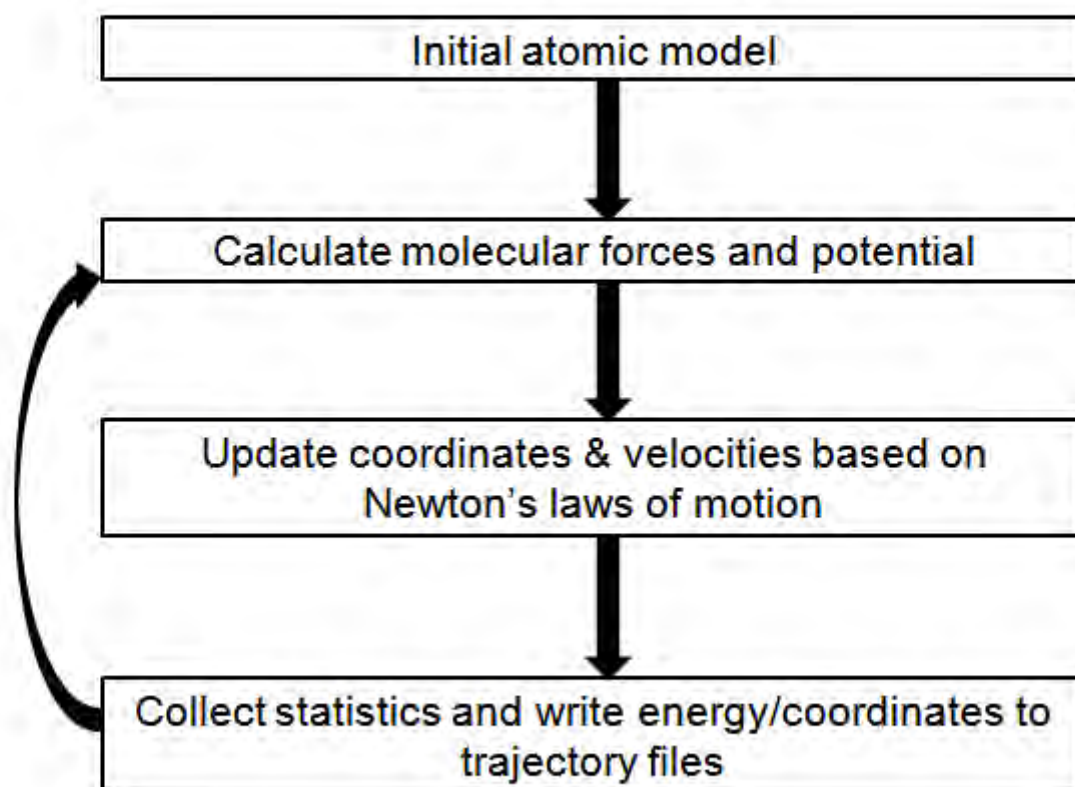


Figure 1.31. Simplified flowchart describes general process of a typical MD simulation. Reproduced (open access) from a version originally created by (Lindahl, 2015).

In order to emulate the actual movement of real molecules, the bonded terms and non-bonded terms are parameterized to fit quantum-mechanical calculations and experimental data. This parameterization comprises identifying the optimal stiffness and lengths of chemical bonds and atomic angles, determining the best partial atomic charges used for calculating electrostatic-interaction energies, ascertaining the proper van der Waals atomic radii. A force field is a combination of the set of equations used to calculate the potential energy and forces from atom coordinates, and a collection of parameters used in the equations. AMBER (Cornell et al., 1996), CHARMM (Brooks et al., 2009), and GROMOS (Christen et al., 2005) are the commonly used force fields in MD simulations that are different in principles of parameterization but generally provide similar results (Durrant and McCammon, 2011; Lindahl, 2015).

After calculation of the forces acting on each of the system atoms, the positions of these atoms are moved based on Newton's laws of motion. The simulation time is then advanced, often by only 1 or 2 femtoseconds to provide an MD trajectory of a ligand–receptor complex, which defines how the positions and velocities of the particles in the

system change with time. The cycle of MD simulations is usually repeated millions of times. Due to the numerous calculations required, MD simulations are generally performed on computer clusters or supercomputers using hundreds of processors in parallel. AMBER (Case et al., 2005b), CHARMM (Lindahl, 2015), GROMACS (Berendsen et al., 1995) and NAMD (Phillips et al., 2005) are the most popular simulation software packages used to run MD simulations.

Macromolecules do not exist in isolation but in an environment with the presence of water molecules and ions. Therefore, in order to achieve a realistic simulation, the complex of ligand-receptor must be solvated by either implicit or explicit solvation. In the implicit-solvent method, the water molecules are not added physically but are replaced by a potential, which describe their average action. This method can be algorithmically/computationally faster but is less accurate than the explicit-solvent approach due to the absence of the effects caused by the presence of water molecules such as hydrogen bonds and ligand solvation effects (Onufriev, 2008; Paquet and Viktor, 2015).

In the explicit-solvent approach, the macromolecule is surrounded by a solvation box constituted of water molecules. Due to the limitation of computer memory, the size of the solvation box has to be finite. Numerous shapes such as cubic, rhombic, dodecahedron truncated, octahedron, and sphere may be utilized in order to minimise the number of molecules required for solvation while maintaining a constant minimum buffer of solvent. In addition, a larger solvation box or a periodic boundary condition is applied to minimise unnatural boundary effects, which are caused by the finite structure of the solvation box (Paquet and Viktor, 2015).

Periodic boundaries work by replication the simulation box throughout space to form an infinite lattice. In the course of the simulation, the movement of a molecule in the central box makes its periodic image in each other boxes moves with exactly the same orientation in exactly the same way. Consequently, if a water molecule eventually leaves the central box, one copy of its will enter through the opposite face. Explicit solvent with periodic boundary is more realistic than the implicit solvent but it is computationally expensive due to the requirement to handle long distance electrostatic interactions between the atoms from various images (Allen and Tildesley, 2017).

1.5.2 Stages of MD simulations

An ordinary MD simulation is performed in 5 steps according to the authors of the CHARMM MD program (Stote, 1999). The first step is the preparation of the system's initial coordinates that can be from a crystal structure obtained from the Brookhaven Protein Data Bank (<http://www.rcsb.org/pdb/>) or from a docking complex generated by one of the docking programs. It is advised to minimize the structure to remove any strong van der Waals interactions that might lead to local structural distortion and result in an unstable simulation. At this stage, the system is solvated by a chosen solvation type, implicit or explicit. Another energy minimization should be done at this point to allow the water molecules to accommodate themselves to the biological system without any overlap. The second step is heating the system. During the heating phase, initial velocities are allocated to the atoms of the system at a low temperature, the simulation is started and the system is propagated over time by solving Newton's equations. Periodically, new velocities are assigned at a slightly higher temperature and the simulation is continuously applied. The process of is repeated while increasing temperature until the desired temperature is achieved. The third step is equilibration. At this stage, the simulation of protein/water system continues at the desired temperature whilst monitoring several properties such as the structure, the pressure, the temperature and the energy until these properties become stable over time. When the properties are stable the system is equilibrated and the production of the actual MD trajectory will be processed. This final phase can be run for any desired period of time (several hundred ps to ns or more) and the resulted trajectory can be inspected to gather information and perform analyses about the biological system.

1.5.3 Amber overview

Amber 16 was the version of Amber that was used to run MD simulations in this work. Amber (assisted model building with energy refinement) is used to refer a set of molecular mechanical force fields for the simulation of biomolecules and also a package of molecular simulation programs (Case et al., 2016). Within Amber, the core component involved in running MD simulations is Sander (simulated annealing with NMR-derived energy restraints). Pmemd (particle mesh Ewald molecular dynamics) is an extensively-modified version of the sander program used to optimize for periodic PME (particle-mesh Ewald) simulations. The program used to generate the parameter-

topology and coordinate files that can be read by sander and pmemd to run MD simulations is LEaP. It can read PDB files and it can add hydrogen atoms, water molecules and neutralising ions. Antechamber is similar to LEaP but is used to generate the input files for small organic molecules that are not included in the standard AMBER force fields. Its output files are then loaded into LEaP to be used with the files for the biological molecule (Wang et al. 2006; Wang et al. 2004). The trajectories generated from various MD runs are analysed by CPPTRAJ. It can calculate a wide range of information including distances between specific atoms, hydrogen bonds, root-mean-squared deviations from a reference structure, atomic fluctuations of the individual residues during a simulation, principal component analysis and many more (Roe & Cheatham 2013).

1.5.4 Molecular docking

Molecular docking or docking is another computational method usually used to find the most favourable binding mode(s) of a ligand to a receptor. Two basic steps involved in the docking process are: prediction of the ligand conformation as well as its position and orientation within the binding sites (usually referred to as pose) and assessment of the binding affinity. These two steps are related to sampling conformations of the ligand in the binding site of the receptor; then ranking these conformations via a fitness function or a scoring function (Morris and Lim-Wilby, 2008; Meng et al., 2011).

GOLD (Genetic Optimisation for Ligand Docking) program is the docking software used to prepare all ligand-protein complexes for MD simulations during the course of this thesis. The docking method used in GOLD program is genetic algorithm, which mimics the process of evolution by manipulating a collection of data-structures called chromosomes for docking flexible ligands into protein binding sites (Jones et al., 1997; Jones et al., 1995). In GOLD docking, the flexible structure of the receptor can be accomplished by some approaches including allowing the side chain to rotate freely, selecting rotamers for the side chain from the Penultimate rotamer library (Lovell et al., 2000) or choosing the rotamers for the side chain that are specified for the protein's PDB file. GOLD provided 4 scoring functions including Astex Statistical Potential (ASP), ChemScore, CHEMPLP and GoldScore in which ChemPLP is the default scoring function due to its highest average success rates for both pose prediction and virtual screening experiments. The ASP scoring function (Mooij and Verdonk, 2005) is

an atom-atom potential which was obtained from a database of existing ligand-protein complexes. ChemScore (Baxter et al., 1998; Eldridge et al., 1997) calculates the binding energies including binding free energy, hydrogen bonding, metal, torsional and lipophilic terms derived from a set of 82 ligand-protein complexes from the Protein Data Bank. The Piecewise Linear Potential (PLP) (Korb et al., 2009) models the attraction and repulsion between heavy-atoms of protein and ligand. GoldScore (Verdonk et al. 2003) calculates energies from hydrogen bonds and van der Waals interactions between the ligand and the receptor, ligand internal van der Waals and torsional strain.

1.6 Aim and Objectives

The first aim of this project is development of allosteric inhibitors of TG2 by modification of the lead allosteric inhibitor (compound **6** Figure 1.8) with a series of objectives include:

- To apply MD simulations to a complex of the parent compound docked into the predicted allosteric binding site.
- To analyse the behaviour of the parent compound into the predicted allosteric binding site.
- To design a new series of potential TG2 inhibitors by modification of the structure of the parent compound.
- To apply MD simulations to complexes of the designed compounds docked into the predicted allosteric binding site.
- To analyse stability and interactions of the modified compounds into the predicted binding site.
- To synthesize the newly-designed compounds.
- To screen potency of the synthesised compounds against human TG2.
- To examine the effects of the binding of the most potent TG2 inhibitors on the open conformation of the whole crystal structure of TG2.

The second aim is building upon the work at Aston University for the development of new class of potent irreversible TG2 inhibitors with these objectives:

- To design a new series of TG2 inhibitors based on the current lead inhibitor developed at Aston (compound **27** Figure 1.26).
- To apply MD simulations to complexes of the designed compounds docked into the active site of TG2.
- To analyse stability and interactions of the newly designed compounds in the active site and to determine the distance between the warhead and Cys277 sulphur atom during MD simulations.
- To synthesize a new series of modified compounds.
- To screen for potency of the newly-synthesised compounds against human TG2.

2 General methodology

2.1 Computational modelling

2.1.1 Programs

Accelrys Discovery Studio (DS) Visualizer Version 4.0 (BIOVIA, 2013) was used for visual inspection of the protein-ligand docked complexes, for direct design of new potential inhibitors from parent compounds and for analysis of interactions between the ligands and the binding sites. All three-dimensional pictures presented in this thesis were taken from this software. VMD (Visual Molecular Dynamics) Version 1.9 (Humphrey et al., 1996) was used for visual assessment and for analysis of MD trajectories.

The Amber software suite including two programs: Amber16 and AmberTools 16 (Case et al., 2016) in which *LeaP*, *antechamber*, *Pmemd* and CPPTRAJ were used for MD simulations during the course of this research. *LEaP* was used to generate input files for the MD simulations. *Antechamber* was used to generate the parameter and topology file for the ligand using the general AMBER force field (GAFF) (Wang et al., 2004) to make them suitable for *LEaP*. *Pmemd* (Particle Mesh Ewald Molecular Dynamics) was used to run MD simulations. The CPPTRAJ program of the AmberTools was used to analyse resulting MD trajectories. Specifically, CPPTRAJ was used to combine various trajectories to generate a new trajectory in which all the water molecules were deleted. This program was also used to perform combined clustering analysis in order to determine conformational modifications of TG2.

2.1.2 Molecular dynamics (MD) simulations

2.1.2.1 Preparation of TG2-ligand complexes for MD simulations

Parent inhibitors were docked into the crystal structure of TG2 in open conformation (code 2Q3Z) (Pinkas et al., 2007) using GOLD docking program by Dr. Dan Rathbone, the School of Life and Health Sciences, Aston University. Protein-ligand complexes of potential inhibitors were designed by direct modification of the parent compounds' structures. The resulting complexes were saved as PDB files. This work was carried out using DS Visualizer Version 4.0. The PDB file of each complex was then edited in a text-editor by deleting anything not protein or ligand, removing the hydrogen atoms

from the protein but not from the ligand and changing CYS277 to CYM277 (deprotonated form) and HIS335 to HIP335 (protonated form). The coordinates of the ligand was saved in a separate PDB file.

The parameter and topology file for the ligand were generated by *antechamber* to make them suitable for *LEaP*. After *antechamber* was finished, *parmchk2* was run to generate a *frmod* template that added substitutions for missing force field parameters. The file was loaded into *LEaP* to prepare the parameter-topology (PRMTOP) and coordinate (INPCRD) files using for the AMBER force field ff14SB (Maier et al., 2015). The complex was neutralised with sodium ions and was solvated in a truncated octahedron of TIP3P (transferable intermolecular potential 3P) water molecules that extended for 8 Å from the protein surface. Finally, the PRMTOP and INPCRD files were generated and saved.

2.1.2.2 Applying energy minimisation

The minimisation of the ligand-TG2 complexes was carried out using the *Pmemd* program of the AMBER package. The process was run for 2,000 cycles (*maxcyc* = 2000) in which steepest descent was used for the first 1,000 cycles and conjugate gradient was used for the second 1,000 cycles (*ncyc* = 1000). The cut-off distance for treating non-bonded interactions was taken as 12 Å (*cut* = 12). The minimisation was processed at a constant volume (*ntb* = 1) using an explicit water model (*igb* = 0) with no restraining atoms (*ntr* = 0).

2.1.2.3 Heating up the system (MD1)

The output file of the minimisation was used as the starting point for the heating stage of the MD simulation (*ntx* = 1). Similar to the minimisation stage, the heating process was processed under constant volume (*ntb* = 1) using an explicit water model (*igb* = 0) with a cut-off distance of 12 Å without any restraints (*ntr* = 0). The temperature of the system was increased from 0 to 300 K using Langevin dynamics (*ntt* = 3) at a collision frequency of 1 ps⁻¹ (*gamma_ln* = 1). The simulation was run for 25000 steps with 0.001 ps time per step (*nstlim* = 25000, *dt* = 0.001) for 25 ps in total. The random number generator was used and the random seed was based on the current date and time (*ig* = -1). No wrapping was performed (*iwrap* = 0).

2.1.2.4 MD simulation at 300 K (MD2)

The restart file accomplished from running MD1 simulation was used as the starting point for this stage of the MD simulation. MD2 was run under constant pressure periodic boundaries ($\text{ntb} = 2$) using isotropic position scaling ($\text{ntp} = 1$). The Monte Carlo barostat was used to control the pressure ($\text{barostat} = 2$). The run was performed at constant temperature (300 K) using Langevin dynamics ($\text{ntt} = 3$) at a collision frequency of 1 ps^{-1} ($\text{gamma_ln} = 1$). The SHAKE algorithm was used to restrain bonds involving hydrogen atoms ($\text{ntc} = 2$, $\text{ntf} = 2$). The simulation was run for 100 ns (50,000,000 steps of 0.002 ps). The output files were updated every 12,500 steps or 25,000 steps. The random number generator was used and the random seed was based on the current date and time ($\text{ig} = -1$). No wrapping was performed ($\text{iwrap} = 0$). New simulations were applied at the end of every 100 ns simulation using the restart file from the last simulation as the starting structure for the new one.

During the heating phase (MD1), using constant pressure will result in an unstable system as the system is cold at the start. However, a constant pressure must be used during the equilibration and the production phase (MD2) to equilibrate the density of the system and water molecules in particular.

2.1.3 Visual inspection and analysis of MD trajectories

The resulting MD trajectories were analysed based on the stability of the ligand into the docking site, the distance between the warhead electrophilic carbon of the potential irreversible inhibitors and the nucleophilic sulphur of the catalytic cysteine (CYS277) and the modification of the conformation of the enzyme. The root of mean square deviation (RMSD), which indicates the mobility of a molecule or the protein in comparison to a reference structure, were calculated and analysed using the “RMSD Trajectory tool” of the VMD program or the CPPTRAJ program of the AmberTools package. The reference frame was not the first frame but a frame where the ligand was settled down in the binding site. The root mean square fluctuation (RMSF) of the protein, which can highlight the most mobile regions of the protein, was calculated and analysed using the CPPTRAJ program. Hydrogen bond analysis was performed using the VMD program. Protein-ligand docked complexes at a specific frame were analysed on interactions between the ligand and the protein which were visualised using the DS Visualizer program.

2.2 Synthetic chemistry experiments

Reactions were monitored by thin layer chromatography (TLC) on Merck silica gel 60 F254 pre-coated plates. The visualisation was made with ultraviolet light ($\lambda = 254/365$ nm) and in some cases, staining with iodine, a solution of potassium permanganate or a solution of vanillin in ethanol. Flash chromatography was carried out using a column packed with Merck 40–70 nm (230–400 mesh) silica gel. The newly synthesised compounds were characterised by TLC, proton NMR spectroscopy (^1H NMR), attached proton test (APT) carbon NMR spectroscopy (^{13}C -NMR), infrared spectroscopy (IR), melting points (m.p.) and high-resolution mass spectrometry (HRMS).

The ^1H and ^{13}C -NMR spectra were recorded by using a 400 MHz Bruker Advance DPX400 in deuterated dimethyl sulfoxide (DMSO- D_6) or deuterated chloroform (CDCl_3). Chemical shifts (δ) were reported in parts per million (ppm) and the coupling constants (J) were reported in units of Hertz (Hz). Multiplicities were indicated as follows: s (singlet), d (doublet), t (triplet), m (multiplet). Residual solvent signals of the ^1H and ^{13}C NMR spectra of DMSO- D_6 ($\delta\text{H} = 2.520$ ppm, $\delta\text{C} = 39.700$ ppm), CDCl_3 ($\delta\text{H} = 7.270$ ppm, $\delta\text{C} = 77.360$ ppm) were used as the internal references.

The infrared (IR) spectra were recorded on a Thermo ScientificTM NicoletTM iSTM5 FT (Fourier Transform)-IR spectrometer equipped with an ID5 Diamond ATR (Attenuated Total Reflection) accessory. Signal intensities were abbreviated as follows: weak (w), medium (m) and strong(s).

The melting points were determined by a Reichert-Jung Thermo Galen - Hot Stage Microscope equipped with a RTD (Resistance Temperature Detector) Pt100 sensor.

The mass spectra were recorded by a Thermo Fischer ScientificTM LTQ Orbitrap XLTM ETD Hybrid Ion Trap-Orbitrap Mass Spectrometer at EPSRC National Mass Spectrometry Centre, Swansea University, Swansea (UK).

2.3 Biological assays for screening the inhibitory effect

The potency of the parent compounds and newly synthesised compounds was evaluated against recombinant human TG2. The IC_{50} values of the tested compounds

were measured using an enzyme linked sorbent assay to measure covalent incorporation of a primary amine substrate N-biotinyl cadaverine (N-(biotinamido)-1,5-diaminopentane hydrochloride) into human fibronectin, a glutamine-containing protein substrate. Details of the protocols used in this work are presented in chapter 7 of this thesis.

3 Molecular dynamics simulations of potential allosteric inhibitors of TG2

To date, irreversible inhibitors of TG2 have showed high potency against TG2 and been the most widely developed. But their electrophilic warheads potentially caused toxicity *in vivo*. Therefore, most inhibitors in this class are in the early discovery stage of development except mercaptamine. Thus, the development of allosteric inhibitors can introduce the possibility to develop safer drugs that contain no reactive functionality.

As mentioned in the introduction, among developed allosteric inhibitors, **LDN_27219** (compound **6** Figure 1.8) showed a good potency toward TG2 with the IC_{50} value of $0.6 \pm 0.1 \mu\text{M}$. This compound was suggested to bind at an allosteric site rather the GTP/GDP binding site or a site that regulates the binding of GTP (Case and Stein, 2007). Recently, a collaborative computer modeling study between Strathclyde University and Aston University predicted the allosteric site, where **LDN_27219** may bind, to be composed of 10 residues and is located in a pocket surrounded by 3 helices at the end of the catalytic core domain of TG2 (Jasim, 2016). The predicted allosteric site and the GTP/GDP binding site in the open conformation of TG2 are pointed out in Figure 3.1.

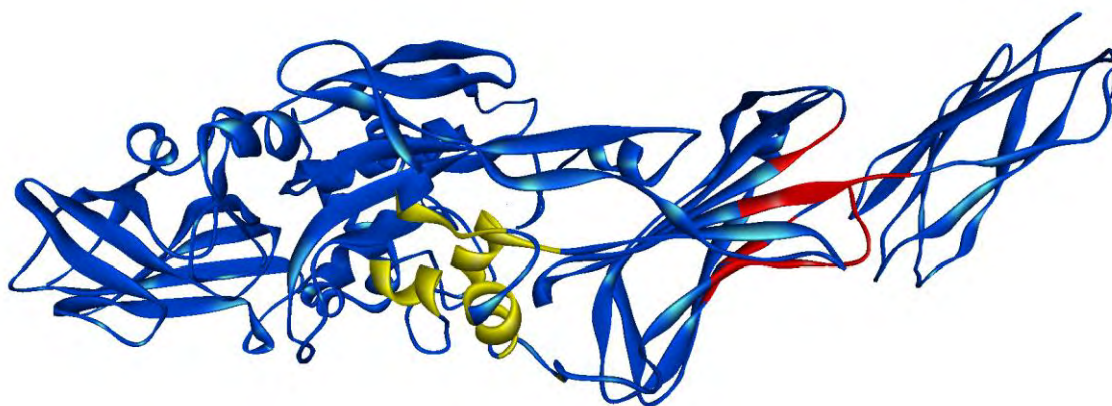


Figure 3.1. The predicted allosteric site used for docking purpose (yellow) and the GTP/GDP binding site (red) in the open (active) conformation of TG2.

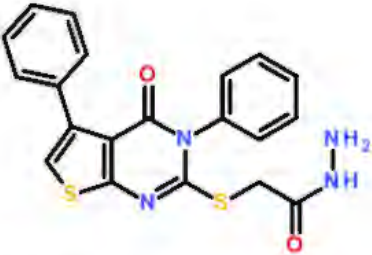
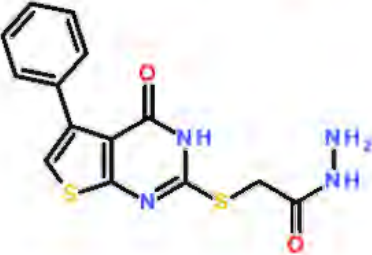
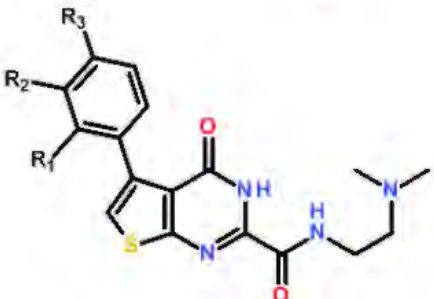

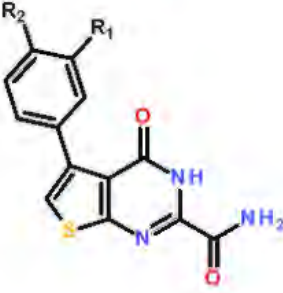
Reproduced (open access) from (Jasim, 2016).

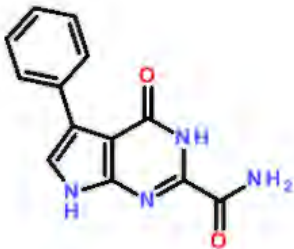
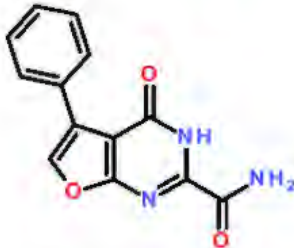
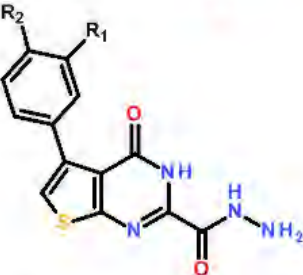
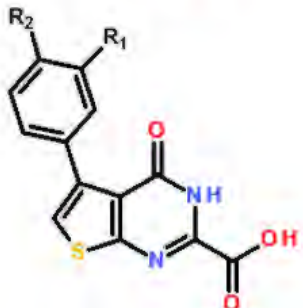
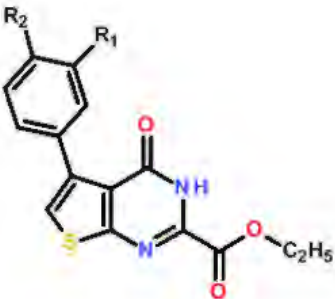
In this chapter, compound **6** was docked into the predicted allosteric site in the open (active) conformation of TG2 using GOLD docking programme by Dr. Dan Rathbone. A short structure of TG2 containing two parts: the catalytic core domain and the first

beta barrel was used instead of the full structure of the enzyme to reduce time of running MD simulations.

The site used for docking purposes was created by adding residues at the beginning, the middle and the end of the segments of the predicted allosteric site. The binding site was structured by 28 residues (flexible residues are in **bold**): ARG377, ALA378, **ILE379**, **LYS380**, **GLU381**, PRO391, PHE392, VAL393, PHE394, ALA395, **GLU396**, VAL397, **ASN398**, ALA399, THR442, TYR443, **LYS444**, TYR445, PRO446, **GLU451**, **GLU452**, ARG453, **GLU454**, ALA455, PHE456, THR457, **LEU462** (Jasim, 2016). The most favourable protein-ligand complex was further subjected to MD simulations in explicit water for 200 nanoseconds (ns). Various parts of the parent compound's structure were examined *in silico* for their interactions with nearby amino acids and their stability in the binding pocket. Effects caused by the binding of the ligands on the conformation of the predicted allosteric site were also analysed. A new set of analogues was designed by direct modification of the parent compound's structure in the docked complex. The structures of the modified compound are displayed in Table 3.1. The resulting complexes were subjected to MD simulations in explicit water. The trajectories of the modified compounds were examined in the similar way as that of the parent compound.

Table 3.1. List of potential allosteric inhibitors subjected to MD simulations.

Name	Structure	R ₁	R ₂	R ₃
6				
31				
32a		H	H	H
32b		H	H	CH ₃
32c		H	CH ₃	CH ₃
32d		CH ₃	CH ₃	CH ₃
33a		H	H	H
33b		H	H	CH ₃
33c		H	CH ₃	CH ₃
33d		CH ₃	CH ₃	CH ₃
34a		H	H	
34b		H	CH ₃	
34c		CH ₃	CH ₃	
34d		H	CH ₂ OH	
34e		H	CONH ₂	

34f			
34g			
35a		H	H
35b		H	CH ₃
35c		CH ₃	CH ₃
36a		H	H
36b		H	CH ₃
36c		CH ₃	CH ₃
37a		H	H
37b		H	CH ₃
37c		CH ₃	CH ₃

In the results that follow, interactions between the ligand and the protein are indicated by various coloured dotted lines. Green dotted lines indicate hydrogen bonds, light purple dotted lines presented alkyl-alkyl, pi-alkyl interactions, dark purple dotted lines marked pi-pi stacked, T-shaped pi-pi interactions and yellow dotted lines denoted pi-

anion/cation, charge-charge interactions. The VMD program was used for hydrogen bond analysis using the default settings: 3.0 Å donor-acceptor distance and 20° angle cut-off. For pi-alkyl interactions, VMD cannot measure a distance between a carbon atom and the centre of a phenyl ring. Instead, it was measured from the carbon atom of the alkyl and C1 and C4 of the phenyl ring and an average was calculated. For pi-pi interactions, a distance between two centrals of two phenyl rings were measured by an average distances between para carbon atoms of two rings. Although these calculations cannot be used as an ultimate judgement for the presence of the hydrophobic interactions, however they do give an insight into the possibility of the formation of these interactions based on the proposed distances.

3.1 MD trajectory of the parent compound

The aromatic phenyl ring attached to the thiophene ring was located within a hydrophobic binding pocket and formed pi-pi and pi-alkyl interactions with nearby amino acids including VAL397, PHE394 and ALA455 (Figure 3.2a). This aromatic part was identified as the head of the ligand. It was also observed that there were some free spaces in this hydrophobic pocket that may be suitable for the attachment of some groups on the phenyl ring. The other phenyl ring was held between 2 residues LYS444 and GLU447 by pi-alkyl, pi-cation and pi-anion bonds (Figure 3.2b). The thieno[2,3-d]pyrimidine ring formed pi-anion interactions with GLU452 and hydrogen bonds with LYS444 (Figure 3.2c). No interaction was formed between the protein and the side chain $S(CH_2)_2CONHNH_2$ which was indicated as the tail of the ligand.

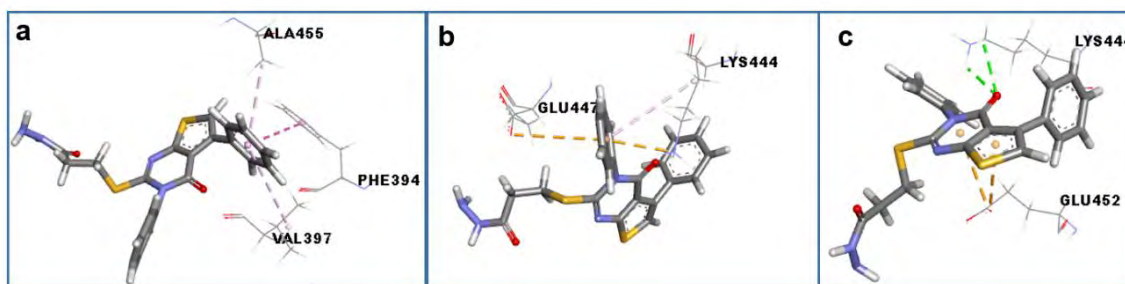


Figure 3.2. Interactions between the parent allosteric inhibitor with nearby residues at the starting frame of the MD simulation.

(a) Interactions between the phenyl ring attached on the ligand thiophene ring and residues of the hydrophobic pocket; (b) interactions between the phenyl ring attached on the ligand pyrimidine ring and two residues LYS444 and GLU447; (c) interactions between the thieno[2,3-d]pyrimidine ring and two residues GLU452 and LYS444.

During 200ns simulation, GLU447 was significantly mobile and the phenyl group attached on the ligand pyrimidine ring had only hydrophobic interactions with LYS444. 18 hydrogen bonds were formed between the ligand and the protein during the simulation time but these were only transient. For example, the hydrogen bonds between the carbonyl group of the ligand pyrimidine and LYS444 occupied only 6.33% of the simulation time. The tail was highly portable and it mainly formed hydrogen bonds with water molecules. Some hydrogen bonds were also generated between the ligand tail and nearby residues and also intramolecularly (Figure 3.3). The significant movement of the tail tended to pull the ligand head out of the hydrophobic pocket. However, due to various hydrophobic interactions with residues nearby such as VAL397, PHE394, LYS444 and ALA455 the head was maintained in the hydrophobic pocket during the 200 ns simulation.

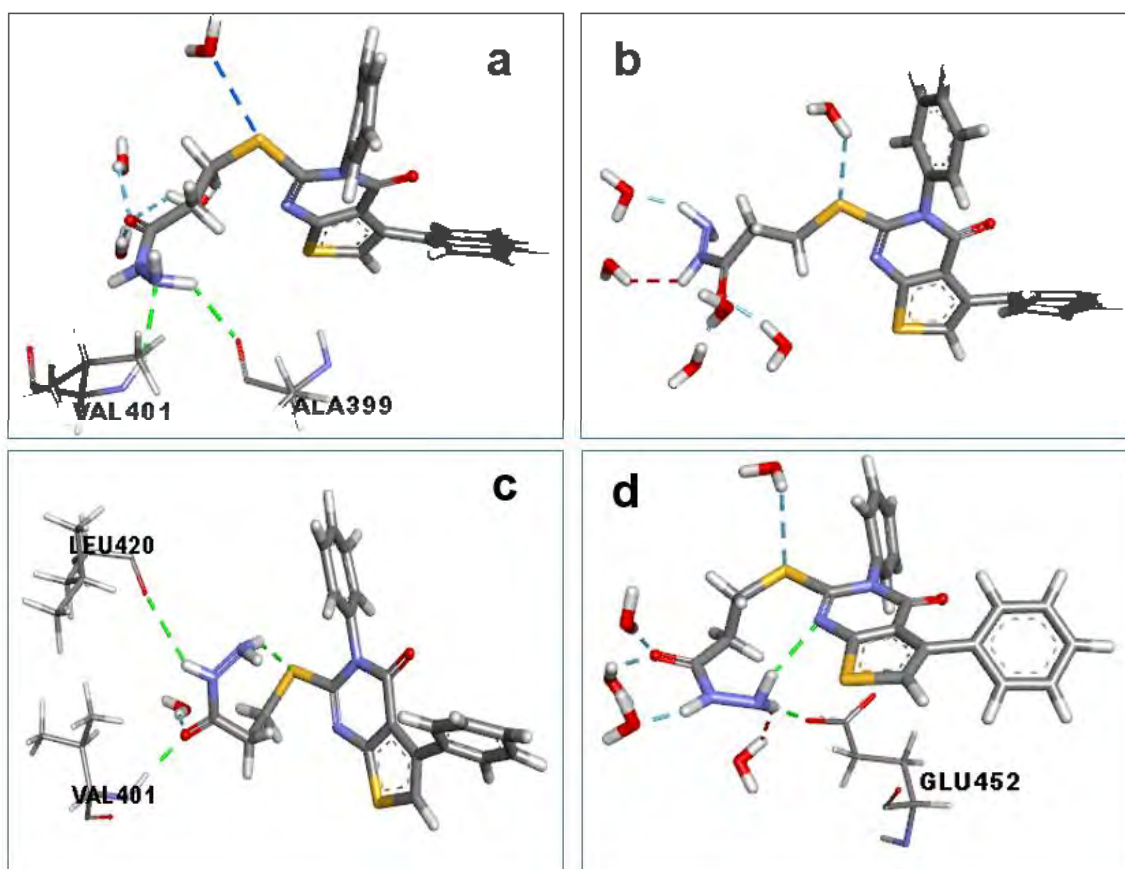


Figure 3.3. Intramolecular and intermolecular hydrogen bonds of the acylhydrazide thioether side chain of the parent compound at various frames of 200 ns MD simulation.

3.2 MD trajectory of compound 31

As mentioned above, during the MD simulation of the complex of compound **6** docked into TG2, the phenyl group attached to the nitrogen atom of the ligand pyrimidine ring was exposed to water and had only pi-interactions with the mobile residue LYS444. In addition, the aromatic structure reduces water solubility of the compound. Thus, this ring was removed to make the first analogue (compound **31**) of the modified series.

During 200 ns simulation, similar to compound **6**, the tail of compound **31** was significantly mobile and it formed transient hydrogen bonds with various residues. The high mobility of the tail caused significant fluctuations of the remaining parts of the ligand. However, the ligand phenyl head was maintained in the hydrophobic pocket due to hydrophobic interactions generated with nearby residues some of which are pointed out in Figure 3.4.

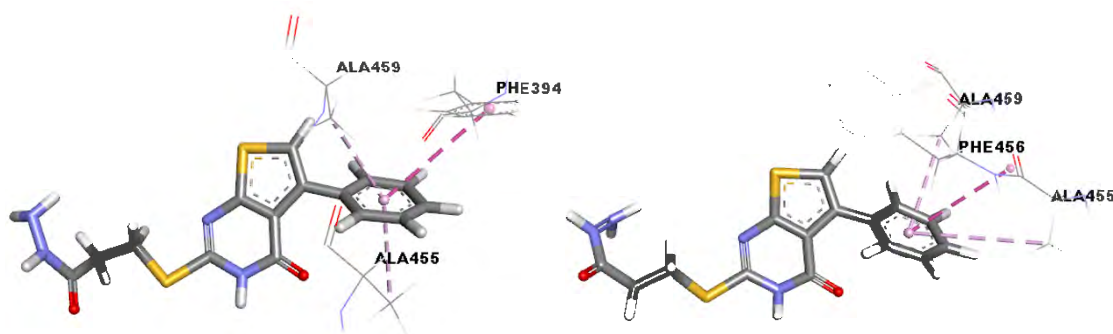


Figure 3.4. Some hydrophobic interactions formed between the phenyl ring of compound **31** and TG2 during 200 ns MD simulation.

In the first 90 ns simulation, the tail was held mainly by the hydrogen bonds between the ligand acylhydrazide NH_2 and LEU420 backbone CO. After that, it moved toward GLU452 residing on the opposite loop and formed hydrogen bonds with the side chain CO of this residue. This hydrogen bond was maintained till the end of the 200 ns simulation. The positions of the ligand when it formed the hydrogen bonds with LEU420 and GLU452 and the distances between the relevant atoms forming the hydrogen bonds are indicated in Figure 3.5.

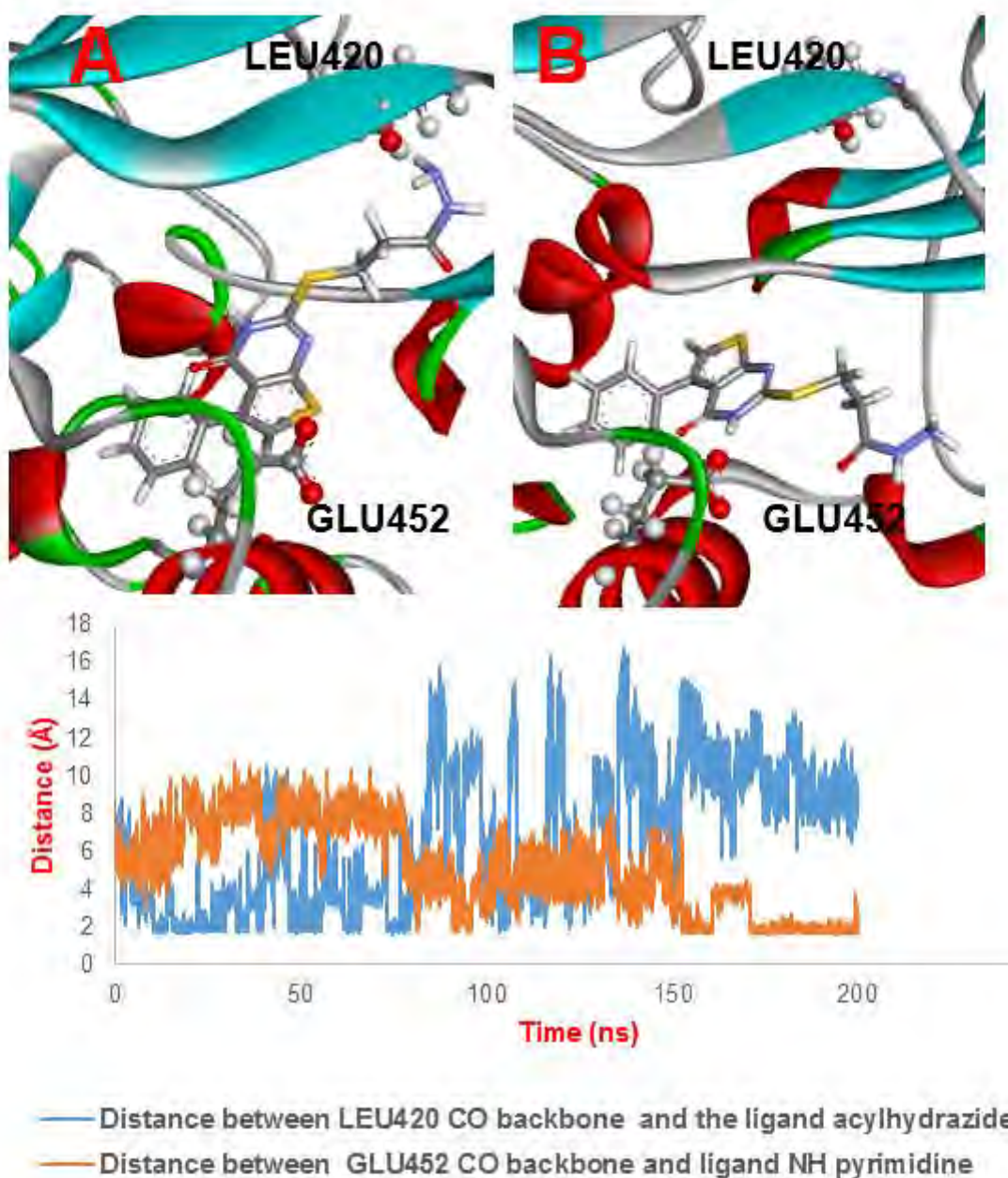


Figure 3.5. Position of compound **31** when it formed hydrogen bonds with LEU420 (A) and GLU452 (B), and distances between the relevant atoms of these hydrogen bonds.

The whole molecule of the ligand stayed inside the predicted binding site despite it highly fluctuated during the MD simulation. Compound **31** was observed to be more mobile than the parent compound and it is obvious from their RMSD values in Figure 3.6. The hydrophobic interactions between the head of the ligand and the hydrophobic pocket together with the hydrogen bonds between the ligand pyrimidine ring and the protein may be the essential interactions that held the ligand inside the predicted binding site although the high mobility of the ligand side chain.

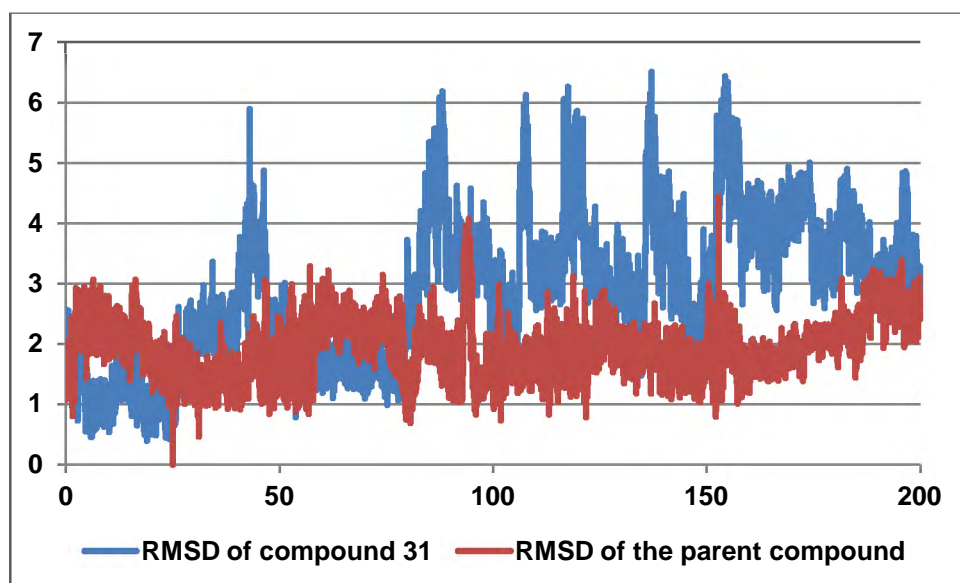


Figure 3.6. RMSD (Å) of compound **31** in comparison to that of the parent compound.

3.3 MD trajectories of compounds having a N,N-dimethyl ethyl amide side chain

The acylhydrazide thioether side chain of compound **31** was modified to N,N-dimethyl ethyl amide to increase the compound's water solubility while keeping the same length of the tail. Four compounds in this series were applied MD simulations in which the modified tail was observed to be more mobile than the original one. The significant mobility of the tail may be the result of the reduction of hydrogen bonds formed between the ligand tail and the enzyme.

3.3.1 MD trajectory of compound **32a**

During the simulation, the phenyl head was held inside the hydrophobic pocket by interactions with nearby amino acids with similar hydrophobic interactions as that formed with compound **31**. The ligand thieno[2,3-d]pyrimidine ring moved towards TYR445 and generated hydrogen bonds with the backbone of this residue (Figure 3.7a) with the highest occupancy (36.52%) among the recorded hydrogen bonds. It is noticeable from Figure 3.7b,c that the distances between the atoms forming the hydrogen bonds between the ligand pyrimidine and TYR445 are mostly less than 3.0 Å. This indicates the strong and stable hydrogen bonds formed between these atoms. The phenyl ring of TYR445 also formed a T-shaped pi-pi interaction with the ligand. These observations indicate the important role of the interactions between the ligand and residue TYR445 in keeping the ligand pyrimidine ring stable when the tail was

dramatically mobile. Therefore, the ligand was maintained in the predicted binding site despite the simulation time was increased to 400 ns.

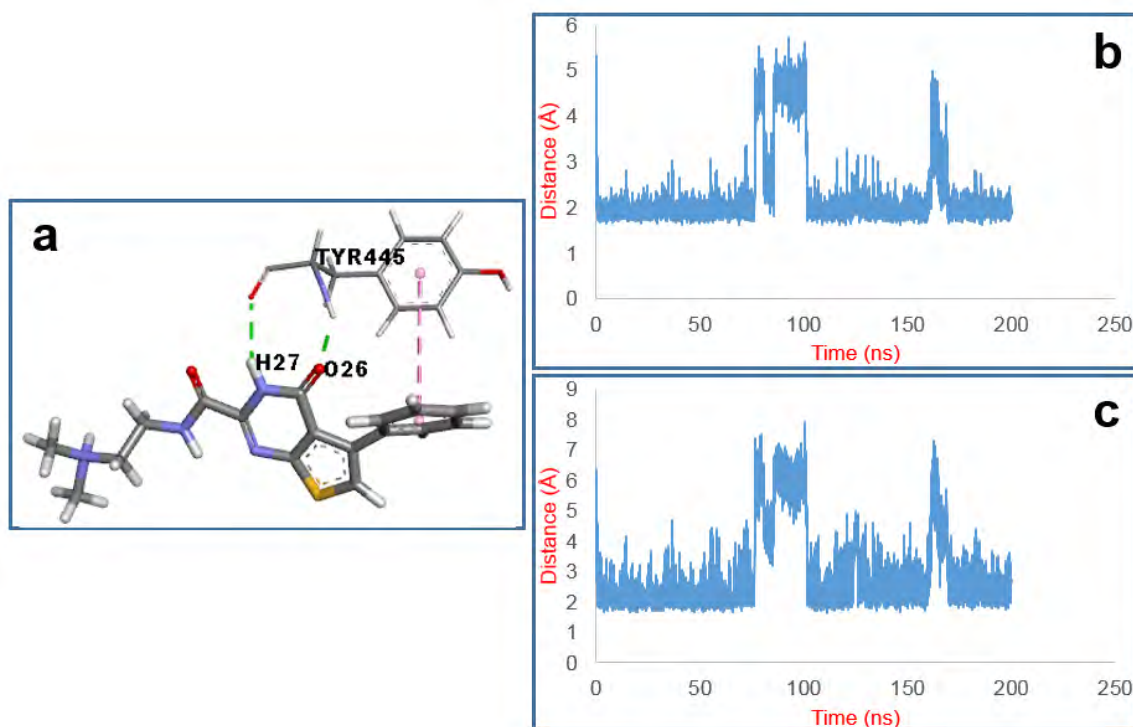


Figure 3.7. (a) Interactions between compound **32a** and TYR445; (b) distance between the ligand O (pyrimidine CO) and TYR445 H (backbone NH); (c) distance between the ligand H (pyrimidine NH) and O (backbone CO) of TYR445.

3.3.2 MD trajectory of compound **32b**

During 200ns MD simulation, compound **32b** only formed transient hydrogen bonds with the enzyme but it established stable pi-pi and hydrophobic interactions with the enzyme's hydrophobic pocket. In addition to pi-interactions between the phenyl ring and adjacent residues, the newly attached methyl group formed an alkyl-alkyl interaction with LYS344. Interestingly, the distance between 2 carbon atoms of this alkyl-alkyl interaction fluctuated mostly lower than 5.5 Å as shown in Figure 3.8. Therefore, the hydrophobic interactions between the head and the nearby residues may be the most important bonds to keep the head into the hydrophobic pocket.

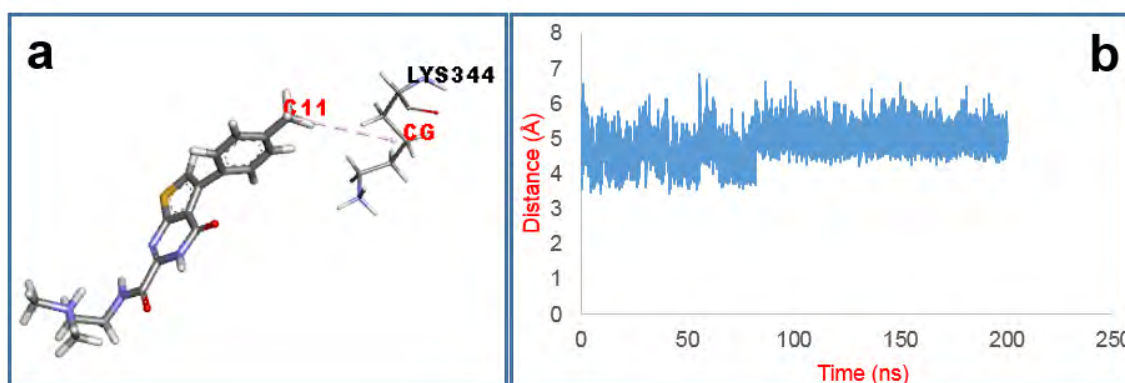


Figure 3.8. (a) An alkyl-alkyl interaction between LYS344 and compound **32b**; (b) distance between C (para CH₃) of compound **32b** and C (CH₂ side chain) of LYS344.

3.3.3 MD trajectory of compound **32c**

The tail of this compound was less mobile than that of compounds **32b** and **32c**. Similar to compound **32a**, the pyrimidine ring of compound **32c** formed high occurrence hydrogen bonds with the predicted allosteric site. However, the high occurrence hydrogen bonds were formed with ALA399 which is located on the loop opposite to the loop containing TYR445. These hydrogen bonds had the highest occurrence (38.04%) among the hydrogen bonds formed between the ligand and the protein and also lasted during the simulation time. The distances between the relevant atoms of these hydrogen bonds are indicated in Figure 3.9. It can be clearly seen that the distance between H atom of the ligand pyrimidine NH and O atom of ALA399 backbone CO is mostly less than 2.5 Å and the distance between O atom of the ligand pyrimidine CO and ALA399 backbone NH is mainly lower than 3.0 Å. This indicated very strong and stable hydrogen bonds between the ligand pyrimidine ring and ALA399. That pointed out the vital role of these interactions in holding the ligand in the predicted allosteric site.

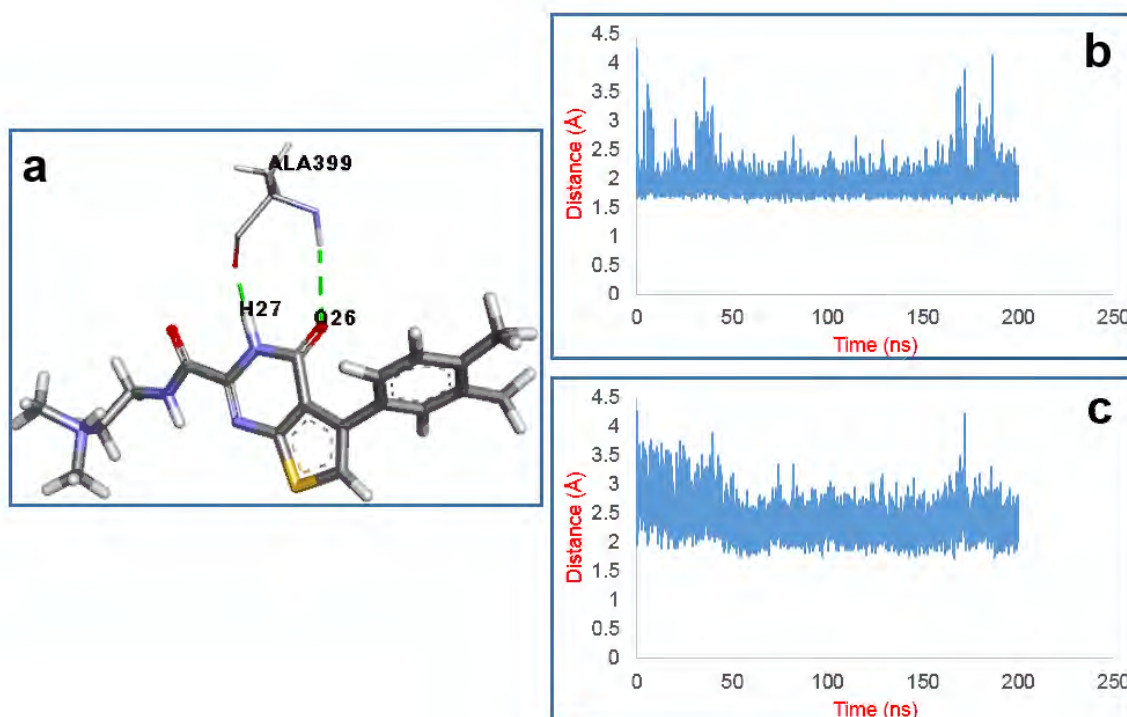


Figure 3.9. (a) Interactions between ALA399 and compound **32c**; (b) distance between the ligand H27 and O of ALA399; (c) distance between the ligand O26 and H of ALA399.

The thieno[2,3-d]pyrimidine ring was clamped between PHE456 and ARG418 with pi-pi stacked interactions and pi-cation interactions, respectively (Figure 3.10). In addition, the two newly attached methyl groups induced hydrophobic interactions with nearby residues. These hydrophobic interactions possibly contributed to the maintaining of the ligand in the allosteric site.

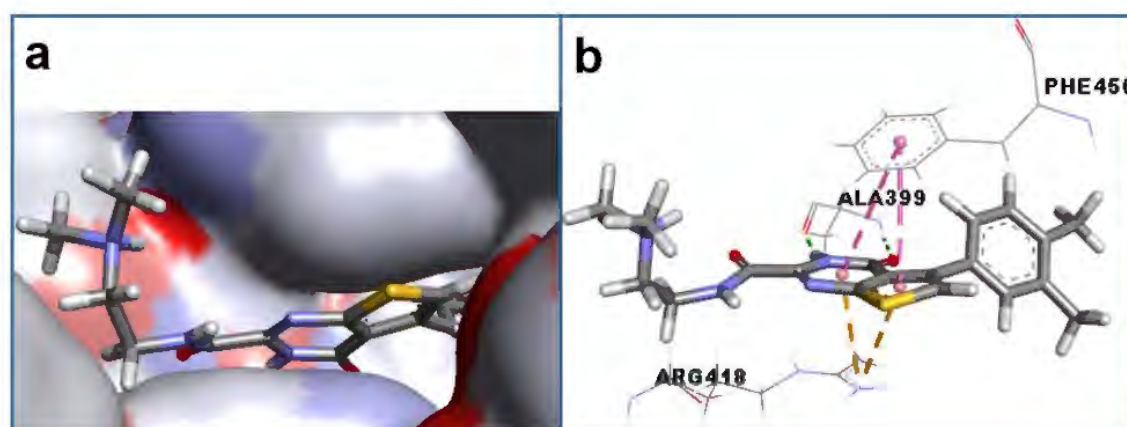


Figure 3.10. (a) The ligand thieno[2,3-d]pyrimidine ring was clamped between PHE456 and ARG418; (b) interactions between the thieno[2,3-d]pyrimidine ring and nearby residues.

3.3.4 MD trajectory of compound 32d

The dramatic mobility of the tail pulled the head out of the hydrophobic pocket after around 42 ns simulation. The whole molecule then detached from the predicted binding site from around 69 ns. In comparison to other compounds in the series of compounds with N,N-dimethyl ethyl amide side chain, it can be clearly seen that compound **32d** is the least stable ligand into the predicted binding site. It indicates the attachment of three methyl groups on the phenyl ring made the head of the ligand become too bulky to sit into the hydrophobic pocket.

Among the compounds having a N,N-dimethyl ethyl amide side chain, compound **32c** was the most stable ligand into the predicted binding site during 200 ns MD simulation. This was reflected via more stable RMSD values of compound **32c** in comparison to those of compounds **32a,b** (Figure 3.11). That suggests the attachment of two methyl groups on the phenyl ring may favour the affinity of the ligand into the predicted binding site.

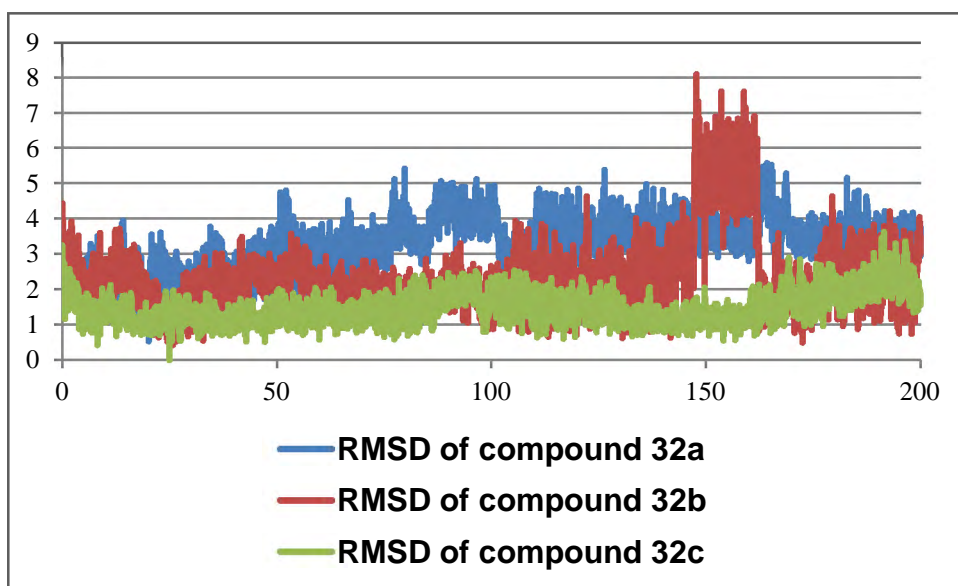


Figure 3.11. RMSD values for compounds **32a,b,c** during 200 ns MD simulations.

3.4 MD trajectories of compounds having an N,N-dimethyl propyl amide side chain

A new set of four compounds with a longer side chain was designed. The N,N-dimethyl propyl amide analogues were chosen to increase water solubility of the ligand. The designed compounds were subjected to MD simulations for 200 ns. Similar to the N,N-

dimethyl ethyl amide side chain, this long tail was observed to be dramatically mobile during all runs.

3.4.1 MD trajectory of compound 33a

During the simulation, 12 hydrogen bonds were formed between the ligand and the protein but their appearance was only transient. The significant mobility of the long tail caused high fluctuations of the thieno[2,3-d]pyrimidine ring. The ligand pyrimidine ring did not form hydrogen bonds with the enzyme as the behaviour of compound **32a**'s pyrimidine ring. The ligand phenyl head was pulled towards the out side of the predicted binding site by the ligand tail. However, it formed hydrophobic interactions with nearby residues such as LYS444, ALA445 and PHE394 (Figure 3.12). The distances of these hydrophobic interactions fluctuated mostly between 5.0 to 6.0 Å as calculated in Figure 3.13. This indicates the stability of the hydrophobic interactions between the ligand head and the predicted allosteric site during 200 ns simulation. Therefore, although the tail was considerably mobile, the compound did not move out of the predicted binding site even at an extended simulation time of 400ns.



Figure 3.12. Hydrophobic interactions between the ligand phenyl head and the nearby residues.

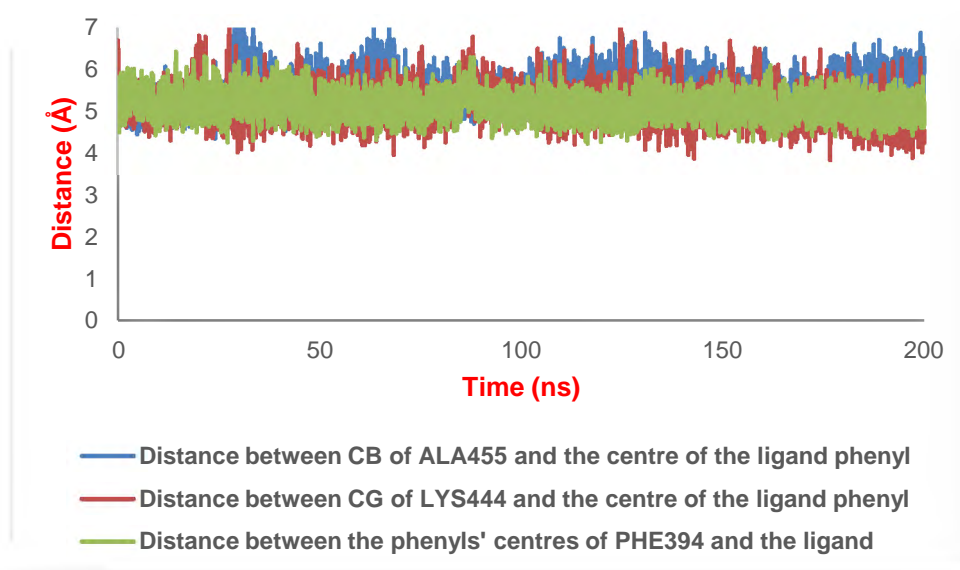


Figure 3.13. Proposed distances of the hydrophobic interactions formed between the ligand phenyl ring and three residues of the hydrophobic pocket: ALA455, LYS444 and PHE394.

3.4.2 MD trajectory of compound **33b**

In the first 100 ns, the phenyl ring was held inside the hydrophobic pocket by interactions with close residues. However, at around 102 ns, it was pulled off from the original hydrophobic pocket due to the high mobility of the long side chain. The head then relocated to a nearby site. That is seen as a jump in the RMSD values of the ligand at that point of the simulation as given in Figure 3.14.

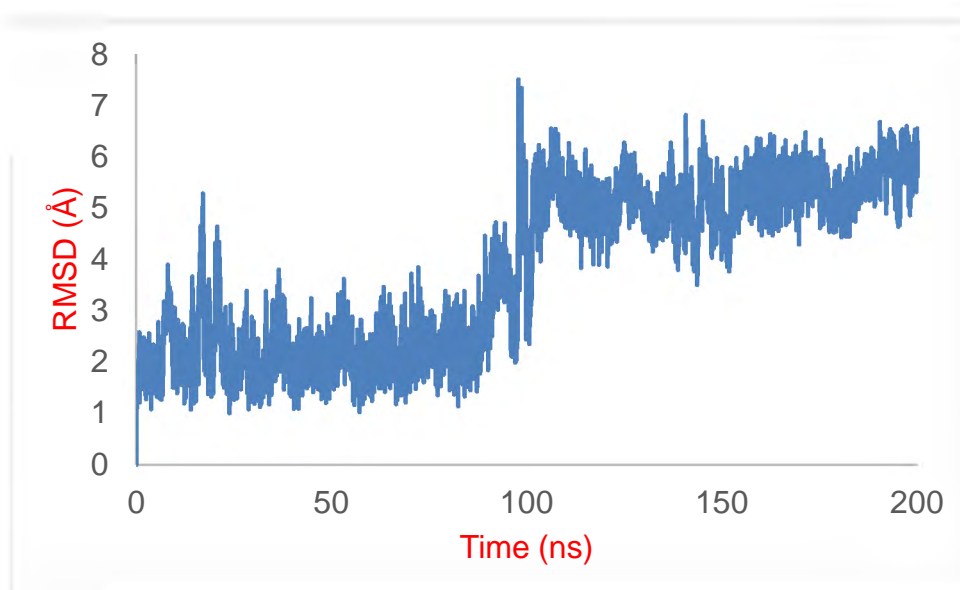


Figure 3.14. RMSD values of compound **33b** during 200 ns MD simulation.

When the ligand relocated to the new position, a hydrogen bond between the pyrimidine ring CO and the backbone NH of ALA399 also started to be formed and that bond lasted till the end of the simulation time. Figure 3.15 showed the hydrogen bond and the distance between the relevant atoms. It is obvious that the distance between the atoms forming the hydrogen bond between the ligand and ALA399 mainly lower than 3.0 Å after 100 ns simulation. That indicated the high occurrence hydrogen between them during that time. Together with hydrophobic interactions between the ligand head and nearby residues, this hydrogen bond may contribute to the stability of the ligand at the new position. The whole molecule was maintained in the predicted allosteric site till the end of the simulation time.

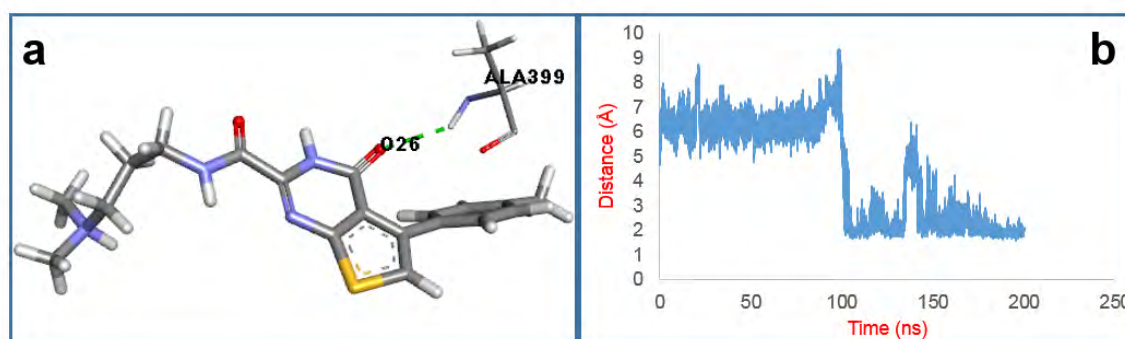


Figure 3.15. (a) Hydrogen bond between compound **33b** and ALA399 and (b) the distance between the relevant atoms of this hydrogen bond during 200 ns simulation.

3.4.3 MD trajectory of compound 33c

During the simulation, the head of the ligand stayed stable in the hydrophobic pocket with numerous hydrophobic interactions with nearby residues. The thieno[2,3-d]pyrimidine ring moved toward TYR445 and formed hydrogen bonds with this residue (Figure 3.16a). The hydrogen bond between the ligand pyrimidine CO and the TYR445 backbone NH occurred 41.21% of the simulation time. It is apparent from Figure 3.16b that the distance between the 2 relevant atoms of this hydrogen bond fluctuated around 2.5 Å during 200 ns simulation. This confirms the stable and sturdy hydrogen bond. The hydrogen bond between the ligand pyrimidine NH and TYR445 backbone CO also appeared in high occurrence (25.71%). The distance between these two atoms is mostly lower than 3.0 Å as shown in Figure 3.16b. This indicates the high occurrence hydrogen bond formed between them. In addition, TYR445 also formed a pi-alkyl interaction with one methyl group of the head. Overall, the hydrogen bonds and the hydrophobic

interaction with TYR445 were critical in restraining the ligand in the predicted allosteric site.

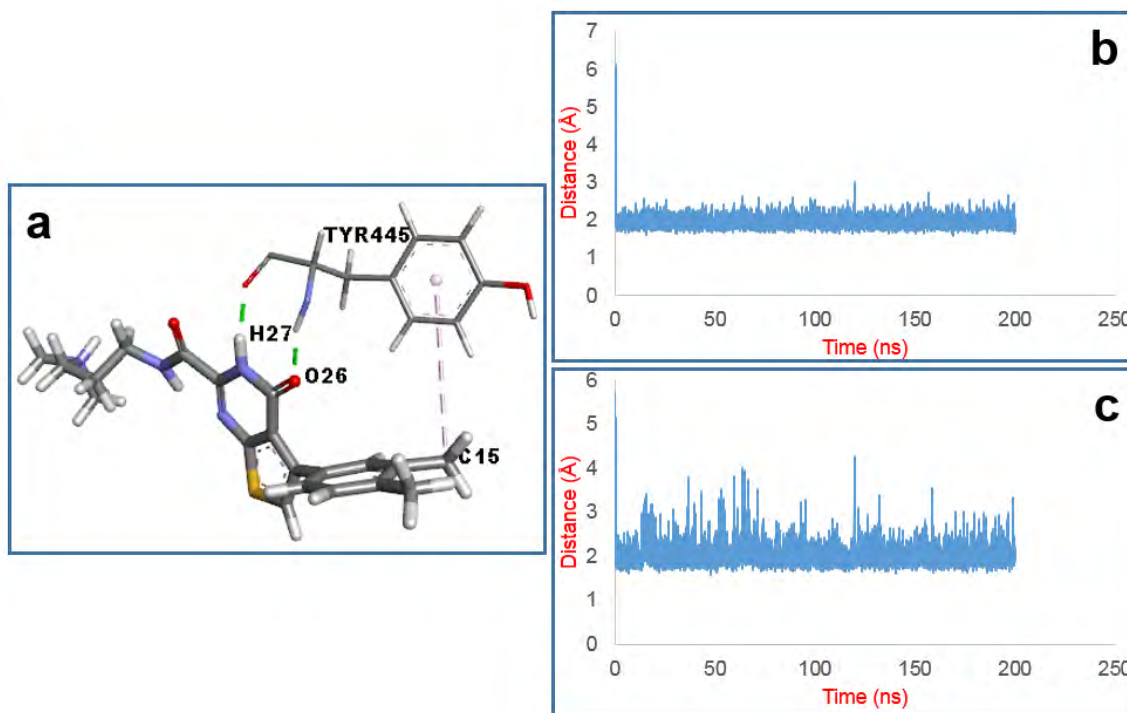


Figure 3.16. (a) Interactions between TYR445 and compound **33c**; (b) distance between O26 of the ligand and H of TYR445 amino; (c) distance between H27 of the ligand and O of TYR445 carbonyl.

3.4.4 MD trajectory of compound 33d

Similar to the analogues in the series of the N,N-dimethyl propyl amides, the long tail of this compound was considerably mobile during 200 ns MD simulation. Some hydrogen bonds were generated between the tail and the thieno[2,3-d]pyrimidine ring with nearby residues but were only transient. The high mobility of the tail and the transient hydrogen bonds formed between the ligand and the enzyme made the ligand move towards the outside of the predicted binding site. From 62.6 ns, the head left the hydrophobic pocket and located to the outside of the pocket. This can be seen in the jump of the RMSD values of the ligand as shown in Figure 3.17.

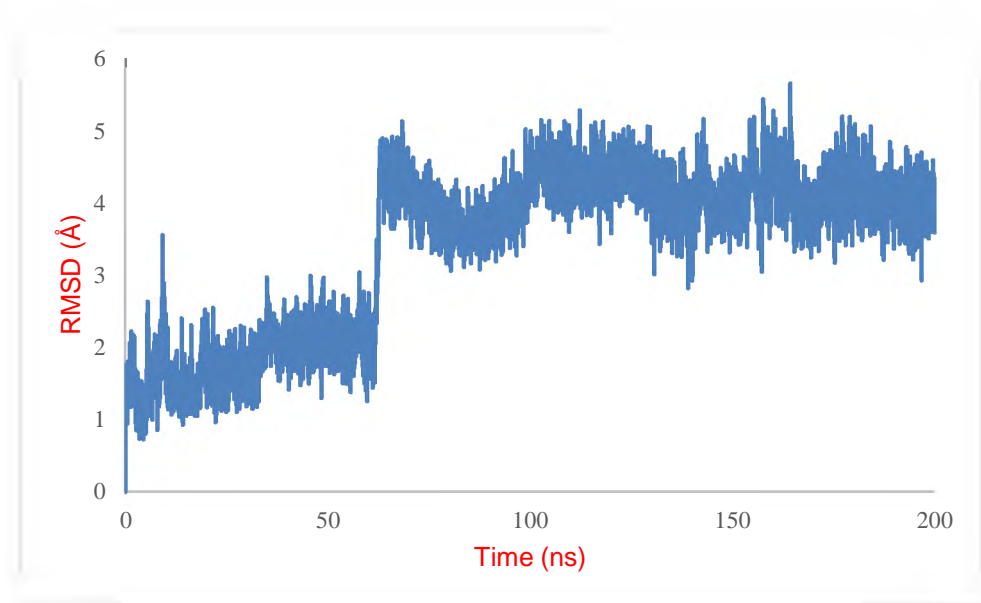


Figure 3.17. RMSD values of compound **33d** during 200 ns MD simulation.

At the new position, the head was held by alkyl-alkyl, pi-alkyl, and pi-pi interactions with ALA455 and PHE394 (Figure 3.18a). The distance between the carbon atoms forming the alkyl-alkyl interaction between the ortho-methyl of the ligand and ALA455 methyl side chain was calculated in Figure 3.18b. It is obvious that this distance dropped to less than 5.0 Å since the ligand RMSD values were doubled. The proposed distance for the ligand C11 and the centre of PHE394 phenyl ring was calculated in Figure 3.18c. The proposed distance between the two centres of the phenyl rings of the ligand and PHE394 was calculated in Figure 3.18d. The distances which reflected the hydrophobic interactions between the ligand head and the close residues indicate the stable hydrophobic interactions between them and that kept the whole molecule in the predicted binding site despite the high mobility of the tail.

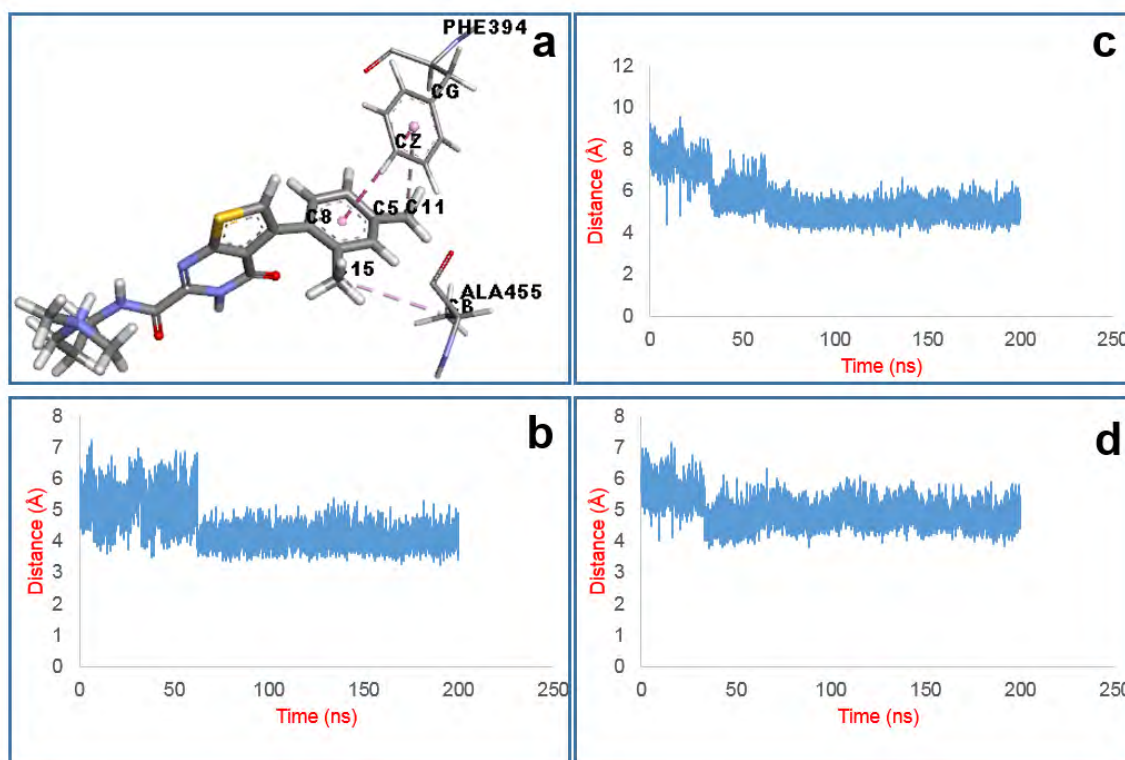


Figure 3.18. (a) Interactions between the head of compound **33d** and 2 residues ALA455 and PHE394; (b) Distance between ligand C15 and ALA455 CB; (c) Distance between the ligand C11 and the centre of the PHE394 phenyl ring; (d) Distance between the centres of the two phenyl rings of the ligand and PHE394.

3.5 MD trajectories of compounds having an amide side chain

The long side chain of compound **31** was modified to an amide side chain in order to reduce the mobility of the ligand tail. A set of 7 compounds with an amide side chain was applied MD simulations for 100 ns.

3.5.1 MD trajectory of compound 34a

During the simulation, high occurrence hydrogen bonds were formed between the ligand tail and three residues: VAL422 (backbone), ALA399 (side chain and backbone) and LEU420 (side chain) as indicated in Figure 3.20 had the highest occurrences (26.85%, 20.10% and 16.30%, respectively). It can be seen from Figure 3.20 that the distances between the relevant atoms of these hydrogen bonds fluctuated mainly less than 3.0 Å. Due to these strong and stable hydrogen bonds, the tail was stabilised during the simulation time. In addition, a high occurrence hydrogen bond (27.80%) was also

formed between the ligand pyrimidine CO and LYS444 side chain NH (Figure 3.19). This interaction contributed to the stability of the ligand in the predicted allosteric site.



Figure 3.19. High occurrence hydrogen bonds between compound **34a** and four residues including ALA399, LEU420, VAL422 and LYS444.

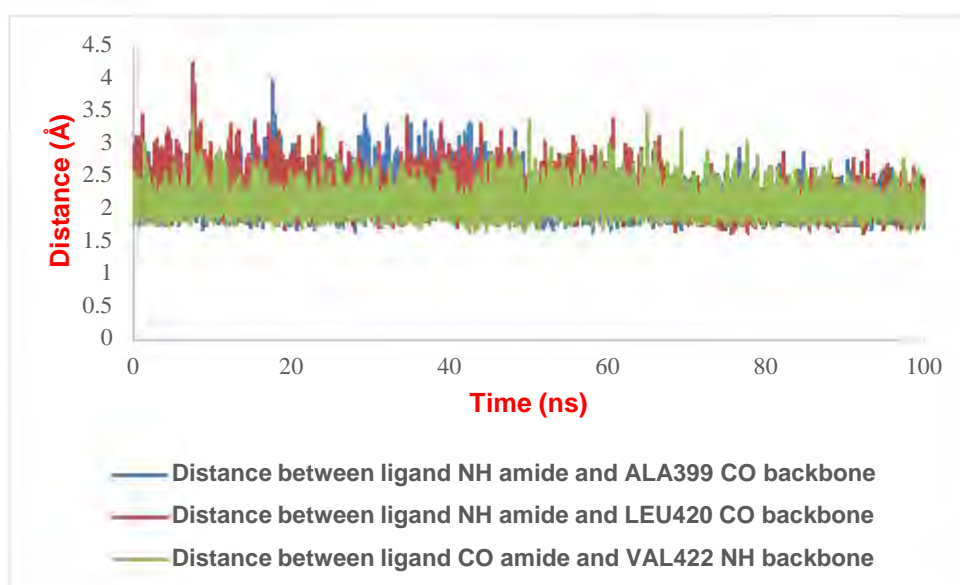


Figure 3.20. Distances between the relevant atoms of the hydrogen bonds between the ligand amide side chain and three residues including ALA399, LEU420 and VAL422.

Similar to the compounds with the phenyl head, the head of compound **34a** formed various hydrophobic interactions with nearby residues such as LYS444, PHE455 and that held the head stably inside the hydrophobic pocket.

Overall, the molecule stayed stable in the predicted binding site. This is reflected via the stable RMSD values of the ligand shown in Figure 3.21.

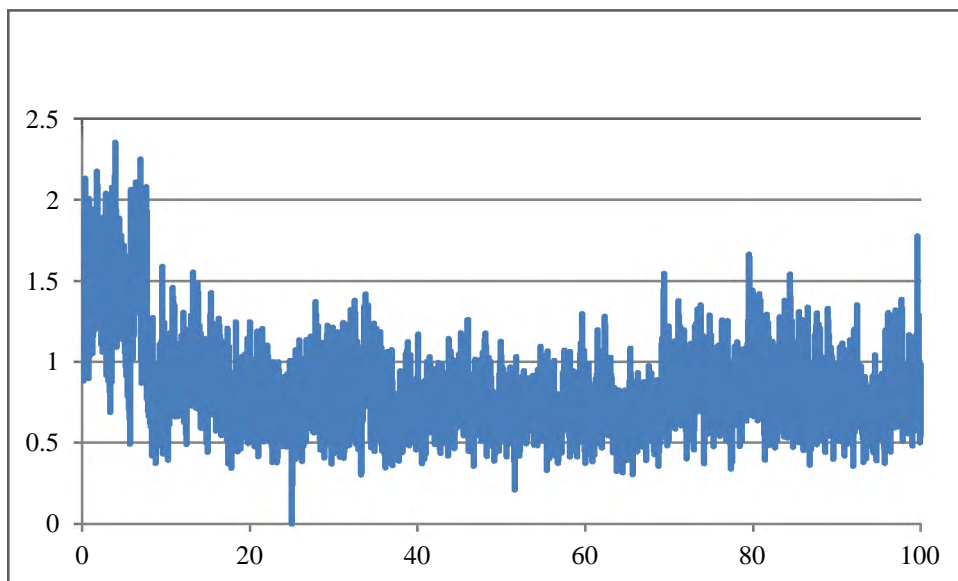


Figure 3.21. RMSD values (Å) of compound **34a** during 100 ns MD simulation.

3.5.2 MD trajectory of compound **34b**

During the simulation, similar to compound **34a**, the hydrogen bond between the ligand amide NH₂ and the ALA399 backbone CO as well as the hydrogen bond between ligand amide CO and the VAL422 backbone NH were dominant among recorded hydrogen bonds with 19.45% and 40.02% occurrences, respectively. These hydrogen bonds and the distances between the related atoms are indicated in Figure 3.22. It is obvious that the distance between the atoms forming the hydrogen bond between the carbonyl group of the ligand and the amino group of VAL422 fluctuated mostly less than 2.5 Å whilst that between the ligand amide NH₂ and the backbone carbonyl of ALA399 mostly lower than 3.0 Å. That indicated very strong and stable hydrogen bonds between the ligand tail and the predicted binding site. Therefore, the tail was held firmly during the simulation time. In contrast to compound **34a**, the hydrogen bond between the pyrimidine CO of compound **34b** and the side chain NH of LYS444 were temporary (occurred only 1.52% of the simulation time). The head of the ligand was surrounded by various hydrophobic interactions and stayed stably in the hydrophobic pocket. Compound **34b** was stable in the predicted binding site as compound **34a**.

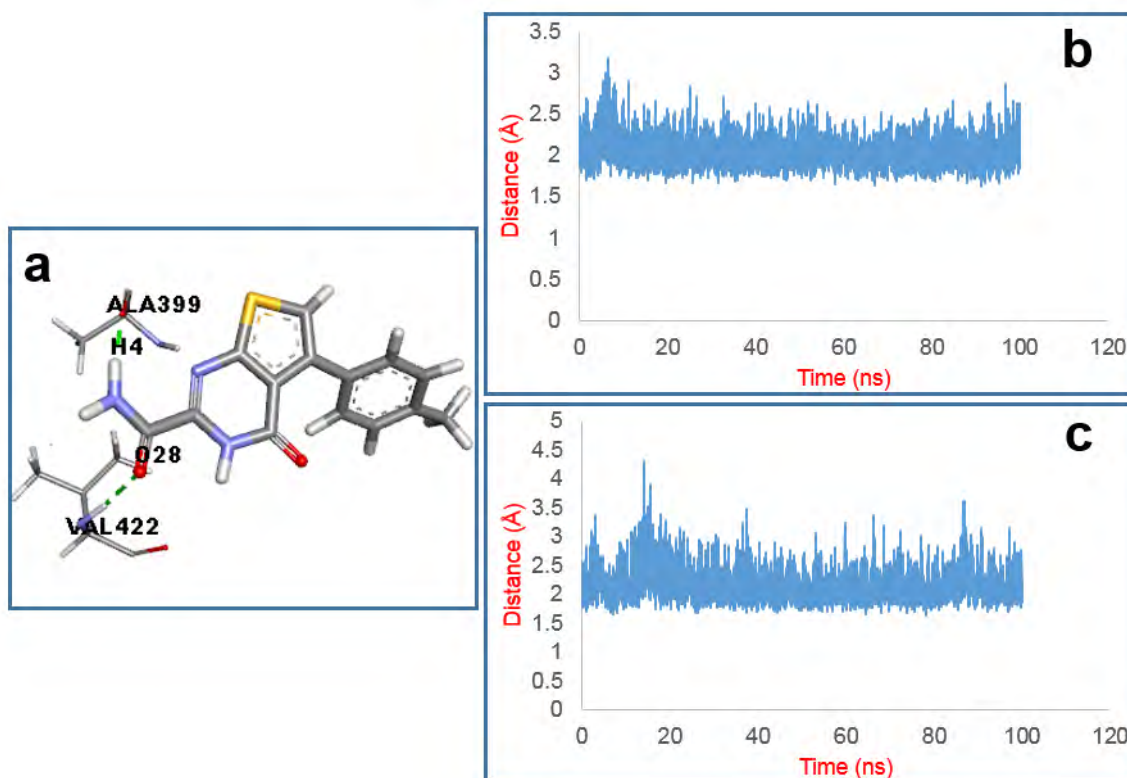


Figure 3.22. (a) Hydrogen bonds between the amide tail of compound **34b** and two residues ALA399 and VAL422; (b) Distance between the ligand amide carbonyl O and the VAL422 amino H; (c) Distance between the ligand amide amino H and the ALA399 carbonyl O.

3.5.3 MD trajectory of compound **34c**

Similar to compound **34a**, the tail was restrained by the hydrogen bonds formed with the backbones of two residues LEU420 and VAL422. These hydrogen bonds had the highest occurrences among reported hydrogen bonds with 22.65% and 32.75%, respectively. The ligand head was also held in the hydrophobic pocket by hydrophobic interactions with nearby residues. Therefore, the whole compound was very stable in the predicted allosteric site.

3.5.4 MD trajectory of compound **34d**

During MD simulation of compound **34a**, there was a constant presence of two water molecules in the hydrophobic pocket which formed hydrogen bonds with ILE379, LYS380, TYR443 and TYR445. In order to fill the gap between the residues of the hydrophobic pocket and the head of compound **34a** and also to enhance hydrogen bonds between them, the ligand was modified by attachment of a polar group at the para

position of the phenyl ring. Two analogues **34d** and **34e** were subjected to the MD simulations as discussed below.

During the simulation, the newly attached amide group of compound **34d** moved towards TYR445 and formed hydrogen bonds with this residue and LYS380 (Figure 3.23a). These hydrogen bonds then became the highest occupancy hydrogen bonds (47.45% and 25.30%, respectively) among recorded hydrogen bonds between the ligand and the protein. The distances between the related atoms fluctuated below 3.0 Å during the simulation as showed in Figure 3.23b. That pointed out the sturdy and stable hydrogen bonds between the newly attached amide and two residues TYR445 and LYS380. These hydrogen bonds were important in stabilising the head stayed stably inside the hydrophobic pocket.

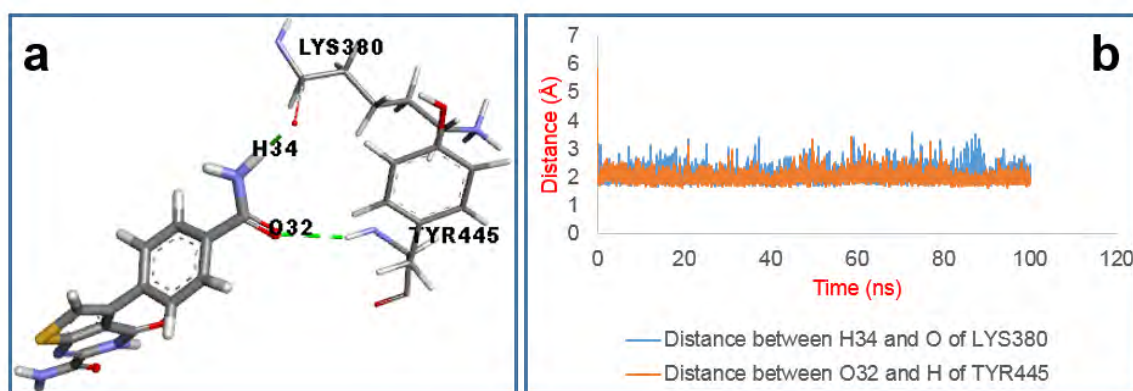


Figure 3.23. (a) Hydrogen bonds between the head of compound **34d** and two residues LYS380 and TYR445; (b) distances between the relevant atoms.

Similar to compound **34a**, the amide tail of the ligand formed hydrogen bonds with LEU420 (backbone), LEU422 (backbone) and ALA399 (backbone) with high occurrences. These interactions held the tail firmly. And the similar hydrogen bond between the thieno[2,3-d]pyrimidine ring and LYS444 (Figure 3.19) lasted during the simulation time. The enzyme formed more and stronger hydrogen bonds with compound **34d** than with compound **34a** but no significant difference in their RMSD values were observed. The RMSD values of compound **34d** (Figure 3.24) are similar to those of compound **34a** (Figure 3.21).

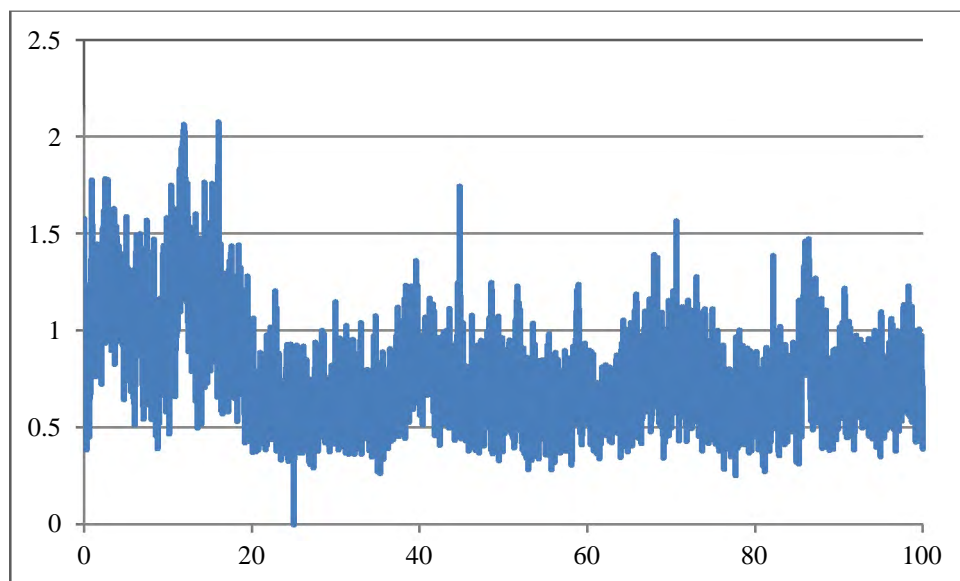


Figure 3.24. RMSD values (Å) of compound **34d** during 100 ns MD simulation.

3.5.5 MD trajectory of compound **34e**

As soon as the simulation started, the newly attached hydroxyl group moved towards to LYS380 and formed a hydrogen bond with the backbone carbonyl of this residue. From 30.4 ns, this hydroxyl group turned back to the original position and reformed a hydrogen bond with the backbone carbonyl of TYR443. The positions of the hydroxyl group when it formed the hydrogen bonds with LYS380 and TYR443 and the distances of the related atoms of the mentioned hydrogen bonds are pointed out in Figure 3.25. The distances between the atoms forming the hydrogen bonds indicated that the hydrogen bonds between the head of the ligand and two residues LYS380 and TYR443 were exchangeable.

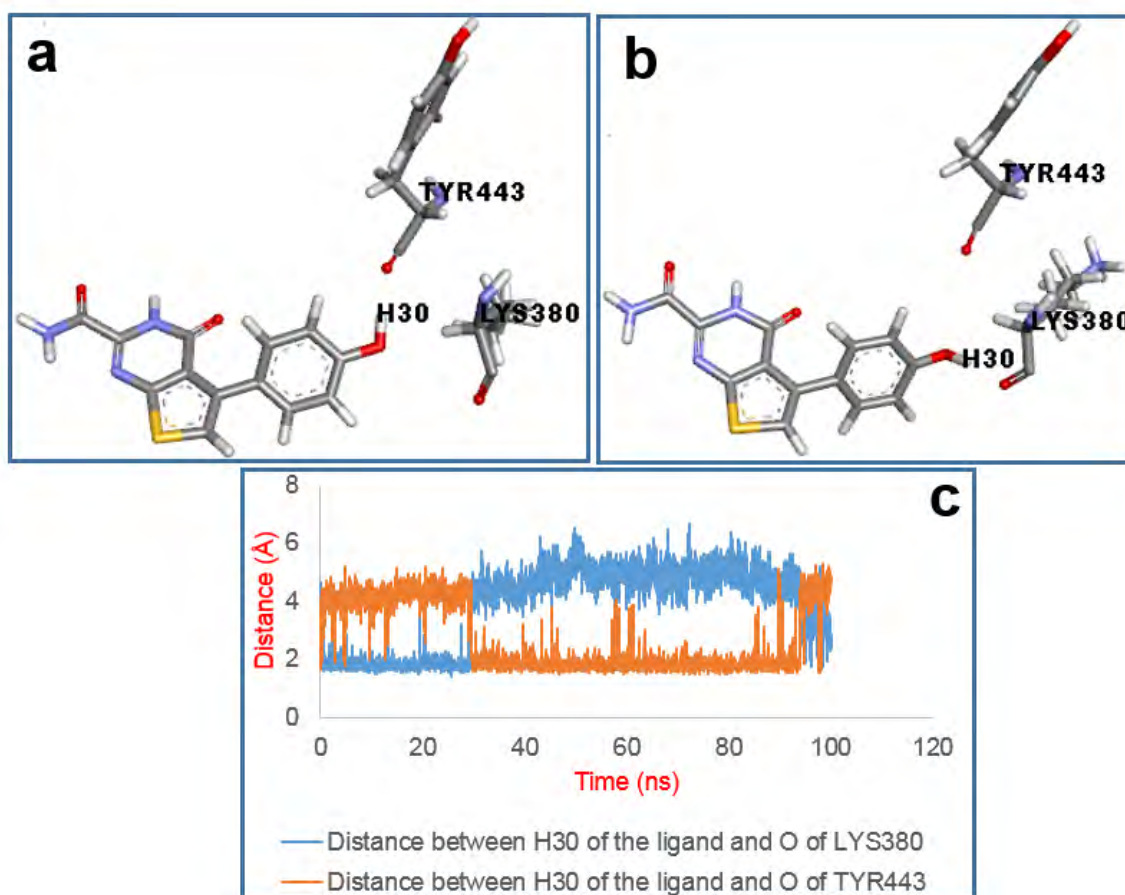


Figure 3.25. (a,b) Positions of the hydroxyl group of compound **34e** when it formed hydrogen bonds with TYR443 and LYS380, respectively; (c) distances between the relevant atoms of these hydrogen bonds.

The replaceable hydrogen bonds between the newly attached hydroxyl group and two residues LYS380 and TYR443 caused the oscillation of the ligand head and indirectly affected the mobility of the tail. After around 43 ns simulation, the tail was pulled out from the original position and became significantly mobile. The ligand pyrimidine ring started forming hydrogen bonds with the backbone of TYR445 (Figure 3.26a). The distances between the related atoms of the hydrogen bonds and the RMSD values of the ligand during 100 ns simulation are indicated in Figure 3.26b. It is obvious that the ligand RMSD values suddenly jumped from around 2.0 Å to higher than 6.0 Å at the same time the distances between the atoms forming hydrogen between the ligand and TYR445 dramatically reduced. This suggests that the hydrogen bonds between the ligand pyrimidine ring and TYR445 backbone may contribute to the stability of the compound when the head was oscillating around. The RMSD values given in Figure 3.27 indicate the binding of compound **34e** in the predicted allosteric site was less stable than compound **34a**.

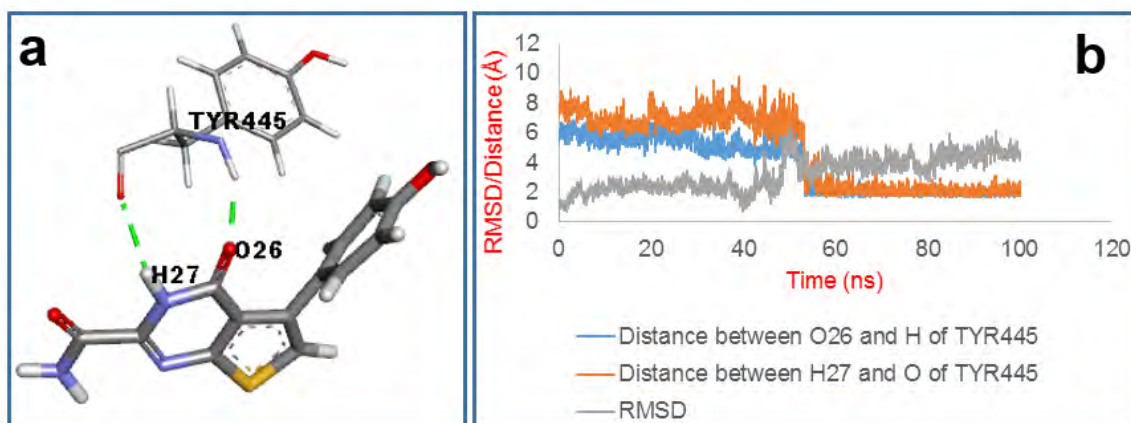


Figure 3.26. (a) Hydrogen bonds between compound **34e** and TYR445; (b) Distance between O26 and H of TYR445, distance between H27 and O of TYR445 and RMSD values.

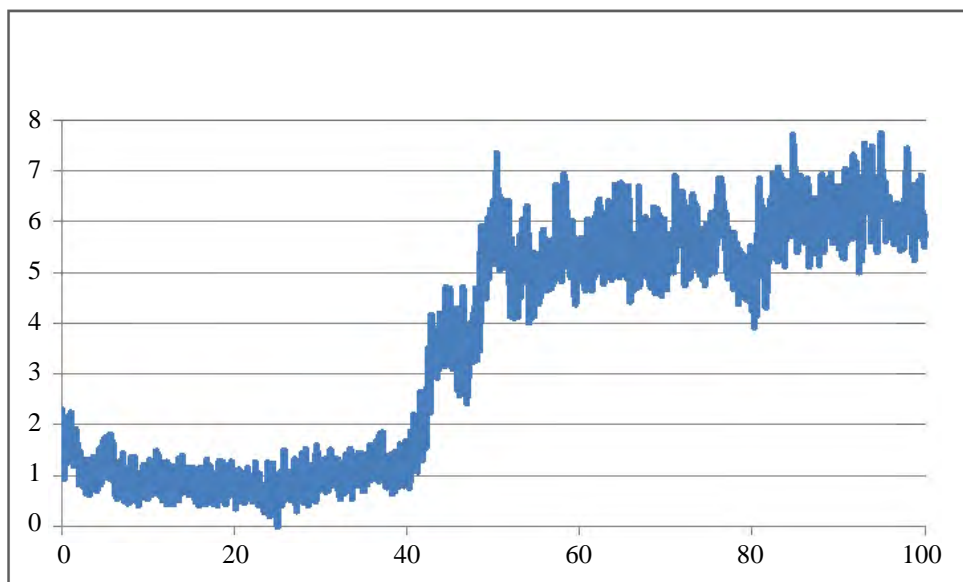


Figure 3.27. RMSD values (Å) of compounds **34e** during 100 ns MD simulation.

3.5.6 MD trajectory of compound **34f**

During the simulation of compound **34a**, **34b** and **34c**, some hydrogen bonds were created between the sulphur atom of the thiophene ring and water molecules. Therefore, the sulphur atom was modified to nitrogen (compound **34f**) or oxygen (compound **34g**) in order to identify any significant changes in the stability of the ligand into the predicted binding site.

As soon as the simulation started, the tail and the pyrrolo[2,3-d]pyrimidine ring of compound **34f** moved away from the original position towards the opposite site where contains residue TYR445. The ligand relocated to the new site due to the high

occupancy hydrogen bonds between the ligand pyrimidine and the backbone of TYR445. The hydrogen bonds between the ligand and TYR445 together with the distances between the related atoms are shown in Figure 3.28. It is noticeable that these distances mostly fluctuated less than 3.0 Å during the simulation time. Especially, the distance between the ligand pyrimidine CO and the backbone NH of TYR445 dropped to less than 2.5 Å from 25 ns. These indicate the strong and stable hydrogen bonds between the ligand and TYR445.

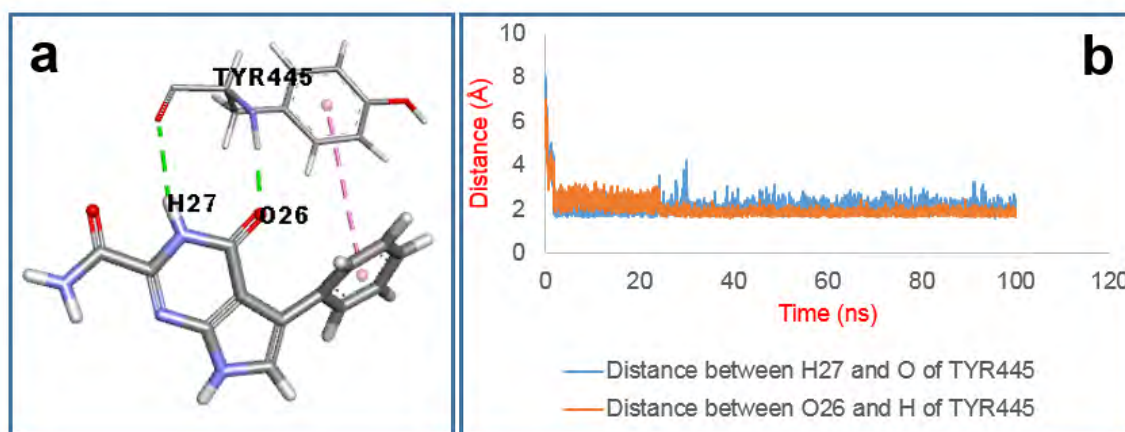


Figure 3.28. Hydrogen bonds between compound **34f** and TYR445 and distances between the relevant atoms of these hydrogen bonds during 100 MD simulation.

In addition to the hydrogen bonds between the ligand pyrimidine ring and TYR445, there was a hydrogen bond between the tail of the ligand and the side chain of GLU447 (Figure 3.29a). The ligand phenyl ring was restrained in the hydrophobic pocket by hydrophobic interactions with close residues such as T-shaped pi-pi bonds with PHE394, TYR445 and a pi-alkyl bond with ALA455 (Figure 3.29b).

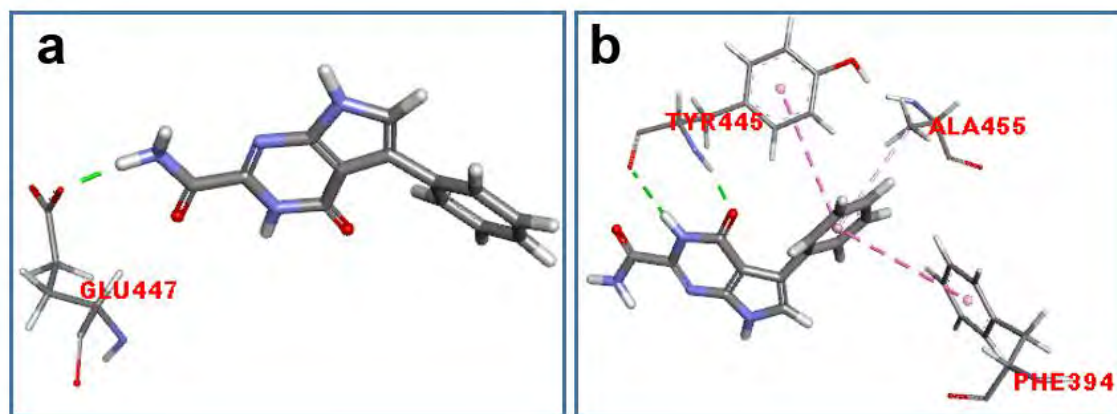


Figure 3.29. The hydrogen bond between the side chain of compound **34f** and GLU447 (a); the hydrophobic interactions between the phenyl head of compound **34f** and nearby residues.

Overall, compound **34f** was maintained in the allosteric site during the simulation time but less stable than compound **34a**. That is reflected via the RMSD values for both compounds as shown in Figure 3.30.

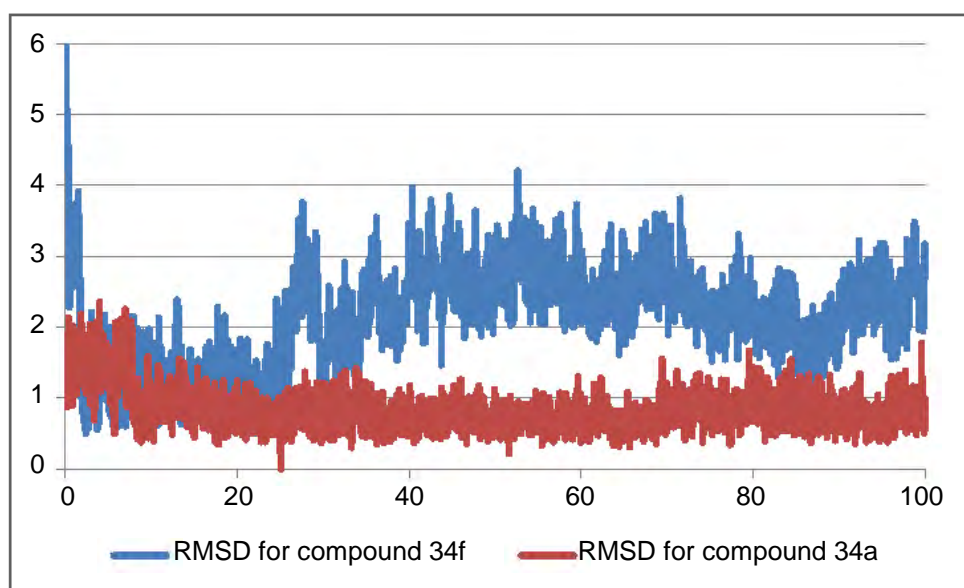


Figure 3.30. RMSD values (Å) of compounds **34a,f** during 100 ns MD simulation.

3.5.7 MD trajectory of compound **34g**

The behaviour of this compound was similar to compound **34f** during 100 ns MD simulation. During the first 27 ns simulation, the ligand furo[2,3-d]pyrimidine ring moved forwards to the side that contains TYR445 and formed hydrogen bonds with this residue. The ligand amide tail also formed a hydrogen bond with GLU447 (side chain), which presented for 15.43% of the simulation time. Similar to compound **34f**,

compound **34g** was maintained in the allosteric site during the simulation time but less stable than compound **34a** as indicated in Figure 3.31.

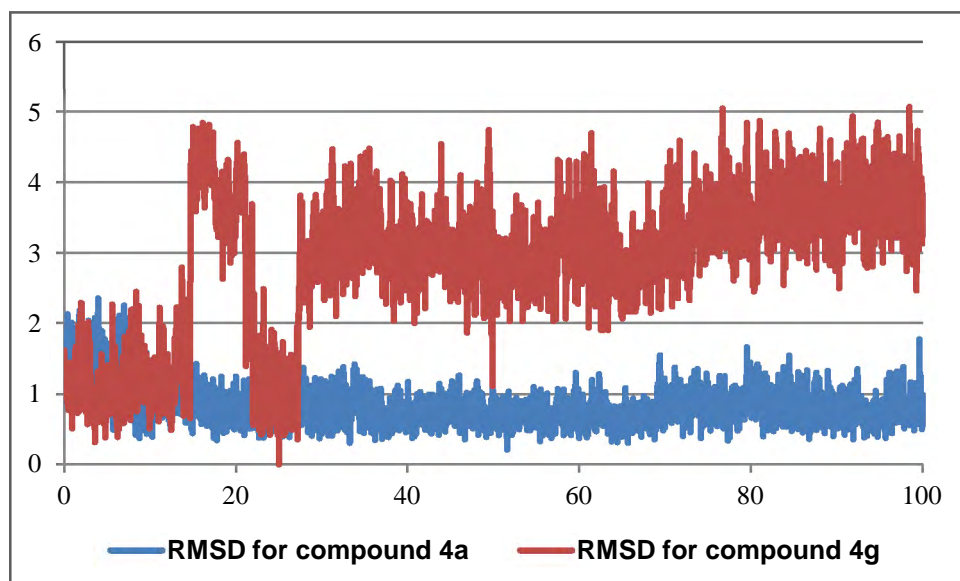


Figure 3.31. RMSD values (Å) of compounds **34a,g** during 100 ns MD simulation.

3.6 MD trajectories of compounds having a hydrazide side chain

3.6.1 MD trajectory of compound 35a

Very soon after the simulation started (after around 2.5 ns), the head relocated more deeply into the hydrophobic pocket. Hydrogen bonds between the ligand pyrimidine ring and two residues ASN398 and ALA399 (Figure 3.32a,b) were dominant among the hydrogen bonds between the ligand and the protein. The ligand pyrimidine formed the hydrogen bond with ASN398 side chain amino only in the first 71 ns of the simulation and with ALA399 backbone after that. The distances between the relevant atoms (Figure 3.32c) indicated the interchange of these hydrogen bonds that pulled the pyrimidine ring toward the loop containing ASN398 and ALA399 and kept the thieno[2,3-d]pyrimidine ring stable. Some hydrogen bonds were created between the tail of the ligand and the protein but only transient. The stability of the ligand therefore was suggested to be mainly contributed by the hydrogen bonds between the pyrimidine ring and two residues ASN398 and ALA399.

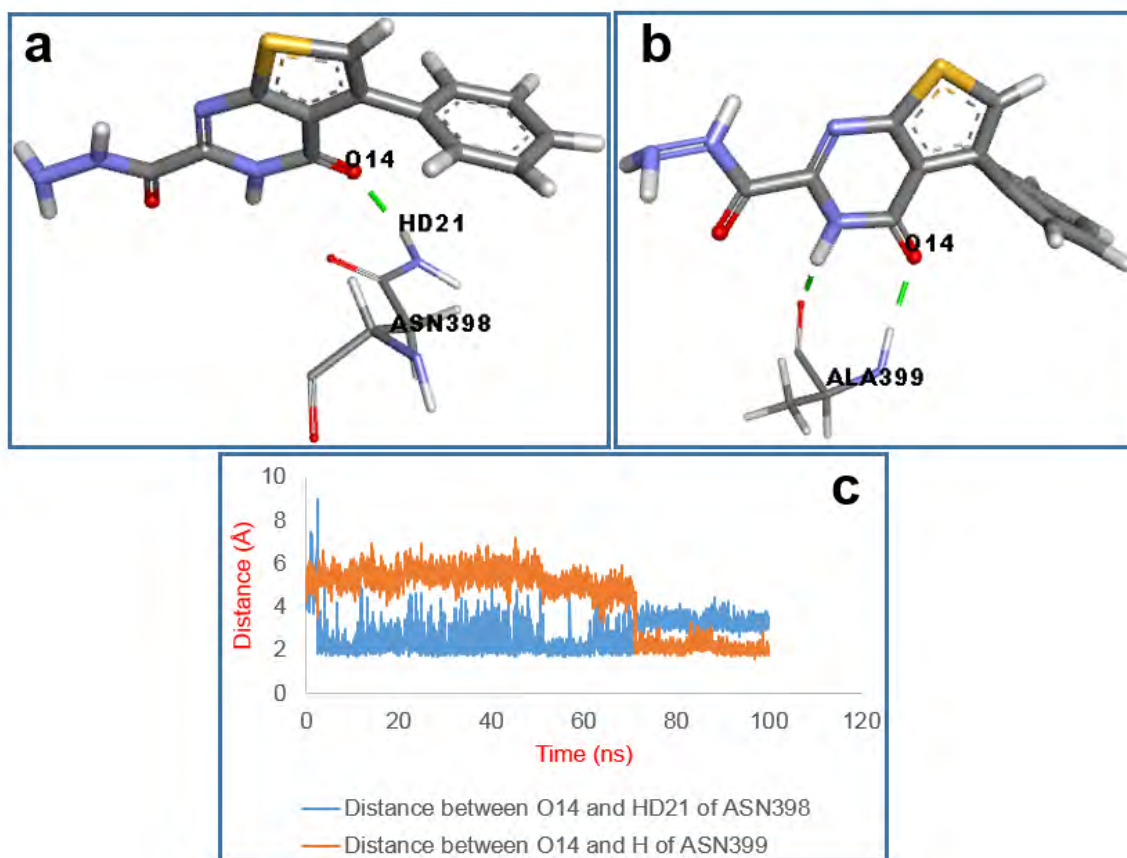


Figure 3.32. (a,b) Hydrogen bonds between compound **35a** and two residues ASN398 and ALA399; (c) distance between the relevant atoms of these hydrogen bonds.

3.6.2 MD trajectory of compound **35b**

The hydrogen bonds between the ligand pyrimidine ring and the side chain amine of ASN398 (Figure 3.33a) had the highest occurrence (26.63%) among hydrogen bonds between the ligand and the protein. Different from compound **35a**, these interactions were maintained during the simulation time. It can be seen from Figure 3.33b that the distance between one hydrogen atom of the amino group of ASN398 and the oxygen of the ligand pyrimidine carbonyl fluctuated mostly less than 3.0 Å during 100 ns. This indicates strong hydrogen bonds between the ligand pyrimidine and ASN398 that suggests their vital role in keeping the ligand pyrimidine ring stable during the simulation.

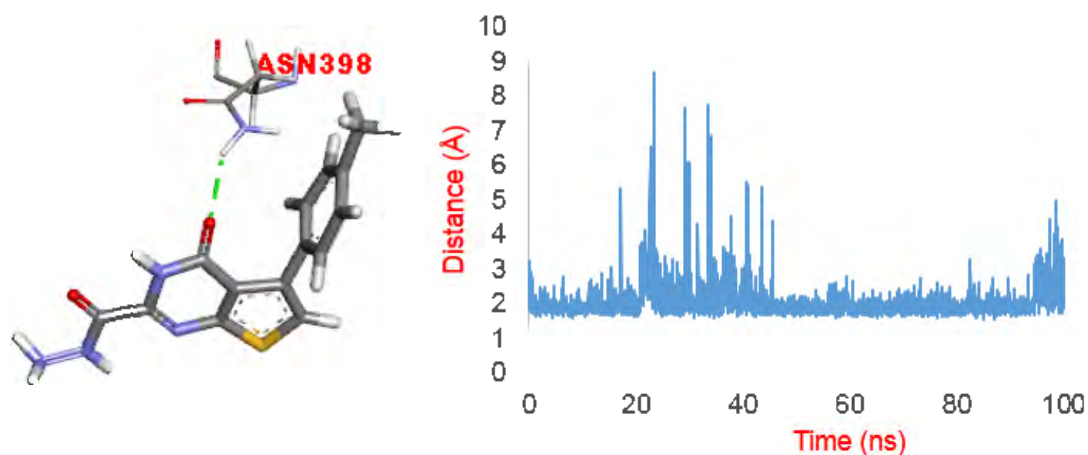


Figure 3.33. (a) Hydrogen bond between compound **35b** and ASN398; (b) Distances between the relevant atoms.

The head was held by hydrophobic interactions with nearby residues such as LYS444 and PHE394 (Figure 3.34). The distance between CG of LYS444 and the centre of the ligand phenyl ring was calculated by an average distances between CG and two ligand carbon atoms C22 and C25. The distance between C19 of the ligand and the central of the phenyl ring of PHE394 was calculated by an average distances between C19 and two ligand carbon atoms CZ and CG. It is noticeable that, these distances fluctuated around 5.0 Å. These calculated distances proposed the stable hydrophobic interactions between the head of the ligand and the residues of the hydrophobic pocket, particularly the alkyl- π interaction between the ligand newly attached methyl and the phenyl ring of PHE394. That indicates the possible role of the newly attached para-methyl in the improvement of the hydrophobic interaction between the head of the ligand and the predicted allosteric site.

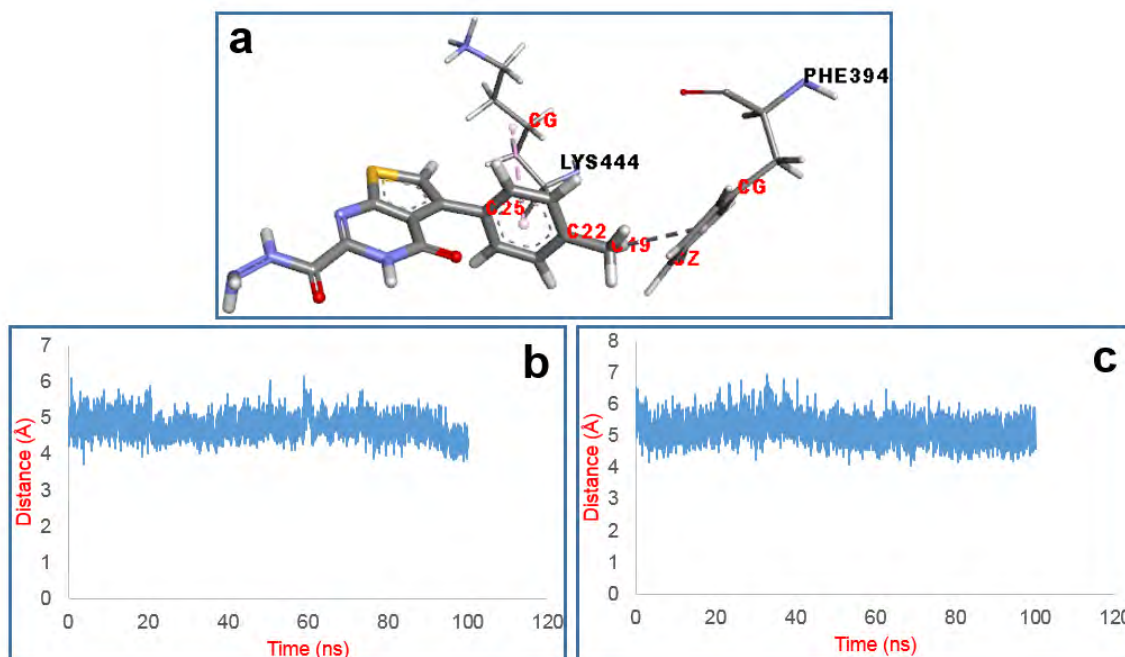


Figure 3.34. (a) Hydrophobic interactions between the head of compound **35b** and LYS444 and PHE394; (b) distance between the carbon atom of LYS444 and the central of the phenyl ring of the ligand; (c) distance between the ligand para-methyl carbon and the central of the phenyl ring of PHE394.

3.6.3 MD trajectory of compound **35c**

Similar to compound **35b**, the head of ligand was kept stable inside the hydrophobic pocket by interactions with nearby residues such as PHE394 and ALA455. Very early in the simulation, the thieno[2,3-d]pyrimidine ring moved towards to the loop that contained ALA399 and formed hydrogen bonds with both the backbone NH and CO of this residue (Figure 3.35a). These hydrogen bonds occurred 31.95% and 32.38% of the simulation time, respectively. The distance between the relevant atoms was mostly less than 3.0 Å during the simulation time as given in Figure 3.35b. This indicates strong and stable hydrogen bonds between them. In addition, hydrogen bonds were generated between the NH₂ of the ligand tail and the backbone CO of LEU420 (Figure 3.35a). The distance between the related atoms of these hydrogen bonds (Figure 3.35c) indicates the high occurrence hydrogen bonds between them. These sturdy hydrogen bonds between the thieno[2,3-d]pyrimidine ring and the tail of the ligand and two residues PHE394 and ALA455 may be the most critical interactions to restrain the ligand firmly during the simulation. Similar to compound **35b**, the head of compound **35c** was held stably inside the hydrophobic pocket.

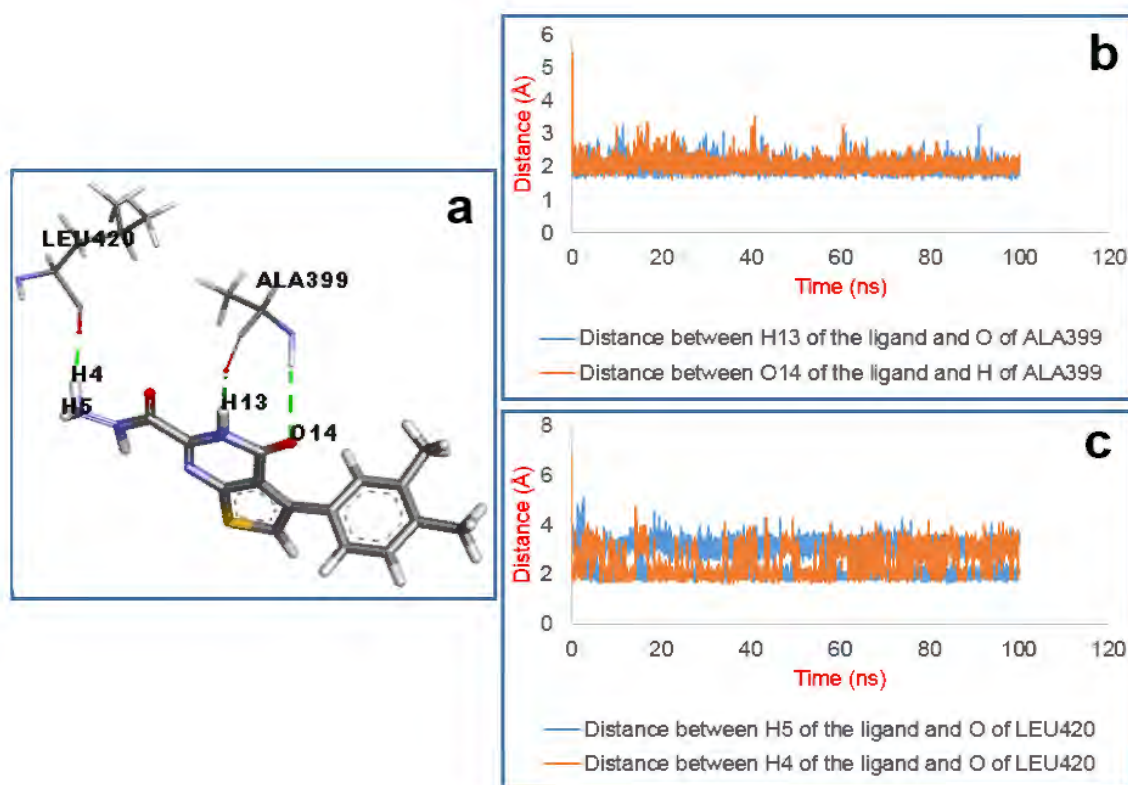


Figure 3.35. Hydrogen bonds between compound **35c** and two residues ALA399 and LEU420 and distances of the relevant atoms of the bonds.

Compounds **35b,c** were more stable in the predicted allosteric site than compounds **35a** as indicated in their RMSD values (Figure 3.36). This indicates the attached methyl groups on the phenyl ring possibly improved the binding of the ligand head in the hydrophobic pocket and consequently stabilised the ligands in the allosteric site.

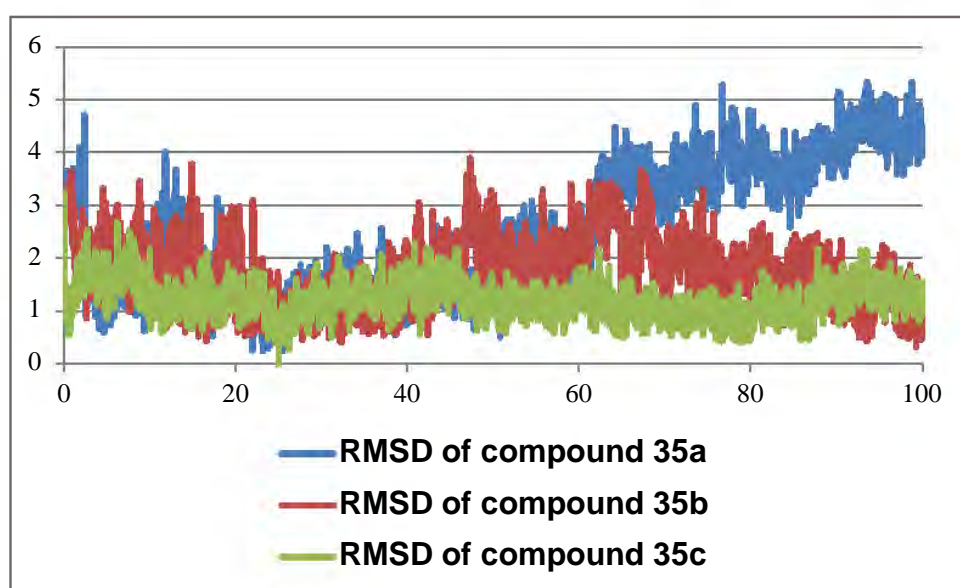


Figure 3.36. RMSD values (Å) of compounds **35a,b,c** during 100 ns MD simulation.

3.7 MD trajectories of compounds having an ethyl acetate side chain

3.7.1 MD trajectory of compound 36a

The tail of the ligand was significantly mobile and did not form any hydrogen bond with the enzyme. The movement of the tail pulled the head out of the hydrophobic pocket although some hydrophobic interactions were formed between the ligand phenyl ring and nearby residues. The whole molecule left the predicted binding site from 16 ns simulation.

3.7.2 MD trajectory of compound 36b

Similar to compound **36a**, the head of the ligand left the hydrophobic pocket early in the simulation and the ligand unbound of the predicted allosteric site and relocated to the outside of this site.

3.7.3 MD trajectory of compound 36c

Similar to compound **36a** and **36b**, the ligand tail was significantly mobile. However, two exchangeable hydrogen bonds between the ligand thieno[2,3-d]pyrimidine ring and two residues ASN398 and ALA399 were generated. The hydrogen bond between the ligand and ALA399 was formed mainly from 10 ns to 75 ns while that between the ligand and ASN398 was created in the remaining time. These constant hydrogen bonds are indicated by the distances between the relevant atoms as given in Figure 3.36.

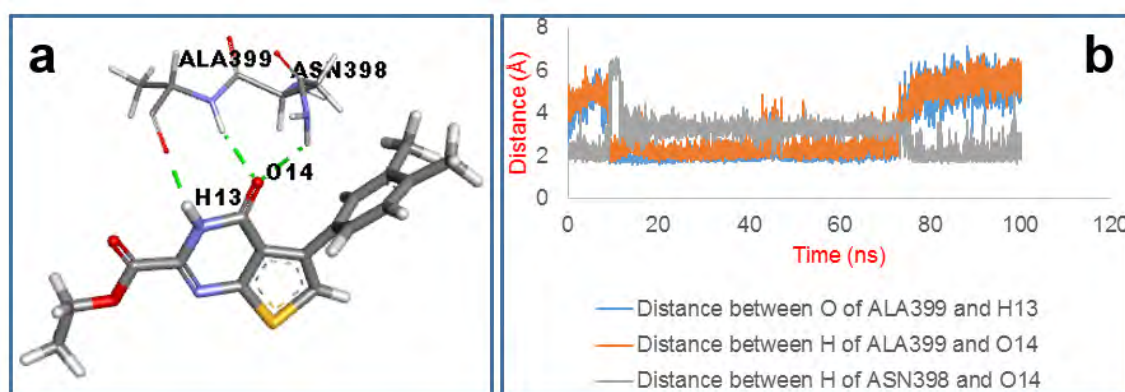


Figure 3.36. (a) Hydrogen bonds between compound **36c** and two residues ASN398 and ALA399; (b) distances between the relevant atoms of these hydrogen bonds.

The head of the ligand was kept stable in the hydrophobic pocket by forming the hydrophobic interactions with nearby residues (Figure 3.37a). The alkyl-alkyl

interaction between ALA455 was mostly maintained during the simulation time with the distance between the two relevant carbons fluctuated around 3.5 to 5.0 Å (Figure 3.37b). ALA455 also formed an alkyl-pi interaction with the ligand phenyl ring. The distance between the carbon atom of ALA455 and the centre of the phenyl head was decreased since the simulation started and it fluctuated less than 5.0 Å from 26 ns (Figure 3.37b). The reduction of the distance related to the pi-alkyl interaction between the ligand phenyl and ALA455 indicated the movement of the head toward the hydrophobic pocket. Along with hydrogen bonds between the ligand pyrimidine and two residues ASN398 and ALA399, these hydrophobic interactions contributed to the stabilisation of the ligand within the predicted binding site. Therefore, compound **36c** was maintained in the predicted allosteric site during the 100 ns MD simulation.

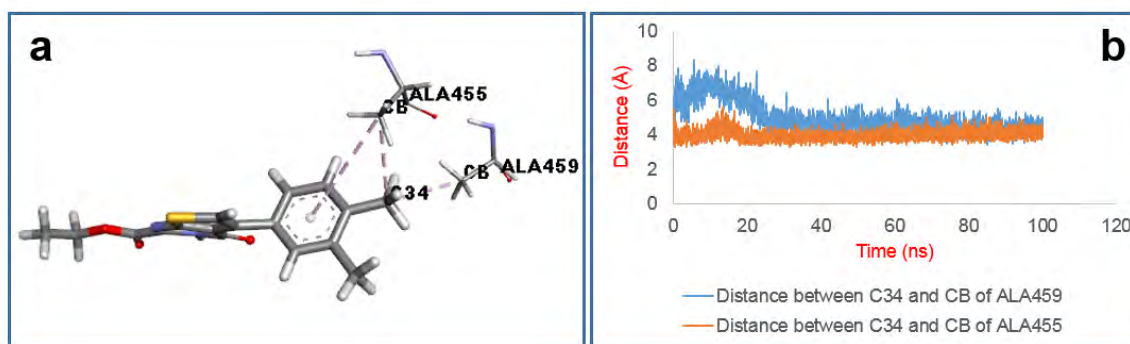


Figure 3.37. (a) Hydrophobic interactions between the head of the ligand and two residues ALA455 and ALA459; (b) distance between the carbon atom of the para-methyl and two methyl carbon atoms of ALA459 and ALA455.

3.8 MD trajectories of the compounds having a carboxylate side chain

During the simulation, the tail and the thieno[2,3-d]pyrimidine ring highly fluctuated and formed transient hydrogen bonds with close residues such as LYS444 (9.75%). The phenyl head also highly fluctuated. Consequently, the ligand RMSD values were unstable. However, these molecules stayed inside the binding site during 100 ns simulation.

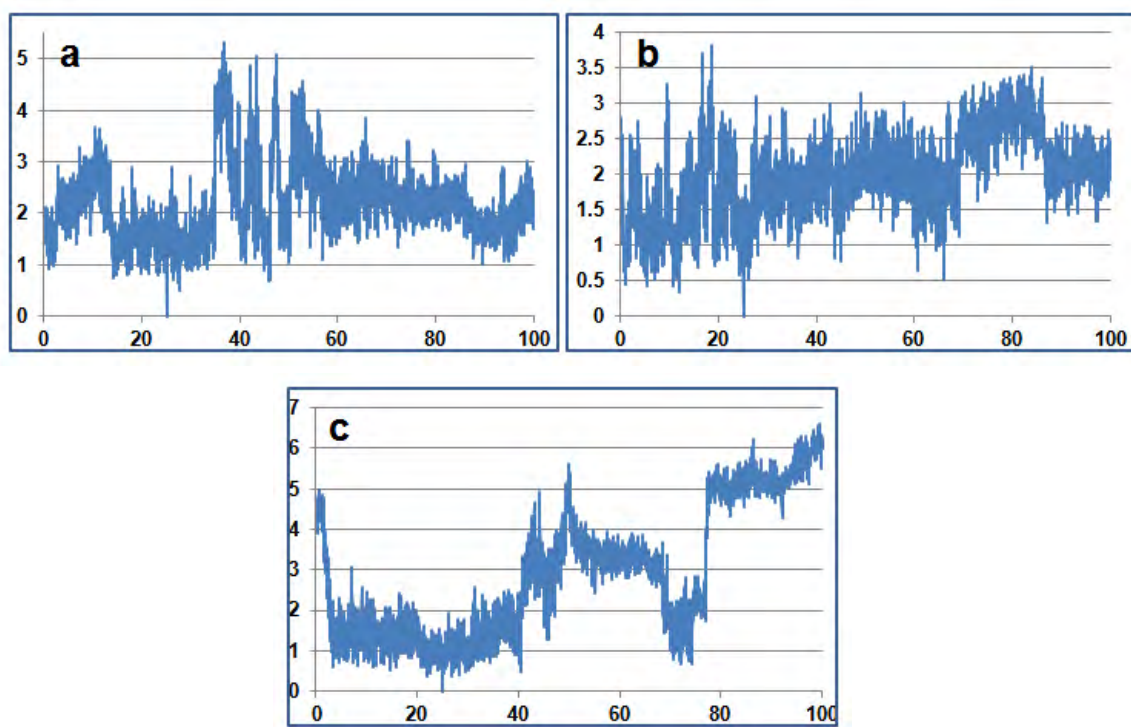


Figure 3.38. RMSD values (Å) of compounds **37a,b,c** during 100 ns MD simulations.

3.9 Conclusion

Three types of interactions between the ligand and the protein were observed to be critical for the maintaining of the designed compounds in the predicted allosteric site. Firstly, the hydrogen bonds between the ligand pyrimidine rings and residues ASN398, ALA399 and TYR445. The hydrogen bonds formed with ASN398, ALA399 were created mainly between the amides and the carbohydrazides whilst those formed with TYR445 were generally found in the MD simulation of the amines. Secondly, the hydrogen bonds between the side chain (tail) of the ligand and residues LEU420 and VAL422 which were found in the MD simulations of the amide and carbohydrazide derivatives. Thirdly, the hydrophobic interactions between the head of the ligand and some residues of the hydrophobic pocket such as LYS444, PHE455 and PHE394.

The removal of the phenyl group attached on the pyrimidine ring of the parent compound in order to increase the ligand water solubility introduced more hydrogen bonds between the pyrimidine ligand and the protein. The compounds with long side chains including compound **31** and the amine derivatives were highly mobile whilst the compounds with short polar side chains such as the amide and carbohydrazide derivatives were stable in the predicted allosteric site. The ethyl acetate derivatives were

the least stable ligands whilst the amide derivatives were the most stable in the predicted allosteric site.

The attachment of methyl groups at meta- and para- positions of the phenyl ring was found to contribute to the stability of the modified head inside the hydrophobic pocket due to the increasing of the hydrophobic interactions with nearby residues. The attachment of a polar group at the para position of the phenyl ring did not improve stability of the ligand because the hydrogen bonds between the polar groups and residues of the hydrophobic pocket caused fluctuations of the ligand head and that movement made the tail more mobile. The modification of the sulphur atom to oxygen or nitrogen atom also did not increase stability of the ligand inside the binding site.

4 Synthesis of potential allosteric inhibitors of TG2

In chapter 3, a large range of potential allosteric inhibitors was designed by modification of various parts of the lead parent compound **LDN-27219**. This chapter focused on the preparation of the designed compounds which shared the common structure as indicated in in Figure 4.1.

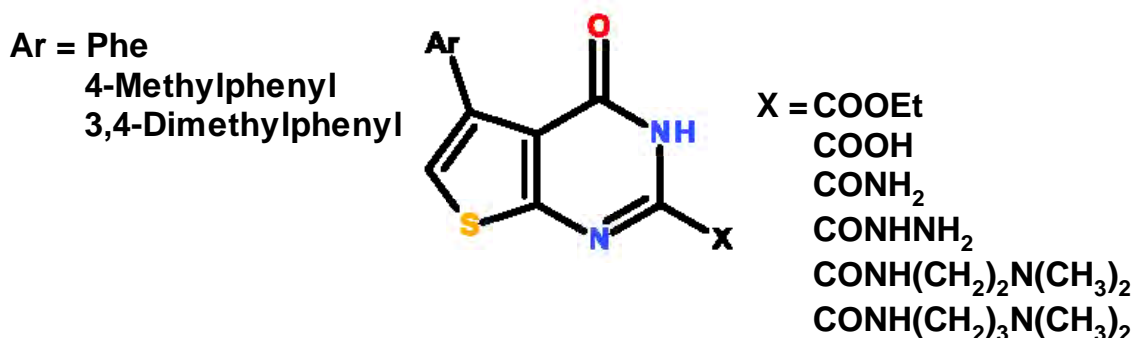
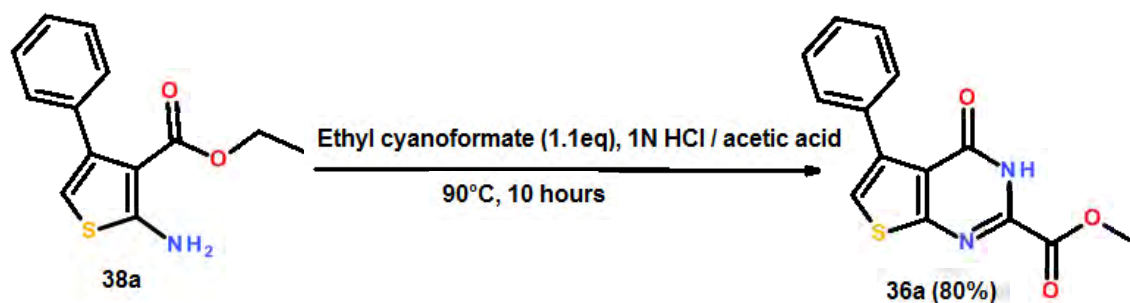


Figure 4.1. General structure of the potential TG2 allosteric inhibitor target compounds.

4.1 Optimisation of conditions to synthesise the key ester



Scheme 4.1. A method to synthesise ethyl 4-oxo-5-phenyl-3H-thieno[2,3-d]pyrimidine-2-carboxylate (compound **36a**) according to the key publication with a reported yield of 80% (Nara et al., 2017).

Ethyl 4-oxo-5-phenyl-3H-thieno[2,3-d]pyrimidine-2-carboxylate (**36a**) and its derivatives were identified as the key intermediate esters to synthesise the target potential allosteric inhibitors of TG2. The method to synthesise compound **36a** from the commercially available ethyl 2-amino-4-phenylthiophene-3-carboxylate (compound **38a**) was based upon a key publication (Nara et al., 2017) as given in Scheme 4.1. Here, a suspension of compound **38a** (1.0 eq) and ethylcyanoformate (1.1 eq) in 1M HCl in acetic acid solution was stirred at 90 °C for 10 hours. The reaction mixture was cooled

down to room temperature, concentrated under reduced pressure, and triturated with water. The precipitate was collected by filtration and washed with water and diethyl ether. It was reported to achieve the desired ester **36a** in 80% yield.

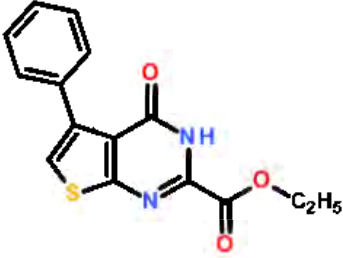
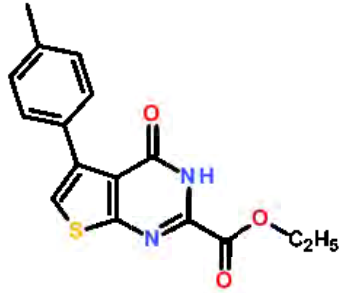
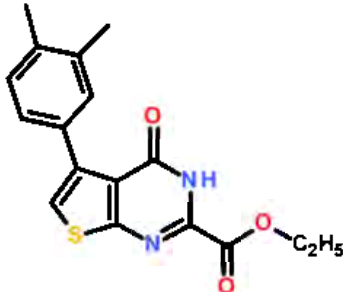
To prepare 1M HCl in acetic acid as the literature mentioned, an appropriate volume of concentrated HCl (37%) was added in to acetic acid 100%. In the first attempt, the reaction conditions including the reaction temperature and the concentration of HCl in acetic acid were followed but instead of stirring for 10 hours, the reaction mixture was stirred overnight (20 hours). The ^1H NMR spectra of the achieving product indicated a mixture of approximately 95% of an unknown compound named compound **39a** and around 5% of the expected ester (compound **36a**). That indicated ester **36a** was formed but it was transferred to compound **39a** due to the overheating of the reaction mixture. However, several repeats of the reaction with variation of the heating time gave similar results in which mostly unknown compound **39a** and very small quantity of compound **36a**.

The ^1H NMR spectra of compound **39a** indicated the absence of the ethyl ester. This may occurred by acid-catalysed hydrolysis of the ester **36a** under the reaction condition. Therefore, further reactions were under taken where the reaction temperature and the concentration of HCl were reduced for compound **36a** to be obtained in acceptable yields and purities (Table 4.1). The reduction of both the reaction temperature and the concentration of HCl increased the yields of compound **36a**. The highest yield (64%) was achieved when the reaction temperature was 75 °C, the concentration of HCl was 0.2 M and time for the reaction was around 3 hours.

In the course of the optimisations, at around 55 - 56 °C, the suspension of the starting materials was observed to become homogenous. A further optimisation attempt was built from this observation. Particularly, the reaction mixture in 0.2 M HCl in acetic acid was heated at 55–56 °C and was stopped after around 3 hour stirring (monitoring the reaction by TLC). Interesting, a significant increase in the yield of the desired ester (78%) was achieved. Therefore, the reaction temperature (55–56 °C) and the concentration of HCl (0.2 M) became the optimised conditions for the reaction to synthesise compound **36a**. High yields were also achieved when applying these conditions for the reactions to synthesise other analogues of compound **36a** including ethyl 4-oxo-5-(p-tolyl)-3H-thieno[2,3-d]pyrimidine-2-carboxylate (compound **36b**) and

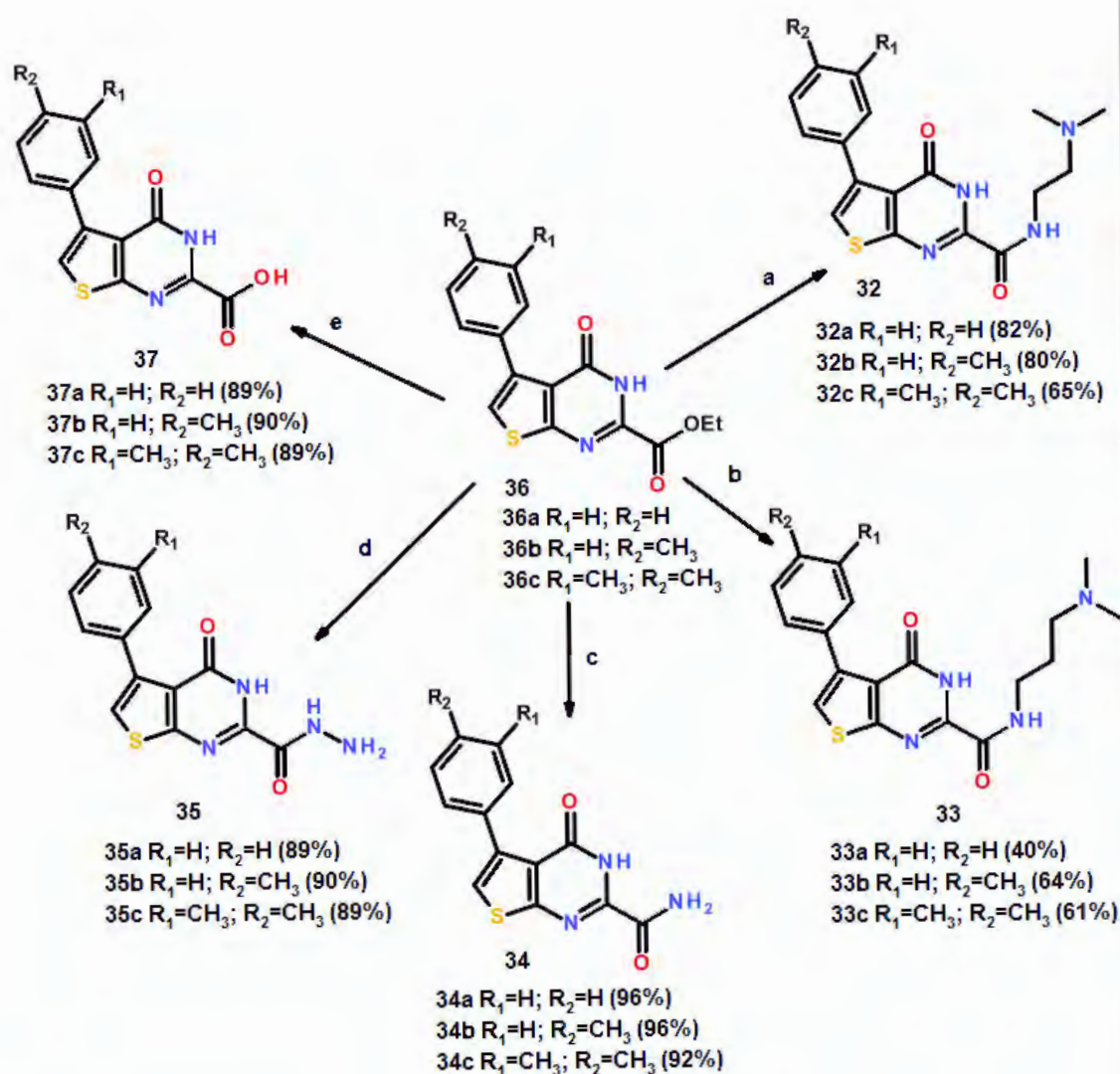
ethyl 5-(3,4-dimethylphenyl)-4-oxo-3H-thieno[2,3-d]pyrimidine-2-carboxylate (compound **36c**). Under the optimised conditions of the reaction temperature and the concentration of HCl, the amino group of compound **38a** reacted with acetic acid (solvent) to form an amide as a side-product of the reaction. Therefore, the acetonitrile was used instead and that helped to increase the yield of the ester **36a** to 83%.

Table 4.1. Optimisation of conditions of the reactions to synthesise the key intermediate esters ethyl 4-oxo-5-phenyl-3H-thieno[2,3-d]pyrimidine-2-carboxylates (compounds **36a,b,c**) from the commercially available ethyl 2-amino-4-phenyl-thiophene-3-carboxylate derivatives (compounds **38a,b,c**).

Name	Structure	Solvent	Temperature (°C)	[HCl] (M)	Time (hrs)	Yield (%)
36a		Acetic acid	90	1.0	20	<5
			90	1.0	8	<5
			90	0.1	15	37
			85	0.1	22	43
			80	0.1	7.5	56
			70	1.0	8	45
			75	0.2	15	64
			56	0.2	3	78
		Acetonitrile	56	0.2	2.5	83
36b		Acetic acid	77	0.4	3.5	50
			59	0.2	5.5	71
			55	0.2	1.5	83
36c		Acetic acid	56	0.2	1.75	78

4.2 Synthesis of the target compounds from the esters **36a,b,c**

From the key intermediate esters **36a,b,c**, a number of synthetic routes were followed to synthesise the target compounds (Scheme 4.2). Alkaline hydrolysis of esters **36a,b,c** with excess NaOH in MeOH / H₂O (40 / 1) at 56 °C for around 2 hours afforded the desired carboxylic acids **37a,b,c** in high yields (around 89%). Reaction of esters **36a,b,c** and an excess of concentrated ammonia in THF / MeOH (3 / 10) at room temperature gave excellent yields (up to 96%) of amides **34a,b,c**. Treatment of a solution of the key esters in THF with an excess of hydrazine monohydrate initially at 0 °C followed by stirring at room temperature provided the corresponding carbohydrazides **35a,b,c** in 65 - 70% yields. Heating the key esters with 1.1 equivalent of N,N-dimethylethylenediamine or N,N-dimethylpropylamine at moderate temperature (56 °C) for around 1 - 2 hours afforded the desired corresponding amines in up to 70% yield after recrystallisation from ethylacetate.



Scheme 4.2. Synthesis of the potential TG2 allosteric inhibitor target compounds from the key intermediate esters **36a,b,c**.

Reagents and conditions (a) NaOH, H₂O / MeOH, 56 °C, 2 hours; (b) Concentrated ammonia / MeOH, THF, room temperature (20 °C) to 40 °C, 2 hours; (c) Hydrazine monohydrate / THF, 0 °C to room temperature, 2.5 hours; (d) N,N-dimethylethylenediamine, 56 °C, 1.5 hours; (e) 3-Dimethylaminopropylamine, 60 °C, 1.5 hours.

4.3 Identification of compound 39a and its derivatives

Here are the NMR spectra of the unknown compound:

¹H NMR (DMSO-D₆): δ = 7.39 (m, 3H); 7.54 (overlap m, 3H); 8.16 (s, 1H); 12.48 (bs, 1H) ppm.

^{13}C NMR (DMSO- D_6): δ = 121.4 (CH), 121.5 (C), 127.8 (CH), 128.0 (CH), 129.7 (CH), 135.6 (C), 138.9 (C), 146.2 (CH), 157.8 (C), 166.0 (C) ppm.

Additionally, molecular weight measured by analysis of mass spectrum indicated the formula structure of compound **39a** as $\text{C}_{12}\text{H}_9\text{ON}_2\text{S}$ (accuracy -0.3 ppm).

Interestingly, the carboxylic acid **37a** was observed to transform cleanly to compound **39a** on melting or after heating in 1M HCl in acetic acid solution at 90 °C for 1 hour. These observations supported the idea that under the reaction conditions in the initial attempt to prepare **36a** (1M HCl in acetic acid at 90 °C), the ester **36a** was hydrolysed to the carboxylic acid **37a**, which was decarboxylated to produce compound **39a**. It was also proposed that the starting material (ester **38a**) was hydrolysed to the corresponding carboxylic acid under the first attempted reaction conditions before it reacted with ethylcyanoformate to give compound **36a**, whose carboxylic group was then leaving to form compound **39a**.

Based on the analytical data and the forming of compound **39a** from the carboxylic acid **37a**, the structure of compound **39a** was identified as 5-phenyl-3H-thieno[2,3-d]pyrimidine-4-one (Figure 4.2a). Two analogues of compound **39a** were also produced from the corresponding carboxylic acids in the same conditions. Particularly, the carboxylic acid **37b** was also transformed cleanly on melting to 5-(p-tolyl)-3H-thieno[2,3-d]pyrimidine-4-one (compound **39b** Figure 4.2b) whose ^1H NMR spectrum and the formula structure indicated by the mass spectrum were reported in the literature (Hill et al., 2013). Compound **37c** was also observed to transform on the melting to 5-(3,4-dimethylphenyl)-3H-thieno[2,3-d]pyrimidin-4-one (compound **39c** Figure 4.2c).

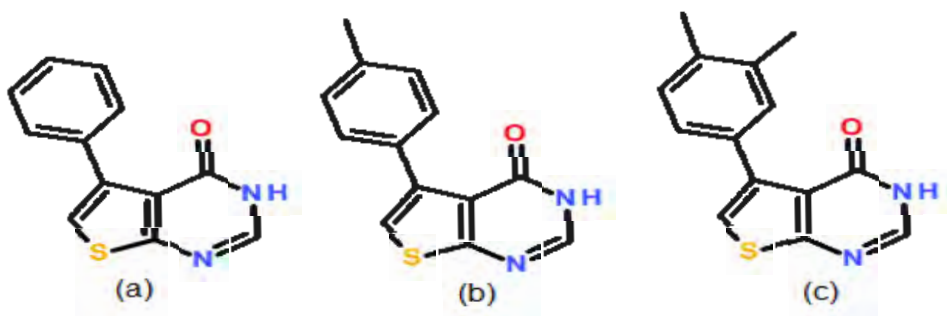
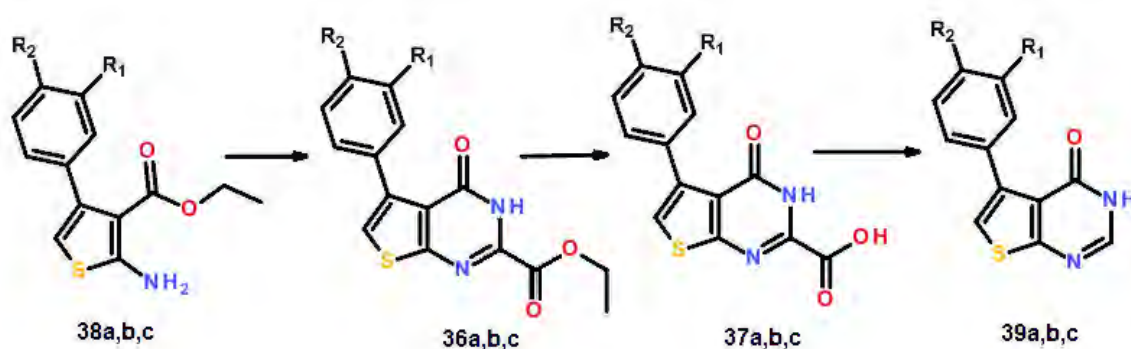


Figure 4.2. Structure of 5-phenyl-3H-thieno[2,3-d]pyrimidine-4-one and its derivatives (compounds **39a,b,c**)

4.4 Optimisation of conditions to synthesise 5-phenyl-3H-thieno[2,3-d]pyrimidine-4-ones (compounds **39a,b,c**)

It was reported that excellent yields (80%) of substituted thieno[2,3-d]pyrimidin-4(3H)-one derivatives were achieved by heating a mixture of formamide and 2-aminothiophene (Golub et al., 2011). However, in the synthesis of 5-phenyl-3H-thieno[2,3-d]pyrimidine-4-one (compound **39a**), heating of a mixture of the thiophene and formamide in a microwave oven at 210 °C (Actis et al., 2016) was indicated to provide the impure product after purifying using flash column chromatography. In addition, it was pointed out that a very low yield (27%) of 5-(p-tolyl)-3H-thieno[2,3-d]pyrimidine-4-one (compound **39b**) was produced by heating in a microwave at 120 °C for 4 hours a mixture of 2-amino-4-(4-methylphenyl)thiophene-3-carboxylate and formamide acetate in ethanol (Hill et al., 2013). Therefore, the forming of 5-phenyl-3H-thieno[2,3-d]pyrimidine-4-ones (compound **39a,b,c**) during the course of this research suggested novel approaches to provide these derivatives in higher yields and acceptable purity.

During the course of optimisations, the highest yield (84%) of the desired compound **39a** was achieved when heating a mixture of compound **38a** (ethyl 2-amino-4-phenylthiophene-3-carboxylate) and 1.1 equivalent of ethylcyanoformate in 0.2M hydrochloric acid in acetonitrile at 56 °C overnight, followed by raising the concentration of HCl to 3M and heating at 80 °C for 24 hours. Based on the clean transformation of the carboxylic acids **37a,b,c** on melting to the corresponding substituted thieno[2,3-d]pyrimidin-4(3H)-ones (**39a,b,c**), the three step scheme (Scheme 4.3) provided the desired compound **39a,b,c** in up to 76% yield in total.



Scheme 4.3. A 3-step scheme to synthesise substituted thieno[2,3-d]pyrimidin-4(3H)-ones (compound **39a,b,c**).

Reagents and conditions (a) Ethylcyanoformate / 0.2M HCl in acetonitrile, 56 °C, 1.5-3 hours; (b) NaOH, H₂O / MeOH, 56 °C, 2 hours; (c) Heating the carboxylic acid **37a,b,c** to completely melt.

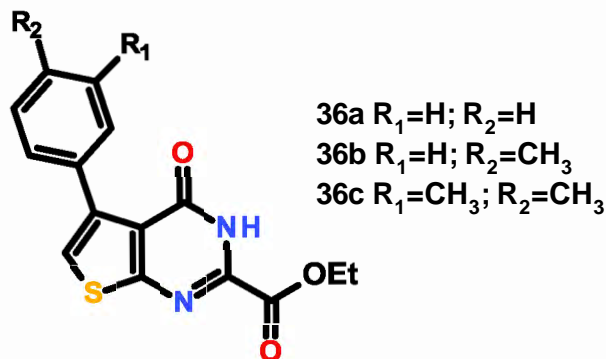
4.5 Conclusion

Attempts were made to synthesise a set of the potential allosteric TG2 inhibitor target compounds from the ethyl 4-oxo-5-phenyl-3H-thieno[2,3-d]pyrimidine-2-carboxylate and its derivatives (compound **36a,b,c**). However, the key literature method provided the corresponding decarboxylated compound **39a** instead of giving the desired compound **36a**. This study succeeded in the optimisation reaction conditions including the reaction temperature, the concentration of hydrochloric acid and the type of the solvent to give the desired compound **36a** and its derivatives (compound **36b,c**) in high yields. From these key esters, a set of target compounds (carboxylic acids **37a,b,c**, amides **34a,b,c** and carbonylhydrazides **35a,b,c**) were synthesised in excellent yields (up to 96%). Six water-soluble amines (**32a,b,c** and **33a,b,c**) were also synthesised in moderate yields from the esters **36a,b,c**.

The unexpected compound **39a** achieved in the first attempt of the synthesis of compound **36a** was identified as 5-phenyl-3H-thieno[2,3-d]pyrimidine-4-one. This compound and its derivatives (compound **39b,c**) were also formed when heating the corresponding carboxylic acids **37a,b,c** at the elevated temperatures with or without acid. These observations provided two novel methods to synthesise compounds **39a,b,c** in excellent yields (up to 84%).

4.6 Chemistry experimental procedures

Synthesis of esters 36a,b,c



Ethyl 4-oxo-5-phenyl-3H-thieno[2,3-d]pyrimidine-2-carboxylate (36a)

Method 1

A suspension of ethyl 2-amino-4-phenyl-thiophene-3-carboxylate (0.8078 g, 3.27 mmol, 1.0 eq) and ethyl cyanofomate (0.7 mL, 7.09 mmol, 2.2 eq) in 0.2 M HCl in acetic acid (a mixture of 0.17 mL concentrated HCl (37%) in 10 mL acetic acid 100%) was stirred at 55 - 56 °C for around 1.5 - 3 hours (the reaction was monitored by TLC). The reaction mixture was diluted with acetic acid 100% (20 mL), stirred at 0 °C in an ice bath and water (40 mL) was added. The resulting precipitate was collected by filtration, washed with water (3×20 mL) and diethyl ether (3×10 mL) and dried under vacuum at room temperature to provide the desired **36a** as a cream solid (0.7902 g, 2.62 mmol, 78%).

Method 2

To solution of ethyl 2-amino-4-phenyl-thiophene-3-carboxylate (1.0301 g, 4.17 mmol, 1.0 eq) in acetonitrile (30 mL), concentrated HCl (37%) (0.52 mL) was added dropwise over 5 min. The resulting suspension was stirred at 56 °C for 2.5 hours, then cooled down to room temperature (20 °C). Water (60 mL) was added and the mixture was stirred for 30 min. The resulting precipitate was collected by filtration, thoroughly washed with water (3 × 30 mL) and diethyl ether (2 × 20 mL) and dry under reduced

pressure at 40 °C overnight. The desired compound **36a** was achieved as a cream solid (1.039 g, 3.46 mmol, 83%).

M.p: 206.5 - 213.1 °C

IR (ATR) ν = 3100 (m, NH stretch), 1753 (s, CO ester), 1673 (s, CO amide), 1569 (m, NH bending), 1497, 1474, 1445, 1431 (w, C=C aromatic) cm^{-1} .

^1H NMR (DMSO- D_6): δ = 1.37 (t, J = 7.1 Hz, 3H, CH_2CH_3); 4.40 (q, J = 7.1 Hz, 2H, CH_2CH_3); 7.41 (overlapping m, 3H, Ph-H); 7.56 (overlapping m, 2H, Ph-H); 7.76 (s, 1H, CH of thiophene ring); 12.83 (bs, 1H, NH) ppm.

^{13}C NMR (DMSO- D_6): δ = 14.1 (CH_3); 63.0 (CH_2); 122.7 (C); 124.6 (Ph-para-CH); 127.7 (2 Phe-meta-CH); 127.8 (2 Ph-ortho-CH); 129.6 (CH of thiophene ring); 135.1 (C), 139.0 (C), 144.8 (C), 157.5 (C), 159.8 (C), 164.1 (C) ppm.

HRMS m/z calcd for $\text{C}_{15}\text{H}_{12}\text{O}_3\text{N}_2\text{S}$ ($\text{M}+\text{H}$) $^+$, 301.0641 g/mol; found, 301.0641 g/mol.

Ethyl 4-oxo-5-(p-tolyl)-3H-thieno[2,3-d]pyrimidine-2-carboxylate (36b)

Compound **36b** was prepared from ethyl 2-amino-4-*p*-tolylthiophene-3-carboxylate using method 1 and on the same scale.

Yield: 0.8470 g, 2.70 mmol, 83%; white solid.

M.p: 197.2 - 200.4 °C.

IR (ATR) ν = 3100 (m, NH stretch), 1753 (s, CO ester), 1673 (s, CO amide), 1569 (m, NH bending), 1497, 1474, 1445, 1431 (m, C=C aromatic) cm^{-1} .

^1H NMR (DMSO- D_6): δ = 1.37 (t, J = 7.1 Hz, 3H, CH_2CH_3); 2.37 (s, 3H, Ph- CH_3); 4.40 (q, J = 7.1 Hz, 2H, CH_2CH_3); 7.22 (d, 2H, Ph-H); 7.44 (d, 2H, Ph-H); 7.70 (s, 1H, CH of thiophene ring); 12.80 (bs, 1H, NH) ppm.

^{13}C NMR (DMSO- D_6): δ = 14.1 (CH_3 , CH_2CH_3); 21.3 (CH_3 , Ph- CH_3); 63.0 (CH_2 , CH_2CH_3); 123.0 (C); 124.1 (2 Ph-meta CH); 128.4 (2 Ph-ortho CH); 129.5 (CH of the

thiophene ring); 132.5 (C), 137.2 (C), 139.3 (C), 143.9 (C), 157.7 (C), 160.0 (C), 164.3 (C) ppm.

HRMS m/z calcd for $C_{16}H_{14}O_3N_2S$ ($M+H$)⁺, 315.0798; found, 315.0797.

Ethyl 5-(3,4-dimethylphenyl)-4-oxo-3H-thieno[2,3-d]pyrimidine-2-carboxylate (36c)

Compound **36c** was prepared from ethyl 2-amino-4-(3,4-dimethylphenyl)-3-thiophenecarboxylate using method 1 and on the same scale.

M.p: 168.4 - 172.0°C.

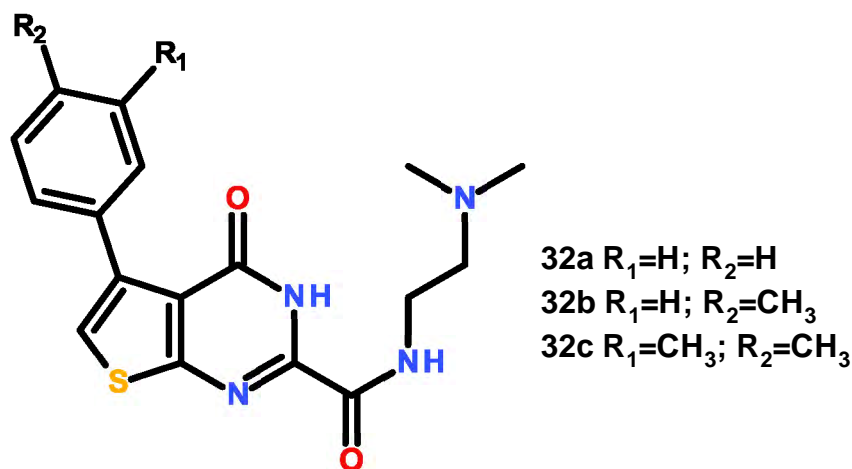
IR (ATR) ν = 3100 (m, NH stretch), 1753 (s, CO ester), 1673 (s, CO amide), 1569 (m, NH bending), 1497, 1474, 1445, 1431 (m, C=C aromatic) cm^{-1} .

¹H NMR (DMSO-D₆): δ = 1.37 (t, J = 7.1 Hz, 3H, CH₂CH₃); 2.27 (s, 6H, Ph-(CH₃)₂); 4.40 (q, J = 7.1 Hz, 2H, CH₂CH₃); 7.17 (d, 1H, Ph-H); 7.26 (dd, 1H, Ph-H); 7.32 (d, 1H, Ph-H); 7.68 (s, 1H, CH of thiophene ring), 12.80 (bs, 1H, NH) ppm.

¹³C NMR (DMSO-D₆): δ = 14.1 (CH₃, CH₂CH₃); 19.3 (CH₃, Ph-(CH₃)₂); 19.6 (CH₃, Ph-(CH₃)₂); 63.0 (CH₂); 122.7 (C); 123.9, 127.0, 128.9 (3 Ph-CH); 130.6 (CH, CH of thiophene ring); 132.6 (C), 135.4 (C), 135.7 (C), 139.2 (C), 143.7 (C), 157.4 (C), 159.7 (C), 164.0 (C) ppm.

HRMS m/z calcd for $C_{17}H_{16}O_3N_2S$ ($M+H$)⁺, 329.0954; found, 329.0956.

Synthesis of amines 32a,b,c



N-[2-(Dimethylamino)ethyl]-4-oxo-5-phenyl-3H-thieno[2,3-d]pyrimidine-2-carboxamide (32a)

A solution of ester **36a** (0.2550g, 0.85 mmol) in N,N-dimethylethylene diamine (3 mL) was stirred at 56 °C for 2 hours. The reaction mixture was cooled down to 0 °C, petroleum ether 60/80 (60 mL) was added, followed by stirring for 30 min. The precipitate was collected by filtration and thoroughly washed with petroleum ether 60/80 (4×20 mL). The obtained crude product was recrystallised from ethylacetate to give the desired amine as a white solid (0.241 g, 0.70 mmol, 82%).

M.p: 207.1 – 208.9 °C.

IR (ATR) ν = 3300 (w, b, NH), 1700 (s, CO), 1570 (s), 1513, 1490, 1455 (w, C=C aromatic) cm⁻¹.

¹H NMR (DMSO-D₆): δ = 2.22 (s, 6H, N(CH₃)₂); 2.48 (t, J = 6.6 Hz, 2H, CH₂CH₂N(CH₃)₂); 3.40 (m, overlap with a peak of water molecule, 2H, NHCH₂CH₂); 7.40 (m, 3H, Ph-H); 7.56 (m, 2H, Ph-H); 7.65 (s, 1H, CH of thiophene); 8.94 (t, 1H, CONHCH₂); 12.80 (bs, 1H, NHCO) ppm.

^{13}C NMR (DMSO- D_6): δ = 37.3 ($\text{CH}_2\text{CH}_2\text{N}(\text{CH}_3)_2$), 45.3 (CH_3); 57.8 ($\text{CH}_2\text{CH}_2\text{N}(\text{CH}_3)_2$); 122.1 (C); 123.2 (CH); 127.6 (CH); 127.7 (CH); 129.6 (CH); 135.2 (C); 138.9 (C); 146.6 (C); 157.7 (C); 159.0 (C); 164.0 (C) ppm.

HRMS m/z calcd for $(\text{M}+\text{H})^+$, 343.1223; found, 343.1225.

N-[2-(Dimethylamino)ethyl]-4-oxo-5-(p-tolyl)-3H-thieno[2,3-d]pyrimidine-2-carboxamide (32b)

A stirred suspension of ester **36b** (0.3598 g, 1.14 mmol) in N,N-dimethylethylene diamine (5 mL) was heated at 56 °C for 1.5 hours. After cooling down to room temperature (20 °C), the reaction mixture was concentrated under reduced pressure / 40 °C. The residue was triturated with ethyl acetate (20 mL) and the precipitate was collected by filtration, washed with ethyl acetate (2×10 mL) and dry under reduced pressure to provide the desired **32b** as a white solid (0.3283 g, 0.92 mmol, 80%).

M.p: 151.2 - 153.2 °C.

IR (ATR) ν = 3389 (w, NH), 1670 (s, CO); 1600, 1564, 1531, 1504, 1455 (w, C=C aromatic) cm^{-1} .

^1H NMR (DMSO- D_6): δ = 2.22 (s, 6H, $\text{N}(\text{CH}_3)_2$); 2.37 (s, 3H, Ph- CH_3); 2.47 (t, J = 6.6 Hz, 2H, $\text{CH}_2\text{CH}_2\text{N}(\text{CH}_3)_2$); 3.40 (m, overlap with a peak of water molecule, NHCH_2CH_2); 7.22 (d, J = 7.6 Hz, 2H, Ph-H); 7.45 (d, J = 7.6 Hz, 2H, Ph-H); 7.61 (s, 1H, CH of thiophene); 8.59 (t, J = 5.9 Hz, NHCH_2) ppm.

^{13}C NMR (DMSO- D_6): δ = 21.0 (Ph- CH_3); 37.3 ($\text{CH}_2\text{N}(\text{CH}_3)_2$); 45.3 ($\text{N}(\text{CH}_3)_2$); 57.8 (CH_2NHCO); 122.1 (C); 122.7 (2 Ph-metaCH); 128.3 (2 Ph-ortho CH); 129.5 (CH of thiophene); 132.4 (C); 136.9 (C); 139.0 (C); 146.5 (C); 157.8 (C); 159.1 (C); 164.0 (C) ppm.

HRMS m/z calcd for $\text{C}_{18}\text{H}_{20}\text{O}_2\text{N}_4\text{S}$ $(\text{M}+\text{H})^+$, 357.1380; found, 357.1381.

N-[2-(Dimethylamino)ethyl]-5-(3,4-dimethylphenyl)-4-oxo-3H-thieno[2,3-d]pyrimidine-2-carboxamide (32c)

Compound **32c** was prepared from ester **36c** by the method using to synthesise compound **32a** on the similar scale.

Yield 0.1312 g, 0.42 mmol, 65%; white solid.

M.p: 203.2 – 205.1 °C.

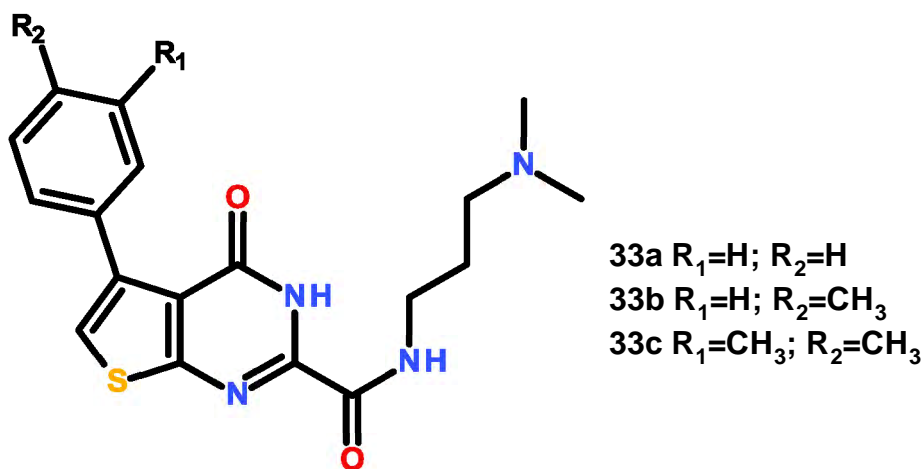
IR (ATR) ν = 3389 (w, NH), 1670 (s, CO), 1564, 1504, 1455, 1432 (w, C=C aromatic) cm^{-1} .

^1H NMR (DMSO- D_6): δ = 2.21 (s, 6H, $\text{N}(\text{CH}_3)_2$); 2.27 (s, 6H, $\text{Ph}(\text{CH}_3)_2$); 2.46 (t, J = 6.6 Hz, 2H, $\text{CH}_2\text{CH}_2\text{N}(\text{CH}_3)_2$); 3.40 (m overlap with a peak of water molecule, 2H, NHCH_2CH_2); 7.16 (d, J = 7.8 Hz, 1H, Ph-H); 7.26 (dd, J = 1.9, 7.8 Hz, 1H, Ph-H); 7.32 (d, J = 1.9 Hz, 1H, Ph-H); 7.59 (s, 1H, -CH of thiophene); 8.59 (t, J = 5.9 Hz, NHCH_2) ppm.

^{13}C NMR (DMSO- D_6): δ = 19.3 (Ph- CH_3); 19.6 (Ph- CH_3); 37.4 ($\text{CH}_2\text{N}(\text{CH}_3)_2$); 45.3 ($\text{N}(\text{CH}_3)_2$); 57.8 (CH_2NHCO); 122.1 (C); 122.5, 126.9, 128.8 (3CH of phenyl ring); 130.6 (CH of the thiophene ring); 132.7 (C); 135.3 (C); 135.6 (C); 139.1 (C); 146.4 (C); 157.5 (C); 159.0 (C); 164.0 (C) ppm.

HRMS m/z calcd for $\text{C}_{19}\text{H}_{23}\text{O}_2\text{N}_4\text{S}$ ($\text{M} + \text{H}$) $^+$, 371.1536; found, 371.1533.

Synthesis of amines 33a,b,c



N-[3-(Dimethylamino)propyl]-4-oxo-5-phenyl-3H-thieno[2,3-d]pyrimidine-2-carboxamide (33a)

A solution of ester **36a** (0.2134g, 0.71 mmol) in N,N-dimethylethylene diamine (2 mL) was stirred at 56 °C for 2 hours. The reaction mixture was cooled down to 0 °C, petroleum ether 60/80 (50 mL) was added and followed by stirring for 30 min. The precipitate was collected by filtration and washed with petroleum ether 60/80 (3×20 mL) to give a solid. The obtained crude product was recrystallised from ethylacetate to give the desired amine as a white solid (0.100 g, 0.28 mmol, 40%).

M.p: 132.8 – 138.6 °C.

IR (ATR) ν = 3246 (w, NH), 3178 (w, NH), 1700 (s, CO), 1690 (s, CO), 1568, 1538, 1500, 1495 (m, w, C=C aromatic) cm^{-1} .

^1H NMR (DMSO- D_6): δ = 1.70 (tt, 2H, $\text{CH}_2\text{CH}_2\text{CH}_2$); 2.18 (s, 6H, $\text{N}(\text{CH}_3)_2$); 2.31 (t, J = 7.0 Hz, 2H, $\text{CH}_2\text{CH}_2\text{CH}_2\text{N}(\text{CH}_3)_2$); 3.31 (m overlap with a peak of water molecule, 2H, NHCH_2CH_2); 7.40 (m, 3H, Ph-H); 7.56 (m, 2H, Ph-H); 7.65 (s, 1H, CH of thiophene); 9.28 (t, J = 5.9 Hz, NHCH_2) ppm.

^{13}C NMR (DMSO- D_6): δ = 26.8 ($\text{CH}_2\text{CH}_2\text{CH}_2$); 38.1 ($\text{CH}_2\text{CH}_2\text{CH}_2\text{N}(\text{CH}_3)_2$); 45.4 (CH_3); 57.0 ($\text{CH}_2\text{CH}_2\text{CH}_2\text{N}(\text{CH}_3)_2$); 122.0 (C); 123.1 (CH); 127.8 (CH); 129.6 (CH); 135.3 (C); 138.9 (C); 146.8 (C); 157.7 (C); 159.1 (C) ppm.

HRMS m/z calcd for $\text{C}_{18}\text{H}_{21}\text{O}_2\text{N}_4\text{S}$ ($\text{M}+\text{H}$) $^+$, 357.1374; found, 357.1380.

Synthesis of compound N-[3-(dimethylamino)propyl]-4-oxo-5-(p-tolyl)-3H-thieno[2,3-d]pyrimidine-2-carboxamide (33b)

A stirred suspension of ester **36b** (0.2715 g, 0.86 mmol) in 3-dimethylaminopropylamine (10 mL) was stirred at 60 °C for 1.5 hours. After cooling down the reaction mixture to 0 °C in an ice bath, ethyl acetate (50mL) and petroleum ether 40/60 (4 mL) were added and followed by stirring for 1 hour. The precipitate was collected by filtration, washed with ethyl acetate (3×10 mL) and dry under vacuum

overnight at room temperature to give compound **33b** as a white solid (0.2102 g, 0.55 mmol, 64%).

M.p: 150.6-153.4 °C.

IR (ATR) ν = 3146 (w, NH), 3088 (w, NH), 1702 (s, CO), 1681 (s, CO), 1568, 1538, 1501, 1461 (m, w, C=C aromatic) cm^{-1} .

^1H NMR (DMSO- D_6): δ = 1.68 (tt, 2H, $\text{CH}_2\text{CH}_2\text{CH}_2$); 2.17 (s, 6H, $\text{N}(\text{CH}_3)_2$); 2.29 (t, J = 7.0 Hz, 2H, $\text{CH}_2\text{CH}_2\text{CH}_2\text{N}(\text{CH}_3)_2$); 2.36 (s, 3H, Ph- CH_3); 3.31 (m overlap with a peak of water molecule, 2H, $\text{NHCH}_2\text{CH}_2\text{CH}_2$); 7.21 (d, 2H, J = 7.6 Hz, Ph-H); 7.45 (d, 2H, J = 7.6 Hz, Ph-H); 7.58 (s, 1H, CH of thiophene); 9.24 (t, J = 5.9 Hz, NHCH_2) ppm.

^{13}C NMR (CDCl_3): δ = 21.0 (Ph- CH_3), 26.9 ($\text{CH}_2\text{CH}_2\text{CH}_2$), 38.1 ($\text{CH}_2\text{CH}_2\text{CH}_2\text{N}(\text{CH}_3)_2$), 45.3 ($\text{N}(\text{CH}_3)_2$), 57.0 ($\text{NHCH}_2\text{CH}_2\text{CH}_2$), 121.9 (C), 122.2 (2 Ph meta-CH); 128.3 (2 Ph ortho-CH); 129.6 (CH of thiophene); 132.3 (C); 136.7 (C); 139.0 (C); 147.1 (C); 158.2 (C); 159.4 (C); 164.2 (C) ppm.

HRMS m/z calcd for $\text{C}_{19}\text{H}_{22}\text{O}_2\text{N}_4\text{S}$ ($\text{M}+\text{H}$) $^+$, 371.1532; found, 371.1536.

N-[3-(Dimethylamino)propyl]-5-(3,4-dimethylphenyl)-4-oxo-3H-thieno[2,3-d]pyrimidine-2-carboxamide (33c)

A solution of ester **36c** (0.3111g, 0.95 mmol, 1.0 eq) in 3-dimethylaminopropylamine (2 mL) was stirred at 56 °C for 2 hours. The reaction mixture was cooled down to 0 °C, petroleum ether 60/80 (50 mL) was added and followed by stirring for 30 min. The precipitate was collected by filtration and thoroughly washed with petroleum ether 60/80 (3×20 mL). The obtained crude product was dissolved in ethyl acetate (100 mL), washed with water (10×10 mL), dried over MgSO_4 and evaporated under reduced pressure / 40 °C to give the desired amine as a white solid (0.2239 g, 0.58 mmol, 61%).

M.p: 126.4 – 127.4 °C.

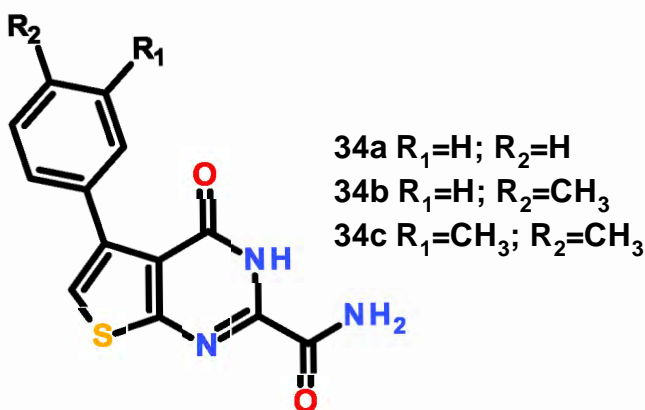
IR (ATR) ν = 3146 (w, NH), 3088 (w, NH), 1702 (s, CO), 1681 (s, CO), 1568, 1538, 1500, 1495 (m, w, C=C aromatic) cm^{-1} .

^1H NMR (DMSO- D_6): δ = 1.69 (tt, 2H, $\text{CH}_2\text{CH}_2\text{CH}_2$); 2.18 (s, 6H, $\text{N}(\text{CH}_3)_2$); 2.27 (s, 6H, $\text{Ph}(\text{CH}_3)_2$); 2.31 (t, J = 7.0 Hz, 2H, $\text{CH}_2\text{CH}_2\text{CH}_2\text{N}(\text{CH}_3)_2$); 3.31 (m overlap with a peak of water molecule, 2H, $\text{NHCH}_2\text{CH}_2\text{CH}_2$); 7.16 (d, J = 7.8 Hz, 1H, Ph-H); 7.26 (dd, J = 1.9, 7.8 Hz, 1H, Ph-H); 7.32 (d, J = 1.9 Hz, Ph-H); 7.58 (s, 1H, CH of thiophene); 9.28 (t, J = 5.9 Hz, NHCH_2) ppm.

^{13}C NMR (DMSO- D_6): δ = 19.3 (Ph- CH_3); 19.6 (Ph- CH_3); 26.7 ($\text{CH}_2\text{CH}_2\text{CH}_2$); 38.1 ($\text{CH}_2\text{CH}_2\text{CH}_2\text{N}(\text{CH}_3)_2$); 45.2 ($\text{N}(\text{CH}_3)_2$); 56.0 ($\text{CH}_2\text{CH}_2\text{CH}_2\text{N}(\text{CH}_3)_2$); 122.0 (C); 122.3 (CH); 127.0 (CH); 128.8 (CH); 130.6 (CH); 132.8 (C); 135.3 (C); 135.5 (C); 139.1 (C); 146.8 (C); 157.9 (C); 159.2 (C); 164.1 (C) ppm.

HRMS m/z calcd for $\text{C}_{20}\text{H}_{25}\text{O}_2\text{N}_4\text{S}$ ($\text{M} + \text{H}$) $^+$, 385.1693; found, 385.1692.

Synthesis of amides 34a,b,c



A stirred solution of ester **36** (0.52 mmol, 1.0 eq) in MeOH / THF (20 mL / 6 mL) was treated with concentrated ammonia solution (4 mL) at room temperature (20 °C). The reaction mixture was stirred at 40 °C for 2 hours then water (100 mL) was added. The resulting precipitate was filtered, washed with water (3 \times 30 mL) and dried under vacuum at 40 °C to provide amide **34** as a powder.

4-Oxo-5-phenyl-3H-thieno[2,3-d]pyrimidine-2-carboxamide (34a)

Yield 0.1355 g, 0.50 mmol, 96%; white solid.

M.p: 223.8 - 230.3°C.

IR (solid, ATR) ν = 3486, 3470 (w, NH amine), 3452 (w, NH amide), 1704 (s, CO); 1682 (s, CO); 1588, 1566, 1504, 1478, 1451 (w, C=C aromatic) cm^{-1} .

^1H NMR (DMSO- D_6): δ = 7.40 (overlapping m, 3H, Ph-H); 7.55 (overlapping m, 2H, Ph-H); 7.67 (s, 1H, CH of thiophene); 8.12 (bs, 1H, CONH_2); 8.51 (bs, 1H, CONH_2); 12.33 (bs, 1H, CONH) ppm.

^{13}C NMR (DMSO- D_6): δ = 122.4 (C); 123.7 (Ph para-CH); 127.9 (2 Ph meta-CH); 128.0 (2 Ph ortho-CH); 129.8 (CH of the thiophene ring); 135.4 (C); 139.2 (C); 146.7 (C); 157.5 (C); 161.2 (C); 164.3 (C) ppm.

HRMS m/z calcd for $\text{C}_{13}\text{H}_9\text{O}_2\text{N}_3\text{S}$ ($\text{M}+\text{H}$) $^+$, 272.0488; found, 272.0489.

4-Oxo-5-(p-tolyl)-3H-thieno[2,3-d]pyrimidine-2-carboxamide (34b)

Yield 0.1425 g, 0.50 mmol, 96%; white solid.

M.p: 250.2 - 254.3°C.

IR (ATR) ν = 3486, 3470 (w, NH amine); 3452 (w, NH amide); 1704 (s, CO); 1682 (s, CO); 1588, 1566, 1504, 1478, 1451 (w, C=C aromatic) cm^{-1} .

^1H NMR (CDCl_3): δ = 2.42 (s, 3H, CH_3); 7.25 (d, J = 8.0 Hz, 2H, Ph-H); 7.29 (s, 1H, CH of the thiophene ring); 7.48 (d, J = 8.0 Hz, 2H, Ph-H); 7.60 (bs, 1H, CONH_2); 8.03 (bs, 1H, CONH_2); 11.92 (bs, 1H, CONH) ppm.

^{13}C NMR (CDCl_3): δ = 21.7 (CH_3); 123.0 (C); 123.2 (2 Ph meta-CH); 129.0 (2 Ph ortho-CH); 129.7 (CH of the thiophene); 132.2 (C); 138.2 (C); 140.4 (C); 144.5 (C); 158.7 (C); 162.3 (C); 164.6 (C) ppm.

HRMS m/z calcd for $\text{C}_{14}\text{H}_{11}\text{O}_2\text{N}_3\text{S}$ ($\text{M}+\text{H}$) $^+$, 286.0645; found, 286.0645.

5-(3,4-Dimethylphenyl)-4-oxo-3H-thieno[2,3-d]pyrimidine-2-carboxamide (34c)

Yield 0.1438 g, 0.48 mmol, 92 %; white solid.

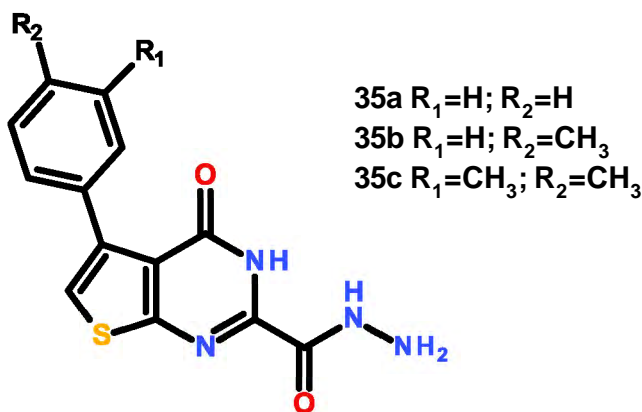
M.p: 225.2 - 226.8 °C.

IR (ATR) ν = 3453 (w, NH); 3328 (w, NH); 1700 (s, b, CO), 1564, 1505, 1482, 1436 (w, C=C aromatic) cm^{-1} .

^1H NMR (DMSO- D_6): δ = 2.27 (s, 6H, 2CH₃); 7.16 (d, J = 7.8 Hz, 1H, Ph-H); 7.26 (dd, J = 1.9, 7.8 Hz, 1H, Ph-H); 7.32 (d, J = 1.9 Hz, 1H, Ph-H); 7.61 (s, 1H, CH of the thiophene); 8.10 (bs, 1H, CONH₂); 8.49 (bs, 1H, CONH₂); 12.18 (bs, 1H, CONH) ppm.

^{13}C NMR (DMSO- D_6): δ = 19.3 (CH₃); 19.6 (CH₃); 122.2 (C); 122.8, 127.0, 128.8 (3 Ph CH); 130.6 (CH of the thiophene); 132.7 (C); 135.3 (C); 135.6 (C); 139.1 (C); 146.4 (C); 157.3 (C); 161.0 (C); 164.0 (C) ppm.

HRMS m/z calcd for C₁₅H₁₃O₂N₃S (M+H)⁺, 300.0801; found, 300.0803.

Synthesis of carbohydrazides 35a,b,c

Excess hydrazine monohydrate (0.3 mL, 6.17 mmol, 10.0 eq) was added dropwise to a solution of ester **36a** (0.2020 g, 0.62 mmol, 1.0 eq) in THF (10 mL) at 0 °C and followed by stirring for 2.5 hours at room temperature. Water (50 mL) was added to the stirred reaction mixture. The precipitate was collected by filtration, washed with water (3 × 20 mL) and dry under reduced pressure / 40 °C overnight.

4-Oxo-5-phenyl-3H-thieno[2,3-d]pyrimidine-2-carbohydrazide (35a)

Yield 0.1350 g, 0.50 mmol, 89%; white solid.

M.p: 148.1-151.4 °C.

IR (solid, ATR) ν = 3400 (w, NH); 3196 (w, NH), 1681 (s, b, CO), 1575, 1510, 1476, 1456, 1427 (w, C=C aromatic) cm^{-1} .

^1H NMR (DMSO- D_6): δ = 5.01 (bs, 2H, NH_2); 7.40 (overlapping m, 3H, Ph-H); 7.55 (overlapping m, 2H, Ph-H); 7.66 (s, 1H, CH of the thiophene ring); 10.51 (bs, 1H, NH); 12.40 (bs, 1H, NH) ppm.

^{13}C NMR (DMSO- D_6): δ = 122.0 (C); 123.2 (Ph para-CH); 127.6 (Ph meta-CH); 127.7 (Ph orthor-CH); 129.6 (Thiophene CH); 135.2 (C); 138.9 (C); 146.2 (C); 157.2 (C); 157.3 (C); 164.0 (C) ppm.

HRMS m/z calcd for $\text{C}_{13}\text{H}_8\text{O}_3\text{N}_2\text{S}$ (M-H) $^-$, 271.0183; found, 271.0184.

4-Oxo-5-(p-tolyl)-3H-thieno[2,3-d]pyrimidine-2-carbohydrazide (35b)

Yield: 0.1430 g, 0.50 mmol, 90%; white solid.

M.p: 137-144 °C.

IR (solid, ATR) ν = 3444 (w, b); 3322 (w), 1722 (w); 1705 (w); 1656 (s), 1575 (w); 1505 (w); 1479 (w); 1434 (w) cm^{-1} .

^1H NMR (CDCl_3): δ = 2.36 (s, 3H, Ph- CH_3); 4.76 (bs, 2H, NH_2); 7.21 (d, J = 8.0 Hz, 2H, Ph-H); 7.44 (d, J = 8.0 Hz, 2H, Ph-H); 7.60 (s, CH of thiophene); 10.46 (bs, NH); 12.00 (bs, 1H, NH) ppm.

^{13}C NMR (CDCl_3): δ = 21.0 (CH_3), 122.0 (C), 122.7 (Ph meta-CH), 128.3 (Ph orthor-CH), 129.4 (CH of the thiophene ring), 132.4 (C), 136.9 (C), 139.0 (C), 146.1 (C), 157.2 (C), 157.3 (C), 164.0 (C) ppm.

HRMS m/z calcd for $C_{14}H_{10}O_3N_2S$ ($M+H$)⁺, 287.0485; found, 287.0484.

5-(3,4-Dimethylphenyl)-4-oxo-3H-thieno[2,3-d]pyrimidine-2-carbohydrazide (35c)

Yield 0.1500 g, 0.50 mmol, 89%; yellow solid.

M.p: 226.1 – 230.6 °C.

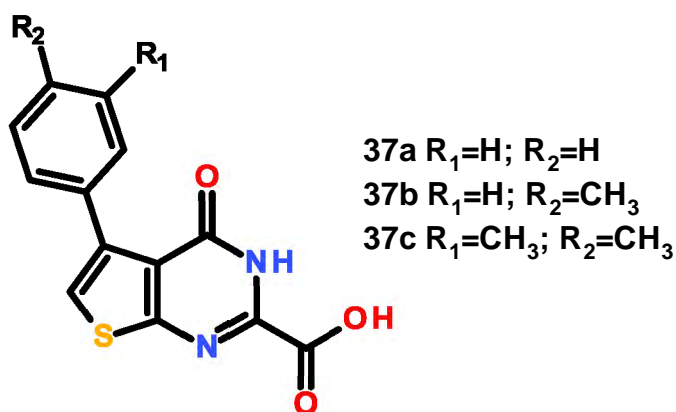
IR (solid, ATR) ν = 3470 (w, NH), 3306 (w, NH), 1697 (s, CO), 1577, 1495, 1467, 1427 (w, C=C aromatic) cm^{-1} .

1H NMR (DMSO- D_6): δ = 2.26 (s, 6H, Ph-(CH₃)₂); 4.76 (bs, NH₂); 7.16 (d, J = 7.7 Hz, 1H, Ph-H); 7.28 (m, 1H, Ph-H); 7.32 (s, 1H, Ph-H); 7.58 (s, 1H, CH of the thiophene); 10.48 (bs, 1H, NH); 12.48 (bs, 1H, NH) ppm.

^{13}C NMR (CDCl₃): δ = 19.3 (CH₃); 19.6 (CH₃); 122.0 (C); 122.7, 127.0, 128.3 (3 Ph CH); 130.6 (CH of the thiophene); 132.4 (C); 135.3 (C); 135.6 (C); 139.0 (C); 146.1 (C); 157.2 (C); 157.3 (C); 164.0 (C) ppm.

HRMS m/z calcd for $C_{15}H_{12}O_3N_2S$ ($M+H$)⁺, 301.0641; found, 301.0644.

Synthesis of carboxylic acids 37a,b,c



A stirred suspension of ester **36a** (0.56 mmol, 1.0 eq) in MeOH (20 mL) was treated with excess NaOH (0.3806 g, 9.50 mmol, 17.0 eq) and water (0.5 mL). The reaction mixture was stirred at 56 °C for 2 hours then was cooled down to room temperature (20 °C). Water (50 mL) was added and the mixture was filtered to get a filtrate. The filtrate

was acidified with concentrated HCl to pH 5-6. The resulting precipitate was collected by filtration, repeatedly washed with water (4×20 mL) and dried under vacuum at 40 °C to achieve carboxylic acid **37a** as a solid.

4-Oxo-5-phenyl-3H-thieno[2,3-d]pyrimidine-2-carboxylic acid (42a)

Yield 0.1350 g, 0.50 mmol, 89%; white solid.

M.p: 148.4 - 151.5 °C.

IR (solid, ATR) ν = 3400 (w, NH), 3200 (w, OH), 1680 (s, CO), 1600, 1510, 1476, 1456, 1427 (m, C=C aromatic) cm^{-1} .

^1H NMR (DMSO- D_6): δ = 7.40 (overlapping m, 3H, Ph-H); 7.56 (overlapping m, 2H, Ph-H); 7.74 (s, 1H, CH of thiophene ring); 12.59 (bs, 1H, NH); 14.58 (bs, 1H, OH) ppm.

^{13}C NMR (DMSO- D_6): δ = 122.8 (C); 124.6 (Ph para-CH); 127.7 (2 Ph meta-CH); 127.8 (2 Ph ortho-CH); 129.6 (CH of thiophene ring); 135.1 (C), 139.0 (C), 144.8 (C), 157.5 (C), 159.8 (C), 164.1 (C) ppm.

HRMS m/z calcd for $\text{C}_{13}\text{H}_8\text{O}_3\text{N}_2\text{S}$ (M-H) $^-$, 271.0183; found, 271.0184.

4-Oxo-5-(p-tolyl)-3H-thieno[2,3-d]pyrimidine-2-carboxylic acid (37b)

Yield 0.1430 g, 0.50 mmol, 90%; white solid.

M.p: 137.4 - 144.8 °C.

IR (solid, ATR) ν = 3100 (w, b, OH), 1722 (s, CO), 1705 (s, CO), 1575, 1505, 1479, 1434 (w, C=C aromatic) cm^{-1} .

^1H NMR (CDCl_3): δ = 2.43 (s, 3H, Ph- CH_3); 7.22 (d, J = 8.0 Hz, 2H, Ph-H); 7.46 (overlapping m, 3H, Ph-H and CH of the thiophene); 13.42 (bs, 1H, NH); 15.35 (bs, 1H, OH) ppm.

^{13}C NMR (CDCl_3): δ = 21.6 (CH_3); 122.8 (C); 125.7 (2 Ph meta-CH); 128.9 (2 Ph ortho-CH); 129.9 (CH of the thiophene ring); 131.5 (C); 138.5 (C); 140.4 (C); 141.9 (C); 160.8 (C); 165.0 (C); 166.3 (C) ppm.

HRMS m/z calcd for $\text{C}_{14}\text{H}_{10}\text{O}_3\text{N}_2\text{S}$ ($\text{M}+\text{H}$) $^+$, 287.0485; found, 287.0484.

5-(3,4-Dimethylphenyl)-4-oxo-3H-thieno[2,3-d]pyrimidine-2-carboxylic acid (37c)

Yield 0.1500 g, 0.50 mmol, 89%; yellow solid.

M.p: 226.4 - 231.7°C °C.

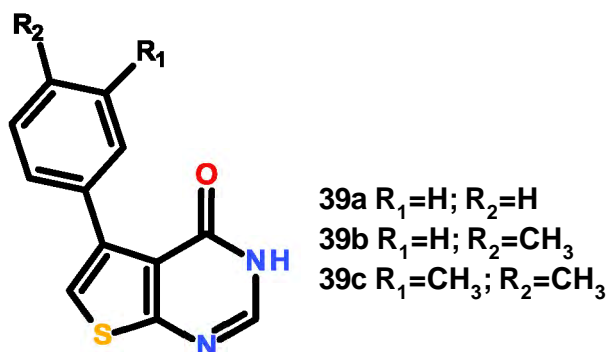
IR (solid, ATR) ν = 3306 (m, NH), 2879 (w, OH), 1697 (s, CO), 1577, 1495, 1467, 1427 (w, C=C aromatic) cm^{-1} .

^1H NMR ($\text{DMSO}-d_6$): δ = 2.26 (s, 6H, $\text{Ph}-(\text{CH}_3)_2$); 7.15 (d, J = 7.7 Hz, 1H, Ph-H); 7.26 (m, 1H, Ph-H); 7.32 (s, 1H, Ph-H); 7.54 (s, 1H, CH of the thiophene); 11.62 (bs, 1H, NH); 14.35 (bs, 1H, OH) ppm.

^{13}C NMR ($\text{DMSO}-d_6$): δ = 19.4, 19.7 ($\text{Ph}-(\text{CH}_3)_2$); 121.5 (C); 122.2, 127.0, 128.9 (3 CH of the phenyl ring); 130.6 (CH of the thiophene ring); 133.0 (C); 135.4 (C); 135.6 (C); 138.9 (C); 148.7 (C); 157.4 (C); 160.9 (C); 165.6 (C) ppm.

HRMS m/z calcd for $\text{C}_{15}\text{H}_{12}\text{O}_3\text{N}_2\text{S}$ ($\text{M}+\text{H}$) $^+$, 301.0641; found, 301.0644.

Synthesis of thieno[2,3-d]pyrimidine derivatives 39a,b,c



5-Phenyl-3H-thieno[2,3-d]pyrimidine-4-one (**39a**)

Method 1

Carboxylic acid **36a** (0.0554 g, 0.20 mmol) was heated until it completely melted to achieve the desired **39a** as a brown solid (0.044 g, 0.19 mol, 100%).

Method 2

A stirred solution of ethyl 2-amino-4-phenyl-thiophene-3-carboxylate (0.3138 g, 1.7 mmol, 1.0 eq) in acetic acid 100% (10 mL) was treated with ethyl cyanofomate (0.25 mL, 2.53 mmol, 2.0 eq) followed by dropwise adding concentrated hydrochloric acid (0.17 mL). The resulting suspension was stirred at 56 °C overnight. Concentrated hydrochloric acid (4.15 mL) was added and the reaction mixture was stirred at 80 °C overnight. The resulting mixture was cooled down to room temperature (20 °C) and water (50 mL) was added. The precipitate was collected by filtration, washed with water (100 mL) and diethyl ether (60 mL) and dried under reduced pressure / 40 °C to give the desired product as a light brown solid (0.1716 g, 0.75 mmol, 59%).

Method 3

A stirred solution of ethyl 2-amino-4-phenyl-thiophene-3-carboxylate (0.2058 g, 0.83 mmol, 1.0 eq) in acetic acid 100% (10 mL) was treated with ethyl cyanofomate (0.15 mL, 1.52 mmol, 1.8 eq) followed by dropwise addition of concentrated hydrochloric acid (0.17 mL). The suspension was stirred at 56 °C for 3.5 hours. Concentrated hydrochloric acid (7.0 mL) was added and the reaction mixture was stirred at 80 °C overnight. The resulting mixture was cooled down to room temperature and water (30 mL) was added. The precipitate was filtered, washed thoroughly with water (100 mL) and diethyl ether (60 mL) and dried under reduced pressure / 40 °C to give the desired product as a cream solid (0.1587 g, 0.70 mmol, 84%).

M.p: 206.5 - 213.1 °C.

IR (solid, ATR) ν = 3171 (w, NH), 1675 (s, CO), 1587, 1525, 1499, 1441 (w, C=C aromatic) cm^{-1} .

^1H NMR (DMSO- D_6): δ = 7.39 (m, 3H, Ph-H); 7.54 (overlap m, 3H, 2 Ph-H and CH of the thiophene); 8.16 (s, 1H, CHNH); 12.48 (bs, 1H, NH) ppm.

^{13}C NMR: δ = 121.4 (Ph para-CH), 121.5 (C), 127.8 (2 Ph meta-CH), 128.0 (2 Ph ortho-CH), 129.7 (CH of the thiophene), 135.6 (C), 138.9 (C), 146.2 (CHNH), 157.8 (C), 166.0 (C) ppm.

HRMS m/z calcd for $\text{C}_{12}\text{H}_8\text{ON}_2\text{S}$ (M-H) $^-$ 227.0285; found, 227.0284.

5-(P-tolyl)-3H-thieno[2,3-d]pyrimidine-4-one (39b)

Carboxylic acid **36b** (0.1045g, 0.36 mmol) was heated until it completely melted to achieve compound **39b** as a purple solid (0.085 g, 0.35 mmol, 97%).

M.p: 203.3 - 207.4°C.

IR (solid, ATR) ν = 3186 (w, NH), 1668 (s, CO), 1592, 1538, 1480, 1453 (w, C=C aromatic) cm^{-1} .

^1H NMR (DMSO- D_6): δ = 2.35 (s, 3H, Ph- CH_3); 7.20 (d, J = 8.0 Hz, 2H, Ph-H); 7.43 (d, J = 8.0 Hz, 2H, Ph-H); 7.46 (s, 1H, CH of the thiophene); 8.14 (s, 1H, CHNH); 12.48 (bs, 1H, NH) ppm.

^{13}C NMR (DMSO- D_6): δ = 20.1 (Ph- CH_3); 120.5 (2 Ph meta-CH); 121.2 (C); 128.3 (2 Ph ortho-CH); 129.4 (CH of the thiophene); 132.7 (C); 136.8 (C); 138.8 (C); 146.0 (CHNH); 157.6 (C); 165.8 (C) ppm.

HRMS m/z calcd for $\text{C}_{13}\text{H}_{10}\text{O}_1\text{N}_2\text{S}$ (M+H) $^+$, 243.0514; found, 243.0513.

5-(3,4-Dimethylphenyl)-3H-thieno[2,3-d]pyrimidin-4-one (39c)

Carboxylic acid **36c** (0.1086g, 0.36 mmol) was heated until it completely melted to give the desired **39c** as a dark brown solid (0.0924 g, 0.36 mmol, 100%).

M.p: 172.1 – 174.5 °C.

IR (solid, ATR) ν = 3100 (w, NH), 1700 (s, CO), 1587, 1525, 1500, 1454 (w, C=C aromatic) cm^{-1} .

^1H NMR (DMSO- D_6): δ = 2.25 (s, 6H, $\text{Ph}-(\text{CH}_3)_2$); 7.10 (m, 2H, Ph-H); 7.27 (m, 1H, Ph-H); 7.32 (m, 1H, CH of the thiophene); 8.03 (s, 1H, CHNH); 12.48 (bs, 1H, NH) ppm.

^{13}C NMR: δ = 19.3 (Ph- CH_3); 19.7 (Ph- CH_3), 116.3 (CH of the phenyl ring), 120.2 (C), 126.9 (CH of the phenyl ring), 128.4 (CH of the phenyl ring), 130.6 (CH of the thiophene), 134.4 (C), 134.6 (C), 134.8 (C), 138.9 (C), 151.7 (CHNH), 164.4 (C), 166.6 (C) ppm.

HRMS m/z calcd for $\text{C}_{14}\text{H}_{13}\text{O}_1\text{N}_2\text{S}$ ($\text{M}+\text{H}$) $^+$ 257.0743; found, 257.0744.

5 Molecular dynamics simulations of potential irreversible inhibitors of TG2

The most potent TG2 irreversible inhibitor developed by the Griffin group (Aston University) (compound **27** Figure 1.26) was the starting point for this project to generate a new set of potential TG2 irreversible inhibitors. The first attention was modifying the acrylamide warhead of the lead compound to other types of Michael acceptor warhead. Secondly, the side chain that connected the piperazine ring and the warhead was modified to a shorter aliphatic sidechain or was added a rigid phenyl ring. The naphthalene ring was also targeted to vary to other aromatic rings or a heterocyclic ring. Finally, the piperazine ring was modified to various heterocycles such as 3-aminorhodanine or 1,2,4-triazole. Compound **26** (Figure 1.25) was also modified by inserting a phenyl ring between the the piperazine ring and the warhead to make compounds with a more rigid side chain. List of compounds applied for MD simulations is displayed in Table 5.1.

In this chapter, compound **27**, **26a**, **40a**, and **41b** were docked into the catalytic binding site in the open (active) conformation of TG2 by GOLD docking programme by Dr. Dan Rathbone. The most favourable protein-ligand complexes were further subjected to MD simulations in explicit water for 200 ns. These mentioned compounds then became the parent compounds to design other analogues by direct modifications of their structures in the complexes with TG2. The resulting complexes were applied MD simulation in explicit water in the same method used for the complexes of the parents. The stability of the ligands and their warheads in the catalytic binding site and essential interactions between the ligands and the protein to maintain that stability were analysed. This was used to predict the affinity of the ligands into the catalytic binding site. The distance between the warhead electrophilic carbon and CYS277 sulphur atom was calculated. The shortest distance was also identified to predict the possibility of the warhead to attack the nucleophilic cystein.

Table 5.1. List of potential irreversible TG2 inhibitors applied for MD simulations.

Name	R	X
27		
27a		
(E)-27b		
(Z)-27b		
(E)-27c		
27e		
(Z)-27f		
27g		
(Z)-27h		
26a		
(Z)-26b		
40a		
40b		
41a		
41b		

5.1 MD trajectory of the lead irreversible inhibitor (compound 27)

At the first frame of the simulation, various interactions were induced between the ligand and the residues of the enzyme catalytic binding site as shown in Figure 5.1. Pi-pi stacked and pi-alkyl interactions were generated between the ligand naphthalene ring and two residues PHE316 and ARG317 of the hydrophobic pocket. The piperazine ring was clamped between MET330 and TRP241 by alkyl-alkyl and pi-sigma interactions. Two hydrogen bonds were formed between the warhead carbonyl group and the backbone amino groups of two residues ASN333 and PHE334. The distance between the warhead electrophilic carbon and CYS277 sulphur atom was 3.9 Å.

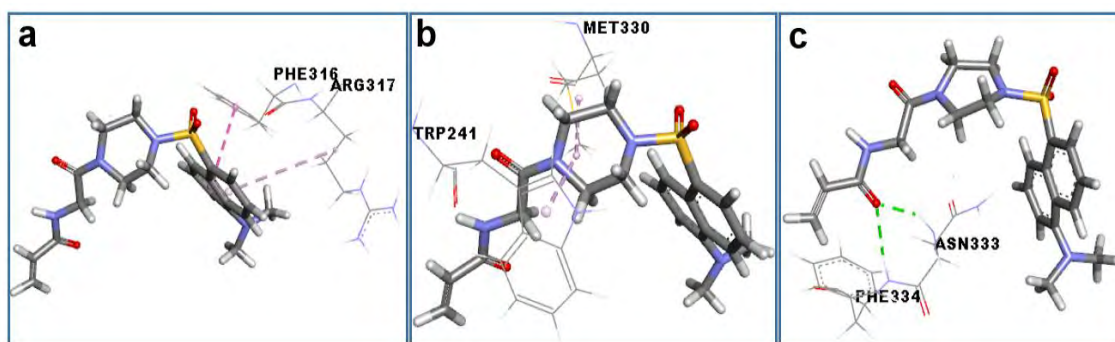


Figure 5.1. Interactions between the lead TG2 irreversible inhibitor and the enzyme catalytic binding site in the starting frame of the MD simulation.

During the simulation time, the naphthalene ring was held in the hydrophobic pocket by the hydrophobic interactions with nearby residues. The warhead left the catalytic tunnel from around 15.0 ns. The side chain was significantly mobile when it left the tunnel. Therefore, the distance between the warhead electrophilic carbon and CYS277 sulphur atom increased up to 25.0 Å. The positions of the ligand in the first frame and in the last frame of the simulation are displayed in Figure 5.2.

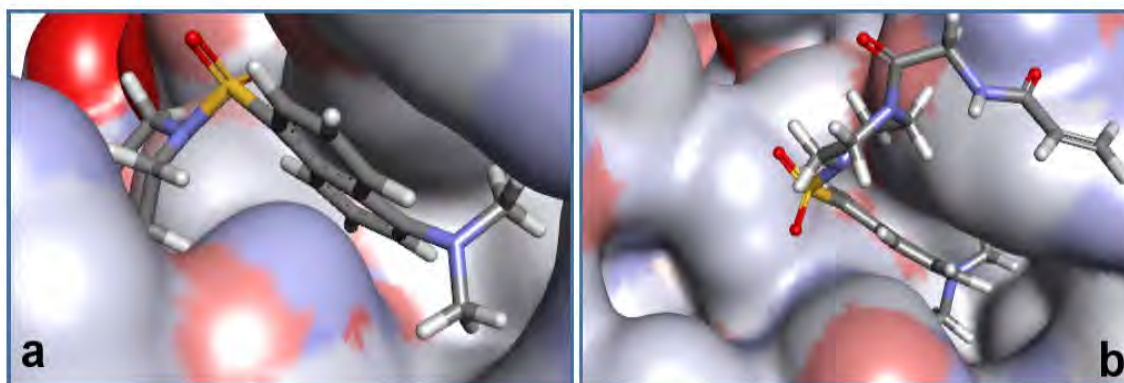


Figure 5.2. Positions of compound **27** in the catalytic binding site in the first frame (a) and in the last frame (b) of 200 ns MD simulation.

Hydrogen bonds between the acrylamide carbonyl and the backbone amines of two residues ASN333 and PHE334 existed during the time the warhead stayed inside the catalytic tunnel. These bonds disappeared at the same time the warhead detached from the tunnel. The distances between the relevant atoms of these hydrogen bonds during the first 15.2 ns MD simulation are displayed in Figure 5.3. It can be seen that these distances were mostly lower than 3.0 Å during the time the warhead was retained in the catalytic tunnel. That indicates the important role of these hydrogen bonds in restraining the warhead inside the catalytic tunnel.

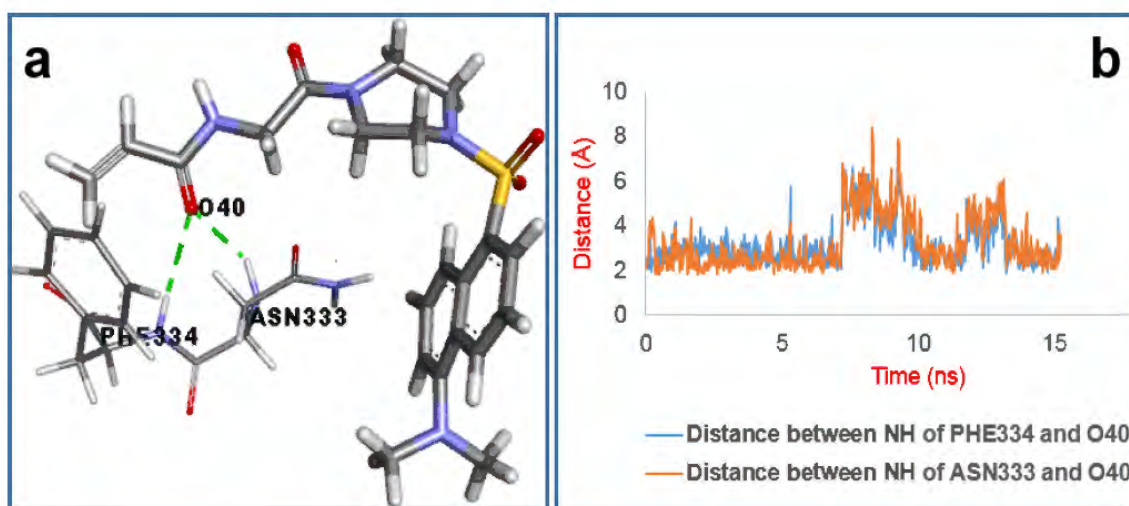


Figure 5.3. Hydrogen bonds between compound **27** and two residues ASN333 and PHE334 and the distances between the relevant atoms during the first 15.2 ns MD simulation.

The distance between the warhead electrophilic carbon and the sulphur atom of CYS277 during the time the warhead stayed inside the catalytic tunnel is pointed out in

Figure 5.4b. The distance was observed to fall below 4.0 Å for only a transient period. The positions of the ligand and CYS277 when the distance was shortest are displayed in Figure 5.4a.

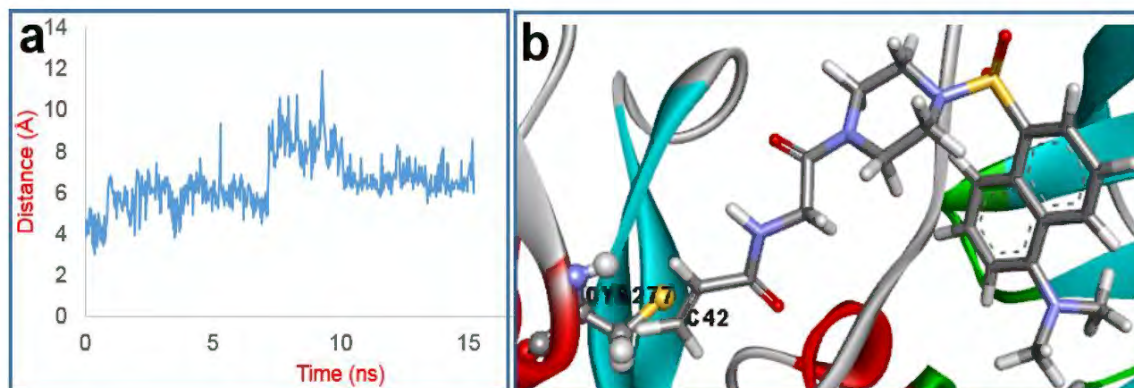


Figure 5.4. Distance between the electrophilic warhead carbon of compound **27** and the CYS277 sulphur during the period the warhead was retained in the catalytic tunnel (a) and the position of the ligand and CYS277 when the distance was the shortest (b).

5.2 MD trajectories of compounds having the same scaffold as the lead compound **27**

5.2.1 MD trajectory of compound **27a**

During the simulation, the warhead moved toward the catalytic tunnel and this movement pulled the lipophilic part of the ligand out of the hydrophobic pocket. However, the ligand was retained in the binding site during 200 ns simulation. The positions of the ligand at the first and the last frame of the simulation are shown in Figure 5.5.

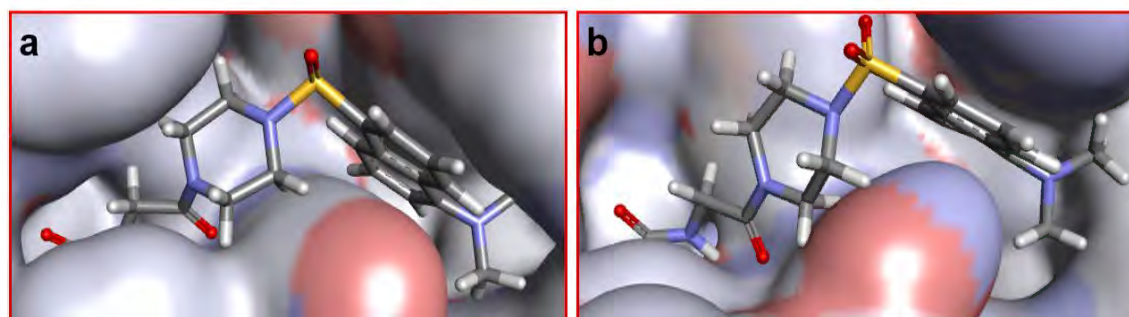


Figure 5.5. Position of compound **27a** at the first frame (a) and at the last frame (b) of 200 ns MD simulation.

Hydrogen bonds were generated between two carbonyl groups of the ligand hydrophilic side chain and four residues ASN333, PHE334, GLN276 and CYS277 (Figure 5.6) during the simulation time. The hydrogen bonds formed between ASN333 backbone NH and the ligand acrylamide CO and between PHE334 backbone CO and the ligand acrylamide NH had high occurrences during the simulation. When these hydrogen bonds disappeared, the hydrogen bonds between the ligand acrylamide carbonyl and the two amino groups of GLN276 side chain and CYS277 backbone were formed. These exchangeable hydrogen bonds possibly restrained the hydrophilic side chain and the warhead of the ligand in the catalytic tunnel during the simulation time.

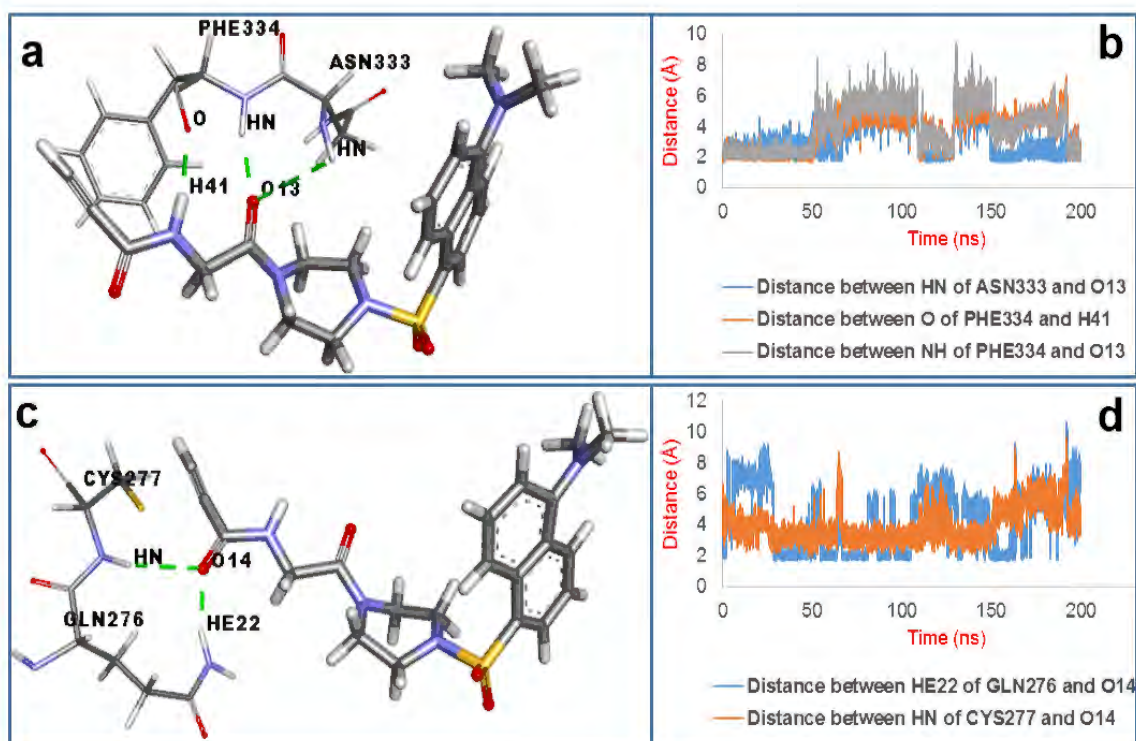


Figure 5.6. Hydrogen bonds between compound **27a** and four residues ASN333, PHE334, GLN276 and CYS277 and the distances between the relevant atoms.

The movement of the warhead toward the catalytic tunnel together with the hydrogen bond between CYS277 and the ligand acrylamide carbonyl helped to shorten the distance between CYS277 sulphur atom and the warhead electrophilic carbon. This distance fluctuated mainly between 3.2 and 6.0 Å during the simulation time and it decreased during the last frames as given in Figure 5.7. The stability of the ligand in the catalytic binding site and the short distance between the warhead electrophilic carbon

and the nucleophilic CYS277 sulphur during 200 ns MD simulation suggested a potential good inhibition of compound **27a**.

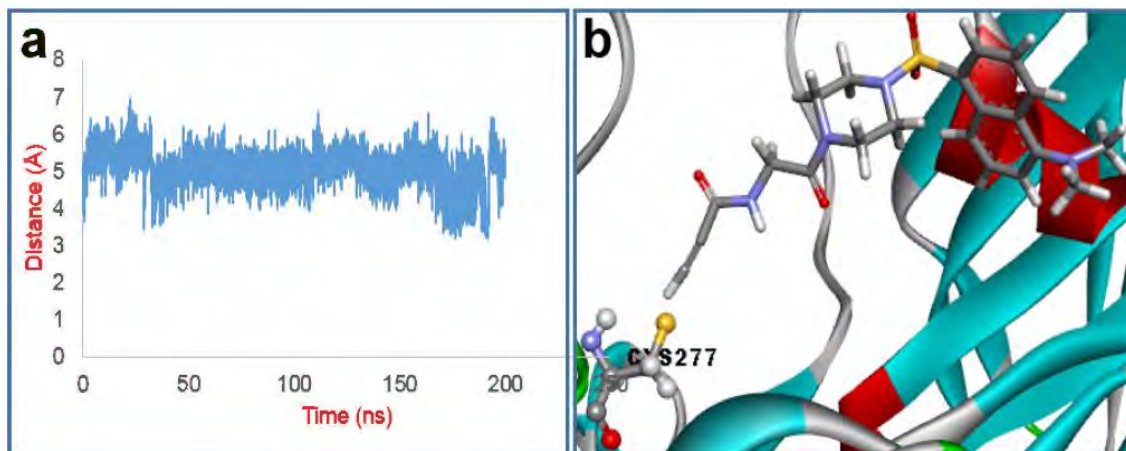


Figure 5.7. Distance between the warhead electrophilic carbon of compound **27a** and CYS277 sulphur atom during 200 ns MD simulation (a) and the position of compound **27a** and CYS277 when the distance was the shortest (b).

5.2.2 MD trajectory of compound (E)-27b

The warhead of this compound left the catalytic tunnel after approximately 1.9 ns MD simulation. The side chain was remarkably mobile and the distance between the warhead electrophilic carbon and CYS277 sulphur atom increased to more than 25.0 Å. The lipophilic part moved towards to the hydrophobic pocket and was held there by hydrophobic interactions with neighbouring residues. The positions of the ligand at the start and at the end of the simulation are shown in Figure 5.8.

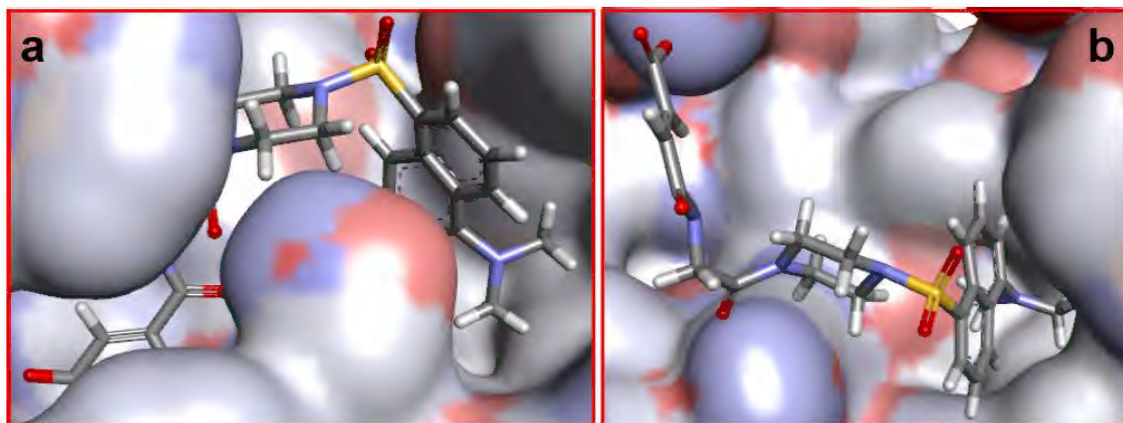


Figure 5.8. Position of compound (E)-**27b** at the beginning (a) and at the end (b) of 200 ns MD simulation.

During the period the warhead stayed in the catalytic tunnel, hydrogen bonds were formed between the ligand hydrophilic side chain and three residues CYS336, PHE334 and ASN333 (Figure 5.9). The interaction between the ligand carboxyl and the CYS336 backbone amino soon disappeared after roughly 0.5 ns simulation. In contrast, the hydrogen bonds between the ligand amide carbonyl and the backbone amino groups of PHE334 and ASN333 were maintained until the warhead left the tunnel. The distances between the related atoms of these hydrogen bonds during the period the warhead was retained inside the catalytic tunnel are shown in Figure 5.9. Similar to the lead compound, the hydrogen bonds between the ligand side chain and two residues PHE334 and ASN333 contributed to the stability of warhead in the catalytic tunnel.

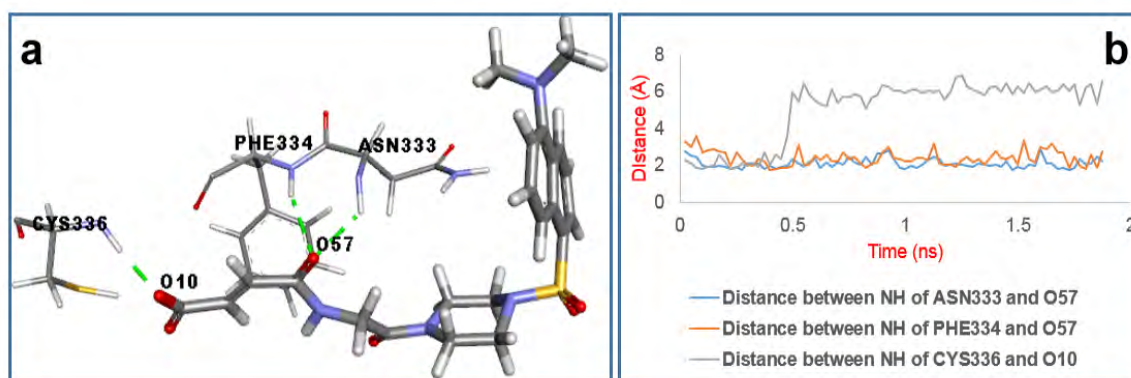


Figure 5.9. Hydrogen bonds between compound (E)-27b and three residues ASN333, PHE334 and CYS336 (a) and the distances between the relevant atoms (b).

The distance between the warhead electrophilic carbon and the sulphur atom of CYS277 fluctuated between 5.0 to 8.9 Å when the warhead stayed inside the catalytic tunnel (Figure 5.10). The shortest distance was appeared in the first frame of the simulation at this the position of the ligand in comparison to CYS277 is displayed in Figure 5.10. The transient maintaining of the warhead in the catalytic tunnel and the long distance between the warhead electrophilic carbon and CYS277 sulphur atom give a prediction of low inhibition effect of compound (E)-27b.

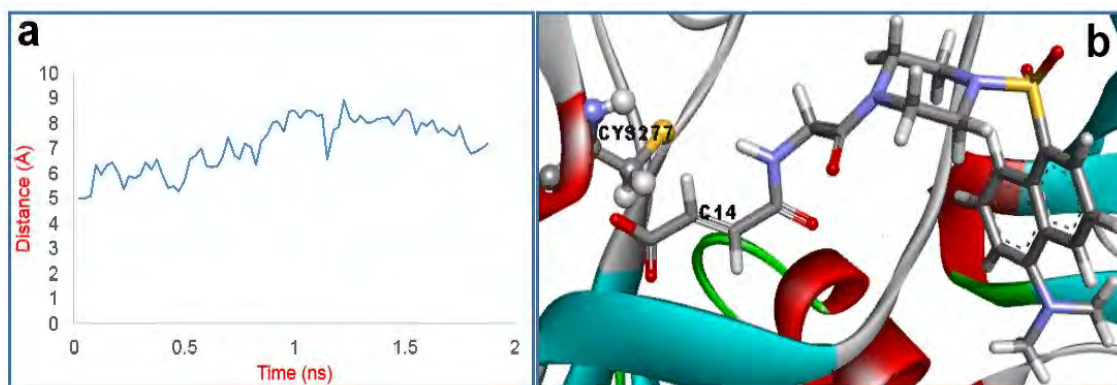


Figure 5.10. Distance between the warhead of compound (**E**)-**27b** and CYS277 sulphur atom during the period the warhead was maintained in the catalytic tunnel (a) and positions of compound (**E**)-**27b** and CYS277 when the distance was the shortest (b).

5.2.3 MD trajectory of compound (**Z**)-**27b**

In contrast to the (**E**)-isomer, the warhead of the (**Z**)-isomer moved towards to the catalytic tunnel and the lipophilic part was pulled towards the catalytic site during the simulation time. This started happening after roughly 16.5 ns simulation. Simultaneously, the distance between the warhead electrophilic carbon and the sulphur atom of CYS277 also decreased and fluctuated mainly less than 6.5 Å (Figure 5.11). The shortest distance was 3.6 Å. The position of the ligand and CYS277 when the distance was shortest is shown in Figure 5.11.

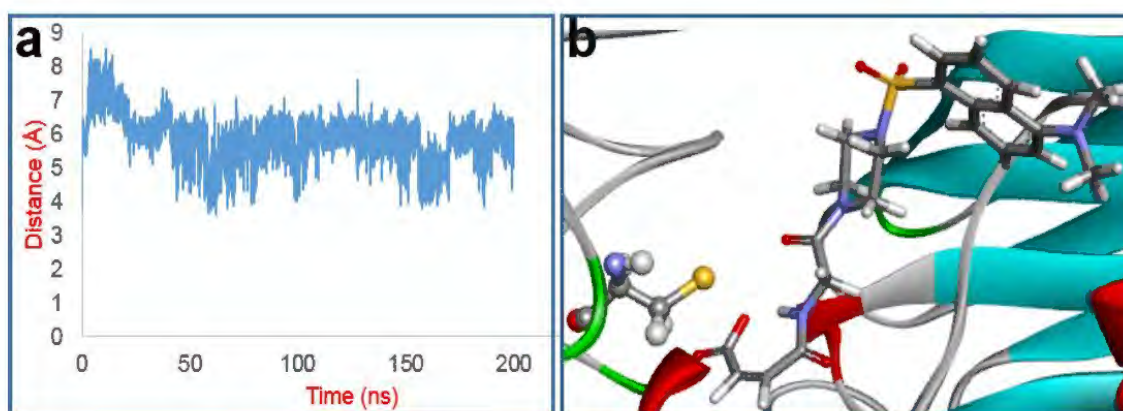


Figure 5.11. Distance between the warhead electrophilic carbon of compound (**Z**)-**27b** and CYS277 sulphur atom during 200 ns MD simulation (a) and positions of compound (**Z**)-**27b** and CYS277 when distance was the lowest (b).

10 hydrogen bonds were generated between the ligand and the protein during the 200 ns simulation. However, most of them only appeared temporarily. The highest occupancy

hydrogen bond was created between the carboxylate group of the ligand's side chain and the protonated HIS335 amine imidazole. This bond was formed from around 42 ns and occurred for 22.43% of the simulation time. In addition, the distance between the atoms forming this hydrogen was mostly lower than 3.0 Å after 42 ns simulation (Figure 5.12). It suggests a significant role of this hydrogen bond in holding the warhead stable inside the catalytic tunnel and consequently stabilised the ligand. Figure 5.12 indicates the position of compound (**Z**)-**27b** in comparison to CYS277 when the hydrogen bond was formed between the ligand and HIS335.

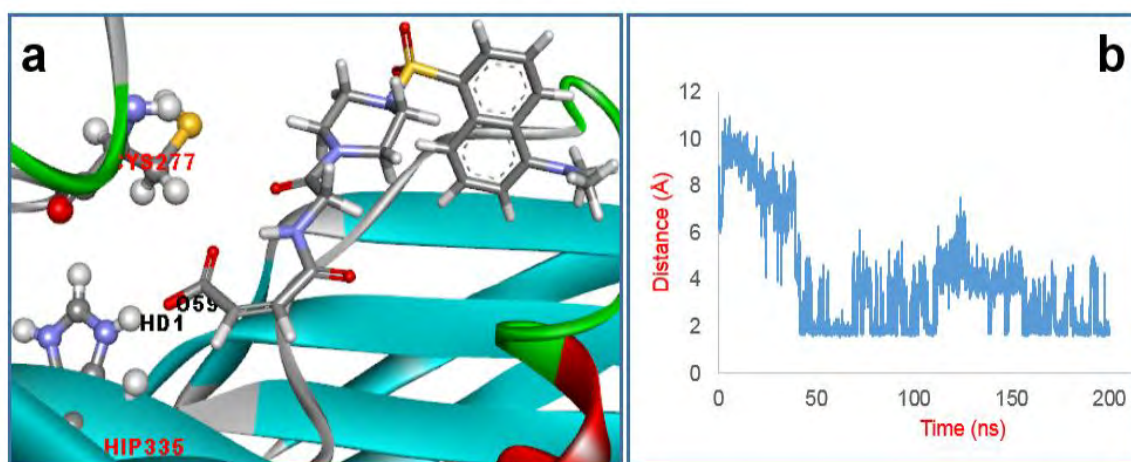


Figure 5.12. Position of compound (**Z**)-**27b** at a frame when the hydrogen bond was formed between the ligand carboxylate and the imidazole amino of protonated HIS335 (a) and the distance between the relevant atoms during 200 ns MD simulation (b).

5.2.4 MD trajectory of compound (**E**)-**27c**

During the simulation, the warhead moved towards the catalytic tunnel and that pulled the lipophilic part out of the hydrophobic pocket. The naphthalene ring left the hydrophobic pocket soon after the simulation started and was remarkably mobile since then. The positions of the ligand in the first frame and in the last frame of the simulation are displayed in Figure 5.13.

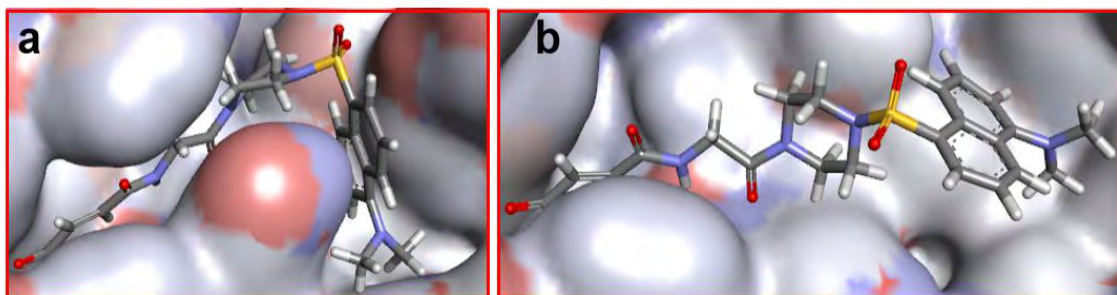


Figure 5.13. Position of compound (E)-**27c** in the first frame (a) and in the last frame (b) of 200 ns MD simulation.

Although the lipophilic part was significantly mobile when it left the hydrophobic pocket, the hydrophilic side chain and the warhead were retained in the catalytic tunnel till the end of the simulation time. Hydrogen bonds between the backbone NH of ASN333 and PHE334 and the amide carbonyl group of the ligand (Figure 5.14) had the highest occurrences (37.90% and 22.64%, respectively) among recorded hydrogen bonds. The distances between the relevant atoms fluctuated mainly less than 3.0 Å during the simulation time as shown in Figure 5.14. Hydrogen bonds between PHE334 backbone CO and the ligand amide NH and between GLN169 side chain NH and the ligand ester CO are also high occurrences. Distances of these bonds are also displayed in Figure 5.14. These hydrogen bonds held the warhead and the hydrophilic side chain firmly in the catalytic tunnel. Consequently, the ligand was stabilised during the simulation time.

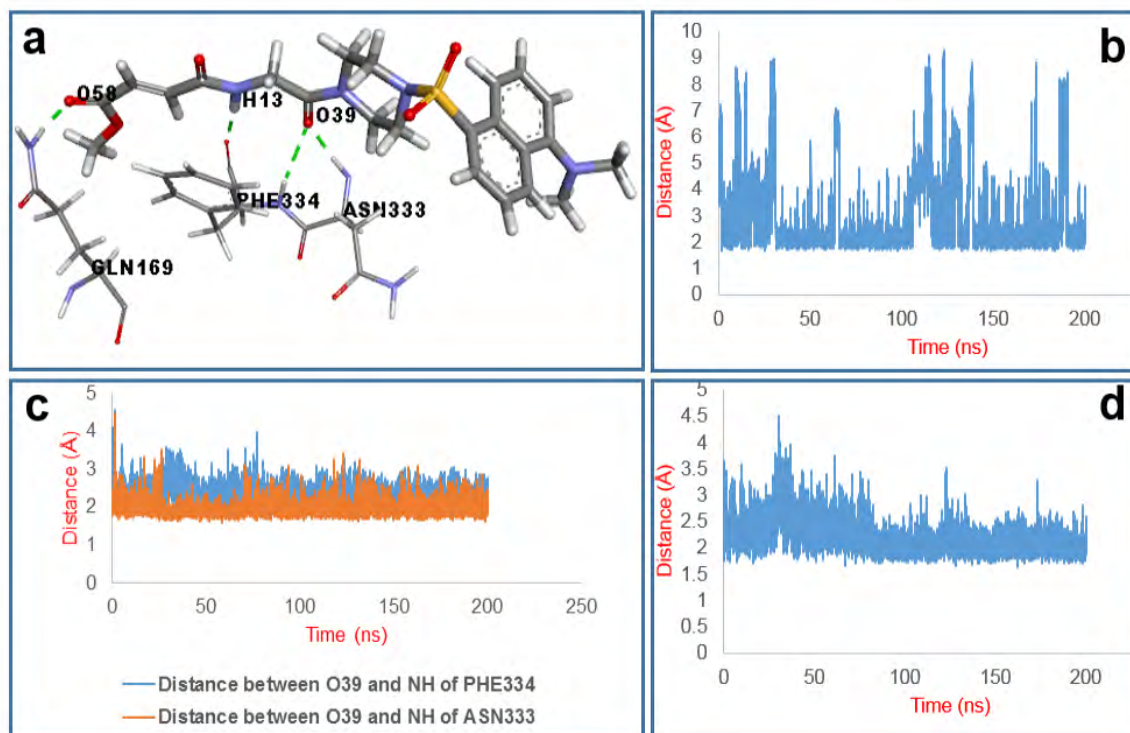


Figure 5.14. (a) Hydrogen bonds between compound (E)-27d and three residues GLN169, ASN333 and PHE334; (b) distance between O the ligand carboxylate CO and H of GLN169 side chain NH; (c) distances between relevant atoms of the hydrogen bonds between the ligand CO and the NH groups of two residues PHE334 and ASN333; (d) Distance between H of the ligand acrylamide NH and O of PHE334 CO.

The distance between the warhead electrophilic carbon and CYS277 sulphur atom during 200 ns simulation and the position of the ligand and CYS277 when the distance was the shortest are indicated in Figure 5.15. It can be seen that the distance between the warhead electrophilic carbon and CYS277 sulphur atom mostly fluctuated higher than 5.0 Å. It was lower than 4.0 Å during some first frames of the simulation and the shortest distance was 3.3 Å. The ligand side chain moved toward the catalytic tunnel but this movement did not shorten the distance between the lipophilic warhead electrophilic carbon and the sulphur atom of CYS277.

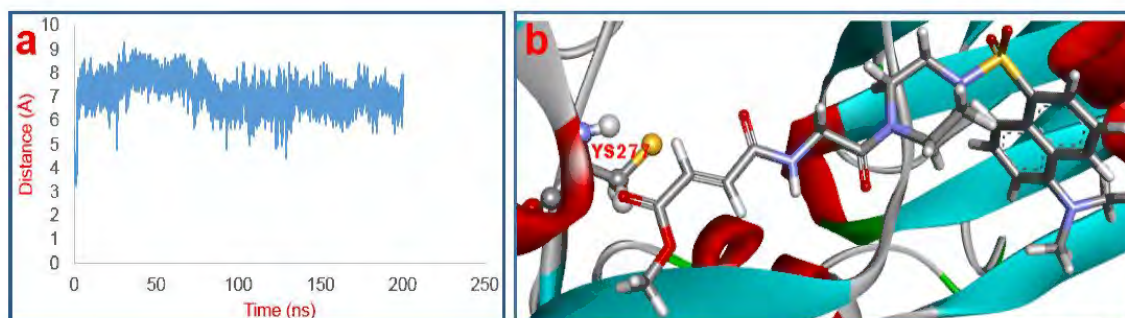


Figure 5.15. The distance between the warhead electrophilic carbon of compound (**E**)-**27c** and CYS277 sulphur atom during 200 ns MD simulation (a) and the position of this compound and CYS277 when the distance was the shortest (b).

5.3 MD trajectories of compounds with a shorter side chain modified from compound 27

5.3.1 MD trajectory of compound 27e

The naphthalene ring left the hydrophobic pocket after about 0.5 ns simulation. It relocated to the outside of the catalytic tunnel and formed T-shaped pi-pi interactions with TRP332. After 107.0 ns simulation, the warhead also moved out from the catalytic tunnel followed by the leaving of the whole molecule. The positions of the ligand in the first frame of MD simulation and when the naphthalene ring relocated to the outside of the catalytic tunnel are shown in Figure 5.16.

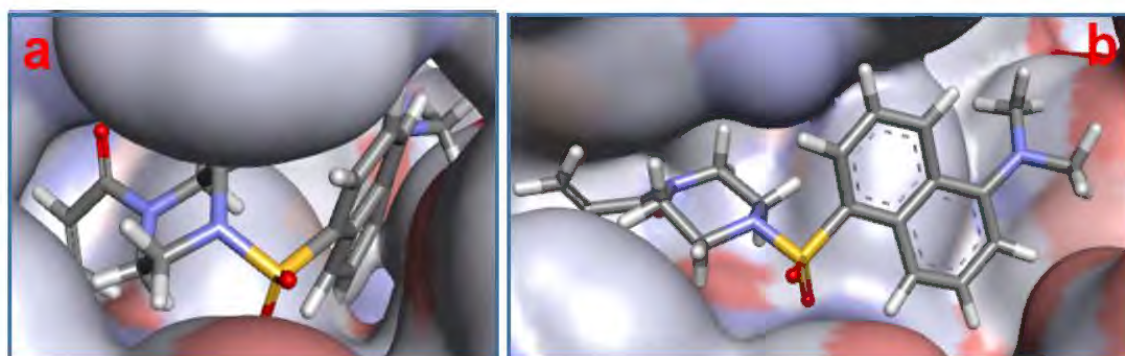


Figure 5.16. Positions of compound **27e** at the first frame and at a frame when the naphthalene ring relocated to the outside of the catalytic tunnel.

During the period the warhead was maintained in the catalytic tunnel, hydrogen bonds were created between the ligand sulfonyl group and the backbone amino of two residues ASN333 and PHE334 and also between the carbonyl group of the ligand hydrophilic side chain and CYS336 amine backbone (Figure 5.17). However, these bonds

disappeared when the warhead left the catalytic tunnel. It can be seen from Figure 5.17 that the distances between the relevant atoms mostly fluctuated less than 3.0 Å during the time the warhead was located in the catalytic tunnel. This indicates the important role of these hydrogen bonds in restraining the warhead.

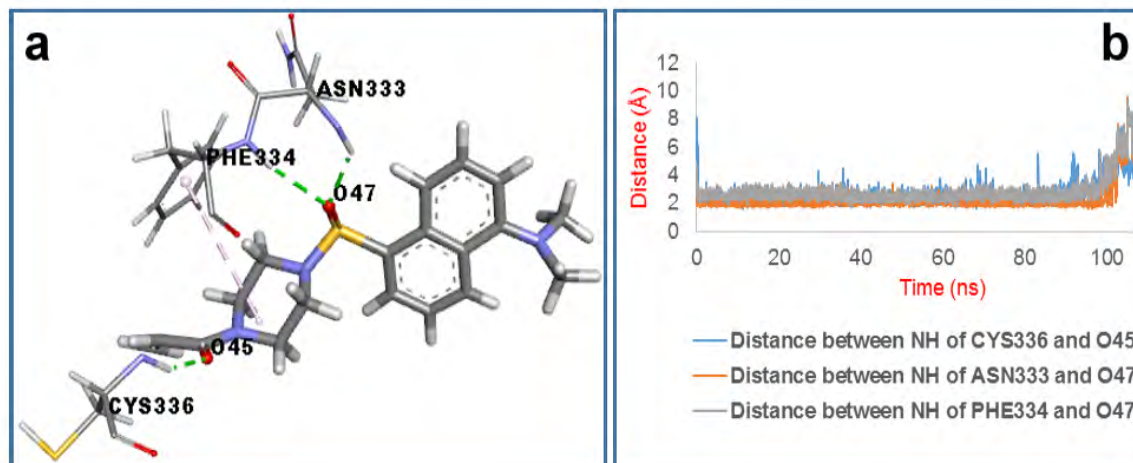


Figure 5.17. Interactions between compound **27e** and three residues ASN333, PHE334 and CYS336 (a) and distances between the relevant atoms of these hydrogen bonds during the first 107.0 ns MD simulation.

During the period the warhead stayed in the catalytic tunnel, the hydrogen bond forming between the ligand acrylamide carbonyl and CYS336 backbone amino caused the movement of the warhead towards this amino acid. Interestingly, the distance between the warhead electrophilic carbon and the sulphur atom of CYS336 was generally lower than that between the warhead electrophilic carbon and the sulphur atom of CYS277. It can be seen from Figure 5.18 that the distance between the warhead electrophilic carbon and CYS336 sulphur atom fluctuated mostly between 3.0 and 7.0 Å whilst that between the warhead electrophilic carbon and CYS277 sulphur atom mainly oscillated around 8.0 Å. That indicated the possibility of the Michael addition reaction occurred between the ligand and CYS366 instead of with CYS277. The position of the ligand in comparison to two residues CYS277 and CYS336 when the distance between the warhead electrophilic carbon and the cystein sulphur of these residues were lowest are shown in Figure 5.18.

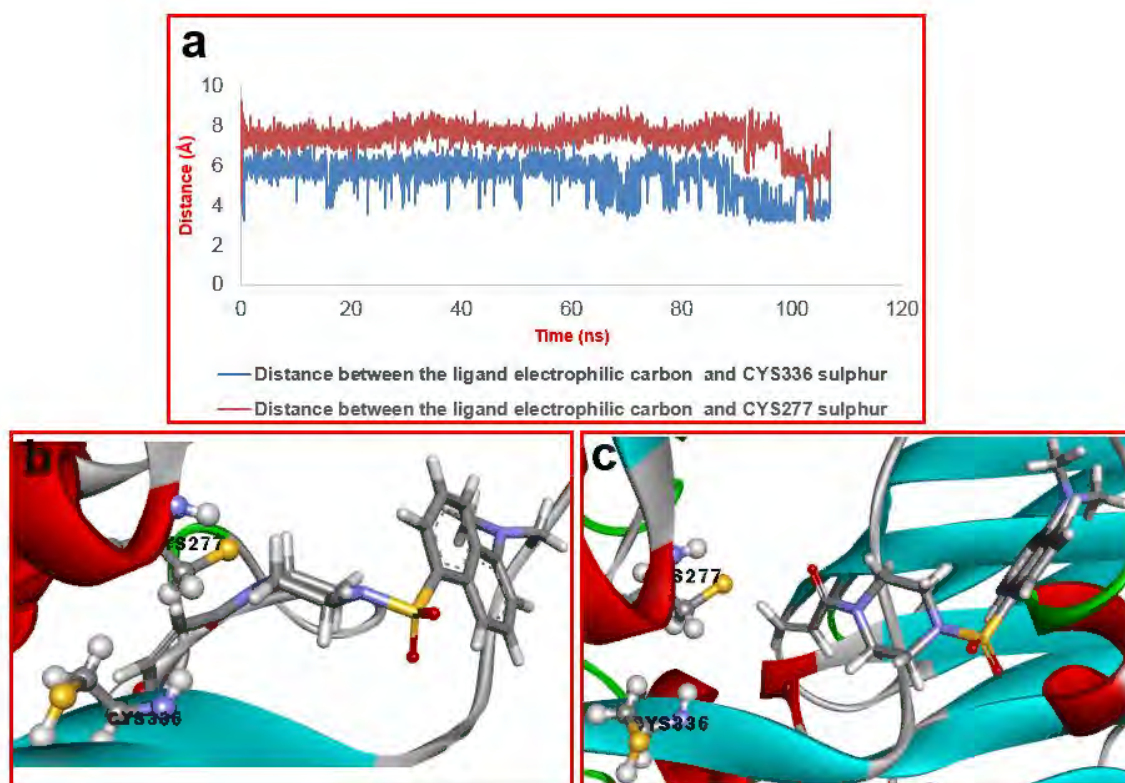


Figure 5.18. Distances between the warhead electrophilic carbon of compound **27e** and sulphur atoms of CYS336 and CYS277 during the period the warhead was retained in the catalytic tunnel (a) and positions of the ligand when these distances were the lowest, respectively (b,c).

5.3.2 MD trajectory of compound (Z)-27f

The ligand warhead moved out of the catalytic tunnel to another binding site from 1.5 ns simulation. During the period the warhead stayed inside the catalytic tunnel, a hydrogen bond was generated between the ligand side chain and TRP241 but only for around 0.05 ns simulation. The lowest distance between the warhead electrophilic carbon and CYS277 sulphur atom was 4.2 Å and that happened in the first frames of the simulation (Figure 5.19). The transient binding of the warhead in the catalytic tunnel and the high distance between the warhead electrophilic carbon and CYS277 sulphur atom suggested a possibly low affinity and low potency of compound (Z)-27f.

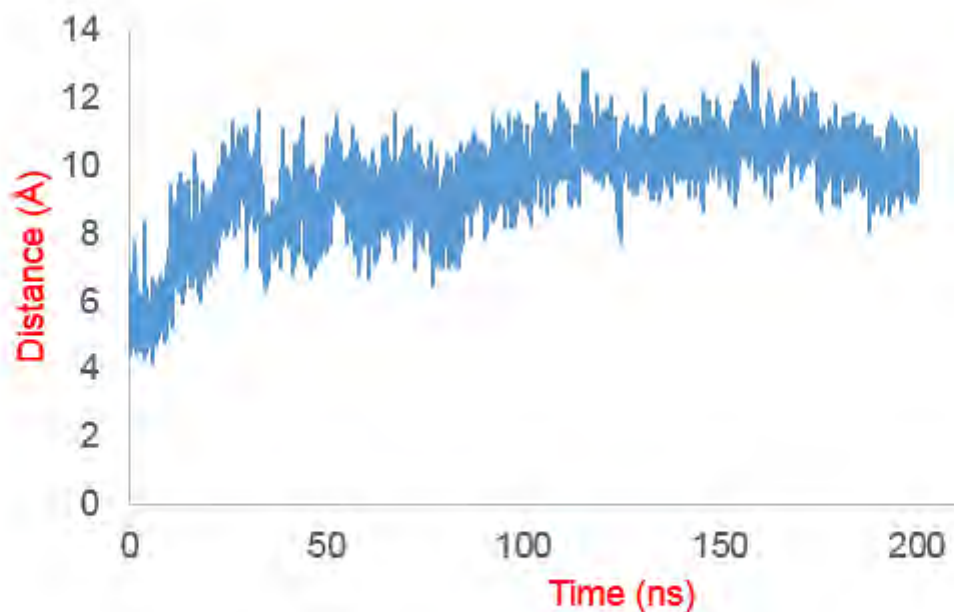


Figure 5.19. The distance between the warhead electrophilic carbon of compound (**Z**)-**27f** and CYS277 sulphur atom during 200 ns MD simulation.

5.4 MD trajectories of compounds with a more rigid side chain modified from compound 27

5.4.1 MD trajectory of compound 27g

The warhead was held in the catalytic tunnel for 26.5 ns, moved out for 0.25 ns and then turned back to the original position. Since 28.4 ns simulation, the warhead left the tunnel again and that made the hydrophilic side chain became significantly mobile. Since that moment, the lipophilic part moved downward to the hydrophobic pocket where it was held by hydrophobic interactions with nearby residues. The ligand was observed to be maintained in the binding site during 200 ns simulation. That was indicated by the ligand RMSD values as shown in Figure 5.20. However, the distance between the warhead electrophilic carbon and CYS277 sulphur atom significantly increased after the moment the warhead left the catalytic tunnel.

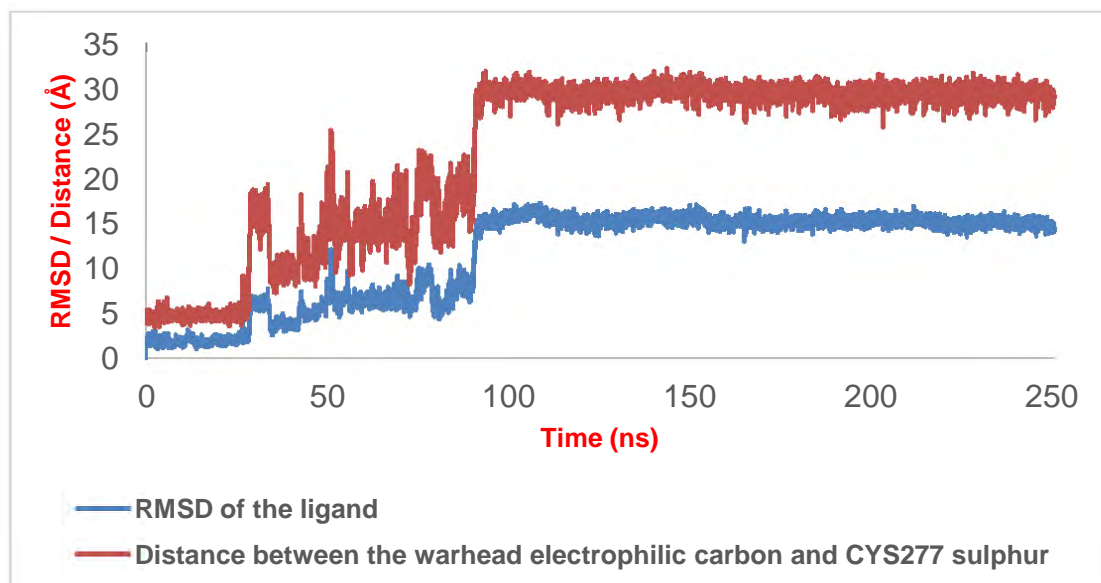


Figure 5.20. RMSD values of compound **27g** and the distance between the warhead electrophilic carbon and CYS277 sulphur atom during 200 ns MD simulation.

During the period the warhead stayed in the catalytic tunnel, the ligand acrylamide NH formed hydrogen bonds with both CYS277 sulphur and PHE334 backbone CO (Figure 5.21). It can be seen from Figure 5.21 that the distance between the acrylamide NH of the ligand and backbone CO of PHE334 was mostly less than 3.0 Å during 28 ns simulation. That indicates a strong hydrogen bond between the acrylamide warhead and PHE334. In addition, the distance between CYS277 sulphur atom and the ligand acrylamide NH also oscillated around 3.0 Å during the time the warhead was maintained inside the tunnel. These hydrogen bonds may play the important role in restraining the warhead in the catalytic tunnel.

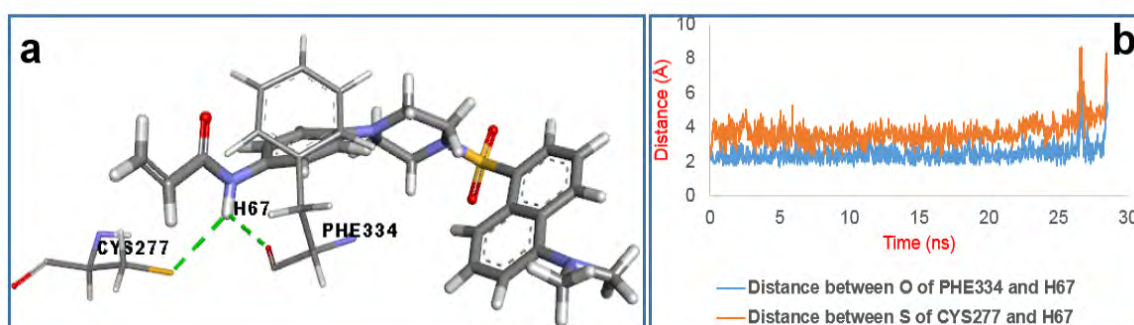


Figure 5.21. Hydrogen bonds between compound **27g** and two residues CYS277 and PHE334 (a) and distances of the relevant atoms during the first 28.5 ns MD simulation (b).

During the period the warhead was held in the catalytic tunnel, the distance between the warhead electrophilic carbon and the sulphur atom of CYS277 mainly fluctuated between 3.4 and 5.0 Å (Figure 5.22). The stability of the compound **27g** and the short distances between the warhead electrophilic carbon and CYS277 sulphur atom during 28.4 ns suggested a possibly high affinity and a potent inhibitory effect against TG2 of this compound.

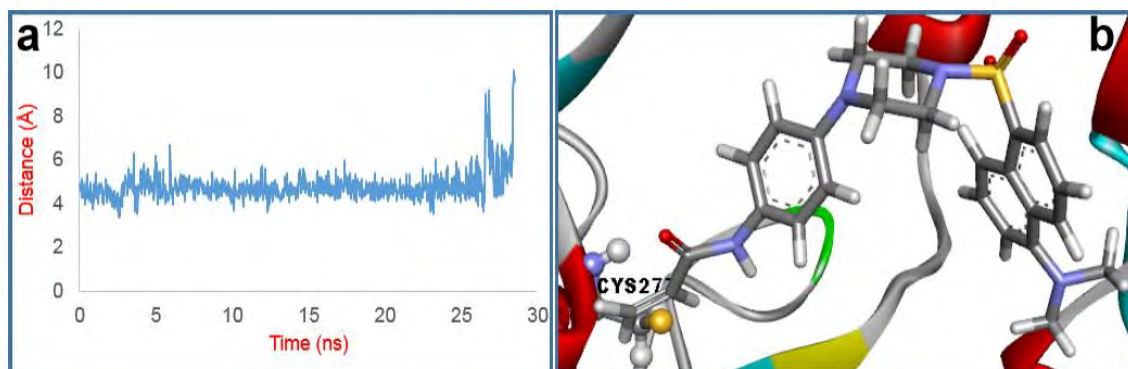


Figure 5.22. Distance between the warhead electrophilic carbon of compound **27g** and CYS277 sulphur atom during the first 28.5 ns MD simulation (a) and the position of this compound when the distance was the shortest (b).

5.4.2 MD trajectory of compound (Z)-27h

The hydrophilic side chain of the ligand left the catalytic tunnel and relocated to a nearby binding site from 1.6 ns simulation. The distance between the warhead electrophilic carbon and CYS277 sulphur atom was the lowest at the first frame of the simulation (3.8 Å) and increased dramatically in later frames (Figure 5.23). The ligand side chain was significantly mobile at the new binding site and that pulled the naphthalene ring out of the hydrophobic pocket. The ligand left the catalytic binding site since 17.3 ns simulation. The transient stability of the warhead in the catalytic tunnel in combination with the high distance between the warhead electrophilic carbon and the sulphur atom of CYS277 suggested a possibly low affinity and a low potency against TG2 of this compound.

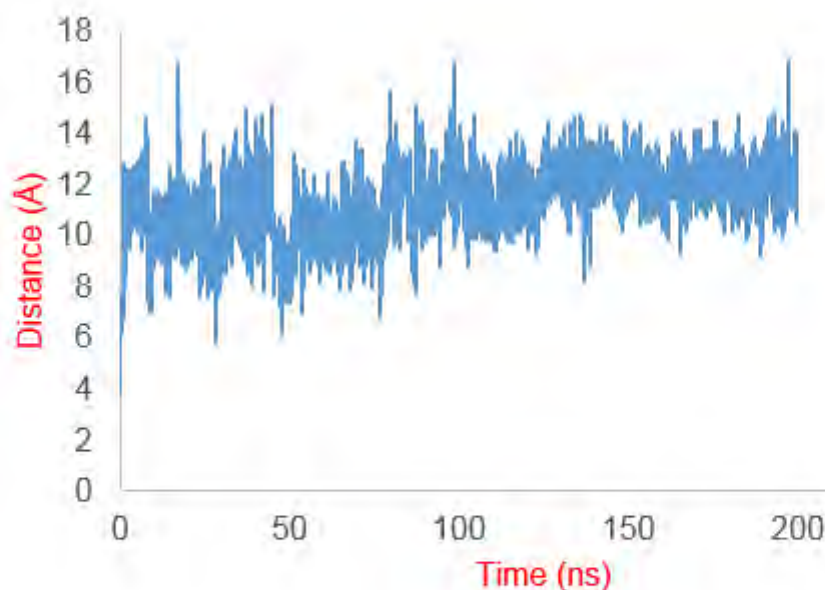


Figure 5.23. The distance between the warhead electrophilic carbon of compound (Z)-27h and CYS277 sulphur atom during 200 ns MD simulation.

5.5 MD trajectories of compounds with a more rigid side chain modified from compound 26

5.5.1 MD trajectory of compound 26a

The warhead stayed inside the catalytic tunnel for 17.3 ns simulation. During that period, the acrylamide carbonyl formed hydrogen bonds with the backbone amino of two residues ASN333 and PHE334 (Figure 5.24). It can be seen that the distance between ASN333 backbone NH (H atom) and the ligand acrylamide CO (O48) was mostly lower than 3.0 Å. That indicated a strong and stable hydrogen bond between the ligand warhead and ASN333. This bond may be the most important interaction in restraining the warhead. Additionally, the distance between H atom (backbone NH) of PHE334 and O atom of the ligand acrylamide fluctuated around 3.0 Å during the period the warhead was maintained in the catalytic tunnel. That indicated the vital role of this hydrogen bond in contribution of to the stability of the warhead into the catalytic tunnel.

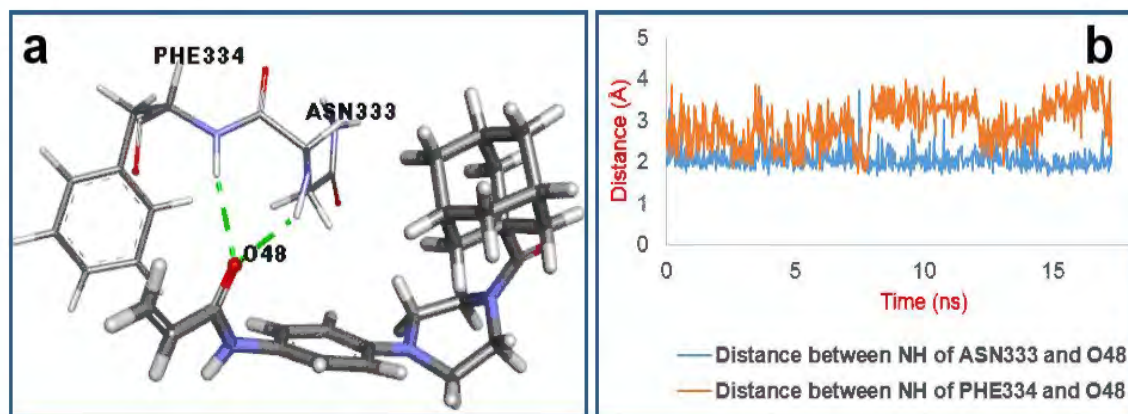


Figure 5.24. Hydrogen bonds between compound **26a** and two residues ASN333 and PHE334 (a) and distances of the related atoms during the first 17.3 ns MD simulation.

The hydrophilic side chain of the ligand was significantly mobile when it left the tunnel and was settled down at the other binding site from 93.1 ns. The ligand adamantyl ring was spinning around but was maintained inside the hydrophilic pocket till the end of the simulation time. The positions of the ligand in the first and the last frame of 200 ns MD simulation were displayed in Figure 5.25.

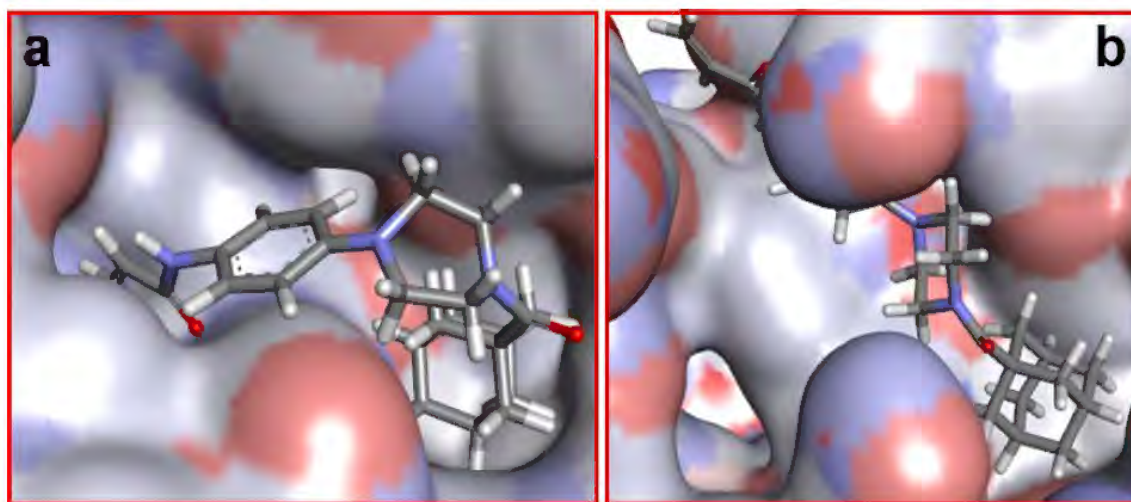


Figure 5.25. Positions of compound **26a** in the first (a) and the last frame (b) of 200 ns MD simulation.

During the period the warhead was held into the catalytic tunnel, the distance between the warhead electrophilic carbon and CYS277 sulphur atom mainly fluctuated between 3.1 and 4.0 Å in the first 7.9 ns (Figure 5.26). That indicated the possibility of potent inhibition of this compound against TG2.

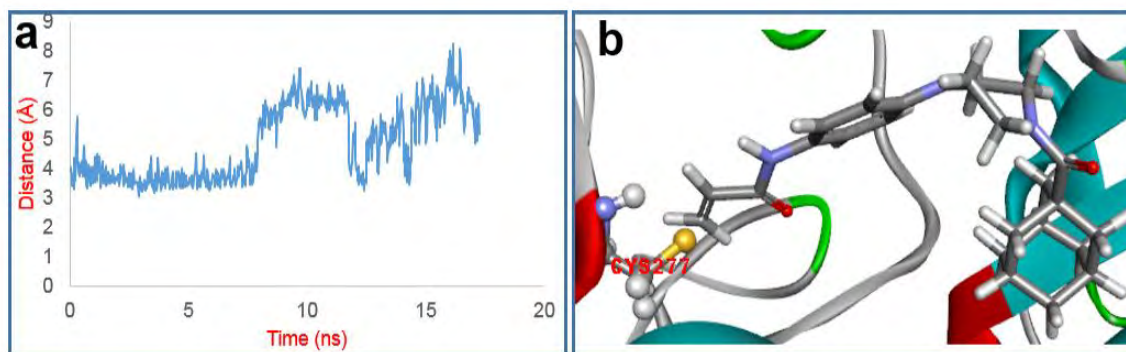


Figure 5.26. The distance between the warhead electrophilic carbon of compound **26a** and CYS277 sulphur atom during the first 17.3 ns MD simulation (a) and the position of this compound when the distance was the shortest (b).

5.5.2 MD trajectory of compound (Z)-26b

The warhead was retained in the catalytic tunnel for 9.4 ns simulation. During that period, the ligand hydrophilic side chain formed hydrogen bonds with three nearby residues including GLN276, TRP278 and PHE334. It can be seen from Figure 5.27 that the distances between the O atom of PHE344 backbone CO and the H atom of the ligand NH acrylamide and between the H atom of GLN276 side chain NH and O atom of the ligand carboxylate CO oscillated around 2.0 Å. The distances between the H atom of TRP278 backbone NH and the O atom of the ligand carboxylate and between H atom of GLN276 side chain NH and the O atom the ligand acrylamide carbonyl were mainly less than 3.0 Å. That distances pointed out that the ligand side chain was held firmly by the strong and stable hydrogen bonds during the period the warhead was retained in the catalytic tunnel. During this time, the adamantyl ring was held inside the hydrophobic pocket by hydrophobic interactions with nearby residues.

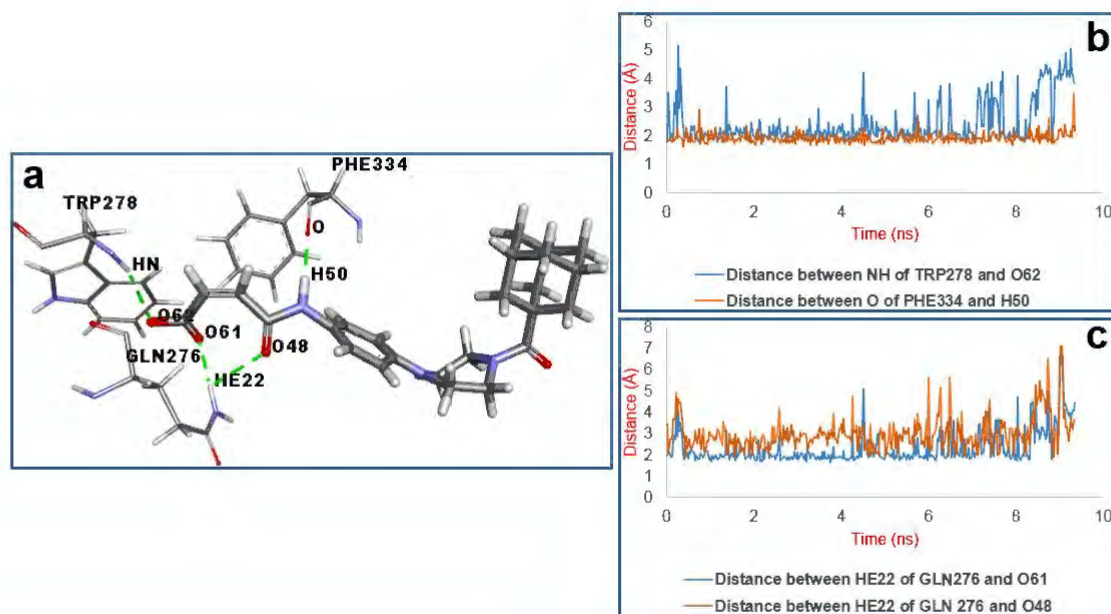


Figure 5.27. Hydrogen bonds between compound (Z)-**26b** and three residues GLN276, TRP278 and PHE334 (a) and distances of the relevant atoms during the first 9.4 ns of the MD simulation.

During the period the warhead was held into the catalytic tunnel, the distance between the warhead electrophilic carbon and CYS277 sulphur atom mainly fluctuated around 4.0 Å (Figure 5.28). The shortest distance was 3.4 Å. After leaving the catalytic tunnel, the warhead became noticeably mobile whilst the adamantyl ring was still retained in the hydrophobic pocket. Therefore, the distance between the warhead electrophilic carbon and CYS277 sulphur was also increased remarkably to nearly 30.0 Å.

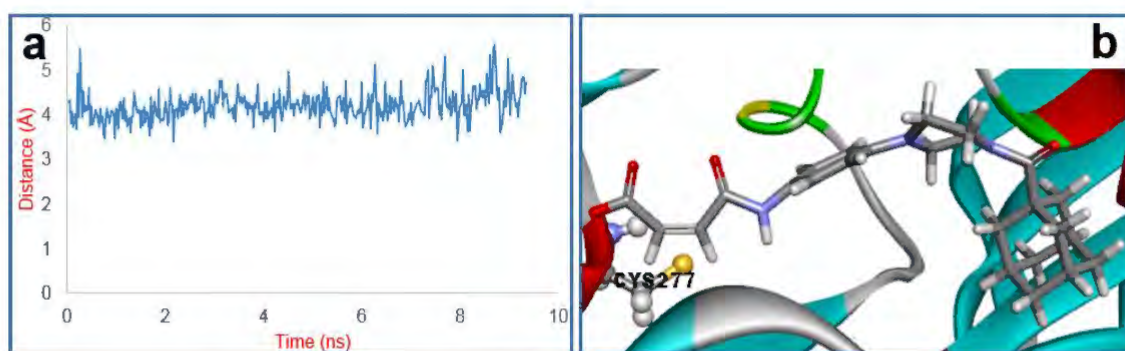


Figure 5.28. The distance between the warhead electrophilic carbon of compound (Z)-**26b** and CYS277 sulphur atom during the first 9.4 ns MD simulation (a) and the position of this compound when the distance was the shortest (b).

5.6 MD trajectories the rhodanine derivatives

5.6.1 MD trajectory of compound 40a

At the first frame of MD simulation, the ligand acrylamide carbonyl formed a hydrogen bond with the backbone amino of ASN333 (Figure 5.29a). As soon as the simulation started, the naphthalene ring moved toward the hydrophobic pocket and was held there by hydrophobic interactions with nearby residues. The warhead was pulled off the catalytic tunnel and was relocated to the outside of the tunnel due to the movement of the naphthalene ring. Therefore, the distance between the warhead electrophilic carbon and CYS277 sulphur atom was dramatically increased and fluctuated around 10.0 Å. At the new position, the acrylamide carbonyl continued forming the hydrogen bond with ASN333 backbone amino group (Figure 5.29).

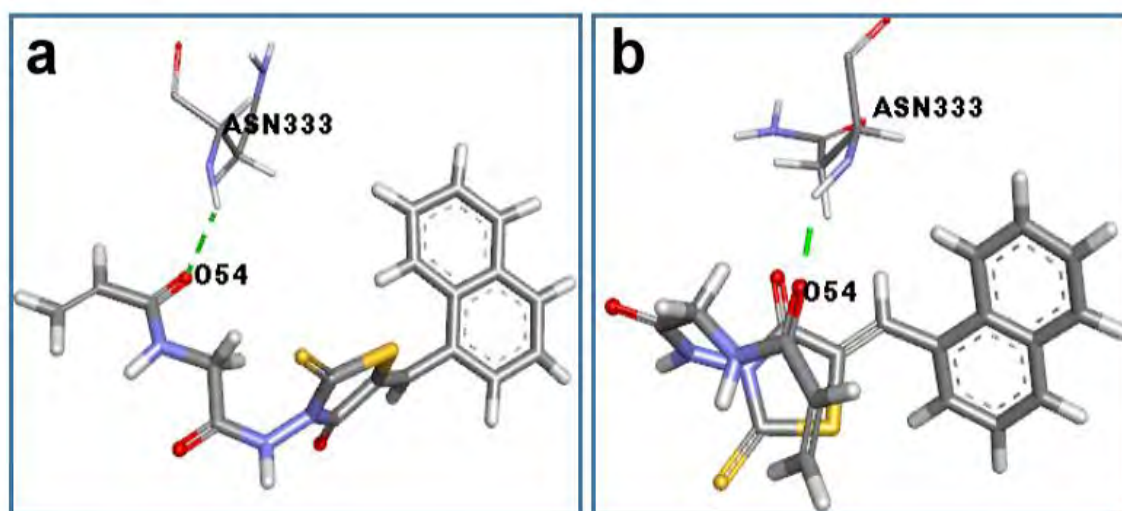


Figure 5.29. The hydrogen bond between compound **40a** and residue ASN333 when the ligand warhead was held in the catalytic tunnel (a) and when it relocated to the outside of the tunnel (b).

The warhead turned back to the catalytic tunnel from 108.6 ns simulation and was maintained there for only 0.4 ns. During this transient period, the distance between the warhead electrophilic carbon and the sulphur atom of CYS277 reached to 3.7 Å (Figure 5.30). The short distance occurred between these two reactive atoms suggested a possibly potent attack of the ligand warhead to the nucleophilic cysteine CYS277. The ligand long scaffold then left the catalytic tunnel and became significantly mobile. That pulled the naphthalene ring off the hydrophobic pocket from 119.4 ns. The movement

of the ligand is indicated by its RMSD values as given in Figure 5.30. The hydrogen bond with ASN333 disappeared and the whole molecule then left the binding site. It can be seen from Figure 5.30 that the distance between the H atom of ASN333 backbone amino and the O atom of the ligand acrylamide carbonyl was mostly less than 3.0 Å before the ligand left the binding site. The data indicated the strong and stable hydrogen between them and that may be the vital interaction to keep the ligand in the catalytic binding site although the warhead was located outside the catalytic tunnel.

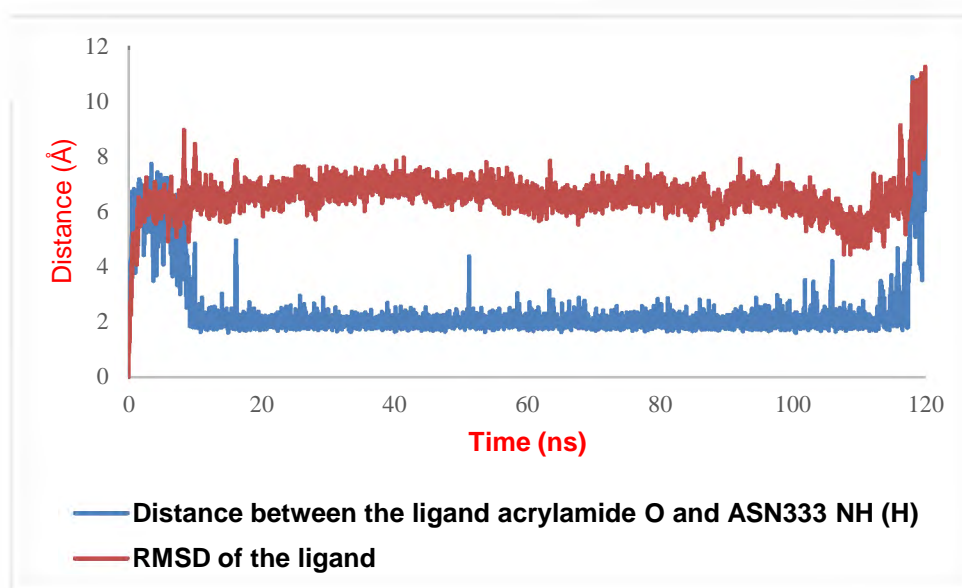


Figure 5.30. RMSD values of compound **40a**, the distance between the O carbonyl warhead and the H amine backbone of ASN333 and the distance between the warhead electrophilic carbon and CYS277 sulphur atom during 120 ns MD simulation.

5.6.2 MD trajectory of compound 40b

Very early since the simulation started, the naphthalene ring left the hydrophobic pocket and became remarkably mobile. However, pi-pi stacked interactions were always existed between the naphthalene and two residues TRP241 and TRP332, which reside opposite the catalytic tunnel (Figure 5.31). These interactions were vital in restraining the ligand lipophilic part and consequently contributed to the stability of the whole molecule during the simulation.

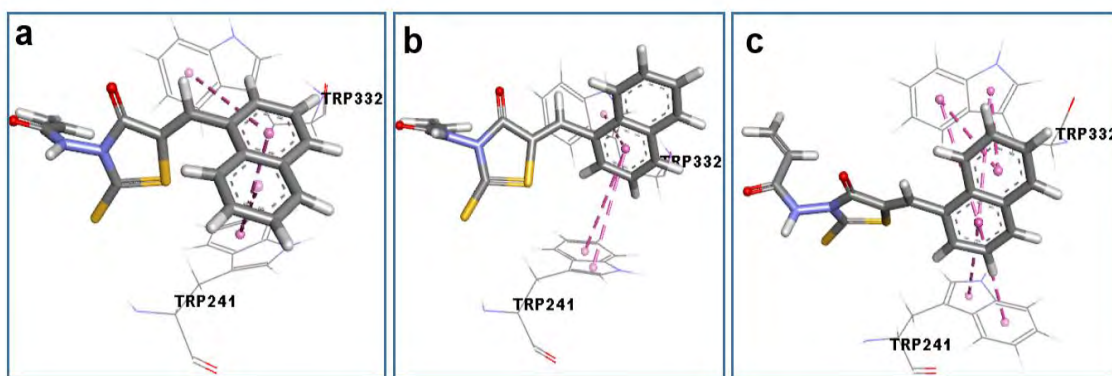


Figure 5.31. Pi-pi stacked interactions between the naphthalene ring of compound **40b** and two residues TRP241 and TRP332 during 200 ns MD simulation.

Whilst the ligand lipophilic part was oscillating, the warhead was retained in the catalytic tunnel. A hydrogen bond between the ligand acrylamide carbonyl and the side chain amino of residue ASN229 was observed to be maintained during the simulation time. It can be seen from Figure 5.32a,b that the distance between O atom of the ligand acrylamide carbonyl and H atom of the ASN229 side chain amino fluctuated mostly less than 3.0 Å during the simulation. Additionally, another hydrogen was created between the ligand sulphur (C=S) and the backbone NH of ARG240 with the distance between the relevant atoms fluctuating around 3.0 Å as shown in Figure 5.32a,c. It indicates that these hydrogen bonds are possibly the important interactions in restraining the scaffold and accordingly in holding the warhead inside the catalytic tunnel.

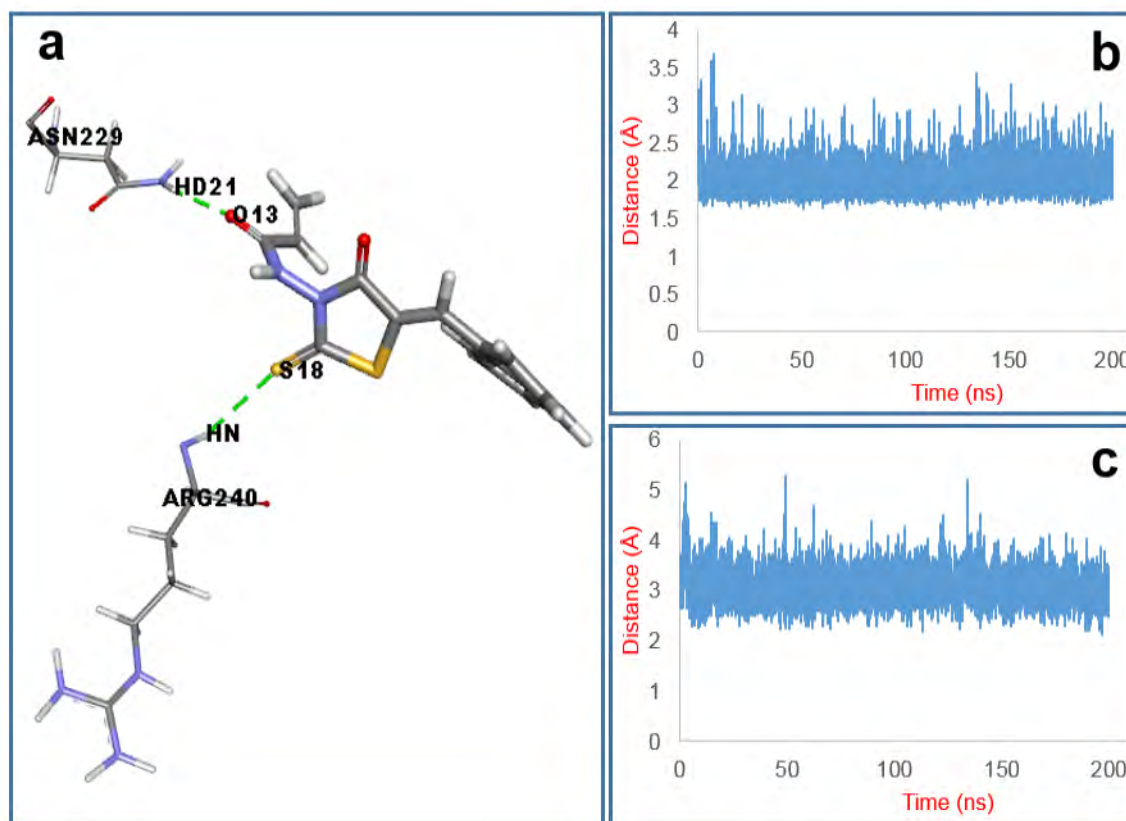


Figure 5.32. Hydrogen bonds between compound **40b** and two residues ASN229 and ARG240 (a), the distance between H atom of ASN229 side chain amino and the O atom of the ligand acrylamide carbonyl (b) and the distance between the H atom of ARG240 backbone amino and the ligand sulphur (C=S) during 200 ns MD simulation.

The warhead was retained in the catalytic tunnel for all the simulation time. Therefore, the distance between the warhead electrophilic carbon and the nucleophilic sulphur of CYS277 oscillated mostly less than 6.5 Å as shown in Figure 5.33. The shortest distance was 3.4 Å. The stable binding of the ligand in the catalytic site and the short distances between the warhead electrophilic carbon and CYS277 sulphur atom indicate compound **40b** is possibly a potent inhibitor of TG2.

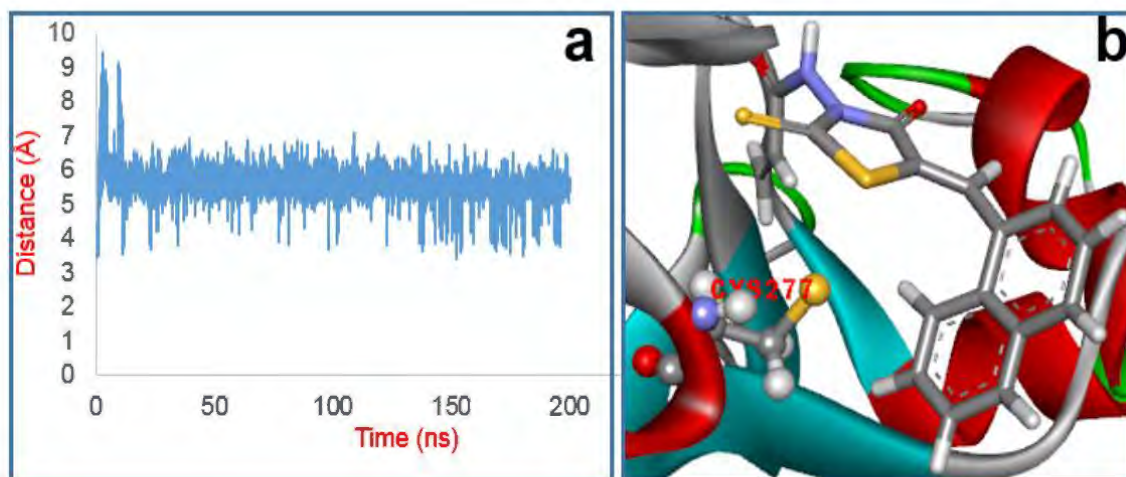


Figure 5.33. The distance between the warhead electrophilic carbon of compound **40b** and CYS277 sulphur atom (a) and the position of this compound at the shortest distance (b).

5.7 MD trajectories of 1,2,4-triazole derivatives

5.7.1 MD trajectory of compound **41b**

At the beginning of the simulation, different from the compounds with the naphthalenyl or adamantyl ring, the pyridine ring of compound **41b** was located just outside the catalytic tunnel (Figure 5.34a). Hydrogen bonds were formed between the acrylamide warhead and the side chains of two residues GLN276 and CYS277. In addition, the pi-pi stacked interactions were generated between the phenyl and the triazole ring of the ligand and the side chain indoles of two residues TRP241 and TRP332. The pyridine ring only had a pi-alkyl interaction with ARG317. These interactions are displayed in Figure 5.34b.

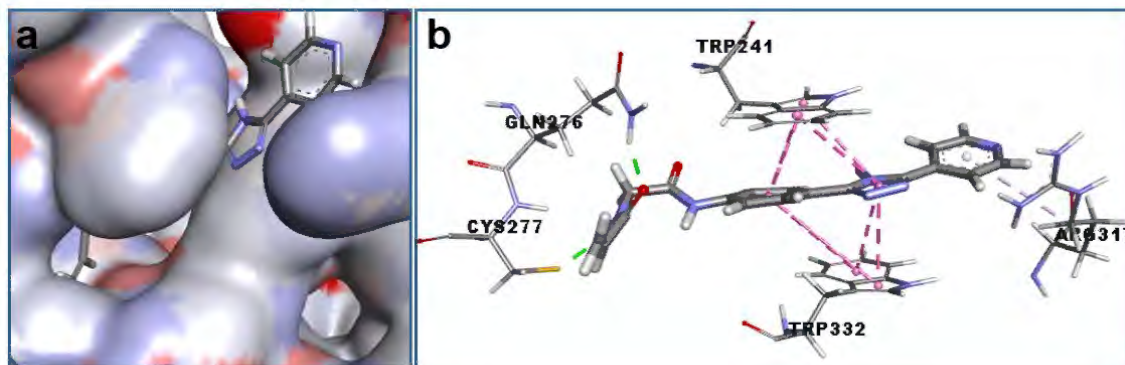


Figure 5.34. The position of compound **41b** (a) and interactions between this compound and the protein (b) in the first frame of the MD simulation.

The warhead left the catalytic tunnel from 18.5 ns simulation and very soon after that the whole molecule also moved out of the catalytic binding site. The hydrogen bonds between the ligand warhead and the side chains of GLN276 and CYS277 also disappeared since then. It can be seen from Figure 5.35 that the distances between the relevant atoms of these hydrogen bonds especially the distance between the sulphur atom of CYS277 and the H acrylamide amino of the ligand mostly fluctuated less than 3.0 Å and then increased dramatically after 18.5 ns. It was also observed that the phenyl and triazole ring of the ligand were always clamped between two residues TRP241 and TRP332 during the first 18.5 ns simulation. That indicated the importance of the hydrogen bonds and the pi-pi interactions in contribution of the stability of the warhead inside the catalytic tunnel.

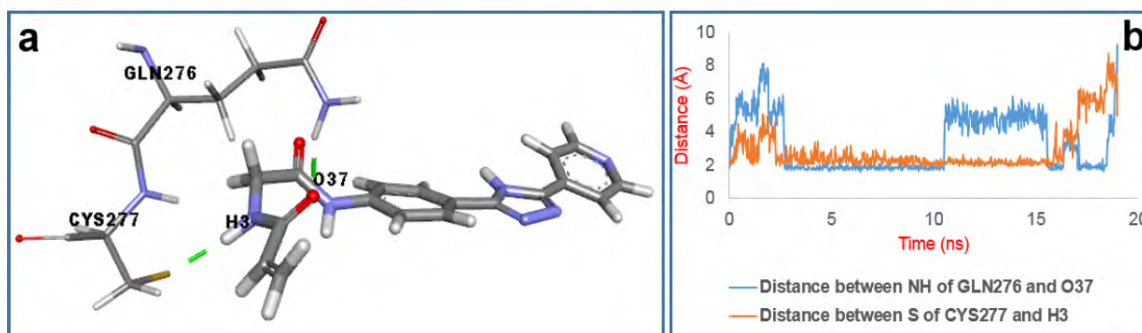


Figure 5.35. Hydrogen bonds between compound **41b** and two residues GLN276 and CYS277 (a) and distances of these bonds during 19.0 ns MD simulation.

During the period the warhead was held in the catalytic tunnel, the distance between the electrophilic carbon and CYS277 sulphur atom mainly fluctuated less than 5.0 Å (Figure 5.36). The distance reached to 3.2 Å when the warhead nearly left the tunnel.

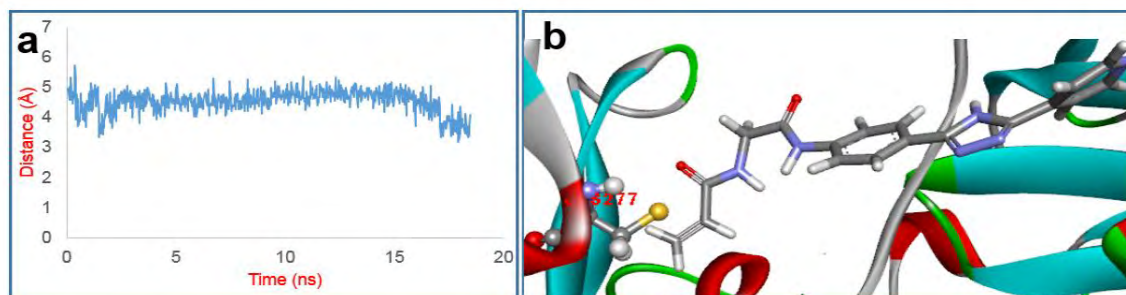


Figure 5.36. The distance between the warhead electrophilic carbon of compound **41b** and CYS277 sulphur atom during the first 18.5 ns MD simulation (a) and the position of this compound at the shortest distance (b).

5.7.2 MD trajectory of compound 41a

Similar to compound **41b**, the acrylamide warhead was located in the catalytic tunnel but the pyridine ring of compound **41a** was not docked into the hydrophobic pocket. After around 0.5 ns simulation, the acrylamide warhead left the catalytic tunnel and moved away from CYS277. The distance between the warhead electrophilic carbon and CYS277 sulphur atom then started to increase to more than 17.0 Å. After 10.5 ns simulation, the warhead turned back to the original position and stayed there for 7.5 ns. After that, the warhead left the tunnel again and relocated to another binding site. Therefore, the distance between the warhead electrophilic carbon and CYS277 sulphur atom increased again. The ligand RMSD values are consistent with the distance between the warhead electrophilic carbon and CYS277 sulphur atom Figure 5.37a. During that period the warhead was maintained into the catalytic tunnel, the distance between the warhead electrophilic carbon and CYS277 sulphur atom fluctuated around 8.0 Å as shown in Figure 5.37b. The shortest distance was 4.7 Å.

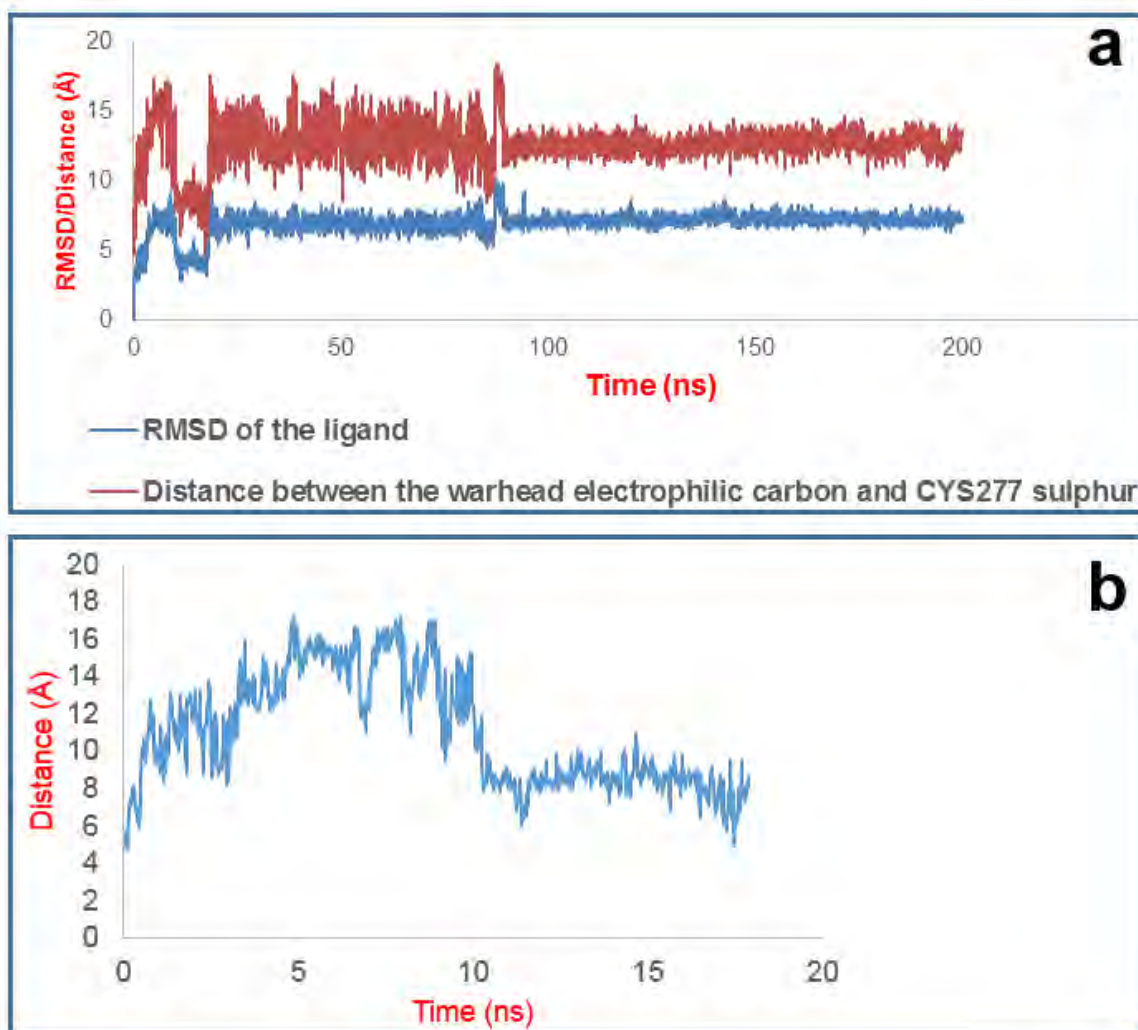


Figure 5.37. (a) RMSD values of compound **41a** and the distance between the warhead electrophilic carbon and CYS277 sulphur atom during 200 ns MD simulation; (b) The distance between the warhead electrophilic carbon and CYS277 sulphur atom during the first 17.9 ns MD simulation.

During the period the warhead stayed inside the catalytic tunnel, a hydrogen bond was induced between the ligand acrylamide NH and the side chain CO of residue GLN276. It can be seen from Figure 5.38 that the distance between the relevant atoms still fluctuated a large range in the period the warhead turned back to the catalytic tunnel. It suggested a weak hydrogen bond between the ligand and GLN276. The instability of the warhead in the catalytic tunnel and the high distance between the warhead electrophilic carbon and the sulphur atom of CYS277 predicted a lower affinity followed by a low inhibitory effect of this compound.

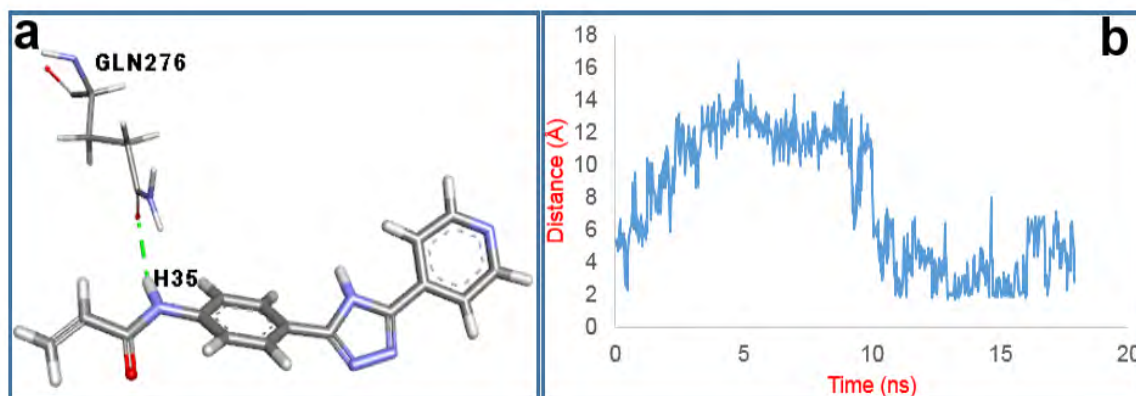


Figure 5.38. A hydrogen bond between compound **41a** and GLN276 (a) and the distance between H atom of the ligand acrylamide NH and the O atom of the side chain CO of GLN276 (b) in the first 17.9 ns MD simulation.

5.8 Conclusion

The modification of the acrylamide warhead of the lead compound **27** to the propynamide warhead provided compound **27a** having high stability in the catalytic binding site and the short distance between the electrophilic warhead carbon and CYS277 sulphur atom. This predicts a high affinity of this ligand and possibly a higher potency than the parent compound whose warhead was observed to only bind in the catalytic tunnel for a transient period.

The attachment of a carboxyl group or a methoxyl group at *trans*-position of the acrylamide warhead of the lead compound ((*E*)-isomers of compounds **27b** and **27c**) were observed to significantly reduce the stability of the warhead in the catalytic tunnel and also lengthening the distance between the warhead electrophilic carbon and the sulphur atom of CYS277. Except for the (*Z*)-isomer of compound **27b**, the compounds with the maleic form of warhead were all predicted to have low inhibition effects owing to the transient binding of their warheads into the catalytic tunnel together with the long distances between the warhead electrophilic carbon and the nucleophilic sulphur.

The alteration of the side chain that connects the piperazine ring and the warhead to a shorter side chain (compound **27e**) did not help to shorten the distance between the warhead electrophilic carbon and CYS277 sulphur atom. However, under the binding of this ligand in the catalytic binding site, the distance between the warhead electrophilic carbon and sulphur atom of CYS336, another cystein residue located in the catalytic

tunnel was decreased. This indicates a possible Micheal reaction between this ligand and CYS336 instead of with CYS277.

The modification of the aliphatic side chain to a more rigid structure by the attachment of a phenyl ring between the piperazine ring and the warhead (compound **26a** and **27g**) significantly improved the stability of the warhead in the catalytic tunnel and also shortened the distance between the warhead electrophilic carbon and CYS277 sulphur atom.

The alteration of the piperazine ring of the parent compound to the 3-amino rhodanine ring (compound **40a**) did not either improve the compound's stability in the catalytic binding site or reduce the distance between the warhead electrophilic carbon and CYS277 sulphur atom. However, the better stability in the catalytic tunnel of the warhead and the shorter distance between the warhead electrophilic carbon and CYS277 sulphur atom were observed in the MD simulation of compound **40b**, a derivative of compound **40a** but having a shorter side chain.

In contrast to the naphthalene or adamantyl ring, the pyridine ring of compound **41a** and **41b** was located outside the hydrophobic pocket. The warhead of compound **41b** is predicted to have a high affinity in the catalytic tunnel due to its stability during the MD simulation. Additionally, the short distance between the warhead electrophilic carbon and CYS277 sulphur atom was recorded. These indicate a possible high potency of this compound. The derivative with a shorter side chain (compound **41a**), however, did not show any sign in the possible improvement of the affinity and the potency.

6 Synthesis of potential irreversible inhibitors of TG2

In chapter 5, a large range of potential irreversible inhibitors was designed by modification various parts of the lead irreversible inhibitor, compound 27. This chapter focused on the preparation of the designed compounds and some additional derivatives whose structures are given in Table 6.1.

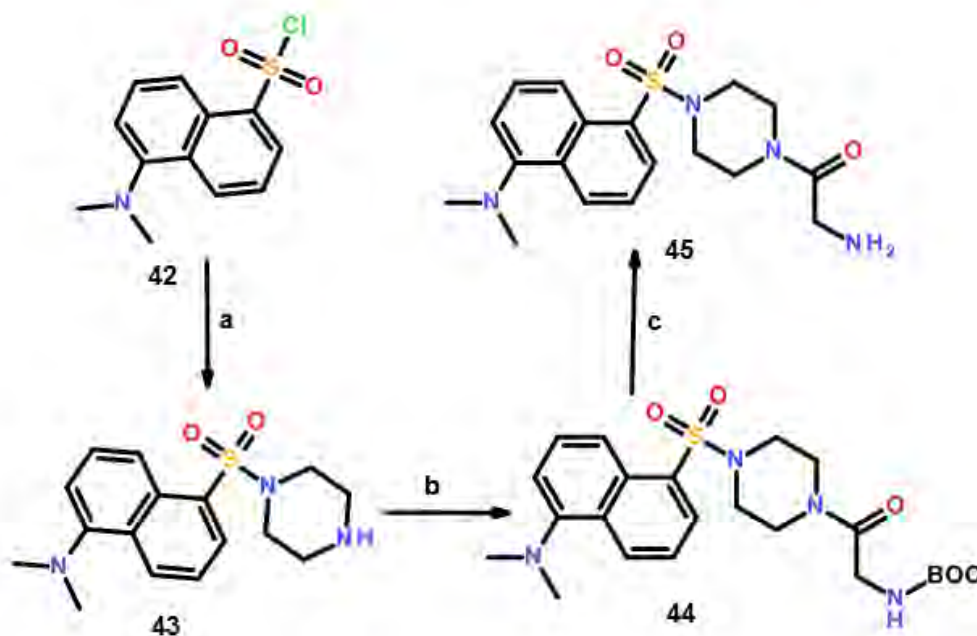
Table 6.1. The target potential irreversible inhibitors attempted to synthesise.

Name	R	X
27a		
(E)-27b		
(Z)-27b		
(E)-27c		
27e		
(Z)-27f		
(E)-27f		
40a		
40b		
40c		
41a		
41b		
41c		
41d		
41e		

6.1 Synthesis of the compounds modified from compound 27

6.1.1 Preparation of the scaffold of compound 27

The scaffold of compound **27** was prepared using the method which is given in Scheme 6.1. Following the published method (Sashuk et al., 2009), a solution of dansyl chloride (compound **42**) in dry DCM was treated with the excess amount of piperazine in dry DCM under argon to give N,N-dimethyl-5-piperazin-1-ylsulfonyl-naphthalen-1-amine (compound **43**) as a light green solid in an excellent yield (93%). Coupling amine **43** with BOC-Gly-OH using the equivalent of coupling reagent EDC in the presence of HOBt and DIPEA based on the literature (Griffin et al., 2014) provided a crude product that needed flash column chromatography to give the pure desired compound **44** in 70% yield. When changing EDC to CDI, the reaction gave the isolated carbamate **44** in a higher yield (94%) without needing purification by flash column chromatography. The BOC group was detached by treatment of the carbamate **44** with excess TFA in DCM based on the literature (Griffin et al., 2014) to give the desired amine **45** with good yield (81%).

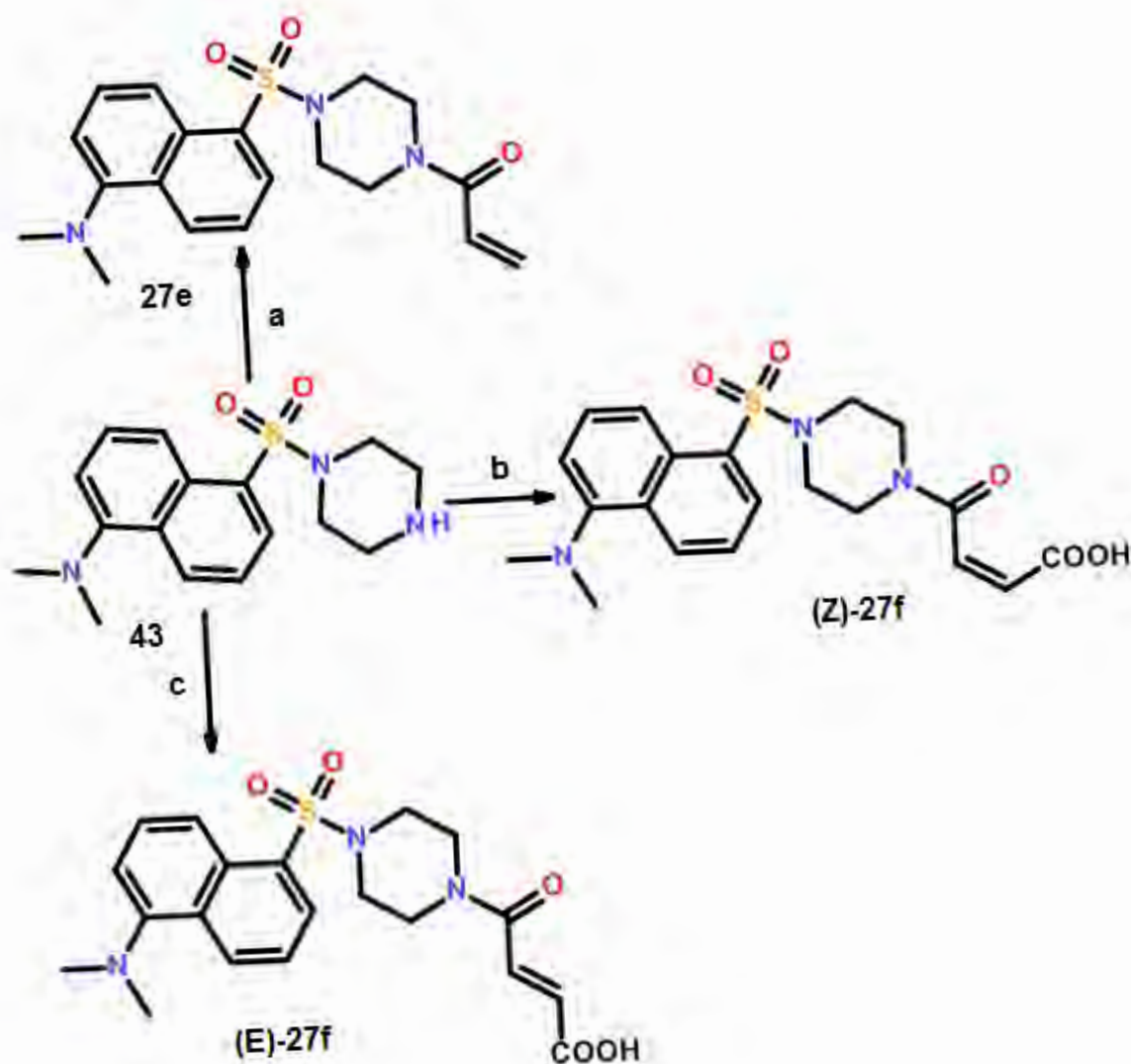


Scheme 6.1. Synthesis of the scaffold of compound **27**.

(a) Piperazine / dry DCM, rt (20 °C), 45 min; (b) Method 1: BOC-Gly-OH, EDC, HOBt / dry DCM, rt, under argon, 24 hours; Method 2: BOC-Gly-OH, CDI / dry DCM, rt, under argon, 20 hours; (c) TFA / DCM, rt, 3 hours.

6.1.2 Synthesis of compounds with a shorter side chain

In order to synthesise the potential irreversible inhibitors with a shorter side chain modified from compound **27** (compound **27e,f**), amine **43** was used as the scaffold to attach the warheads (Scheme 6.2). Acryloylation of amine **43** with 2 equivalents of acryloyl chloride in the presence of DIPEA in dry DCM gave the desired acrylamide **27e** in 70% yield. Treatment amine **43** with the equivalent of maleic anhydride in DCM at room temperature (20 °C) gave exclusively (Z)-isomer **27f** in 70% yield. That was indicated by the coupling constant for the alkene protons ($J = 12.5$ Hz). In an attempt to synthesise the (E)-isomer of **27f**, the reaction of **43** with maleic anhydride was carried out at reflux based on a published method (Banik and Becker, 2001). However, it failed to provide the desired compound. Attempted isomerisation the (Z)-isomer **27f** with iodine in chloroform at reflux based on another published reaction (Gaukroger et al., 2001) also failed to transform the (Z)-isomer to the corresponding (E)-isomer. Heating the (Z)-isomer in chloroform at reflux using bisacetonitrile dichloro-palladium II as the catalyst based on a publish from the literature (Yu et al., 2002) also did not succeed in achieving the desired (E)-isomer.



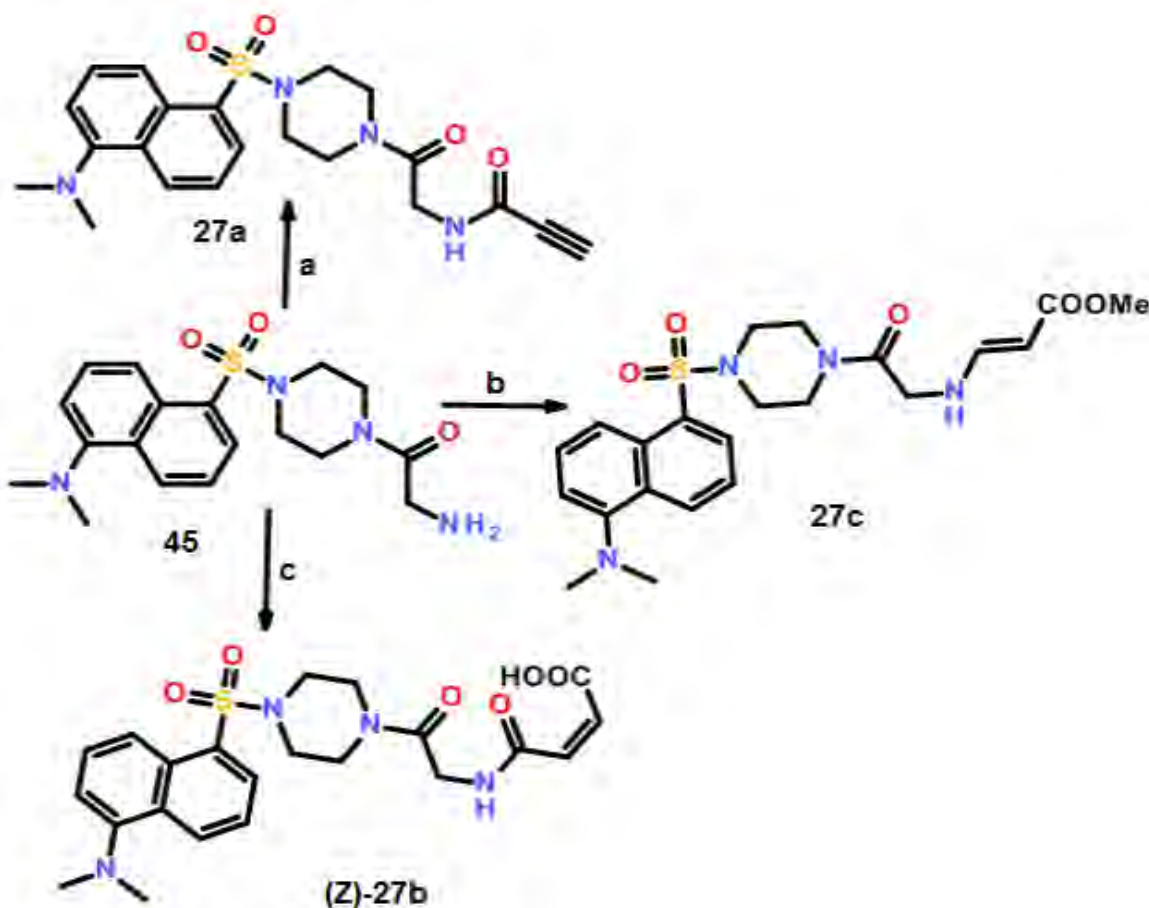
Scheme 6.2. Attachment of acrylamide and 4-amino-4-oxo-2-butenic acid warheads on the short amine **43**.

(a) Acryloyl chloride, DIPEA / dry DCM, under argon, 0 °C, 3 hours; (b) Maleic anhydride / DCM, rt (20 °C), 24 hours; (c) Maleic anhydride / chloroform, reflux, 5 hours.

6.1.3 Modification of the acrylamide warhead of compound **27**

Various attempts were made to modify the acrylamide warhead of the lead irreversible inhibitor as given in Scheme 6.3. In the first attempt to synthesise compound **27a**, compound **45** was coupled with propionic acid with the equivalent of EDC in the presence of HOBt and DIPEA. However, it failed to provide the desired product but instead giving a polymerised mixture. EDC was changed to a more reactive coupling reagent, ethylchloroformate. Nonetheless, this could not prevent the unwanted

polymerisation. Treatment of compound **45** with the equivalent of maleic anhydride in DCM at room temperature gave exclusively the desired (*Z*)-isomer **27b** in 72% yield. An attempted preparation of (*E*)-**27c** by stirring a solution of the amine **45** and the equivalent of methyl propiolate in DCM at room temperature (20 °C) was carried out. However, after 24 hours, the reaction did not occur.

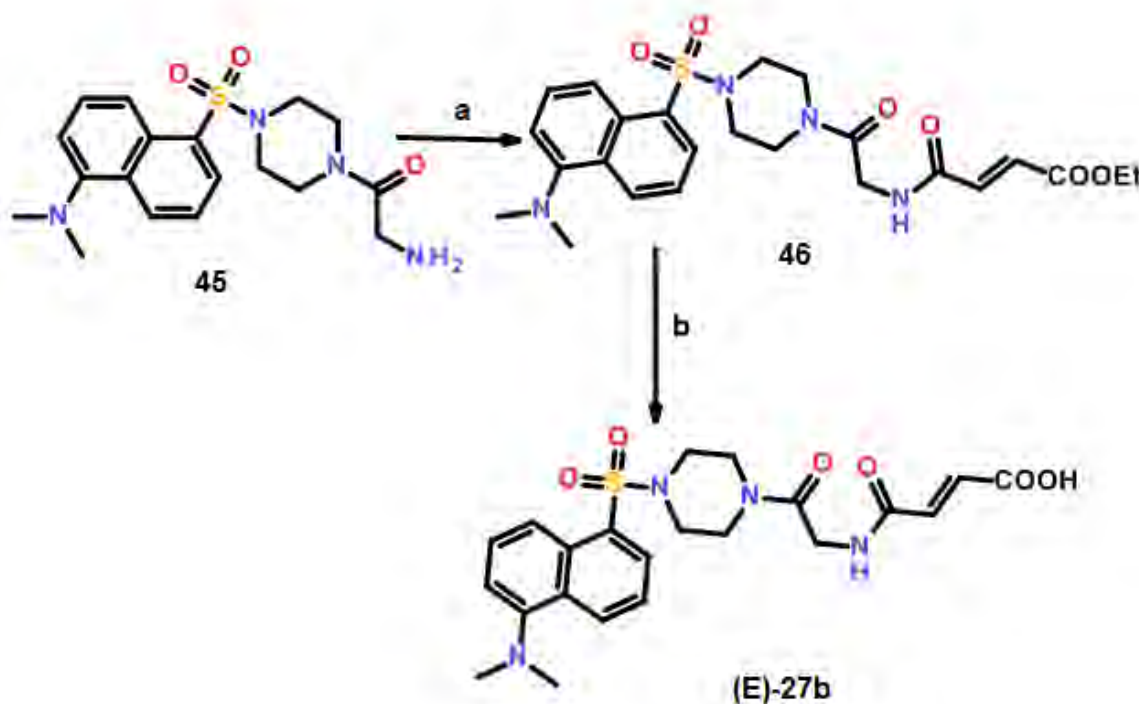


Scheme 6.3. Attachment of various electrophilic warheads on the the scaffold of compound **27**.

(a) Attempt 1: Propiolic acid, EDC, HOBT, DIPEA / dry DCM, 0 °C, under argon, 6 hours; Attempt 2: Propiolic acid, ethylchlorformate, DIPEA / dry THF, 0 °C, under argon, 3 hours; (b) Methyl propiolate / DCM, rt (20 °C), 24 hours; (c) Maleic anhydride / DCM, rt (20 °C), 20 hours.

In an attempt to transform the (*Z*)-isomer **27b** to the corresponding (*E*)-isomer, a method of 2 reactions was carried out as given in Scheme 6.4. Firstly, compound **45** was treated with ethyl fumaroyl chloride (1.1 eq) in the presence of DIPEA in dry THF at 0 °C under argon. The desired ester **46** was accomplished in 74% yield that was

hydrolysed with excess aqueous sodium hydroxide in THF / MeOH. Unfortunately, the resulting acid could not be isolated when using ion exchange resin (Dowex 50WX8 hydrogen form).

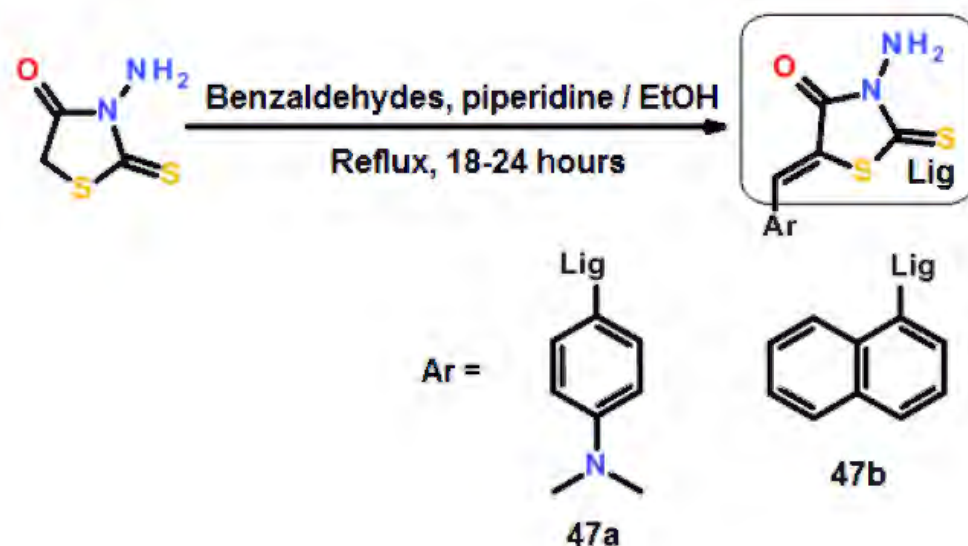


Scheme 6.4. Attempted synthesis of the (E)-isomer of compound **27b**.

(a) Ethyl fumaroyl chloride, DIPEA / dry THF, light was excluded, under argon, 0 °C, 5 hours; (b) NaOH, H₂O / THF, MeOH, rt (20 °C), 3 hours.

6.2 Synthesis of rhodanine derivatives

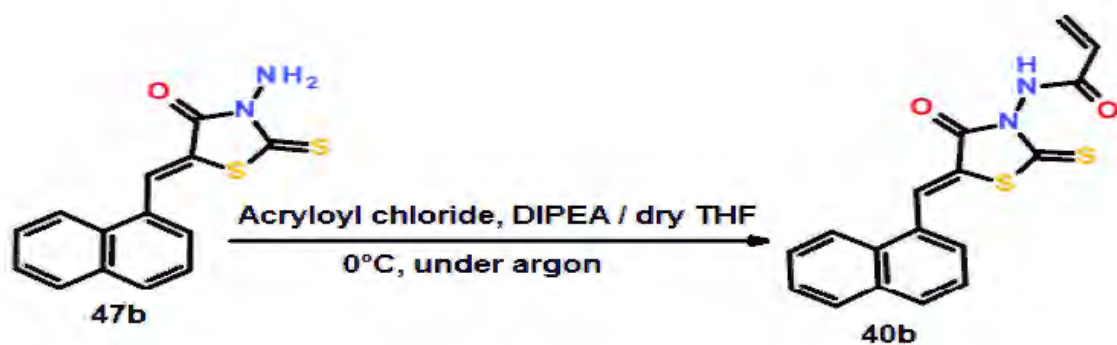
6.2.1 Preparation of the scaffold



Scheme 6.5. Synthesis of 3-amino-5-benzylidenerhodanine derivatives.

Following a method published in the literature (Powers et al., 2006), 3-aminorhodanine was condensed under reflux with a substituted benzaldehyde (1.1 eq) in ethanol in the presence of piperidine to provide the corresponding 3-amino-5-benzylidenerhodanine (Scheme 6.5). After thoroughly washing with ethanol, the desired **47b** was gained in a high yield (71%) whilst the crude **47a** needed to be recrystallised from ethylacetate to give the desired product in 41% yield.

6.2.2 Attachment of the acrylamide warhead

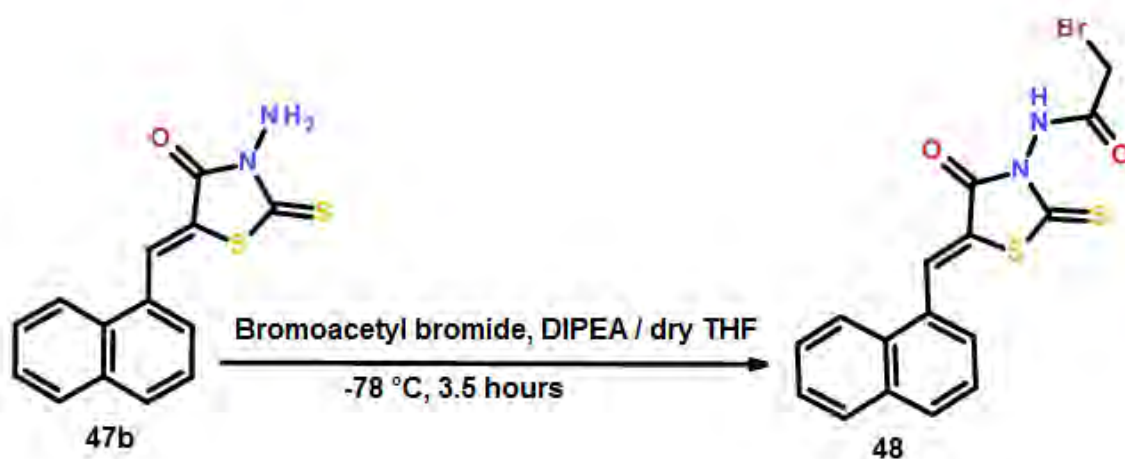


Scheme 6.6. Attempted attachment of the acrylamide warhead on **47b**.

To prepare acrylamide **40b**, amine **47b** was treated dropwise with excess acryloyl chloride in dry THF under argon at 0 °C in the presence of DIPEA. The reaction mixture was then stirred at room temperature (25 °C) for 24 hours. However, a polymerised mixture was formed instead of the desired product. In order to avoid the unwanted polymerised, further attempts were made where the concentration of acryloyl chloride was increased by nearly 4 times, the reaction temperature was reduced to 0 °C and light was excluded. The reaction was monitored by TLC to stop as soon as no starting amine remained in the reaction mixture. Unfortunately, all that attempts failed to stop the unwanted polymerised.

6.2.3 Attachment of the dimethylsulfonium ketone warhead

The failure in the synthesis of compound **40b** due to the unwanted polymerisation led to the attempt to synthesise the sulfonium methyl ketone derivative (compound **40c**) from the amine **47b**. In particular, the amine **47b** was firstly treated with bromoacetyl bromide (1.1 eq) in the presence of DIPEA in dry THF at -78 °C (Scheme 6.7). However, the highly electrophilic 2-bromo amide soon reacted with the nucleophilic amine when it was formed. Therefore, the reaction failed to provide the desired product. In addition, it was indicated that rhodanines are highly toxic on TAMH cells, a metabolically competent rodent liver cell line and HepG2 cells, a model of human hepatocytes (Tang et al., 2015). That led to the stop of the synthesis of the rhodanine derivatives.

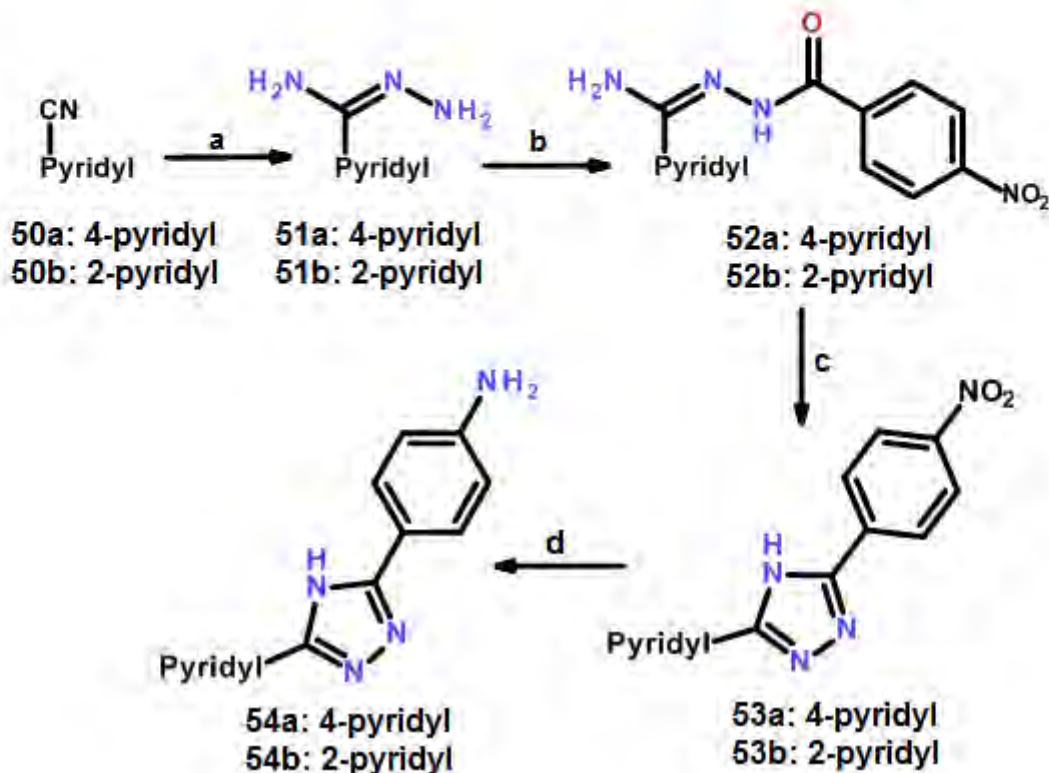


Scheme 6.7. Attempted synthesis of the 2-bromo amide derivative from amine **47b**.

In order to synthesise compound **40a**, compound **47b** were firstly attempted to couple with BOC-Gly-OH. Coupling reagent CDI was firstly used based on a method published in the literature (Nakane et al., 1990) but it failed to activate the carboxylic acid. More reactive coupling reagent, ethyl chloroformate, was applied in the presence of triethylamine (TEA) in dry THF/DMF under argon based on the literature (Kim et al., 1985). However, this method also did not succeed in the synthesis of the expected amide (compound **49**).

6.3 Synthesis of 1,2,4-triazole derivatives

6.3.1 Synthesis of pyridyl triazole scaffolds



Scheme 6.8. Synthesis of pyridyl triazole scaffolds.

(a) Hydrazine monohydrate / EtOH, rt; (b) 4-nitrobenzoic acid, CDI / dry THF, DMF, rt, under argon; (c) ethylene glycol, reflux, 24 hours; (d) ammoniumformate, Pd/C, dry DMF, 65°C, 1 hour.

6.3.1.1 Synthesis of pyridyl carboxamidrazone amides

The synthetic route employed to prepare the potential TG2 irreversible inhibitors containing a pyridyl triazole benzamide scaffold is described in Scheme 6.8. Following the synthetic procedure of the literature (Rathbone et al., 2006), the pyridyl carboxamide compounds (**51a,b**) were prepared by treatment of the cyanopyridines (compound **50a,b**) with excess amount of hydrazine monohydrate in ethanol at room temperature. The 4-pyridyl carboxamidine (**51a**) was isolated in 49% yield whilst the yield of 2-pyridyl carboxamidine (**51b**) was nearly doubled. The synthesised pyridyl carboxamidines (**51a,b**) were then coupled with 4-nitrobenzoic acid using CDI as the coupling reagent in dry THF / DMF under an inert atmosphere at room temperature

following the method reported in a PhD thesis (Gunthey, 2013). The desired pyridyl carboxamidrazone amides (**52a,b**) were produced in moderate yields (53% and 73%).

The ^1H NMR spectra of compounds **52a,b** at room temperature exhibited an extra set of minor peaks in the range of 10.2 – 10.6 ppm alongside the amide peaks and in the range of 7.6 – 8.8 ppm alongside the pyridine ring peaks. However, at the higher temperature (60 °C), the minor peak merged into the corresponding large peak to make a single peak and some doublet peaks also merged into a single one. These can be seen from Figure 6.1 and Figure 6.2. The interconverting keto-enol forms of these compounds as given in Scheme 6.9 are the reason of these observations.

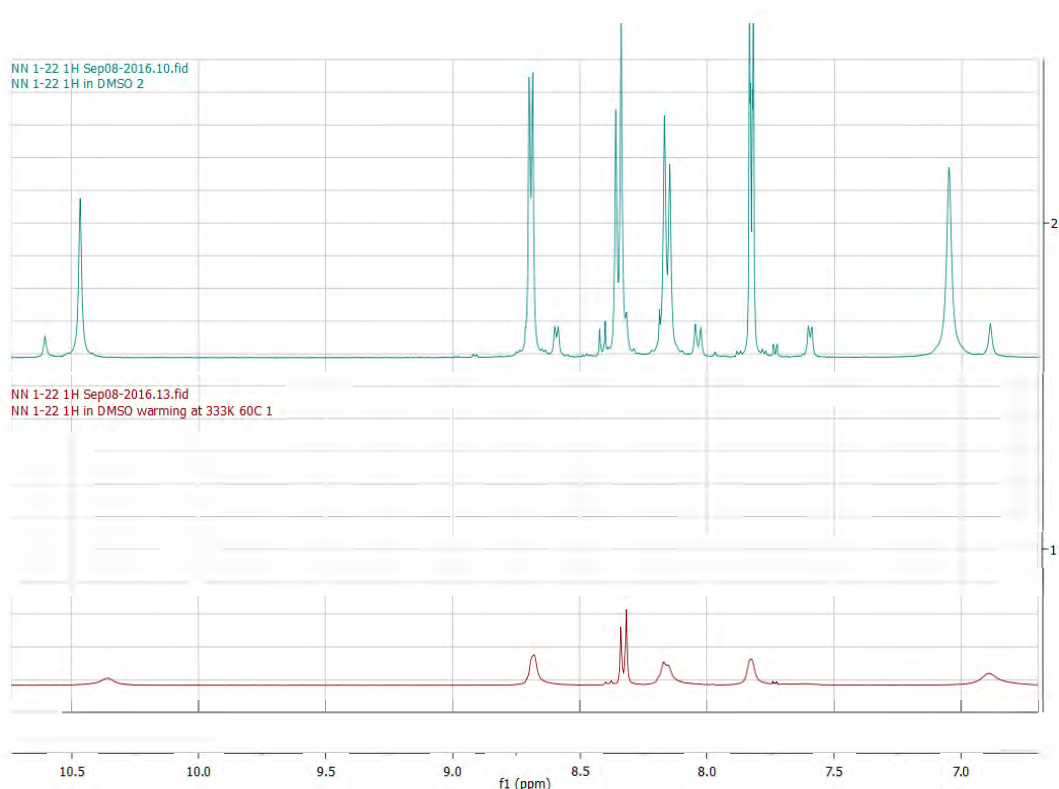


Figure 6.1. ^1H NMR spectra of compound **52a** taken at room temperature (upper) and at 60 °C (lower).

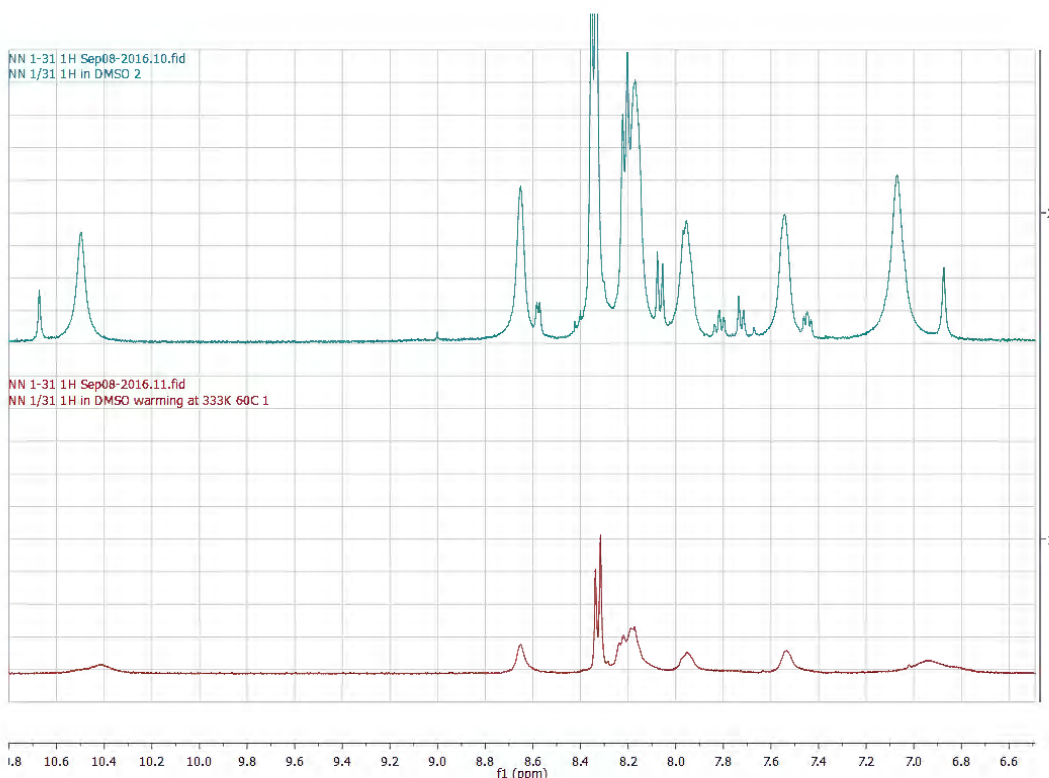
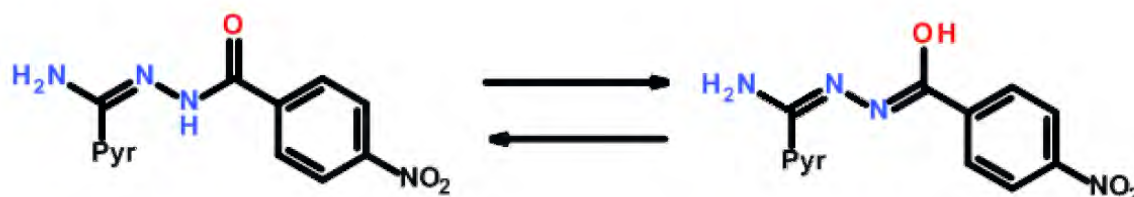


Figure 6.2. ^1H NMR spectra of compound **52b** taken at room temperature (upper) and at 60 °C (lower).



Scheme 6.9. Possible interconverting keto-enol forms of **52a,b**.

6.3.1.2 Cyclisation of the pyridyl carboxamidrazone amides

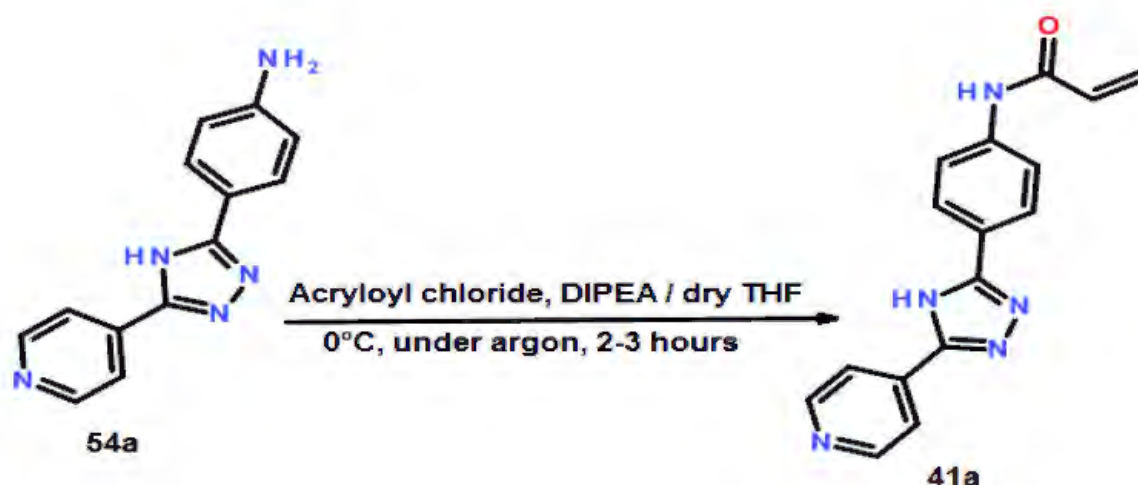
Following the method reported in a PhD thesis (Gunthey, 2013), the synthesised pyridyl carboxamidrazone amides (**52a,b**) were cyclised by heating to reflux in ethylene glycol for 24 hours. The reaction gave the desired 1,2,4-triazole derivatives in high yields (76% for **53a** and 81% for **53b**).

6.3.1.3 Hydrogenation of pyridyl triazolyl 3-nitro phenyl derivatives

The pyridyl triazolyl nitrophenyl derivatives (compound **53a,b**) was hydrogenated before the attachment of the sidechain. According to the literature (Ram and Ehrenkauf, 1988), the use of ammonium formate in catalytic hydrogen transfer reduction of aromatic nitro compounds can selectively and rapidly convert the nitro

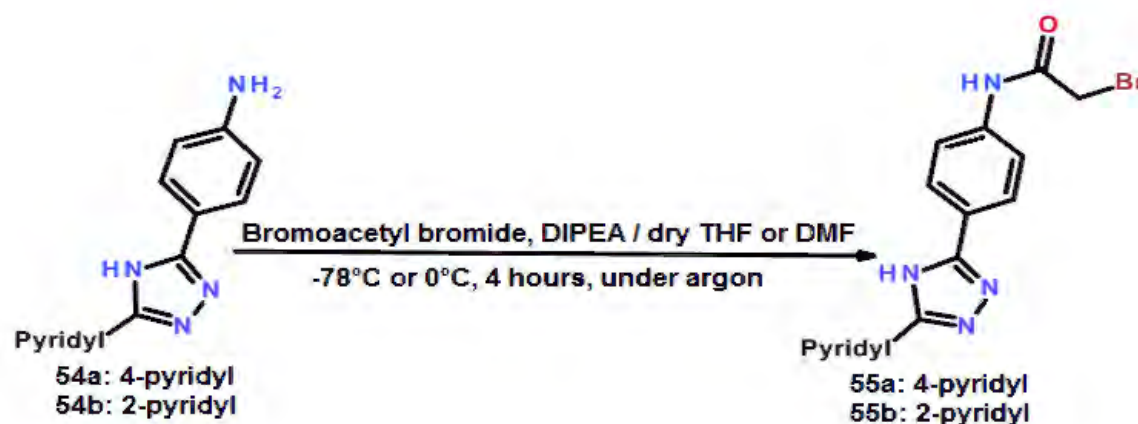
compound into the corresponding amines in high yields. Therefore, the nitrophenyl derivatives (**53a,b**) were hydrolysed by treatment with excess amount of ammonium formate in the presence of 10% Pd/C in dry DMF under argon at 65 °C based on the literature (Shi et al., 2010). The desired anilines (**54a,b**) was accomplished in high yields (81% for **54a** and 89% for **54b**).

6.3.2 Attachment of warheads on the pyridyl triazolyl aniline scaffolds



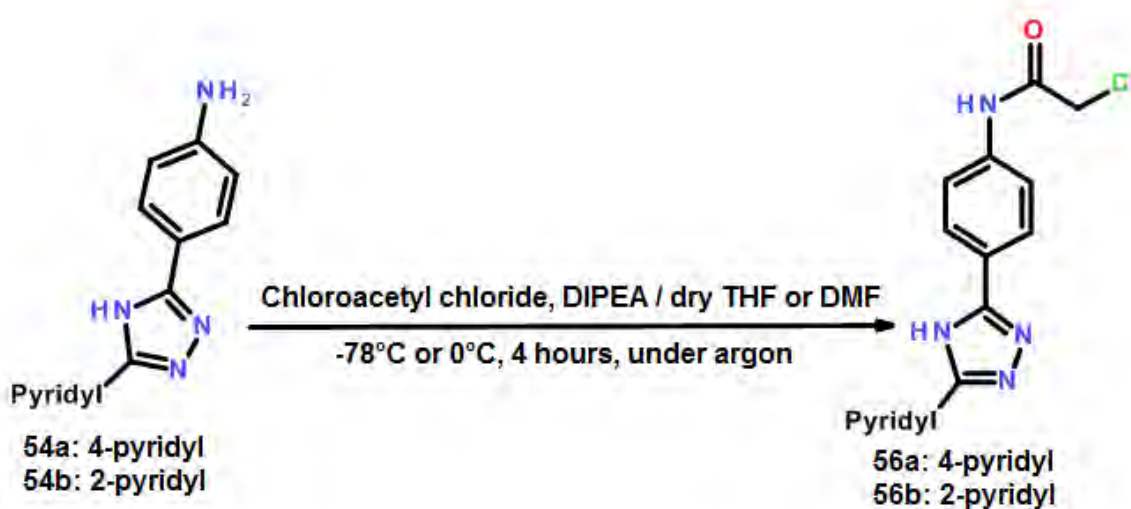
Scheme 6.10. Synthesis of the acrylamide having a short scaffold (compound **41a**).

The acrylamide warhead was attached on the aniline **54a** by treatment a solution of this compound with 2 equivalents of acryloyl chloride in the presence of DIPEA in dry THF under argon at 0 °C for 2 - 3 hours. The reaction succeeded to give the isolated **41a** in 52% yield.



Scheme 6.11. Attempted synthesis of 2-bromoacetamide derivatives.

The first step in the attempt to synthesis the dimethyl sulfonium ketones (compounds **41c,e**) was the preparation of the bromoacetamides (compounds **55a,b**) based on a published method (Pitta et al., 2016). In particular, the aniline **54a** was treated with the equivalent of bromoacetyl bromide in the presence of DIPEA in dry THF under argon at $-78\text{ }^{\circ}\text{C}$ for 4 hours. However, the reaction provided a polymerised mixture instead of the desired product. The same method except for the higher reaction temperature ($0\text{ }^{\circ}\text{C}$) to prevent the solvent THF/DMF from freezing was applied to synthesise compound **55b**. However, the same unwanted polymerisation was observed.

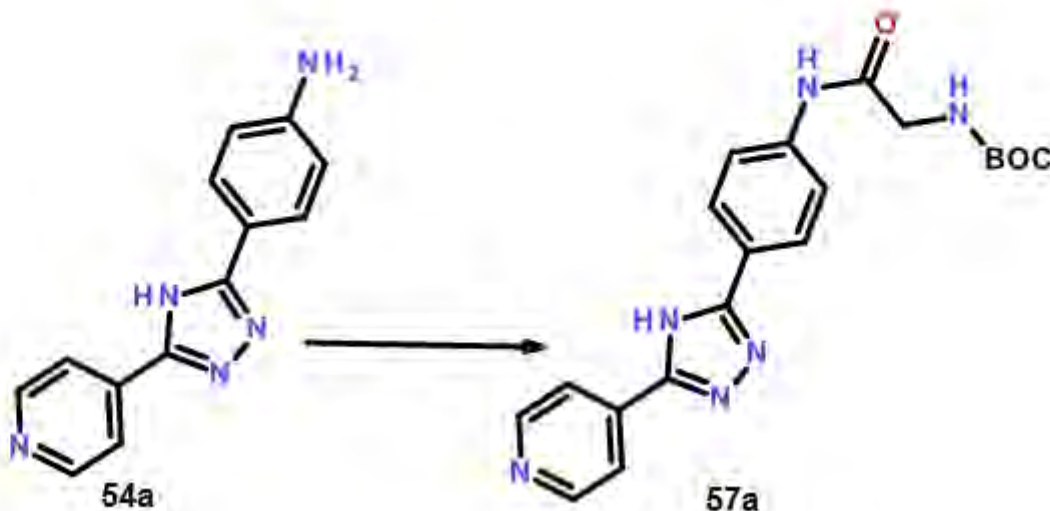


Scheme 6.12. Synthesis of 2-chloroacetamide derivatives from anilines **54a,b**.

In the attempt to avoid the unwanted polymerisation caused by the highly reactive 2-bromoacetamides, the 2-chloroacetamide derivatives (compounds **56a,b**) were prepared (Scheme 6.12) to attach the dimethyl sulfonium ketone warhead. Under the same reaction to synthesise the bromoacetamides, the treatment of the aromatic amines **54a,b** with the equivalent of 2-chloroacetyl chloride gave the isolated **56a** in 85% yield and **56b** in 84% yield. The synthesised 2-chloroacetamides were treated with excess dimethyl sulphide in a suitable solvent (**56a** in methanol, **56b** in DMF) at room temperature ($20\text{ }^{\circ}\text{C}$). That method was based on the literature (Griffin et al., 2014) which synthesised dimethyl sulfonium ketones from 2-bromoacetamides. Unfortunately, the reaction did not happen due to the lower reactivity of the 2-chloroacetamide compounds in comparison to the 2-bromoacetamides. Therefore, sodium iodide was used as a catalyst to transfer chloride to a better leaving group,

iodide. The temperature of the reaction was also increased to 40 °C. However, it did not help the reaction to occur.

6.3.3 Attachment of a side chain on the pyridyl triazolyl anilide scaffolds



Scheme 6.13. The attachment of a BOC group on amine **54a**.

In attempt to synthesise the compound with a longer side chain (compound **41b**), the first step was coupling the synthesised aniline **54a** with BOC-Gly-OH as given in Scheme 6.13. The coupling reagent CDI was used but the reaction did not provide the desired carbamate. Therefore, it was changed to a more reactive coupling reagent, ethylchloroformate, which was used in the presence of TEA (2.0 eq). Unfortunately, the reaction provided a mixture of products, in which there was very low portion of the desired carbamate. TEA was replaced by DIPEA, which is more sterically hindered, more basic and less nucleophilic. The replacement of the base helped to increase the proportion of the desired carbamate **57a** in the product mixture. The pure desired **57a** in 51% yield was achieved after flash column chromatography.

An attempt to detach BOC group of compound **57a** using excess TFA following the literature method (Hartwig et al., 2010) was failed. Then, the high concentration hydrochloric acid (up to 12 M) used instead but it could not succeed. This suggested the insolubility of the salt formed between the pyridyl and the strong acid in THF possibly prevented the deprotection of BOC group. Therefore, a more polar solvent, DMF, was

used alternatively to resolve this solubility issue. However, this attempt could not make the reaction succeed.

An attempt to attach Fmoc-group was made to overcome the failure in deprotection of BOC group. Fmoc-Gly-OH was treated with ethylchloroformate in the presence of DIPEA in dry THF under argon from 0 °C to room temperature (27 °C) for 1 hour. The resulting mixture was treated with the aniline **54a**. However, the reaction provided a complicated complex that contained a very small portion (<5%) of the expected product.

6.4 Conclusion

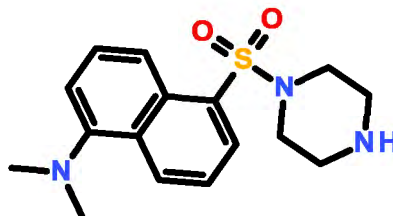
The study gained success in the modification of the acrylamide warhead of the lead irreversible inhibitor (compound **27**) to the (2Z)-4-amino-4-oxo-2-butenic warhead. The attachment of the acrylamide warhead and the maleic form of the acrylate type warhead on the short scaffold of compound **27** was successful. However, the synthesis of the fumaric form of the warhead did not succeed. The preparation of the propynamide (compound **27a**) also failed due to the unwanted polymerised of the product.

The attempted development of a series comprised an aminorhodanine ring was successful in the step to prepare 3-amino-5-benzylidenerhodanine scaffolds. However, it proved to be problematic in adding the acrylamide warhead or the dimethylsulfonium ketone warhead due to the polymerisation side-reactions.

The pyridyl triazolyl aniline scaffolds (**54a,b**) were synthesised in good yields. The attachment of the acrylamide warhead in the 4-pyridyl triazolyl aniline provided the desired compound **41a** in a good yield. Some attempts were made to prepare the acylmethylene dimethylsulfonium derivatives. However, it failed due to the intermediate halogenoacetamides were either polymerised (bromoacetamides) or deactivated to dimethylsulfide (chloroacetamides). Attempted lengthening the side chain of the pyridyl triazolyl aniline scaffolds before the attachment of the acrylamide warhead was also unsuccessful because of the problem in the detachment of BOC group and the failure in coupling with Fmoc-Gly.

6.5 Chemistry experimental session

Preparation of N,N-dimethyl-5-piperazin-1-ylsulfonyl-naphthalen-1-amine (43)

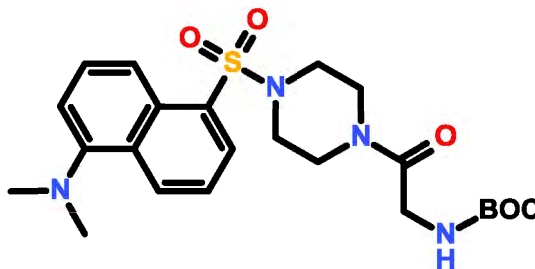


A solution of dansyl chloride (4.1789 g, 0.02 mol, 1.0 eq) in dry DCM (80 mL) was added dropwise over 30 min to a stirred solution of piperazine (8.6732 g, 0.10 mol, 6.7 eq) in dry DCM (50 mL) under argon. The reaction mixture was stirred at room temperature (23 °C) for 15 min, washed with water (4×30 mL) and evaporated by a rotary evaporation / 40 °C to give a solid, which was dried under vacuum / room temperature overnight. A clean desired product was gained as a light green solid (4.412 g, 0.014 mol, 93%).

^1H NMR (DMSO- D_6): δ = 2.20 (bs, 1H, NH); 2.67 (t, J = 4.8; 5.2 Hz, 4H, $(\text{CH}_2)_2\text{NH}$); 2.90 (s, 6H, $\text{N}(\text{CH}_3)_2$); 2.97 (t, 4H, $(\text{CH}_2)_2\text{NSO}_2$); 7.29 (dd, J = 0.9; 7.6 Hz, 1H, Napht-H); 7.66 (m, 2H, Napht-H); 8.13 (dd, J = 7.3, 1.3 Hz, 1H, Napht-H); 8.35 (dt, J = 8.8, 0.9 Hz, 1H, Napht-H); 8.54 (dt, J = 8.6, 1.1 Hz, 1H, Napht-H) ppm.

^1H NMR data are with agreement with those reported in (Sashuk et al., 2009).

Preparation of tert-butyl N-[2-[4-[[5-(dimethylamino)-1-naphthyl]sulfonyl]piperazin-1-yl]-2-oxo-ethyl]carbamate (44)



Method 1

A solution of EDC (6.3932 g, 33.35 mmol, 1.0 eq) in dry DCM (180 mL) was added to a solution of Boc-Gly-OH (8.8343 g, 50.43 mmol, 1.6 eq), HOBt (4.8589 g, 35.96 mmol, 1.1 eq) and DIPEA (12 mL, 68.89 mmol, 2.1 eq) in dry DCM (80 mL). The resulting mixture was stirred for 30 min at 0 °C under argon. This was then treated with a solution of amine **43** (10.3511 g, 32.41 mmol, 1.0 eq) in dry DCM (70 mL). The reaction mixture was stirred at room temperature (20 °C) under argon for 24 hours. The resulting suspension was washed with citric acid 10% (6×150 mL) then with water (6×150 mL). The organic layers were dried over MgSO₄, evaporated under reduced pressure / 40 °C to give a yellow solid. The crude product was purified by flash chromatography (DCM / MeOH = 98 / 2) to give the desired product (10.76 g, 22.69 mmol, 70%).

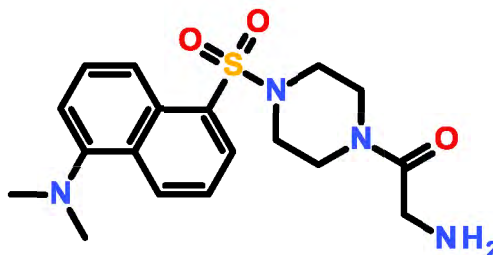
Method 2

A solution of Boc-Gly-OH (2.0097 g, 11.47 mmol, 1.1 eq) and CDI (1.8672 g, 11.52 mmol, 1.1 eq) in dry DCM (50 mL) was stirred at room temperature (20 °C) for 2 hours. A solution of amine **43** (3.3174 g, 10.39 mmol, 1.0 eq) in dry DCM (45 mL) was added and the reaction was followed by stirring for 20 hours. The reaction mixture was thoroughly washed with brine (4×200 mL), dried over MgSO₄, evaporated to get a solid under reduced pressure / 40 °C. A desired clean product was gained as a yellow solid (4.6444 g, 9.79 mmol, 94%).

¹H NMR (DMSO-D₆): δ = 1.34 (s, 9H, (CH₃)₃); 2.85 (s, 6H, N(CH₃)₂); 3.09 (m, 4H, 2CH₂); 3.47 (m, 4H, 2CH₂); 3.73 (d, *J* = 5.8 Hz, 2H, CH₂NH); 6.73 (t, *J* = 5.8 Hz, 1H, CH₂NH); 7.29 (dd, *J* = 0.9; 7.4 Hz, 1H, Napht-H); 7.57 (m, 2H, Napht-H); 8.15 (dd, *J* = 7.4, 1.1 Hz, 1H, Napht-H); 8.32 (d, *J* = 8.7 Hz, 1H, Napht-H); 8.55 (dt, *J* = 8.7, 1.1 Hz, 1H, Napht-H) ppm.

¹H NMR data are with agreement with those reported in a published paper (Griffin et al., 2014) which recorded melting point of this product: 176 -177 °C.

Preparation of 2-amino-1-[4-[[5-(dimethylamino)-1-naphthyl]sulfonyl]piperazin-1-yl]ethanone (45)



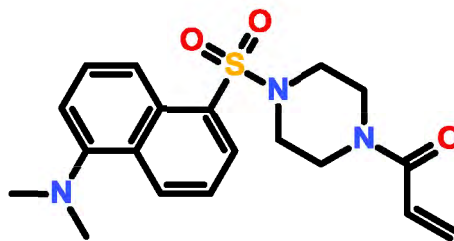
A solution of **44** (4.6147 g, 9.73 mmol, 1.0 eq) in DCM (70 mL) was treated with TFA (10 mL, 129.80 mmol, 13.3 eq), stirred for 3 hours at room temperature (20 °C) then extracted with HCl 1N (5×30 mL). The aqueous layers were collected, basified with saturated NaHCO₃ to pH 8 then extracted with DCM (6×30 mL). The organic layers were collected, dried over MgSO₄ and evaporated under reduced pressure / 40 °C to get a solid. The achieving solid was further dried at room temperature under vacuum overnight. The reaction provided a clean desired product as a yellow solid (2.9580 g, 7.86 mmol, 81%).

M.p: 81.6 – 83.4 °C.

¹H NMR (DMSO-D₆): δ = 2.83 (s, 6H, N(CH₃)₂); 3.11 (overlap m, 8H, 4-CH₂); 3.41 (t, *J* = 5.0 Hz, 2H, CH₂NH₂) ; 3.52 (t, *J* = 5.0 Hz, 2H, CH₂NH₂); 7.27 (dd, *J* = 0.9, 7.4 Hz, 1H, Napht-H); 7.66 (m, 2H, Napht-H); 8.16 (dd, *J* = 7.4, 1.1 Hz, 1H, Napht-H); 8.33 (d, *J* = 8.8 Hz, 1H, Napht-H); 8.54 (dt, *J* = 8.8, 1.0 Hz, 1H, Napht-H) ppm.

¹H NMR data are with agreement with those reported in (Griffin et al., 2014).

Preparation of 1-[4-[[5-(dimethylamino)-1-naphthyl]sulfonyl]piperazin-1-yl]prop-2-en-1-one (27e)



DIPEA (1.1 mL, 6.32 mmol, 5.2 eq) was added into a solution of amine **43** (0.3875 g, 1.21 mmol, 1.0 eq) in dry DCM (15 mL) under argon. The resulting solution was cooled down to 0 °C and acryloyl chloride (0.2 mL, 2.46 mmol, 2.0 eq) was added dropwise over 5 min. The reaction mixture was stirred at 0 °C for 3 hours. This was diluted with DCM (20 mL), washed with water (5×60 mL), dried over MgSO₄ and evaporated under reduced pressure / room temperature to give a solid. The resulting solid was dried under vacuum / room temperature overnight. The pure desired product as a yellow solid was achieved (0.3015 g, 0.81 mmol, 70%).

M.p: 111.0 – 113.0 °C.

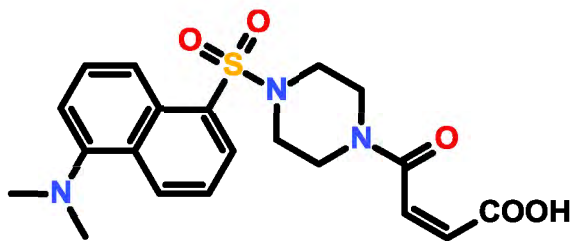
IR (solid, ATR) ν = 3450 (w); 2950 (w); 2900 (w); 2800 (w); 2700 (w); 1650 (s, CO), 1610 (m, C=C alkene), 1522, 1441 (m, aromatic) cm⁻¹.

¹H NMR (DMSO-D₆): δ = 2.85 (s, 6H, N(CH₃)₂); 3.13 (t, J = 4.8; 5.2 Hz, 4H, 2CH₂); 3.61 (m, 4H, 2CH₂); 5.66 (dd, J = 2.3; 10.5 Hz, 1H, CH); 6.06 (dd, J = 2.3; 16.7 Hz, 1H, CH); 6.72 (dd, J = 10.5; 16.7 Hz, 1H, CH); 7.29 (dd, J = 0.9; 7.6 Hz, 1H, Napht-H); 7.66 (ddd, J = 0.9; 7.4; 20.0 Hz, 2H, Napht-H); 8.15 (dd, J = 1.2; 7.4 Hz, 1H, Napht-H); 8.32 (dt, J = 1.0, 8.7 Hz, 1H, Napht-H); 8.55 (dt, J = 1.1, 8.5 Hz, 1H, Napht-H) ppm.

¹³C NMR (DMSO-D₆): δ = 44.9 (piperazine-CH₂); 45.2 (N(CH₃)₂); 45.5 (piperazine-CH₂); 45.9 (acrylamide-CH₂); 115.5 (CH); 119.0 (CH); 123.9 (CH); 128.1 (CH); 129.4 (Napht-C); 129.8 (Napht-C); 130.2 (CH); 130.6 (CH); 132.6 (Napht-C); 151.6 (Napht-C-S); 164.5 (CO) ppm.

HRMS m/z calcd for C₁₉H₂₄O₃N₃S (M+H)⁺, 374.1533; found, 374.1532.

Preparation of (Z)-4-[4-[[5-(dimethylamino)-1-naphthyl]sulfonyl]piperazin-1-yl]-4-oxo-but-2-enoic acid ((Z)-27f)



DCM (10 mL) was added to a mixture of amine **43** (0.3931 g, 1.23 mmol, 1.0 eq) and maleic anhydride (0.1208 g, 1.23 mmol, 1.0 eq). The resulting solution was stirred at room temperature (20 °C) for 24 hours. The volatiles were removed by evaporation under reduced pressure / 40 °C to give the desired clean product as a yellow solid (0.3015 g, 0.81 mmol, 70%).

M.p: 112.3 – 114.4 °C.

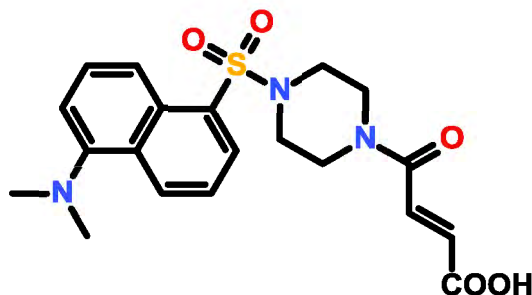
IR (solid, ATR) ν = 2900 - 2700 (w, b, OH); 1650, 1610 (m, CO), 1522, 1441 (m, C=C aromatic) cm^{-1} .

^1H NMR (DMSO- D_6): δ = 2.85 (s, 6H, $\text{N}(\text{CH}_3)_2$); 3.13 (t, J = 4.8; 5.2 Hz, 4H, 2CH_2); 3.61 (m, 4H, 2CH_2); 5.66 (dd, J = 2.3; 10.5 Hz, 1H, CH); 6.06 (dd, J = 2.3; 12.5 Hz, 1H, CH); 6.72 (dd, J = 10.5; 12.5 Hz, 1H, CH); 7.29 (dd, J = 0.9; 7.6 Hz, 1H, Napht-H); 7.66 (ddd, J = 0.9; 7.4; 20.0 Hz, 2H, Napht-H); 8.15 (dd, J = 1.2; 7.4 Hz, 1H, Napht-H); 8.32 (dt, J = 1.0, 8.7 Hz, 1H, Napht-H); 8.55 (dt, J = 1.1, 8.5 Hz, 1H, Napht-H) ppm.

^{13}C NMR (DMSO- D_6): δ = 45.0 (piperazine- CH_2), 45.3 ($\text{N}-(\text{CH}_3)_2$), 45.5 (piperazine- CH_2), 115.6 (CH), 119.0 (CH), 123.9 (CH), 124.4 (CH), 128.5 (CH), 129.4 (Napht- $\underline{\text{C}}$), 129.8 (Napht- $\underline{\text{C}}$), 130.3 (CH), 130.7 (CH), 132.8 (Napht- $\underline{\text{C}}$), 137.7 (CH), 151.7 (Napht- $\underline{\text{C}}-\text{S}$), 165.6 (acrylamide- $\underline{\text{C}}\text{O}$), 166.0 ($\underline{\text{C}}\text{OOH}$) ppm.

HRMS m/z calcd for $\text{C}_{20}\text{H}_{22}\text{O}_5\text{N}_3\text{S}$ (M-H) $^-$, 416.1286; found, 416.1282.

Attempted preparation of (E)-4-[4-[[5-(dimethylamino)-1-naphthyl]sulfonyl]piperazin-1-yl]-4-oxo-but-2-enoic acid ((E)-27f)



Attempt 1

Chloroform (20 mL) was added to a mixture of amine **43** (0.3120 g, 0.98 mmol, 1.0 eq) and maleic anhydride (0.0970 g, 0.98 mmol, 1.0 eq). The resulting solution was stirred at reflux for 5 hours. The volatiles were removed by evaporation under reduced pressure / 40 °C to give a solid. Unfortunately, the ¹H NMR spectra of the achieving product indicated the (**Z**)-**27f**.

Attempt 2

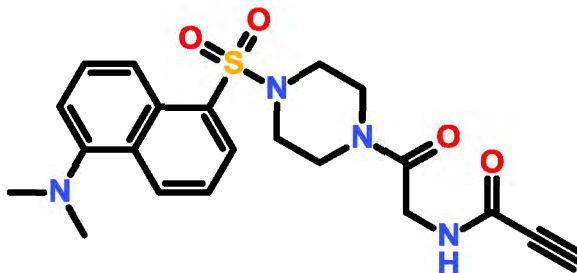
Bisacetonitrile dichloro-palladium II (0.0391g, 0.15 mmol) was added to a solution of (**Z**)-**27f** (0.3099 g, 0.74 mmol) in DCM (20 mL) followed by stirring at reflux for 10 hours. The reaction mixture was cooled down to the room temperature, filtered via a celite pad and thoroughly washed with ethyl acetate (3×20 mL). The filtrate was evaporated by a rotary evaporator to give an orange solid, which was dried under vacuum overnight at the room temperature. Unfortunately, the ¹H NMR spectrum of the achieving product indicated the (**Z**)-**27f**.

Attempt 3

Iodine (0.0046 g, 0.0036 mmol) was added to a stirred solution of (**Z**)-**27f** (0.0733g, 0.18 mmol) in chloroform (12 mL) and followed by stirring at reflux for 30 min. The reaction mixture was washed thoroughly via sodium metabisulfate to get rid of iodine. The filtrate was washed with water (3×10 mL), dried over MgSO₄ and evaporated under

reduced pressure / 40 °C. The achieving orange solid was dried under vacuum / room temperature over night. Nonetheless, the procedure could not give the desired (E)-**27f**.

*Attempted preparation of N-[2-[4-[[5-(dimethylamino)-1-naphthyl]sulfonyl]piperazin-1-yl]-2-oxo-ethyl]prop-2-ynamide (**27a**)*



Attempt 1

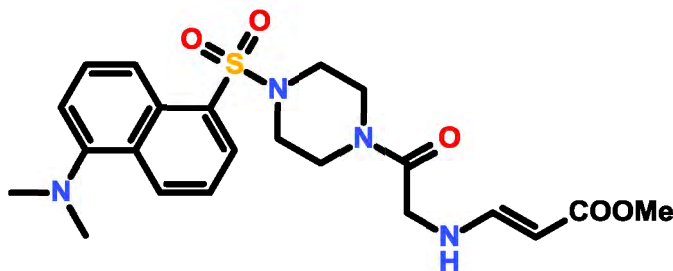
Propiolic acid (0.02 mL, 0.32 mmol, 1.0 eq) was added dropwise over 10 min to a solution of HOBt (0.0088 g, 0.06 mmol), EDC (0.0613 g, 0.32 mmol, 1.0 eq) and DIPEA (0.35 mL, 2.0 mmol, 6.2 eq) in dry DCM (12 mL) at 0 °C under argon. The resulting suspension was warmed up to room temperature (20 °C) and was stirred for 1 hour. This was then cooled down to 0 °C followed by treatment with a solution of amine **43** (0.1200 g, 0.32 mmol, 1.0 eq) in dry DCM (12 mL) and stirred for 6 hours. The reaction mixture was washed with water (4×25 mL), dried over MgSO₄ and evaporated under reduced pressure / room temperature to get a yellow solid. Unfortunately, the ¹H NMR spectrum of the achieving product showed a polymerised mixture.

Attempt 2

DIPEA (0.3 mL, 1.72 mmol, 2.7 eq) was added to a solution of propiolic acid (0.05 mL, 0.81 mmol, 1.3 eq) in dry THF (10 mL). To this ethylchloroformate (0.08 mL, 0.84 mmol, 1.4 eq) was added dropwise over 5 min at 0 °C under argon. The resulting suspension was stirred at room temperature (20 °C) for 1.5 hours then cooled down to 0 °C before a solution of amine **43** (0.2400 g, 0.64 mmol, 1.0 eq) in dry THF (20 mL) was added dropwise over 10 mins. The reaction was stopped after 3 hour stirring at the room temperature (monitoring the reaction by TLC). Ice water (100 mL) was added to the reaction mixture. The precipitate was collected by filtration and thoroughly washed with

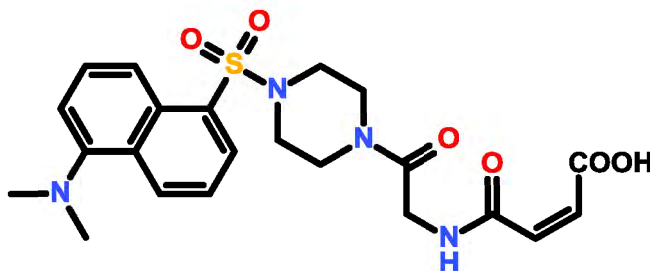
water (3×20 mL) to give a yellow solid, which was dried under reduced pressure / room temperature overnight. Unfortunately, the ^1H NMR spectrum of the product indicated a partly polymerised mixture.

Attempted preparation of methyl (E)-3-[[2-[4-[[5-(dimethylamino)-1-naphthyl]sulfonyl]piperazin-1-yl]-2-oxo-ethyl]amino]prop-2-enoate ((E)-27c)



A solution of amine **43** (0.1946 g, 0.52 mmol, 1.0 eq) and methyl propiolate (0.05 mL, 0.56 mmol, 1.1 eq) in DCM was stirred at room temperature (20 °C) for 24 hours. The volatiles were removed under reduced pressure / 40 °C to give a solid. However, the ^1H NMR spectrum of the achieving solid indicated no new compound was formed.

Preparation of (Z)-4-[[2-[4-[[5-(dimethylamino)-1-naphthyl]sulfonyl]piperazin-1-yl]-2-oxo-ethyl]amino]-4-oxo-but-2-enoic acid ((Z)-27b)



A solution of amine **43** (0.1618 g, 0.43 mmol, 1.0 eq) and maleic anhydride (0.04639 g, 0.47 mmol, 1.1 eq) in DCM (10 mL) was stirred at room temperature (20 °C) for 16 hours. This was diluted with DCM (20 mL), washed with water (3×20 mL), dried over MgSO_4 and evaporated under reduced pressure / 40 °C to give a yellow solid, which was dried under vacuum / room temperature overnight. The reaction provided the clean desired product as a yellow solid (0.1465 g, 0.31 mmol, 72%).

M.p: 198.1 – 201.6 °C.

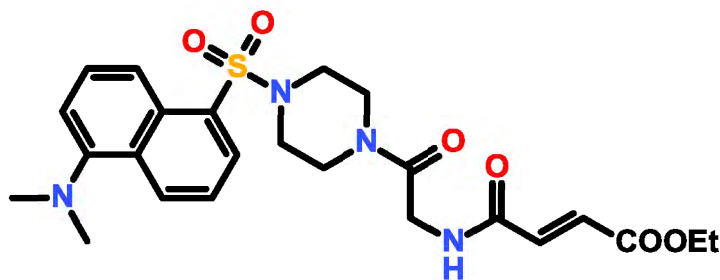
IR (solid, ATR) ν = 3350 (NH); 2870 (w, OH); 1900 (w); 1700 (s, CO); 1650 (s, CO); 1550, 1500, 1400 (s and m, C=C aromatic) cm^{-1} .

^1H NMR (DMSO- D_6): δ = 2.85 (s, 6H, $\text{N}(\text{CH}_3)_2$); 3.14 (m, 4H, 2CH_2); 3.50 (m, 4H, 2CH_2); 4.09 (d, J = 5.4 Hz, 2H, CH_2NH); 6.27 (d, J = 12.5 Hz, 1H, CHCHCOOH); 6.50 (d, J = 12.5 Hz, 1H, CHCHCOOH); 7.27 (dd, J = 0.9, 7.7 Hz, 1H, Napht-H); 7.67 (m, 2H, Napht-H); 8.16 (dd, J = 7.3, 1.2 Hz, 1H, Napht-H); 8.32 (dt, J = 0.9, 8.9 Hz, 1H, Napht-H); 8.56 (dt, J = 8.6, 1.1 Hz, 1H, Napht-H); 9.09 (t, J = 5.4 Hz, 1H, CH_2NH); 14.53 (s, 1H, COOH) ppm.

^{13}C NMR (DMSO- D_6): δ = 41.2 (CH_2); 44.0 (piperazine- CH_2); 45.3 (CH_3); 45.5 (piperazine- CH_2); 115.6 (CH); 119.1 (CH); 123.9 (CH); 128.5 (CH); 129.4 (Napht-C); 129.8 (Napht-C); 130.3 (CH); 130.6 (CH); 132.6 (Napht-C); 133.2 (CH); 151.6 (Napht-C-S); 165.3 (CO); 166.0 (acrylamide-CO); 166.2 (COOH) ppm.

HRMS m/z calcd for $\text{C}_{22}\text{H}_{27}\text{O}_6\text{N}_4\text{S}$ ($\text{M}+\text{H}$) $^+$, 475.1646; found, 475.1649.

Preparation of ethyl (E)-4-[[2-[4-[[5-(dimethylamino)-1-naphthyl]sulfonyl]piperazin-1-yl]-2-oxo-ethyl]amino]-4-oxo-but-2-enoate (46)



Ethyl fumaroyl chloride (0.23 mL, 1.72 mmol, 1.1 eq) was added dropwise to a solution of compound **43** (0.6124 g, 1.63 mmol, 1.0 eq) and DIPEA (0.8 mL, 3.44 mmol, 2.1 eq) in dry THF at 0 °C, in the dark followed by stirring for 5 hours. Water (200 mL) was added and the precipitate was collected by filtration, thoroughly washed with water (3×30 mL) and dry under reduced pressure / room temperature to give the desired product as a yellow solid (0.6035 g, 1.20 mmol, 74%).

M.p: 103.1 – 105.4 °C.

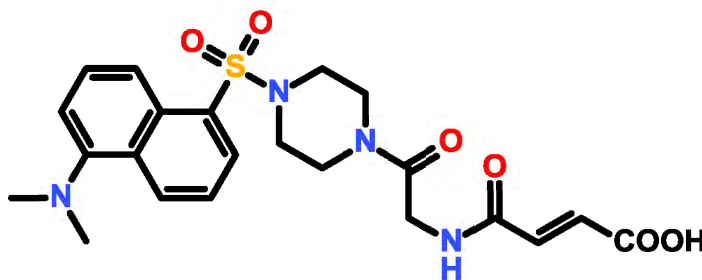
IR (solid, ATR) ν = 3500, 3350 (w, NH); 1720 (s, CO ester); 1680, 1650 (s, CO amide); 1600, 1480, 1400 (m, C=C aromatic) cm^{-1} .

^1H NMR (DMSO- D_6): δ = 1.25 (t, J = 7.2 Hz, 3H, CH_2CH_3); 2.85 (s, 6H, $\text{N}(\text{CH}_3)_2$); 3.13 (m, 4H, 2CH_2); 3.50 (m, 4H, 2CH_2); 4.05 (d, J = 5.4 Hz, 2H, CH_2NH); 4.20 (q, J = 7.2 Hz, 2H, CH_2CH_3); 6.55 (d, J = 16.7 Hz, 1H, CHCHCOOEt); 7.15 (d, J = 16.7 Hz, 1H, CHCHCOOEt); 7.29 (dd, J = 0.9; 7.7 Hz, 1H, Napht-H); 7.67 (m, 2H, Napht-H); 8.16 (dd, J = 7.4, 1.1 Hz, 1H, Napht-H); 8.32 (d, J = 8.7 Hz, 1H, Napht-H); 8.56 (dt, J = 8.7, 1.1 Hz, 1H, Napht-H); 8.66 (t, J = 5.4 Hz, 1H, NH) ppm.

^{13}C NMR (DMSO- D_6): δ = 14.3 (CH_2CH_3); 44.0 (CH_2CH_3); 43.5 ($\text{N}(\text{CH}_3)_2$); 45.6 (piperazine- CH_2); 60.9 (piperazine- CH_2); 115.6 (CH); 119.1 (CH); 123.9 (CH); 128.5 (CH); 128.9 (CH); 129.4 (Napht-C); 129.9 (Napht-C); 130.3 (CH); 130.7 (CH); 132.6 (Napht-C); 137.4 (CH); 151.6 (C); 163.1 (CO); 165.2 (CO); 166.7 (CO).

HRMS m/z calcd for $\text{C}_{24}\text{H}_{31}\text{O}_6\text{N}_4\text{S}$ ($\text{M} + \text{H}$) $^+$, 503.1959; found, 503.1948.

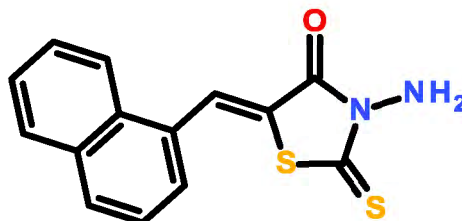
Attempted preparation of (E)-4-[[2-[4-[[5-(dimethylamino)-1-naphthyl]sulfonyl]piperazin-1-yl]-2-oxo-ethyl]amino]-4-oxo-but-2-enoic acid ((E)-27b)



Water (1.5 mL) was added to a solution of ester **11** (0.2412 g, 0.49 mmol, 1.0 eq) in MeOH / THF (25 mL / 10 mL). The resulting solution was cooled down to 0 °C and treated with NaOH (0.4341g, 10.85 mmol, 22.1 eq). This was warmed up to room temperature (20 °C) and stirred for 2 hours. TLC (ethylacetate/methanol: 20/5) indicated no ester **11** was remained in the mixture. The reaction mixture was isolated using ion exchange chromatography (Dowex 50WX8 hydrogen form). The resulting solution was

extracted with ethylacetate (3×20 mL). The organic layers were collected, dried over MgSO_4 , evaporated under reduced pressure. However, no solid was achieved.

Preparation of (5Z)-3-amino-5-(1-naphthylmethylene)-2-thioxo-thiazolidin-4-one (47b)

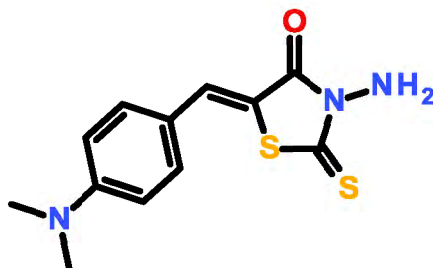


To a stirred solution of 3-aminorhodanine (4.9654 g, 33.52 mmol, 1.0 eq) and 1-naphthaldehyde (6.1 mL, 37.11 mmol, 1.1 eq) in ethanol (150 mL), a drop of piperidine was added. The reaction mixture was heated to reflux for 18 hours, then cooled down to 0 °C. The precipitate was collected by filtration, thoroughly washed with ethanol (100 mL) and dried under reduced pressure / room temperature to give a brown solid. The obtained crude product was recrystallised from ethylacetate to give the desired pure compound as a dark yellow solid (3.9305 g, 13.73 mmol, 41%).

^1H NMR (DMSO- D_6): δ = 6.00 (s, 2H, NH_2); 7.70 (m, 4H, Napht-H); 8.05 (m, 1H, Napht-H); 8.12 (d, 1H, J = 7.6 Hz, Napht-H); 8.21 (d, 1H, J = 8.4 Hz, Napht-H); 8.52 (s, 1H, NH) ppm.

^{13}C NMR (DMSO- D_6): δ = 123.7 (CH), 123.9 (C), 126.0 (CH), 127.1 (CH), 127.4 (CH), 127.9 (CH), 129.1 (CH), 130.2 (C), 130.3 (CH), 131.2 (C), 131.6 (CH), 133.5 (C), 163.4 (C), 188.8 (C) ppm.

Preparation of (5Z)-3-amino-5-[[4-(dimethylamino)phenyl]methylene]-2-thioxo-thiazolidin-4-one (47a)

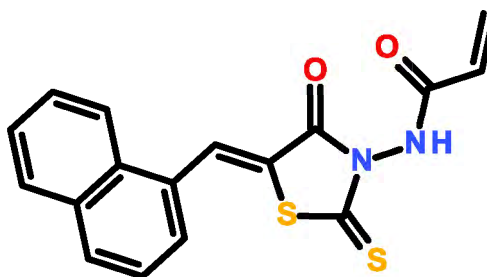


To a stirred solution of 3-aminorhodanine (0.4854 g, 3.28 mmol, 1.0 eq) and 4-(dimethylamino) benzaldehyde (0.5218 g, 3.50 mmol, 1.1 eq) in ethanol (20 mL), a drop of piperidine was added. The reaction mixture was heated to reflux for 18 hours, cooled down to 0 °C, filtered and repeatedly washed with ethanol (50 mL). The volatiles were removed under the reduced pressure / room temperature for 24 hours to give the clean desired amine as a bright red solid (0.599 g, 2.09 mmol, 71%).

^1H NMR (DMSO- D_6): δ = 3.06 (s, 6H, Me_2N); 5.96 (s, 2H, NH_2); 6.85 (d, 2H, J = 9.0 Hz, Ph-H3 and H5); 7.51 (d, 2H, J = 9.0 Hz, Ph-H2 and H6); 7.74 (s, 1H, CH) ppm.

^1H NMR data are with agreement with those reported in (Powers et al., 2006).

Attempted preparation of N-[(5Z)-5-(1-naphthylmethylene)-4-oxo-2-thioxo-thiazolidin-3-yl]prop-2-enamide (40b)



Attempt 1

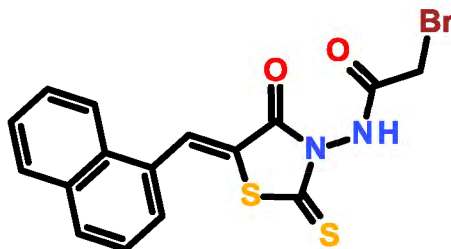
Acryloyl chloride (0.4 mL, 4.92 mmol, 4.0 eq) added dropwise to a solution of amine **47b** (0.3523 g, 1.23 mmol, 1.0 eq) in dry THF (40 mL) in the presence of DIPEA (1.7

mL, 9.84 mmol, 8.0 eq) under argon at 0 °C. The reaction mixture was stirred at room temperature (25 °C) for 20 hours. This was poured into an ice water bath (100 mL). The precipitate was collected by filtration, thoroughly washed with water (100 mL) and dried under reduced pressure / room temperature to give a yellow solid. However, the ^1H NMR spectrum of the accomplished product indicated a very complex mixture.

Attempt 2

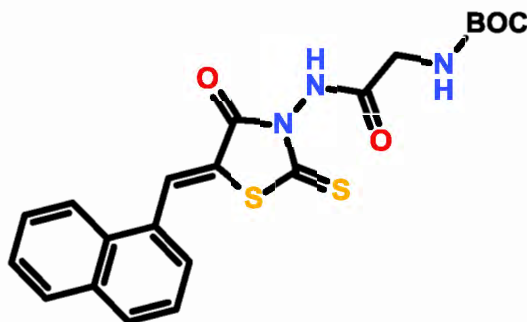
Acryloyl chloride (0.55 mL, 6.77 mmol, 4.4 eq) was added in to a solution of amine **47b** (0.4451 g, 1.55 mmol, 1.0 eq) in dry THF (35 mL) in the presence of DIPEA (1.2 mL, 6.89 mmol, 4.4 eq) under argon, in the dark, at 0 °C. The reaction mixture was stirred at 0 °C for 3 hours. To this water (100 mL) was added and the precipitate was collected by filtration, thoroughly washed with water (3×50 mL) and dry under reduced pressure / room temperature to give a yellow solid. However, the ^1H NMR spectrum of the product indicated a polymerised mixture.

Attempted preparation of 2-bromo-N-[(5Z)-5-(1-naphthylmethylene)-4-oxo-2-thioxo-thiazolidin-3-yl]acetamide (48)



Bromoacetyl bromide (0.09 mL, 0.63 mmol, 1.1 eq) was added dropwise to a solution of **47b** (0.1566 g, 0.55 mmol, 1.0 eq) in dry THF (17 mL) in the presence of DIPEA (0.16 mL, 0.92 mmol, 1.7 eq) at -78 °C under argon. The reaction mixture was stirred for 3.5 hours. Water (50 mL) was added and the resulting suspension was extracted with ethylacetate (3×25 mL). The organic layers were collected, dried over MgSO_4 , evaporated under reduced pressure / 40 °C to give a yellow solid. However, the ^1H NMR spectrum of the product indicated a very complex mixture.

Attempted preparation of tert-butyl N-[2-[[[(5Z)-5-(1-naphthylmethylene)-4-oxo-2-thioxo-thiazolidin-3-yl]amino]-2-oxo-ethyl]carbamate (49)



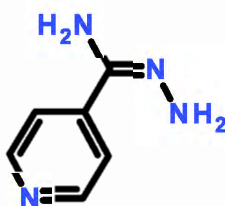
Attempt 1

A solution of BOC-Gly-OH (0.0288 g, 0.16 mmol, 1.1 eq) and CDI (0.0301g, 0.19 mmol, 1.4 eq) in dry THF (2 mL) was stirred at room temperature (25 °C) under argon. This was treated with a solution of **47b** (0.0410 g, 0.14 mmol, 1.0 eq) in dry THF (4 mL). However, after 24 hours, TLC of the reaction mixture against the starting amine in ethylacetate / toluene (60/40) indicated no new compound was formed.

Attempt 2

Ethylchloroformate (0.08 mL, 0.84 mmol, 1.0 eq) was added dropwise to a solution of Boc-Gly-OH (0.1408 g, 0.80 mmol, 1.0 eq) in dry THF (5 mL) under argon at 0 °C. This was stirred at room temperature (25 °C) for 2 hours, then a solution of **47b** (0.2343 g, 0.82 mmol, 1.0 eq) in dry THF / DMF (10 mL / 1 mL) was added. After 24 hours, water (40 mL) was added and the resulting suspension was extracted with ethyl acetate (3×25 mL). The organic layers were combined, dried over MgSO₄ and evaporated to get a solid. However, ¹H NMR spectra has no indication of a new formed compound.

Preparation of N'-aminopyridine-4-carboxamidine (51a)

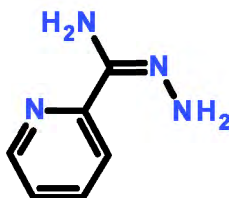


Hydrazine monohydrate (32 mL, 0.95 mol, 6.3 eq) was added to a stirred solution of 4-cyanopyridine (15.2019 g, 0.15 mol, 1.0 eq) in ethanol (60 mL) at room temperature (20 °C). The reaction mixture was set aside without stirring at room temperature for 3 weeks. Ethanol and hydrazine were removed by evaporation under reduced pressure / 40 °C. The resulting material was cooled down to 0 °C then triturated with petroleum ether 40/60 (20 mL). The precipitate was collected by filtration, washed with petroleum ether 40/60 (5 × 40 mL) and dry under vacuum at room temperature for 24 hours to give the desired N'-aminopyridine-4-carboxamidine as a yellow solid (10.002 g, 0.074 mol, 49%).

¹H NMR (DMSO-D₆): δ = 5.26 (s, 2H, C-NH₂), 5.72 (s, 2H, N-NH₂), 7.63 (dd, 2H, *J* = 1.6, 4.4 Hz, Pyr-H₂ and H₆); 8.50 (dd, 2H, *J* = 1.6, 4.4 Hz, Pyr-H₃ and H₅) ppm.

¹H NMR data are with agreement with those reported in (Sikdar, 2010) which did not provide data on melting point.

Preparation of N'-aminopyridine-2-carboxamidine (51b)



A stirred solution of 2-cyanopyridine (15.063 g, 144.7 mmol, 1.0 eq) in ethanol (30 mL) was treated with hydrazine monohydrate (30 mL, 946.33 mmol, 6.5 eq) at room temperature (25 °C). The reaction mixture stirred for 30 min then set aside at room temperature for 3 days. The volatiles were removed by evaporation at 40 °C under reduced pressure. The resulting mixture was triturated with petroleum ether 40/60 (20 mL). The precipitate was collected by filtration, washed with petroleum ether 40/60 (2 × 10 mL) and dry under vacuum to give a cream solid (17.840 g, 132.96 mmol, 92%).

M.p: 86.4 – 90.0 °C.

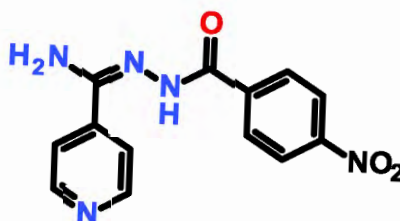
IR (solid, ATR) ν = 3441 (m, NH₂), 3173- 3283 (m, NH₂), 1634 (s, C=N), 1587, 1560, 1487, 1435 (skeletal Ar) cm⁻¹.

^1H NMR (DMSO- D_6): δ = 5.31 (s, 2H, C-NH $_2$), 5.72 (s, 2H, N-NH $_2$), 7.31 (ddd, 1H, J = 1.2, 4.8, 7.4 Hz, Pyr-H4); 7.74 (ddd, 1H, J = 1.6, 7.6, 8.1 Hz, Pyr-H6); 7.91 (dt, 1H, J = 0.8, 1.6, 8.1 Hz, Pyr-H5); 8.49 (ddd, 1H, J = 0.8, 1.6, 4.8 Hz, Pyr-H3) ppm.

^{13}C NMR (DMSO- D_6): δ = 119.5 (CH), 123.4 (CH), 136.7 (CH), 148.1 (C), 143.5 (CH), 152.2 (C) ppm.

^1H NMR data are with agreement with those reported in the literature (Sikdar, 2010).

Preparation of *N*-[(*E*)-[amino(4-pyridyl)methylene]amino]-4-nitrobenzamide (52a)



A solution of 4-nitrobenzoic acid (0.6348 g, 3.79 mmol, 1.0 eq) and CDI (0.6146 g, 3.79 mmol, 1.0 eq) in dry THF / DMF (20 mL / 10 mL) was stirred at room temperature (20 °C) under argon for 1.5 hours. To this was added a solution of amine **51a** (0.5041 g, 3.75 mmol, 1.0 eq) in anhydrous THF / DMF (30 mL / 10 mL). The reaction mixture was stirred for 21 hours at room temperature under argon. THF was removed by evaporation under reduced pressure at 40 °C and the remaining mixture was added water (60 mL) while stirring. The precipitate was collected by filtration, washed with water (3 \times 20 mL) and dry under vacuum at room temperature overnight to give the desired 4-nitro-benzamide as a light yellow solid (0.5082 g, 2.00 mmol, 53%).

M.p: 296.9 - 301.5°C.

IR (solid, ATR) ν = 3349 (m, NH $_2$), 3184 (m, NH), 3047 (w, Ph-CH), 1639 (m, CO), 1594 (s, C=N), 1512, 1345 (s, NO $_2$), 1544, 1413 (m, skeletal Ph or Pyr) cm^{-1} .

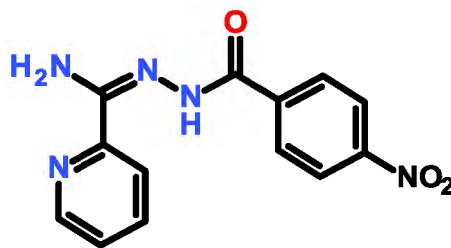
^1H NMR (DMSO- D_6) (room temperature): δ = 7.04 (s, 2H, NH $_2$); 7.82 (dd, J = 1.6, 4.4 Hz, 2H, Pyr- H2 and H6); 8.16 (d, 2H, J = 8.4 Hz, Ph-H3 and H5); 8.34 (d, 2H, J = 8.4

Hz, Ph-H2 and H6); 8.68 (d, 2H, $J = 5.6$ Hz, Pyr-H3 and H5), 10.35 (s, 1H, NH-CO or N=COH) ppm.

^1H NMR (DMSO- D_6) (60°C): $\delta = 6.88$ (s, 2H, NH_2); 7.82 (s, 2H); 8.15 (s, 2H); 8.32 (m, 2H); 8.68 (s, 2H), 10.35 (s, 1H, NH-CO or N=COH) ppm.

^{13}C NMR (DMSO- D_6): $\delta = 121.3$ (Pyr-CH); 123.8 (Ph-CH); 129.6 (Ph-CH); 140.5 (C); 141.8 (C); 149.3 (C); 150.4 (Pyr-CH); 150.9 (Ph-C- NO_2); 161.9 (CO) ppm.

Preparation of *N*-[(*E*)-[amino(2-pyridyl)methylene]amino]-4-nitrobenzamide (52b**)**



A solution of 4-nitrobenzoic acid (6.2836 g, 37.59 mmol, 1.0 eq) and CDI (6.0350 g, 37.15 mmol, 1.0 eq) in dry THF / DMF (70 mL / 80 mL) was stirred at room temperature (20 °C) under argon for 1.5 hours. To this a solution of **51b** (5.0008 g, 37.27 mmol, 1.0 eq) in dry THF / DMF (40 mL / 20 mL) was added. The reaction mixture was stirred at room temperature under argon for 24 hours and then was concentrated under reduced pressure at 40 °C. The remaining mixture was treated with water (400 mL) and the precipitate was collected by filtration, thoroughly washed with water (300 mL) and dry under reduced pressure at room temperature to give the desired **52b** as a light yellow solid (6.8896 g, 27.20 mmol, 73%).

M.p: 284.3 - 286.4 °C.

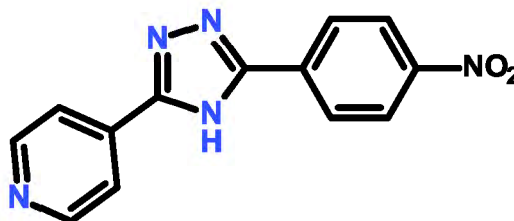
IR (solid, ATR): 3371 (m, NH₂), 3257 (m, NH); 3010 (s, Ph-H); 1689 (s, CO); 1636 (s, C=N), 1509, 1340 (s, NO₂), 1571, 1544, 1467, 1437 (skeletal Ph or Pyr) cm⁻¹.

¹H NMR (DMSO-D₆) (room temperature): δ = 6.92 (s, 2H, NH₂), 7.52 (s, 1H, Pyr-H₄), 7.95 (s, 1H, Pyr-H₅); 8.19 (m, 3H, Pyr-H₃, Ph-H₃ and H₅); 8.31 (d, 2H, *J* = 8.8 Hz, Ph-H₂ and H₆); 8.64 (s, 1H, Pyr-H₃); 10.41 (s, 1H, NHCO or N=COH) ppm.

¹H NMR (DMSO-D₆) (60°C): δ = 6.92 (s, 2H, NH₂), 7.52 (s, 1H, Pyr-H₄), 7.95 (s, 1H, Pyr-H₅); 8.19 (m, 3H, Pyr-H₃, Ph-H₃ and H₅); 8.31 (d, 2H, *J* = 8.8 Hz, Ph-H₂ and H₆); 8.64 (s, 1H, Pyr-H₃); 10.41 (s, 1H, NHCO or N=COH) ppm.

¹³C NMR (DMSO-D₆): δ = 121.3 (Pyr-CH), 123.3 (Pyr-CH), 123.8 (Pyr-CH), 125.5 (Ph-CH), 129.6 (Ph-CH), 141.8 (C), 148.7 (C), 150.4 (Pyr-CH), 150.9 (Pyr-C-NO₂), 161.9 (CO) ppm.

Preparation of 4-[5-(4-nitrophenyl)-4H-1,2,4-triazol-3-yl]pyridine (53a)



A suspension of the carboxamidrazone amide **52a** (0.2021 g, 0.798 mmol) in ethylene glycol (2 mL) was heated to reflux for 24 hours. The stirred reaction mixture was cooled down to room temperature (25 °C) and water (30 mL) was added. The precipitate was collected by filtration, washed with water (50 mL) and dry under reduced pressure overnight to give the desired product as a yellow solid (0.1423 g, 0.602 mmol, 76%).

M.p: 307.1 - 311.9 °C.

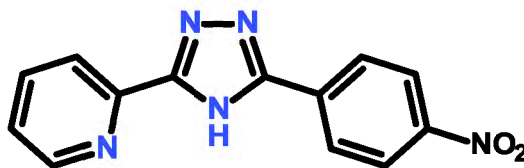
IR (solid, ATR) ν = a wide peak from 2200 to 3000 (m, Ph-CH, Triazole-NH), 1603 (s, C=N), 1517, 1347 (s, NO₂), 1454, 1418 (w, skeletal Ph or Pyr) cm⁻¹.

¹H NMR (DMSO-D₆): δ = 8.02 (dd, 2H, J = 1.6, 4.4 Hz, Pyr-H2 and H6); 8.35 (d, 2H, J = 8.8 Hz, Ph-H3 and H5); 8.42 (d, 2H, J = 9.2 Hz, Ph-H2 and H6); 8.78 (dd, 2H, J = 6.0, 4.4 Hz, Pyr-H3 and H5); 15.25 (s, 1H, Triazole-NH) ppm.

¹³C NMR (DMSO-D₆): δ = 62.1 (C), 98.9 (C), 120.6 (CH), 124.9 (CH), 127.7 (CH), 148.5 (C), 151.2 (CH) ppm.

HRMS m/z calcd for C₁₃H₁₀O₂N₅ (M+H)⁺, 268.0829; found, 268.0830.

Preparation of 2-[5-(4-nitrophenyl)-4H-1,2,4-triazol-3-yl]pyridine (53b)



A suspension of compound **52b** (6.6316 g, 26.18 mmol) in ethylene glycol (66 mL) was heated to reflux for 26 hours. The stirred reaction mixture was cooled down to room temperature (25 °C) and water (50 mL) was added. The precipitate was collected by filtration, washed with water (150 mL) and dry under reduced pressure at room temperature overnight to give the desired product as a yellow solid (5.0827 g, 21.51 mmol, 82%).

M.p: 302.8 – 309.1 °C.

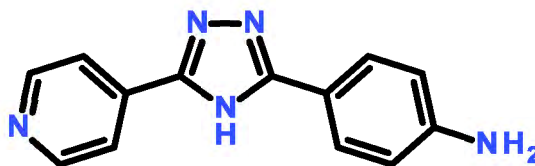
IR (solid, ATR) ν = a wide peak from 2600 to 3100 (m, Ph-CH, Triazole-NH), 1514, 1339 (NO₂), 1600, 1480, 1456, 1428 (s and w, skeletal Ph or Pyr) cm⁻¹.

¹H NMR (DMSO-D₆): δ = 7.59 ppm (ddd, 1H, J = 1.2, 4.8, 7.6 Hz, Pyr-H3); 8.05 ppm (td, 1H, J = 1.6, 8.0 Hz, Pyr-H4); 8.21 ppm (dt, 1H, J = 0.8, 8.0 Hz, Pyr-H5); 8.37 (m, 4H, Ph-H); 8.76 ppm (ddd, 1H, J = 0.8, 1.6, 4.8 Hz, Pyr-H3); 15.18 ppm (s, 1H, Triazole-NH).

¹³C NMR (DMSO-D₆): δ = 113.7 (Pyr-CH), 121.5 (Pyr-CH), 124.5 (Pyr-CH), 127.3 (Ph-CH), 137.5 (Ph-CH), 149.6 (Pyr-CH), 150.2 (C) ppm.

HRMS m/z calcd for C₁₃H₁₀O₂N₅ (M+H)⁺, 268.0829; found, 268.0830.

Preparation of 4-[5-(4-pyridyl)-4H-1,2,4-triazol-3-yl]aniline (54a)



Ammonium formate (1.2013 g, 19.05 mmol, 4.2 eq) and palladium on charcoal 10% (0.4908 g) were added to a stirred solution of compound **53a** (1.0614 g, 4.49 mmol, 1.0 eq) in anhydrous DMF (30 mL) at 0 °C under argon. This was heated under argon at 65 °C for 45 min, then cooled down to room temperature. A filtrate, which was collected by filtration via a celite pad and washed with MeOH (50 mL), was evaporated under reduced pressure at 40 °C to remove MeOH then at 60 °C to concentrate DMF. Water (50 mL) was added to the resulting mixture. The precipitate was collected by filtration, washed with water (150 mL) and dry under vacuum for 24 hours to give the desired product as a dark yellow solid (0.9419 g, 3.99 mmol, 89%).

M.p: 253.8 – 256.9 °C.

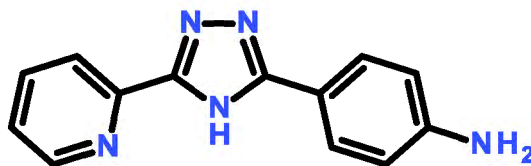
IR (solid, ATR) ν = 3469-3323 (m, NH₂), 3173 (m, NH), 1607, 1509, 1461, 1407 (s and m, skeletal Ph, triazole or Pyr) cm⁻¹.

¹H NMR (DMSO-D₆): δ = 5.64 (s, 2H, NH₂); 6.67 (d, 2H, J = 8.8 Hz, Ph-H₂ and H₆); 7.74 (d, 2H, J = 8.8 Hz, Ph-H₃ and H₅); 7.97 (d, 2H, J = 1.6, 4.4 Hz, Pyr-H₂ and H₆); 8.69 (d, 2H, J = 1.6, 4.4 Hz, Pyr-H₃ and H₅); 14.16 (s, 1H, triazole-NH) ppm.

¹³C NMR (DMSO-D₆): δ = 113.7 (Ph-CH), 114.4 (Ph-C-NH₂), 120.4 (Ph-CH), 128.0 (Pyr-CH), 138.4 (C), 150.8 (Pyr-CH); 151.1 (C) ppm.

HRMS m/z calcd for C₁₃H₁₂N₅ (M+H)⁺, 238.1087; found, 238.1090.

Preparation of 2-[5-(p-tolyl)-4H-1,2,4-triazol-3-yl]pyridine (54b)



Ammonium formate (0.9679 g, 15.35 mmol, 3.4 eq) and palladium on charcoal 10% (0.4172 g) were added to a solution of compound **53b** (1.0574 g, 4.48 mmol, 1.0 eq) in dry DMF (133 mL) at 0 °C. After stirring at 65 °C under argon for 1 hour, the reaction mixture was cooled down to room temperature, filtered via a celite pad and washed with MeOH (5× 20 mL). The filtrate was evaporated under reduced pressure at 40 °C to remove MeOH, and then at 60 °C to concentrate DMF. Water (50 mL) was added and the suspension was stirred at 0 °C for 30 min. The precipitate was collected by filtration, washed with water (4×40 mL) and dry under vacuum at room temperature for 24 hours to give the desired product as a grey solid (0.8558 g, 3.62 mmol, 81%).

M.p: 257.8 – 264.8 °C.

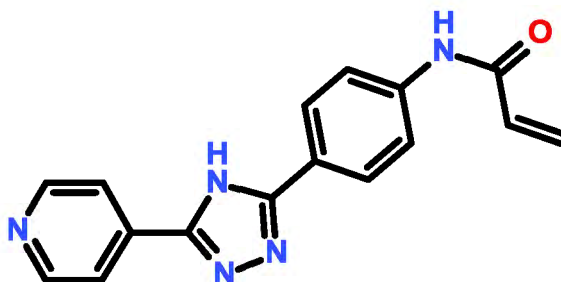
IR (solid, ATR) ν = 3468 (m, NH₂), 3299 (m, NH), 1607, 1505, 1486, 1391 (s and m, skeletal Ph, Triazole or Pyr) cm⁻¹.

¹H NMR (DMSO-D₆): δ = 5.47 (s, 2H, Ph-NH₂); 6.65 (d, 2H, J = 8.8 Hz, Ph-H₂ and H₆); 7.48 (ddd, 1H, J = 1.2, 4.8, 7.6 Hz, Pyr-H₄); 7.75 (d, 2H, J = 8.8 Hz, Ph-H₃ and H₅); 7.94 (td, J = 1.6, 7.6 Hz, 1H, Pyr-H₆); 8.12 (dt, J = 1.2, 8.0 Hz, 1H, Pyr-H₅), 8.67 (m, 1H, Pyr-H₃), 14.38 (s, 1H, Triazole-NH) ppm.

¹³C NMR (DMSO-D₆): δ = 114.0 (Ph-CH); 121.7 (Ph-CH); 124.7 (Pyr-CH); 127.5 (Pyr-CH); 137.8 (Pyr-CH); 150.0 (Pyr-CH); 150.6 (C) ppm.

HRMS m/z calcd for C₁₃H₁₂N₅ (M+H)⁺, 238.1087; found, 238.1090.

Preparation of *N*-[4-[5-(4-pyridyl)-4*H*-1,2,4-triazol-3-yl]phenyl]prop-2-enamide (*41a*)



Acryloyl chloride (0.7 mL, 5.17 mmol, 2.3 eq) was added dropwise over 20 min to a solution of **54a** (0.528 g, 2.23 mmol, 1.0 eq) and DIPEA (1.7 mL, 9.76 mmol, 4.4 eq) in dry THF (25 mL) under argon and at 0 °C. The resulting mixture was stirred at 0 °C for 3 hours followed by adding water (30 mL). The precipitate was collected by filtration, thoroughly washed with water (100 mL) and dry under reduced pressure at room temperature to give the desired product as a light yellow solid (0.3375 g, 1.16 mmol, 52%).

M.p: 226.7 – 229.7 °C

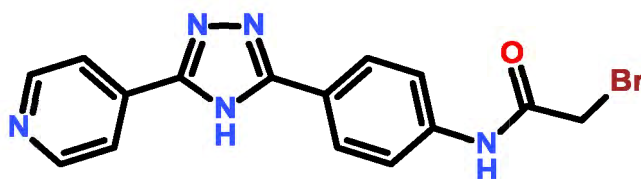
IR (solid, ATR) ν = 3050, 3100 (m, NH), 1700 (s, CO), 1650 (m, C=C), 1550, 1500, 1400, 1450 (s and m, skeletal Ph, Triazole or Pyr) cm^{-1} .

^1H NMR (DMSO- D_6): δ = 5.83 (dd, J = 10.0, 2.0 Hz, 1H, CH); 6.32 (dd, J = 17.0, 2.0 Hz, 1H, CH); 6.49 (dd, J = 17.0, 10.1 Hz, 1H, CH); 7.82 (d, 2H, J = 8.4 Hz, Ph-H3 and H5); 8.08 (m, 4H, Pyr-H2 and H6, Ph-H2 and H6); 8.79 (dd, 2H, J = 1.6, 4.4 Hz, Pyr-H3 and H5); 10.65 (s, 1H, Ph-NH); 14.90 (s, 1H, Triazole-NH) ppm.

^{13}C NMR (DMSO- D_6): δ = 43.8 (CH_2), 119.7 (CH); 120.2 (CH); 127.1 (CH); 127.6 (C); 131.8 (CH); 140.9 (C); 150.6 (CH); 163.6 (CO) ppm.

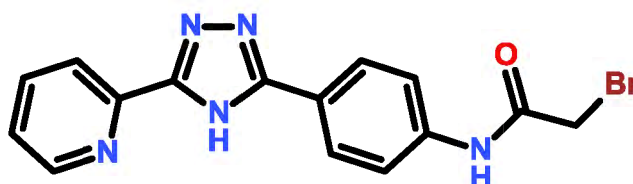
HRMS m/z calcd for $\text{C}_{16}\text{H}_{14}\text{ON}_5$ ($\text{M}+\text{H}$) $^+$, 292.1193; found, 292.1193.

Attempted preparation of 2-bromo-N-[4-[5-(4-pyridyl)-4H-1,2,4-triazol-3-yl]phenyl]acetamide (55a)



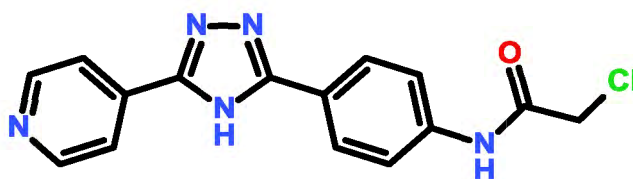
Bromoacetyl bromide (0.10 mL, 0.70 mmol, 1.0 eq) was added dropwise to a stirred solution of amine **22a** (0.1735 g, 0.69 mmol, 1.0 eq) and DIPEA (0.15 mL, 0.86 mmol, 1.2 eq) in dry THF (15 mL) under argon at -78 °C (dry ice bath). After 4 hour stirring, water (100 mL) was added to the reaction mixture at room temperature followed by stirring for 30 min and extracting with ethylacetate (3×50 mL). The organic layers were collected, dried over MgSO₄ and evaporated under reduced pressure at 40 °C. A sticky gel, which was not dissolved in any available solvent, was achieved. This indicates a polymerised mixture.

Attempted preparation of 2-bromo-N-[4-[5-(2-pyridyl)-4H-1,2,4-triazol-3-yl]phenyl]acetamide (55b)



Bromoacetyl bromide (0.24 mL, 1.68 mmol, 1.0 eq) was added to a stirred solution of amine **54b** (0.4170 g, 1.65 mmol, 1.0 eq), DIPEA (0.43 mL, 2.47 mmol, 1.5 eq) in dry THF / DMF (15 mL / 5 mL) under argon at 0 °C. After 4 hour stirring, water (150 mL) was added followed by stirring for 30 min and extracting with ethylacetate (4×50 mL). The organic layers were collected, dried over MgSO₄ and evaporated under reduced pressure at 40 °C. The achieving sticky gel was not dissolved in any available solvent that indicates a polymerised mixture.

Preparation of 2-chloro-N-[4-[5-(4-pyridyl)-4H-1,2,4-triazol-3-yl]phenyl]acetamide (56a)



Chloroacetyl chloromide (0.09 mL, 1.13 mmol, 1.0 eq) was added dropwise to a stirred solution of amine **54a** (0.2771 g, 1.17 mmol, 1.0 eq) and DIPEA (0.25 mL, 1.43 mmol, 1.2 eq) in dry THF (20 mL) under argon at -78 °C. After 3 hour stirring, water (100 mL) was added to the reaction mixture at room temperature (16 °C) followed by stirring for 30 min. The precipitate was collected by filtration, thoroughly washed with water (3×30 mL) and dry under reduced pressure at room temperature. The pure desired product as a cream solid was achieved in 0.3106 g, 0.99 mmol, 85% yield.

M.p: 311.3 – 313.8 °C.

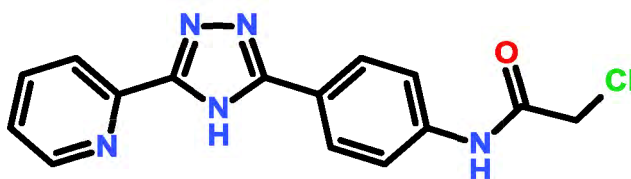
IR (solid, ATR) ν = 3134 and 3203 (m, NH amide), 3090 (m, NH), 1675 (s, CO), 1612, 1547, 1504, 1443, 1405 (s and m, skeletal Ph, Triazole or Pyr) cm^{-1} .

^1H NMR (DMSO- D_6): δ = 4.32 (s, 2H, CH_2); 7.82 (d, 2H, J = 8.4 Hz, Ph-H3 and H5); 8.08 (m, 4H, Pyr-H2 and H6, Ph-H2 and H6); 8.79 (dd, 2H, J = 1.6, 4.4 Hz, Pyr-H3 and H5); 10.65 (s, 1H, Ph-NH); 14.90 (s, 1H, Triazole-NH) ppm.

^{13}C NMR (DMSO- D_6): δ = 43.8 (CH_2), 120.0 (CH), 121.2 (CH), 127.2 (CH), 127.7 (CH), 141.1 (C), 147.7 (C), 165.5 (CO) ppm.

HRMS m/z calcd for $\text{C}_{15}\text{H}_{13}\text{ON}_5\text{Cl}$ ($\text{M}+\text{H}$) $^+$, 314.0805; found, 314.0803.

Preparation of 2-chloro-N-[4-[5-(2-pyridyl)-4H-1,2,4-triazol-3-yl]phenyl]acetamide (56b)



To a stirred solution of compound **54b** (0.1032g, 0.44 mmol, 1.0 eq) in dry DMF (5ml) was added DIPEA (0.14 mL, 0.80 mmol, 1.8 eq) followed by adding dropwise chloroacetyl chloride (0.033 mL, 0.44 mmol, 1.0 eq) at 0 °C under argon. After 20 hours stirring, water (50 mL) was added to the reaction mixture at room temperature (16 °C), followed by stirring for 30 min. The precipitate was collected by filtration, washed with water (3×30 mL) and dry under reduced pressure at room temperature to give the pure desired product as a brown solid (0.2702 g, 0.86 mmol, 84%).

M.p: 257.8 – 264.8 °C.

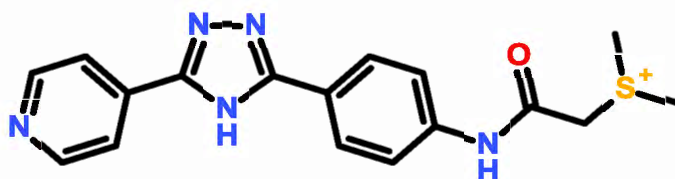
IR (solid, ATR) ν = 3098, 2938 (m, NH), 1674 (s, CO), 1607, 1545, 1504, 1439 (s and m, skeletal Ph, triazole or Pyr) cm^{-1} .

^1H NMR (DMSO- D_6): δ = 4.30 (s, 2H, CH_2); 7.62 (ddd, 1H, J = 0.8, 4.8, 7.6 Hz, Pyr-H4); 7.77 (d, 2H, J = 8.8 Hz, Ph-H3 and Ph-H5); 8.10 (m, 3H, Pyr-H6, Ph-H2 and Ph-H6); 8.24 (d, 1H, J = 8.0 Hz, Pyr-H5); 8.75 (d, 1H, J = 4.8 Hz, Pyr-H3); 10.61 (s, 1H, Ph-NH); 14.90 (s, 1H, triazole-NH) ppm.

^{13}C NMR (DMSO- D_6): δ = 42.0 (CH_2), 44.0 (C), 120.0 (CH), 122.4 (CH), 125.7 (CH), 127.3 (CH), 139.7 (CH), 140.2 (C), 146.5 (C), 149.0 (CH), 165.3 (CO) ppm.

HRMS m/z calcd for $\text{C}_{15}\text{H}_{13}\text{ON}_5\text{Cl}$ ($\text{M}+\text{H}$) $^+$, 314.0805; found, 314.0803.

Attempted preparation of dimethyl-[2-oxo-2-[4-[5-(4-pyridyl)-4H-1,2,4-triazol-3-yl]anilino]ethyl]sulfonium (41c)



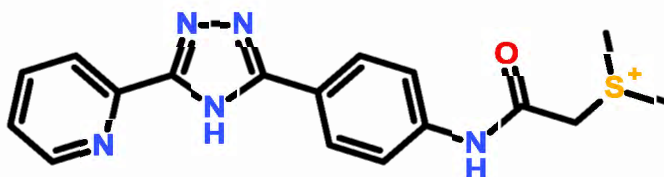
Attempt 1

Adding dimethyl sulphide (0.3 mL, 4.08 mmol, 6.6 eq) to a stirred solution of **56a** (0.1574 g, 0.62 mmol, 1.0 eq) in methanol (10 mL) at room temperature. After 30 hours, the volatiles were removed by evaporation under reduced pressure / 40 °C giving a solid whose ¹H NMR spectra showed no indication of a new formed compound.

Attempt 2

Adding dimethyl sulfide (0.4 mL, 5.45 mmol, 16.5 eq) to a solution of **56a** (0.1033 g, 0.33 mmol, 1.0 eq) and NaI (0.0333 g) in DMF (6 mL). The reaction mixture was stirred at 60 °C for 48 hours followed by adding water (50 mL) and extracting with ethylacetate (2×25 mL). The combined organic layers were dried over MgSO₄ and evaporated under reduced pressure / 40 °C to give a yellow solid (0.0962 g). Analysis ¹H NMR spectrum of the achieving solid indicated compound **56a**. The reaction failed to give the expected compound.

Attempted preparation of dimethyl-[2-oxo-2-[4-[5-(2-pyridyl)-4H-1,2,4-triazol-3-yl]anilino]ethyl]sulfonium (41d)



Attempt 1

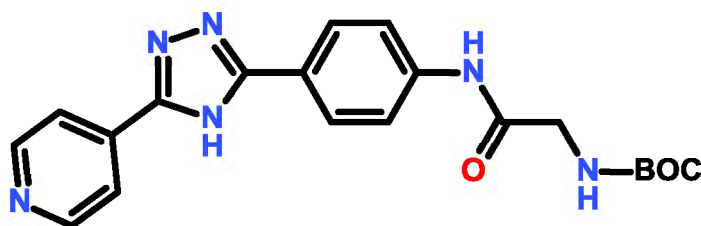
To a stirred solution of the previously attained **56b** (0.2640 g, 0.84 mmol, 1.0 eq) in dry DMF (5 mL), dimethyl sulphide was added dropwise at 0 °C, under argon. The reaction

mixture was stirred at room temperature (18 °C) for 20 hours followed by adding water (70 mL). The precipitate was collected by filtration, thoroughly washed with water (50 mL) and dry under reduced pressure at room temperature to give a brown solid (0.2194 g). However, analysis ^1H NMR spectrum indicated the product was the starting material.

Attempt 2

Dimethyl sulfide (0.35 mL, 4.77 mmol, 19.1 eq) was added to a mixture of **56b** (0.0781 g, 0.25 mmol, 1.0 eq) and NaI (0.0010 g) in DMF (6 mL), followed by stirring at 42 °C for 26 hours. Water (50 mL) was added and the precipitate was collected by filtration, washed with water (40 mL) and dry under reduced pressure / 40 °C. However, analysis ^1H NMR spectrum of the attained solid indicated the starting material **56b**.

Preparation of tert-butyl N-[2-oxo-2-[4-[5-(4-pyridyl)-4H-1,2,4-triazol-3-yl]anilino]ethyl]carbamate (57a)



To a solution of Boc-Gly-OH (1.4877 g, 8.49 mmol, 2.3 eq) and DIPEA (3 mL, 17.22 mmol, 4.6 eq) in anhydrous THF / DMF (10 mL / 5 mL), ethylchloroformate (0.8 mL, 8.37 mmol, 2.3 eq) was added dropwise over 10 min at 0 °C under argon. The resulting mixture was stirred at room temperature (25 °C) for 1 hour then was treated with a solution of amine **54a** (0.8752 g, 3.70 mmol, 1.0 eq) in a mixture of dry THF / DMF (30 mL / 5 mL) followed by stirring for 19 hours. Water (200 mL) was added and the reaction mixture was extracted with ethyl acetate (4×30 mL). The organic layers were collected, washed with saturated aqueous sodium bicarbonate (3×30 mL), dried over MgSO_4 and concentrated under reduced pressure / 40 °C to a 20 mL solution. The crude product was purified by flash chromatography through (ethyl acetate - ethanol 95:5, R_f = 0.25) afforded the desired product as a white solid (0.7293 g, 1.85 mmol, 50%).

M.p: 219.9 - 221.4 °C.

IR (solid, ATR) ν = 3180, 3110 (NH amide), 2957 (NH triazole), 2934 (aromatic CH) 2829 (CH, alkane), 1670 (C=O), 1610, 1522 (C=N), 1508, 1441 (aromatic C=C) cm^{-1} .

^1H NMR (DMSO- D_6): δ = 1.41 (s, 9H, $\text{C}(\text{CH}_3)_3$); 7.10 (t, 1H, J = 12.4 Hz, NHCH_2); 7.77 (d, 2H, J = 8.8 Hz, Ph-H3 and H5); 7.99 (d, 2H, J = 6.0 Hz, Pyr-H2 and H6); 8.03 (d, 2H, J = 8.8 Hz, Ph-H2 and H6); 8.72 (d, 2H, J = 6.0 Hz, Pyr-H3 and H5); 10.19 (s, 1H, Ph-NH); 14.71 (s, 1H, Triazole-NH) ppm.

^{13}C NMR (DMSO- D_6): δ = 28.8 (CH_3), 44.0 (CH_2), 78.3 (C), 113.7 (CH), 119.3 (CH), 120.3 (CH), 150.9 (CH), 156.1 (C), 168.8 (C) ppm.

HRMS m/z calcd for $\text{C}_{20}\text{H}_{23}\text{O}_3\text{N}_6$ ($\text{M}+\text{H}$) $^+$, 395.1826 g/mol; found, 395.1823 g/mol.

Attempted deprotection of BOC group from 57a

A stirred solution of **57a** (0.5193 g, 1.27 mmol, 1.0 eq) in THF (30 mL) was cooled down to 0 °C, concentrated trifluoroacetic acid (10 mL) was added dropwise. The resulting suspension was stirred at room temperature (25 °C) for 20 hours, then was basified with saturated sodium bicarbonate to basic pH (8) and extracted with ethyl acetate (4×20 mL). The organic layers were collected, dried over MgSO_4 and evaporated to obtain a solid. Unfortunately, TLC (ethylacetate-methanol 95:5) and ^1H NMR spectra of the achieving solid indicated no new compound was generated.

The reaction was carried out again in the same condition but using hydrochloric acid instead of trifluoroacetic acid with the higher portion (5 mL of hydrochloride acid 5M in a 12 mL solution of the carbamate in THF). Time for the reaction was 19 hours and the work up process was similar to the previous procedure. However, analysis the ^1H NMR spectra identified the resulting solid was the starting material. Using DMF, a more polar solvent than THF and carrying out the reaction in the same condition was also unsuccessful to detach BOC group.

Attempted coupling 54a and Fmoc-Gly-OH

A solution of Fmoc-Gly-OH (0.3113g, 1.05 mmol, 1.4 eq) and CDI (0.1500 g, 0.93 mmol, 1.3 eq) in dry THF (15 mL) was stirred at 30 °C under argon for 1 hour. The resulting mixture was treated with a solution of amine **54a** (0.1770g, 0.75 mmol, 1.0 eq) in dry THF (15 mL) and stirred at room temperature (23 °C) under argon for 24 hours. Water (70 mL) was added to the reaction mixture. The precipitate was collected by filtration, thoroughly washed with water (150 mL) and dry under reduced pressure / 40 °C overnight. Analysis ¹H NMR spectrum of the product indicated a complex mixture with a very small portion (<5%) of the expected compound.

7 Screening potency of potential inhibitors of TG2

7.1 Method

7.1.1 Preparation of inhibitors

All tested inhibitors were dissolved in DMSO to make a stock concentration of 10 mM. The stock was diluted in DMSO to prepare various concentrations of the inhibitors for screening assays. The solution of inhibitors was stored at -20 °C until use.

7.1.2 Data analysis

The potency of the tested compounds was measured in terms of the half-maximal inhibitory concentration (IC_{50}). GraphPad Prism Version 7 and Version 8 was used to draw log[inhibitor]-%TG2 activity curves and to calculate IC_{50} (relative IC_{50}) value which is defined as “the concentration required to bring the curve down to the half way point between the top and bottom plateaus of the curve” (Motulsky, 2019).

7.1.3 Protocol

7.1.3.1 Screening potency of compounds as irreversible inhibitors of TG2

The potency of the potential irreversible TG2 inhibitors successfully synthesised in chapter 6 was tested against human tissue transglutaminase recombinantly produced in insect cells (rhTG2) (Zedira, Germany). TG2 activity was measured using an enzyme linked sorbent assay technique to measure the covalent incorporation of a primary amine substrate N-biotinyl cadaverine (N-(biotinamido)-1,5-diaminopentane hydrochloride) into human fibronectin, a glutamine-containing protein substrate. Briefly, a 96-well microtitre plate was coated with 50 μ L of fibronectin human plasma (10 mg/mL) in TBS-Tween at 4°C over night or at 37 °C for one hour, then it was washed 3 times with 50 mM Tris-HCl pH 7.4. A reaction mix (100 μ L) containing rhTG2 (400 ng/mL), N-biotinyl cadaverine (0.1 mM), $CaCl_2$ (10 mM) and DTT (1 mM) with various concentrations of a tested compound in 50 mM Tris-HCl pH 7.4 was added into the coated wells and was incubated for 1 h at 37 °C. DTT (dithiothreitol) is a water-soluble reducing reagent used to prevent the oxidation of TG2. RhTG2 (400 ng/mL) in 50 mM Tris-HCl pH 7.4 containing N-biotinyl cadaverine (0.1 mM), $CaCl_2$ (10 mM)

and DTT (1 mM) was used as the positive control. RhTG2 (400 ng/mL) in 50 mM Tris-HCl pH 7.4 containing N-biotinyl cadaverine (0.1 mM) and EDTA (10 mM) was used as the negative control. EDTA (ethylenediamine tetraacetic acid) is a calcium chelator used to block TG2 activity. The plate was then washed 3 times with 50 mM Tris-HCl pH 7.4 before being blocked with 100 μ L of blocking buffer (3% (w/v) BSA in 50 mM Tris-HCl pH 7.4) for 30 min at 37 °C. BSA (bovine serum albumin) is a small, stable, non-reactive protein that binds non-specific binding sites. After blocking of non-specific binding, the wells were incubated with 100 μ L HRP (horse radish peroxidase) - conjugated ExtrAvidin-Peroxidase (Sigma-Aldrich, UK), a biotin binding protein, in the blocking buffer (1:1,000 dilution) for 1 h at 37 °C. After another set of washes, the colour was developed by adding 100 μ L developing buffer containing OPD (o-phenylenediamine dihydrochloride), a water-soluble substrate for HRP that produces a yellow-orange product detectable at 490nm by an ELx808TM Spectrafluor plate reader. The OPD solution was prepared by dissolving of two Sigma Fast OPD tablets (1 in gold coloured film and 1 in silver coloured film) into 20 mL distilled H₂O. The colour development was stopped by adding 50 μ L of 3M HCl and the absorbance was read at 490 nm.

7.1.3.2 Screening potency of compounds as allosteric inhibitors of TG2

The parent allosteric inhibitor (compound **6**) was identified as a slow-binding inhibitor which binds to the enzyme on a time scale of minutes rather than the time scale of classical inhibitors (milliseconds) (Case and Stein, 2007). Therefore, the protocol to screen the potency of the potential allosteric inhibitors of TG2 started with a pre-incubation step where the reaction mix containing TG2 (400 ng/mL), DTT (1 mM) with varying concentrations of inhibitor in 50 mM Tris-HCl pH 7.4 was incubated for 30 min on ice before adding of N-biotinyl cadaverine (0.1 mM) and CaCl₂ (10 mM). The remaining steps followed the method used to test the inhibitory effect of the potential irreversible inhibitors as described above. The positive and negative controls were similar to the ones described in the above protocol.

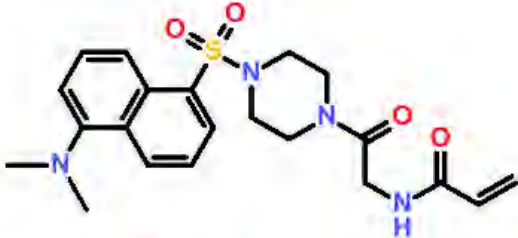
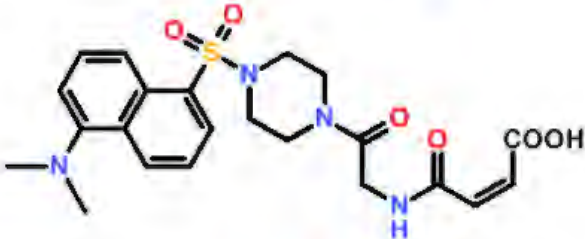
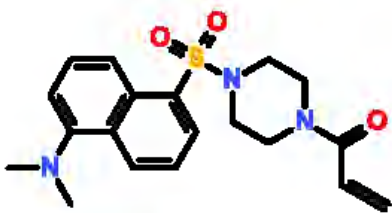
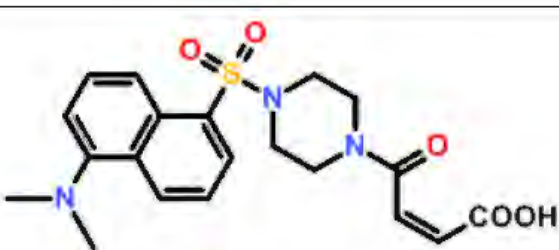
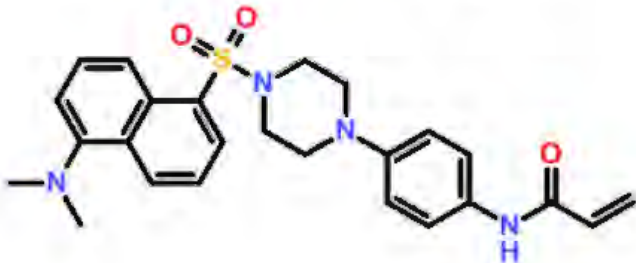
7.2 Results and discussion

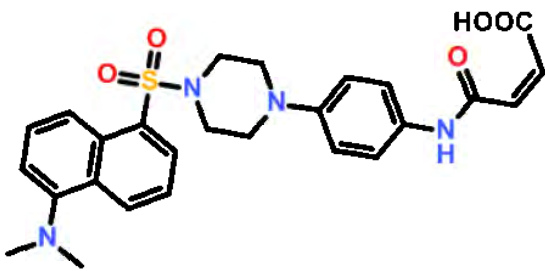
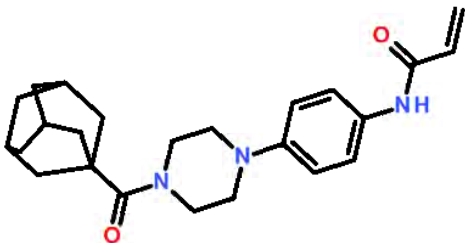
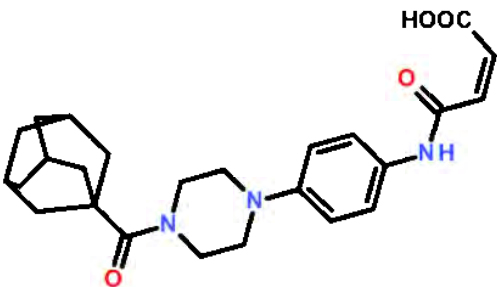
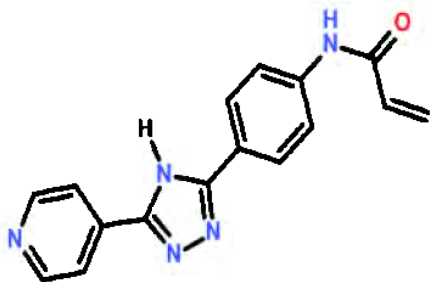
7.2.1 Potency of potential irreversible inhibitors of TG2

The potential TG2 inhibitors synthesised in chapter 6 and some compounds prepared by an Aston MSc. student under the supervision of Dr. Dan Rathbone were screened for their potency against rhTG2 during the course of this PhD research. The inhibition data against rhTG2 of the lead irreversible inhibitor of TG2 developed by the Griffin group (compound **27**) and the newly synthesised compounds are summarised in Table 7.1. Log [inhibitor] - %TG2 activity curves of all the tested compounds are shown in Table 10.1. Compound **27** had an IC_{50} value of 20 ± 0.003 nM which is more than 3 times higher than the result from published resource (Badarau et al., 2015). All the newly synthesised compounds had lower potency than the lead developed inhibitor. The shortening of the scaffold (compound **27e**) significantly reduced the inhibitory effect. Compound **27g** which was modified from compound **27** by adding a phenyl ring between the piperazine ring and the acrylamide warhead had a significant higher IC_{50} value (13.5 ± 3.0 μ M) than compound **27**. The same reduction in the potency was observed in compound **26a**, which was modified from compound **26**. The data suggests the distance between the N atom of the piperazine ring and the acrylamide warhead in compound **27** is possibly the optimal. The attachment of a carboxylic group on the *cis* position of the acrylamide warhead in the attempt to reduce the potential toxicity of the highly electrophilic warhead was observed to halt the inhibitory activities.

Similar to compound **26** and **27**, two compounds **26a** and **27g** share the same structure except for the lipophilic ring which was indicated in chapter 5 to bind into the hydrophobic pocket of the catalytic binding site. The higher potency achieved in compound **27g** confirmed the advantage of the N,N-dimethyl-naphthalene over the adamantyl ring in the improving the potency. The acrylamide compound with a 4-pyridyl triazolyl phenyl scaffold (compound **41a**) shares the similar rigid sidechain, a phenyl acrylamide warhead, as compounds **27g**. However, the IC_{50} value of compound **41a** is less than one third of that of compound **27g**. That suggests the compact 4-(4H-1,2,4-triazol-3-yl)pyridine possibly favours the potency than the bulky N,N-dimethyl-5-piperazin-1-ylsulfonfyl-naphthalen-1-amine when the warhead was held by a rigid phenyl.

Table 7.1. Inhibition data for the lead TG2 irreversible inhibitor (compound **27**) and the newly synthesised irreversible TG2 inhibitors.

Compound	Structure	IC ₅₀ (μ M)
27		0.020 ± 0.003
(Z)-27b		>50
27e		8.9 ± 1.6
(Z)-27f		>50
27g		13.5 ± 3.0

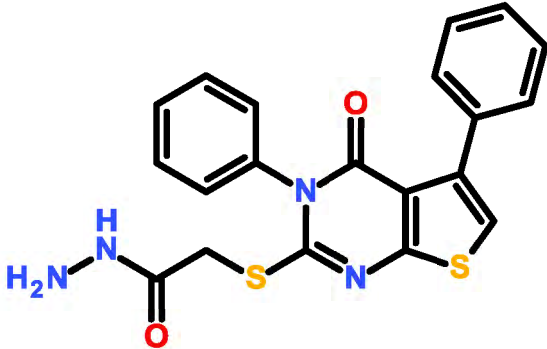
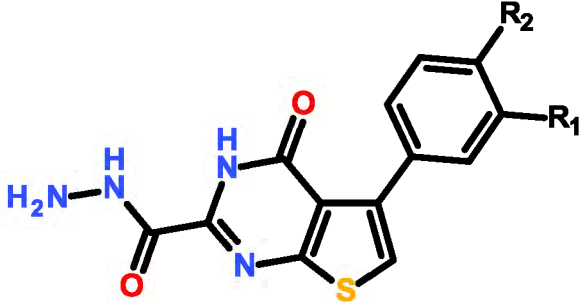
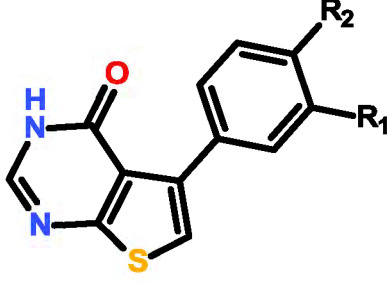
(Z)-27h		>50
26a		>25
(Z)-26b		>50
41a		3.9 ± 0.7

7.2.2 Potency of the potential allosteric inhibitors of TG2

The inhibition data against rhTG2 for the parent allosteric inhibitor (compound **6**) and the potential TG2 inhibitors synthesised in chapter 5 are summarised in Table 7.2. Log [inhibitor]-%TG2 activity curves of all the tested compounds are shown in Table 10.2. In the absorbance assay used in this study, compound **6** had an IC_{50} value of 7.3 ± 0.8 μ M against rhTG2 while its IC_{50} was 0.6 μ M in the kinetics assay (Duval et al., 2005). Among the potential allosteric TG2 inhibitors successfully synthesised in chapter 5, all the carboxylic acids and esters and amides showed very low inhibitory effects against rhTG2 at 100 μ M. Those results are in good agreement with the key published paper (Duval et al., 2005) which indicated that acid, ester, amide analogs showed very little potency against hTG2. An attempt to increase solubility by introducing a basic amine into the amide side-chain caused a complete loss of inhibitory activity.

The acylhydrazides showed the highest inhibition with the IC_{50} value of the two most potent compounds reaching nearly half the parent compound. According to Case and co-workers (Duval et al., 2005) the acylhydrazone thioether side-chain was vital for inhibitory activity. Here it indicates that the acylhydrazone group possibly played a key role in the potency of this class of TG2 inhibitors. Interestingly, 5-phenyl-3H-thieno[2,3-d]pyrimidin-4-one derivatives, which have no side chain, expressed inhibitory effects with IC_{50} values slightly lower than the parent inhibitor. The results suggest that the potency of this class of TG2 inhibitors is significantly affected by the type of the side-chain attached on the pyrimidine ring. Among the compounds having high potency: the acylhydrazides and the 5-phenyl-3H-thieno[2,3-d]pyrimidin-4-ones, the compounds having one methyl group attached on the para position of the phenyl ring expressed the highest potency. This indicates the attachment of one methyl group on the para position of the phenyl ring possibly can enhance the stability of the inhibitors when it bound to the allosteric site consequently improving the potency. However, the adding of two methyl groups on the phenyl ring did not show clear and consistent effects on the potency.

Table 7.2. Inhibition data for the lead allosteric TG2 inhibitor (compound **6**) and the newly synthesised allosteric TG2 inhibitors.

Compound	Structure	R ₁	R ₂	IC ₅₀ (μM)
6				7.3 ± 0.8
35a		H	H	6.0 ± 1.5
35b		CH ₃	H	4.1 ± 0.7
35c		CH ₃	CH ₃	4.3 ± 0.6
39a		H	H	6.6 ± 1.0
39b		CH ₃	H	5.7 ± 1.0
39c		CH ₃	CH ₃	8.2 ± 1.0

7.2.3 Investigation of the inhibitory effect against rhTG2 of the most potent newly synthesised allosteric inhibitor in the presence of GTP

The same absorbance read at 490 nm for the positive control in the TG2 assay was observed when changing the concentration of CaCl₂ from 10.0 mM to 2.0 mM. This result pointed out that rhTG2 maintained the same activity when reducing the

concentration of CaCl_2 from 10.0 mM to 2.0 mM. The assay used to measure the potency of GTP was carried out in the same protocol used to evaluate the potency of the potential allosteric inhibitors as described in part 7.1.3.2. However, in this assay, the concentration of CaCl_2 was reduced from 10.0 mM to 2.0 mM. The result showed that at 0.5 mM, GTP inhibited around 50% of TG2 activity and at 2.0 mM it blocked nearly all TG2 activity. These values are in good agreement with the data from previously published experiments (Bergamini, 1988; Bergamini and Signorini, 1993) in which TG2 was proven to bind 6 molecules of calcium with the same affinity for each ion while it binds only one molecule GTP. Our data is consistent with the reported results (Bergamini, 1988) which proved that GTP reduces the affinity of the enzyme for calcium in addition to the alteration of the conformation of the enzyme.

The protocol to evaluate the effect of the binding of the most potent newly synthesised allosteric inhibitor on the binding site of GTP was similar to the protocol described in 7.1.3.2 except for the pre-incubation mixture contained GTP (0.5 mM) and the concentration of CaCl_2 was 2.0 mM. Log [inhibitor]-%TG2 activity curves of compound **35b** with and without the addition of GTP are shown in Figure 7.1. The combination of the two inhibitors was observed to improve the potency especially when concentrations of compound **35b** are lower than its IC_{50} value. However, there is no significant increase in the potency when concentrations of **35b** are higher than its IC_{50} value. The combination of compound **35b** and GTP cannot completely block rhTG2 activity when both compounds are at IC_{50} concentrations. This indicates the inhibitory effect of compound **35b** and GTP do not combine. The parent compound was proved to be mutually exclusive inhibitor of GTP in a published report (Case and Stein, 2007). Here, the preliminary data can not indicate whether compound **35b** and GTP can bind at the same time (non-exclusive) at two different sites or not.

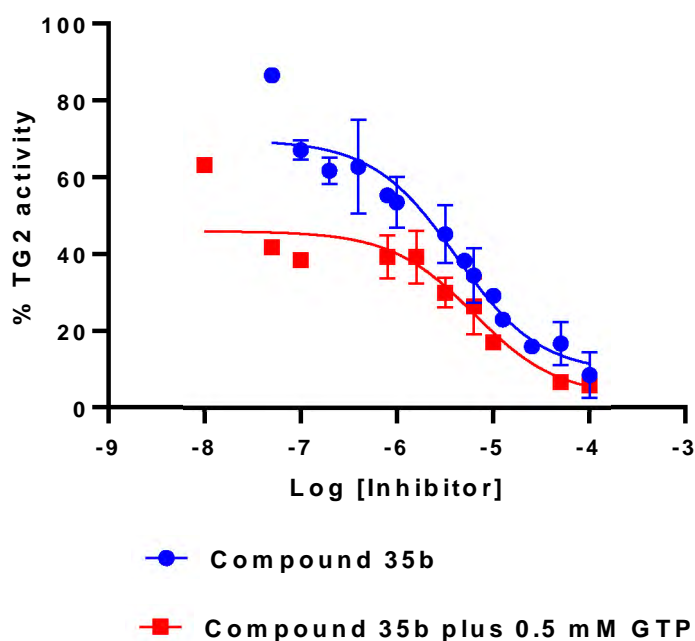


Figure 7.1. Log [inhibitor]-%TG2 activity curves of compound **35b** with and without addition of GTP.

7.3 Conclusion

All the newly synthesised irreversible inhibitors of TG2 expressed lower potency than the parent inhibitors (compound **26** and **27**). The compound modified from compound **27** but having a shorter side chain (compound **27e**) significantly reduced the potency. The inserting a phenyl ring between the piperazine ring and the acrylamide warhead (compound **26a** and **27g**) significantly reduced the potency. Among the acrylamide compounds having the warhead attached on the phenyl ring, lower potency was observed in the compounds having a more bulky lipophilic part. Particularly, the pyridyl ring favours the potency than the N,N-dimethyl-naphthalene which was also confirmed to have more advantage than the adamantyl ring in the improving of the potency. The attachment of a carboxyl group on the *cis* position of the acrylamide warhead in the attempt to reduce the potential toxicity caused the loss of the potency.

Among the newly synthesised allosteric inhibitors of TG2, all the acylhydrazide derivatives expressed higher potency than the parent compounds. The IC_{50} values of the two most potent compounds are nearly half the parent compound. The compounds with acid, ester, amide and amine side chains showed little inhibitory effects while two

compounds with no side chain were slightly more potent than the parent compound. The attachment of one methyl group at the para-position of the phenyl ring showed the increase of the potency in both the acylhydrazides and the 5-phenyl-3H-thieno[2,3-d]pyrimidin-4-ones. However, the effect on the potency caused by the attachment of methyl groups at meta- and para- positions is not clear and consistent. The preliminary assay indicates that the most potent allosteric inhibitor (compound **35b**) and GTP do not have additive effects in inhibition of rhTG2.

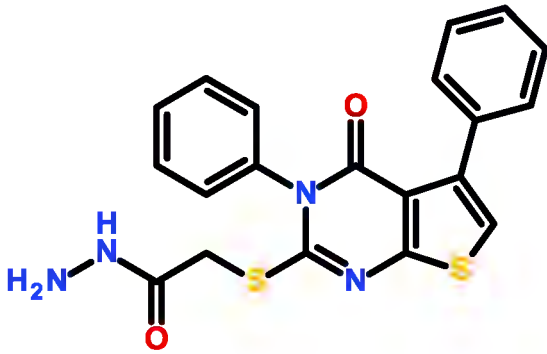
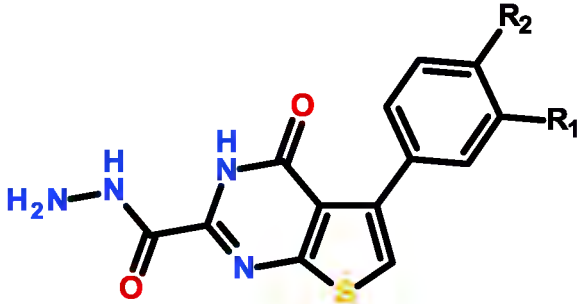
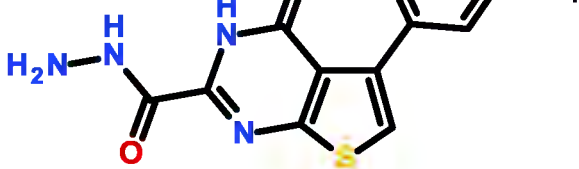
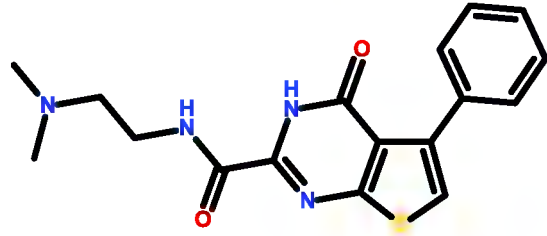
8 Long molecular dynamics simulations of TG2 allosteric inhibitors

8.1 MD simulations applied for the whole TG2 structure

The empty TG2 and some complexes having a ligand docked into the predicted allosteric site of TG2 were subjected to long MD simulation (around 800 ns). Here, the parent inhibitor (compound **6**), the two most potent inhibitors (compound **35b** and **35c**) and an amine without any inhibitive effect (compound **32a**) were used as the ligands. The process of preparation of TG2 coordinates, docking of the ligands into the predicted allosteric site and running MD simulations of TG2 without binding or surrounding of any ligand was carried out by Dr. Dan Rathbone. The structures and IC₅₀ values of the compounds being subjected to the MD simulations are listed in Table 8.1.

In these MD simulations, a repaired version of the whole crystal structure of TG2 in the open conformation (2Q3Z) was used in order to identify any bending of the enzyme structure that may affect the approaching of the substrates into the catalytic tunnel under the binding of a potential allosteric inhibitor. The behaviours of TG2 was analysed using a clustering method which gathers similar conformational states from MD trajectories. The structures of TG2 in the two most different clusters (the first and the last cluster) were superimposed to compare the modification of the enzyme conformation. The RMSF values of individual residues of the enzyme in the complexes were compared to those of the empty TG2 to identify the most mobile residues. The effect of the binding of the ligand into the predicted allosteric site on the catalytic core domain was also observed and analysed.

Table 8.1. Ligands used for long MD simulations of TG2-ligand complexes.

Name	Structure	R ₁	R ₂	IC ₅₀ (μM)
6				7.3 ± 0.8
35b		H	CH ₃	4.1 ± 0.7
35c		CH ₃	CH ₃	4.3 ± 0.6
32a				No inhibition

8.1.1 MD simulation of the empty TG2 (run 1)

This run was used to evaluate the behaviour of TG2 in the absence of any ligand docked. It was used as the control for other runs. The atomic fluctuations of the individual residues (Figure 8.1) showed that the C terminal β-barrel (residue 592 to 687) had the highest degree of fluctuation compared to other regions of TG2. The fluctuation of this terminal β-barrel was observed to induce bending conformations which both toward and outward the catalytic tunnel. It can be clearly seen from the differences of

the TG2 conformation in the first cluster and the two other clusters as shown in Figure 8.2.

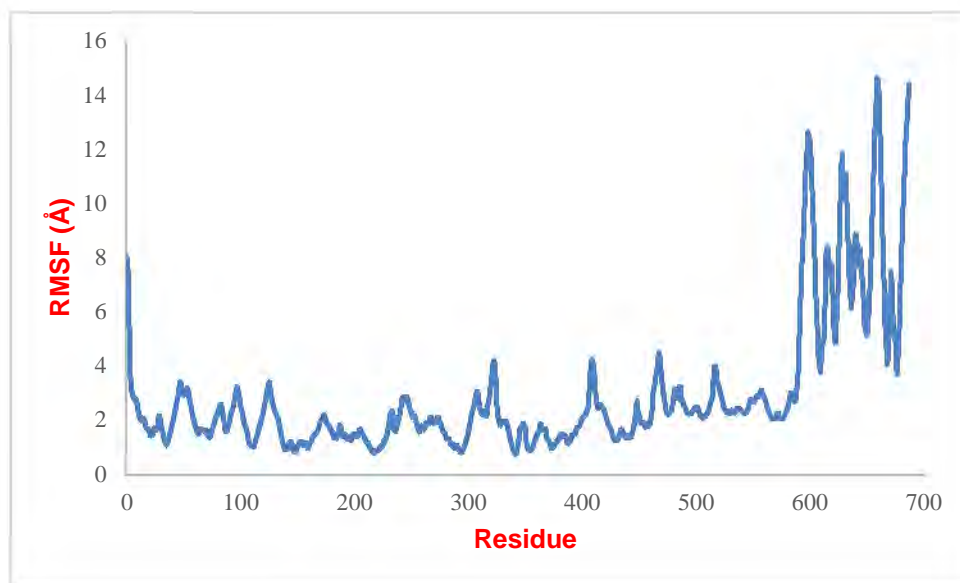


Figure 8.1. RMSF values of empty TG2 during 800 ns MD simulation.

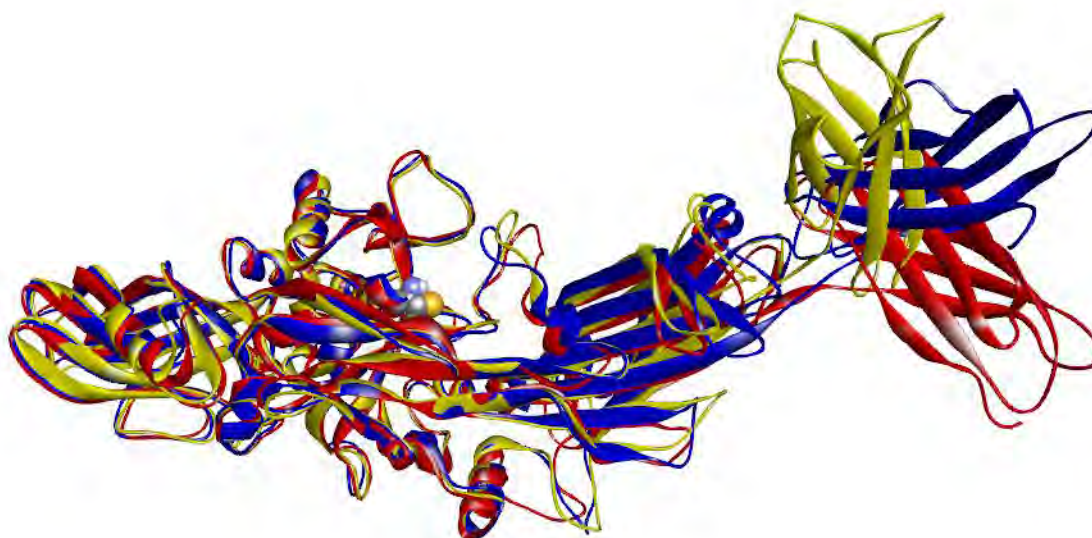


Figure 8.2. Conformations of TG2 in the first cluster (blue), cluster 3 (yellow) and the final cluster (red) in run 1.

Two tryptophan residues TRP241 and TRP332 are located on separate loops opposite to the catalytic tunnel which contains the nucleophilic CYS277. These two tryptophan residues were observed to be stable during the 800 ns MD simulation and hydrophobic interactions were formed between the two five-membered rings facing each other and the benzene rings were parallel to each other. During the simulation, the loop containing

TRP332 was observed to be held firmly by hydrogen bonds between a residue located in this loop, SER328 and two residues PRO361 and GLN362 which reside on the opposite loop. These two loops are located in front of the proposed acyl-acceptor entrance. The mentioned loops and residues are indicated in Figure 8.3.

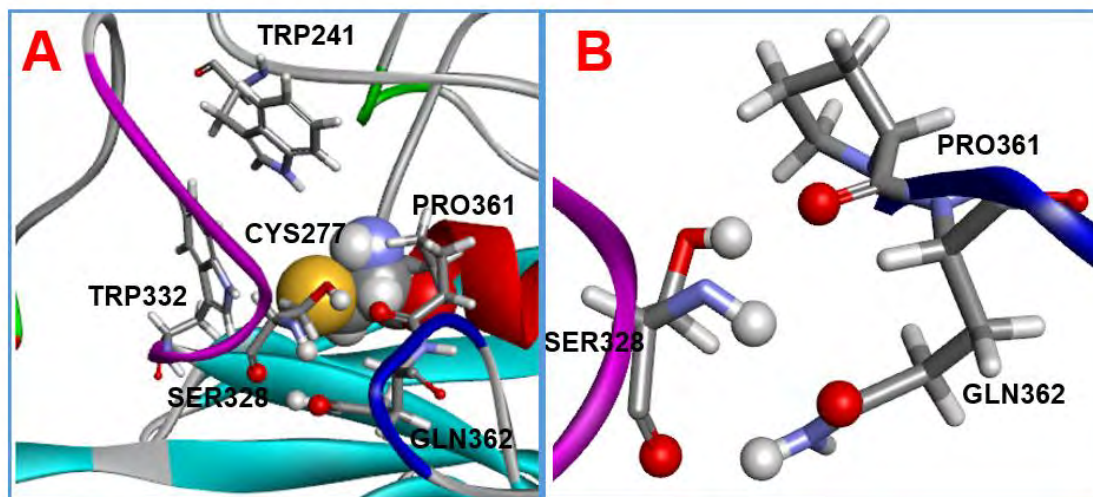


Figure 8.3. Positions of CYS277, TRP241, TRP332 and two loops (coloured in purple and blue) residing in front of the proposed acyl-acceptor entrance (A) and the residues forming hydrogen bonds between these loops (B).

It can be seen from Figure 8.4 that the distance between the hydrogen of SER328 backbone amine and the oxygen of GLN362 side chain carbonyl as well as that between the hydrogen of SER328 hydroxyl and the oxygen of PRO361 backbone carbonyl were mostly lower than 3.0 Å during the simulation time. In addition, the distance between the relevant atoms of the hydrogen bond between the SER328 backbone carbonyl and the GLN362 side chain amine also fluctuated mainly less than 4.0 Å. The data indicated the strong and long-lasting hydrogen bonds formed between these residues and that restrained the loops containing them. It suggests that the hydrogen bonds between those two loops contributed to the stability of TRP332 and therefore stabilised TRP241. Two tryptophan residues TRP241 and TRP332 are critical for the transamidating activity since they stabilise the enzyme-thiol intermediates that are formed during catalysis. Dual hydrogen bonds formed between the backbone NH of the catalytic CYS277 and the side chain NH of TRP241 with the intermediates were indicated by both the computer model and biochemical data to stabilise the tetrahedral oxyanion intermediates (Pinkas et al., 2007; Iismaa et al., 2003). The stability of TRP241 and

TRP332, especially the NH of the indole side chain of TRP241 in the catalytic tunnel, during the long simulation may be necessary for their indicated roles.

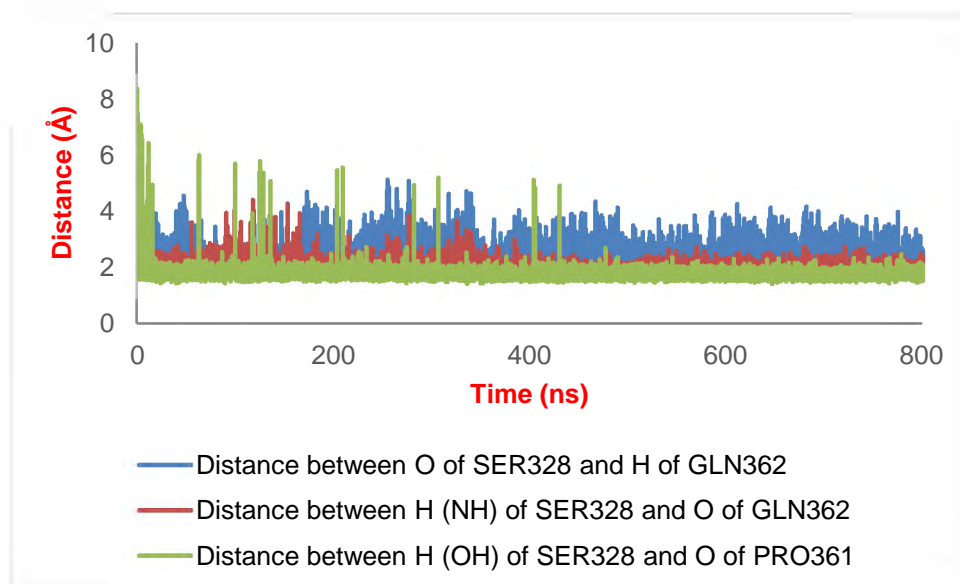


Figure 8.4. Distances between the relevant atoms of the hydrogen bonds between SER328 and two residues PRO361 and GLN362 during 800 ns MD simulation of the empty TG2.

8.1.2 MD simulation of the compound having no inhibitory effect (run2)

The ligand started leaving the predicted binding site after around 190 ns and then was completely unbound after about 250 ns simulation. This can be clearly seen from the RMSD values of the ligand as given in Figure 8.5. The transient binding of this compound into the predicted allosteric inhibitor during the MD simulation may be the evidence for the lack of inhibitory effect in this compound.

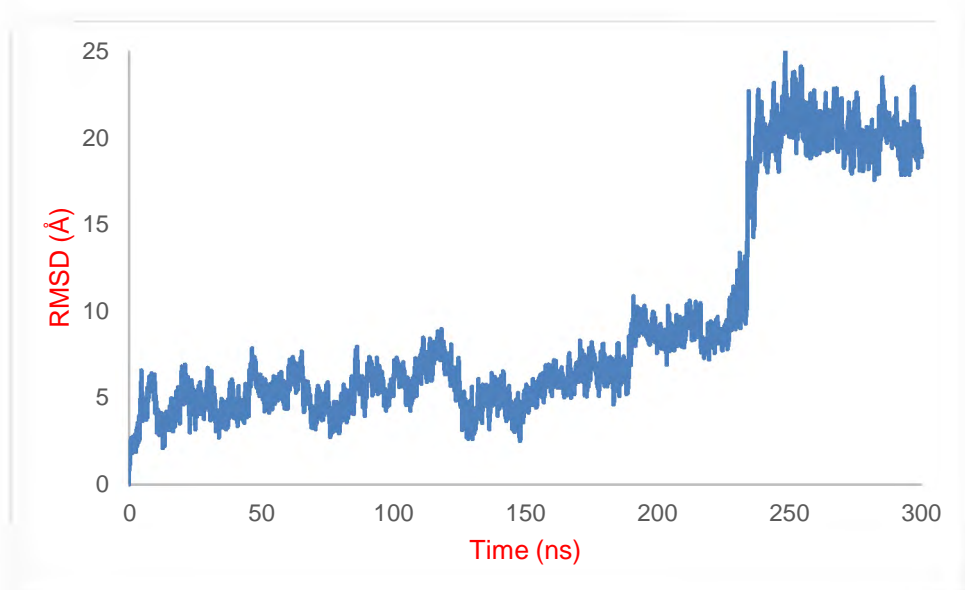


Figure 8.5. RMSD values of compound **32a** during 300 ns MD simulation.

8.1.3 MD simulation of TG2 docked potent inhibitors complexes

8.1.3.1 MD simulation of the parent inhibitor-TG2 complex (run 3)

The tail of the parent compound was significantly mobile and that made this ligand portable and it moved towards the outside of the predicted binding site. It was maintained in the predicted binding site but not as deep as the starting position. It left the predicted binding site after around 750 ns simulation. During the period the ligand stayed inside the predicted binding site the whole structure of TG2 was stable and no significant modification of TG2 conformation was observed. The stable conformation of the enzyme during this run is indicated in Figure 8.6 which shows the superimposed structures of TG2 in the two most different clusters (the first and the final). Comparing the RMSF values of the enzyme (Figure 8.7) in run 1 and run 3, it is observable that most of the residues fluctuated more significantly in run 1 than in run 3, especially the C terminal β -barrel. The modification of the TG2 conformation in this model is different from results from the previous accelerated MD simulations (Jasim, 2016) which indicated a bending towards to the catalytic site of the enzyme being similar to the effect caused by the binding of GTP into the GTP/GDP binding site.



Figure 8.6. Conformations of TG2 in the first (blue) and the final (red) cluster of 700 ns MD simulation of the parent allosteric inhibitor – TG2 complex.

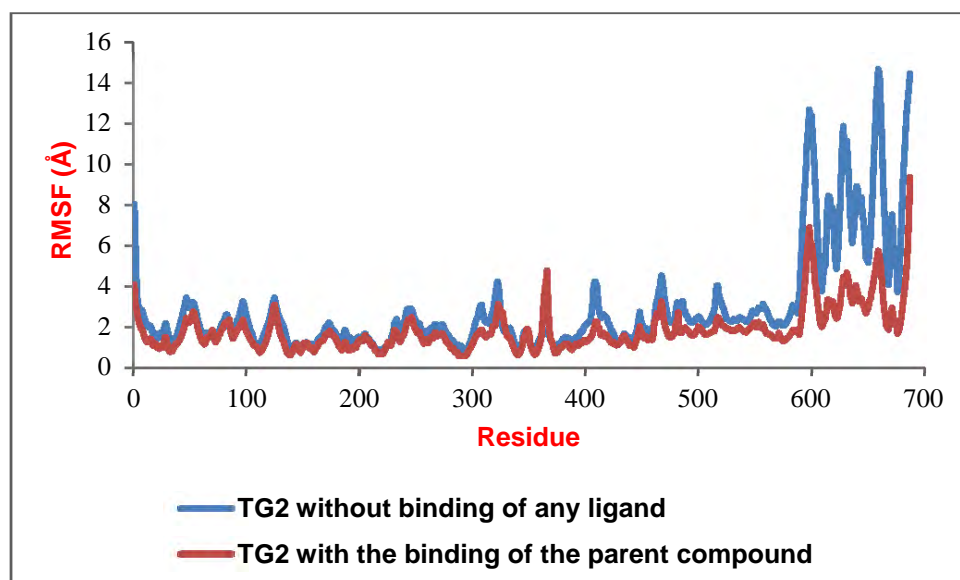


Figure 8.7. RMSF values of the empty TG2 and TG2 under the binding of the parent allosteric inhibitor during 700 ns MD simulation.

During the simulation, hydrogen bonds formed between the ligand and residue ALA399 (backbone) had the highest occurrence (28.40%). It can be seen from Figure 8.8 that the distance between the oxygen of ALA399 backbone carbonyl and the hydrogen of the ligand amino side chain mostly fluctuated less than 4.0 Å during the simulation time.

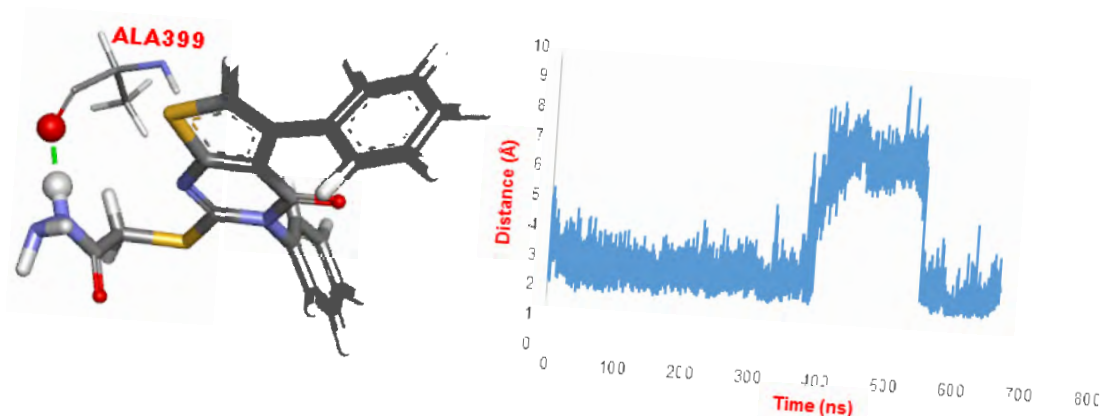


Figure 8.8. A hydrogen bond between the parent allosteric inhibitor and residue ALA399 and the distance between the relevant atoms.

8.1.3.2 MD simulation of compound **35c** - TG2 complex (run 4)

Very early in the simulation, the aromatic ring left the hydrophobic pocket and relocated to the entrance of the predicted binding site. The ligand was still maintained in the predicted binding site during 800 ns simulation but in the opposite orientation. The conformation of TG2 in the first and the final cluster are shown in Figure 8.9. It is visible that there is a slight movement of the C terminal β -barrel towards the outside of the catalytic tunnel. Comparison of RMSF values of TG2 in complex with compound **35c** and that of the empty TG2 in Figure 8.10 confirmed the more stable fluctuation of TG2 residues under the binding of compound **35c**.

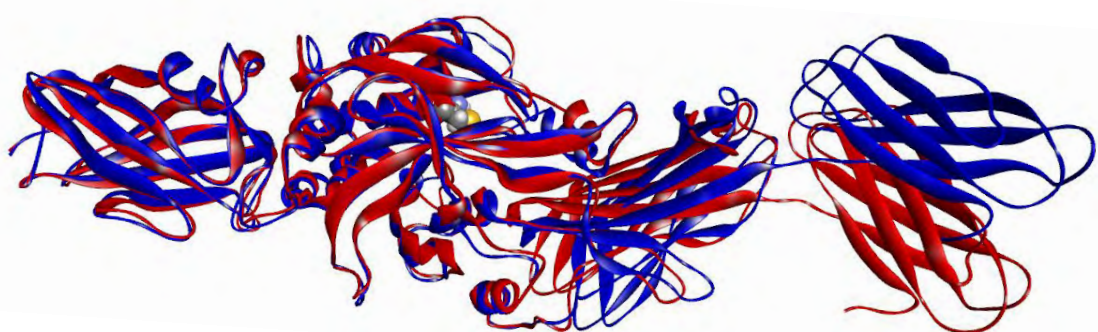


Figure 8.9. Conformations of TG2 under the binding of compound **35c** in the first (blue) and the final (red) cluster during 800 ns MD simulation.

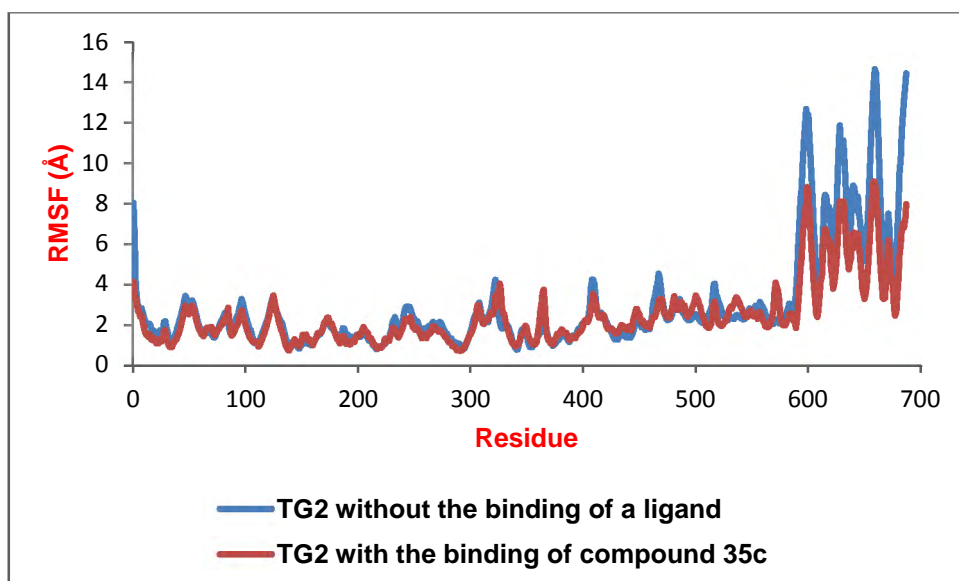


Figure 8.10. RMSF values of the empty TG2 and TG2 under the binding of compound **35c** during 800 ns MD simulation.

During the simulation, hydrogen bonds formed between the ligand and two residues ALA399 (backbone) and ASP400 (side chain) (Figure 8.11) had the highest occurrences. The hydrogen bonds between the amino groups of the ligand and the carbonyl group of ALA399 dominated during the first 500 ns simulation and that disappeared after 500 ns. In contrast, the hydrogen bonds between the ligand and ASP400 were formed after 600 ns and were maintained till the end of the simulation. That can be seen from the distances between the relevant atoms during the simulation as given in Figure 8.12. Overall, the ligand formed the strong and stable hydrogen bonds with the loop containing residues ALA399 and ASP400.

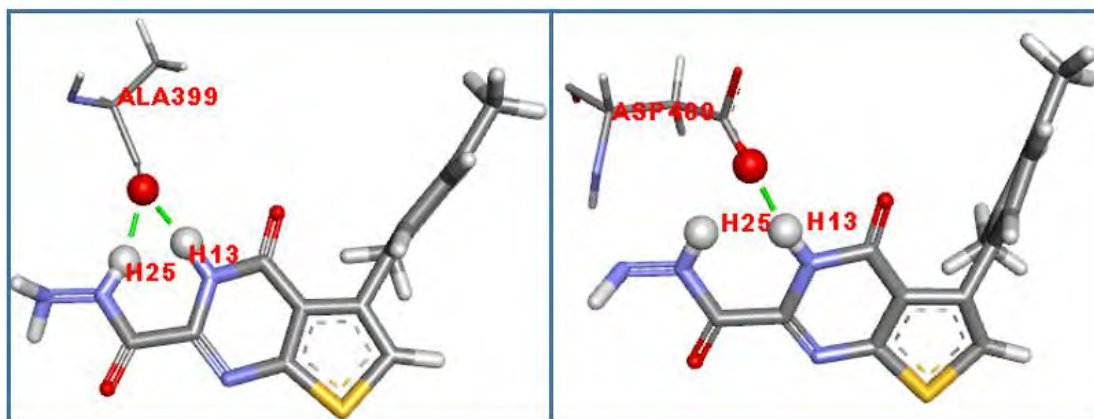


Figure 8.11. Hydrogen bonds between compound **35c** and two residues ALA399 and ASP400.

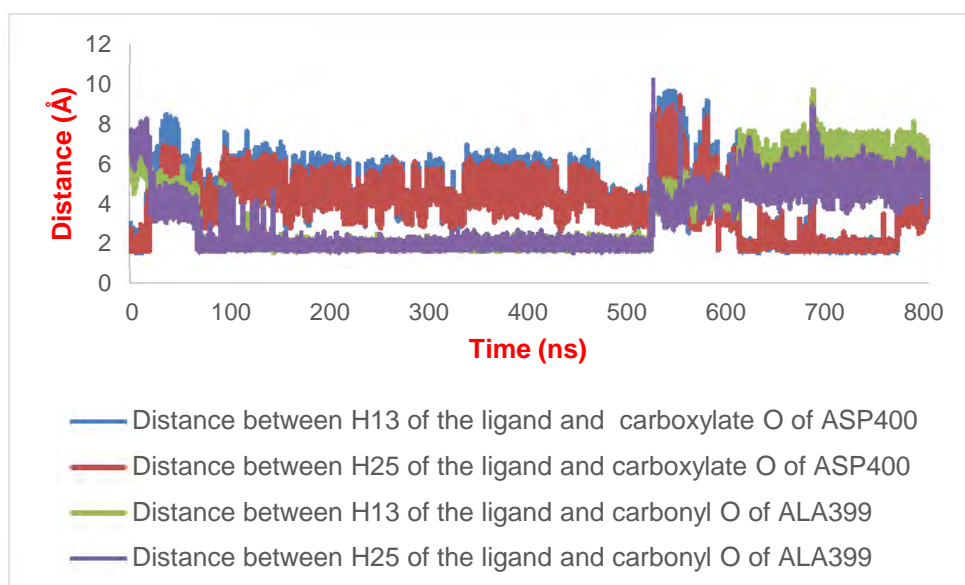


Figure 8.12. Distances between the relevant atoms of the hydrogen bonds formed between compound **35c** and two residues ALA399 and ASP400.

8.1.3.3 MD simulation of compound **35b** - TG2 complex (run 5)

In contrast to the parent compound and compound **35c**, this inhibitor stayed stable into the predicted binding site during the 800 ns MD simulation. This can be clearly seen from the RMSD values of compound **35b** in comparison to those of compound **35c** and the parent compound as shown in Figure 8.13.

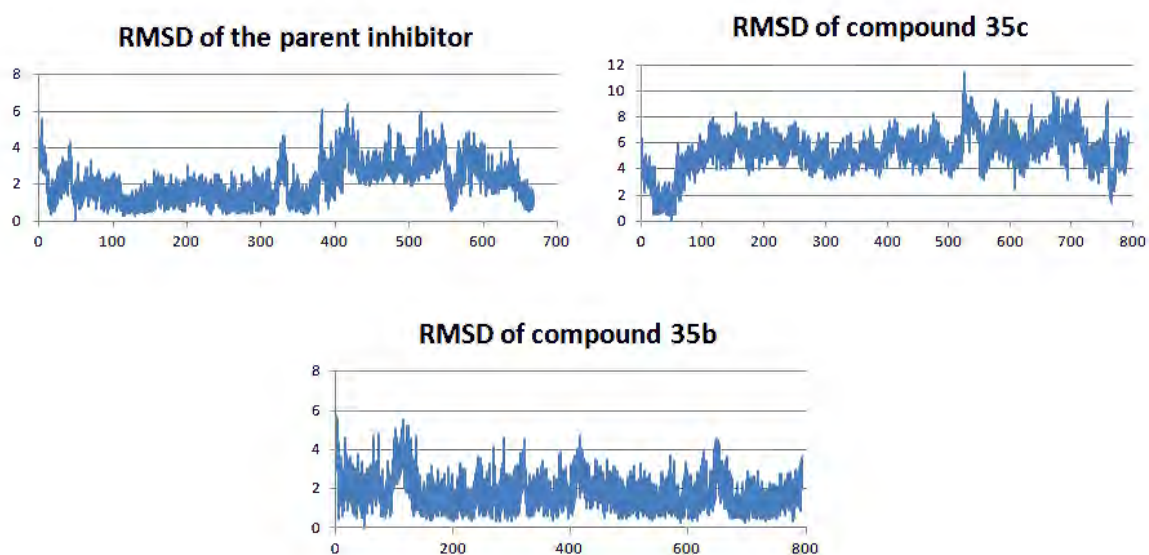


Figure 8.13. RMSD (Å) of the parent compound, compounds **35b** and **35c** during the MD simulations.

Similar to the MD trajectories of the parent compound, during this run, TG2 was maintained in the open conformation without any significant change as shown in Figure 8.14 which compares the conformations of TG2 in the first and the final cluster.

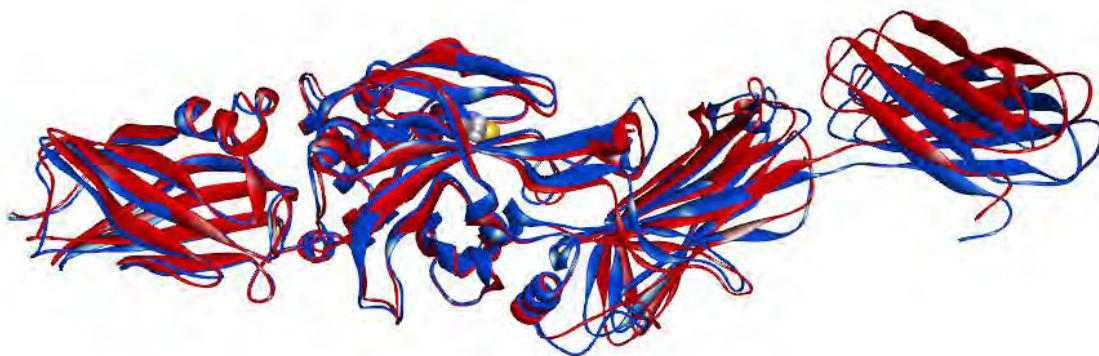


Figure 8.14. Conformations of TG2 under the binding of compound **35b** in the first (blue) and the final (red) cluster.

The RMSF values of the enzyme with the binding of compound **35b** in comparison to that of the empty TG2 are shown in Figure 8.15. The data indicated a more stable structure of TG2 was achieved when the enzyme was bound by this inhibitor.

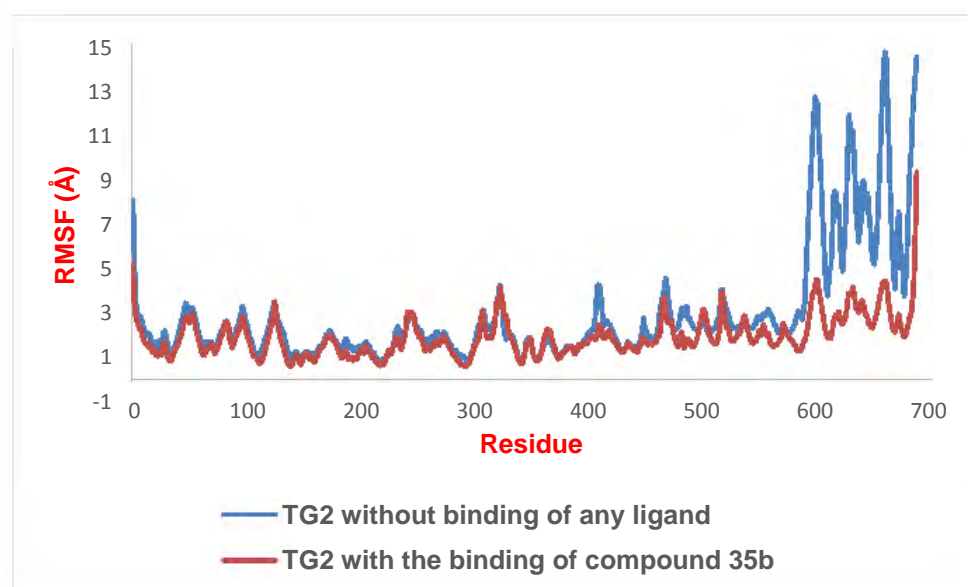


Figure 8.15. RMSF values of the empty TG2 and TG2 under the binding of compound **35b** during 800 ns MD simulation.

During the simulation, hydrogen bonds formed between the two NH (acylhydrazide and amide) groups of the ligand and the carboxylate group of residue ASP400 (Figure 8.16) had the highest occurrences. It is obvious that the distances between the relevant atoms fluctuated mainly less than 3.0 Å during the simulation. This indicated a strong holding between the ligand and ASP400.

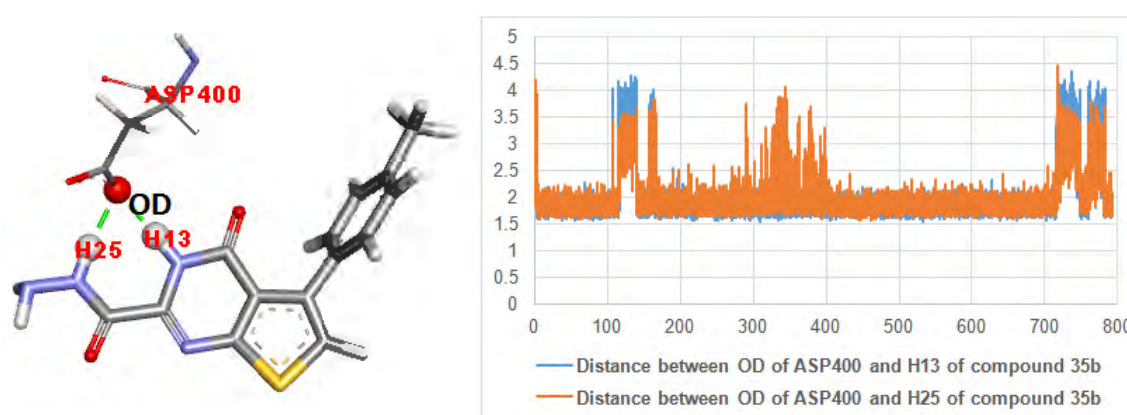


Figure 8.16. Hydrogen bonds between compound **35b** and ASP400 and the distances between the relevant atoms.

8.1.3.4 General observation from MD simulations of the potent inhibitors

It was observed from the MD simulations of the potent inhibitors that TG2 was more stable under the binding of the potent inhibitors in the predicted allosteric site. The most

potent inhibitor, compound **35b** was the most stable ligand in the predicted binding site and the structure of TG2 in the complex with this inhibitor was also the most stable. RMSD values of the protein (backbone) during run 1, 3, 4 and 5 given in Figure 8.17 confirmed these observations. It indicates that the binding of the potent inhibitors into the predicted binding site may stabilise the extended conformation of TG2.

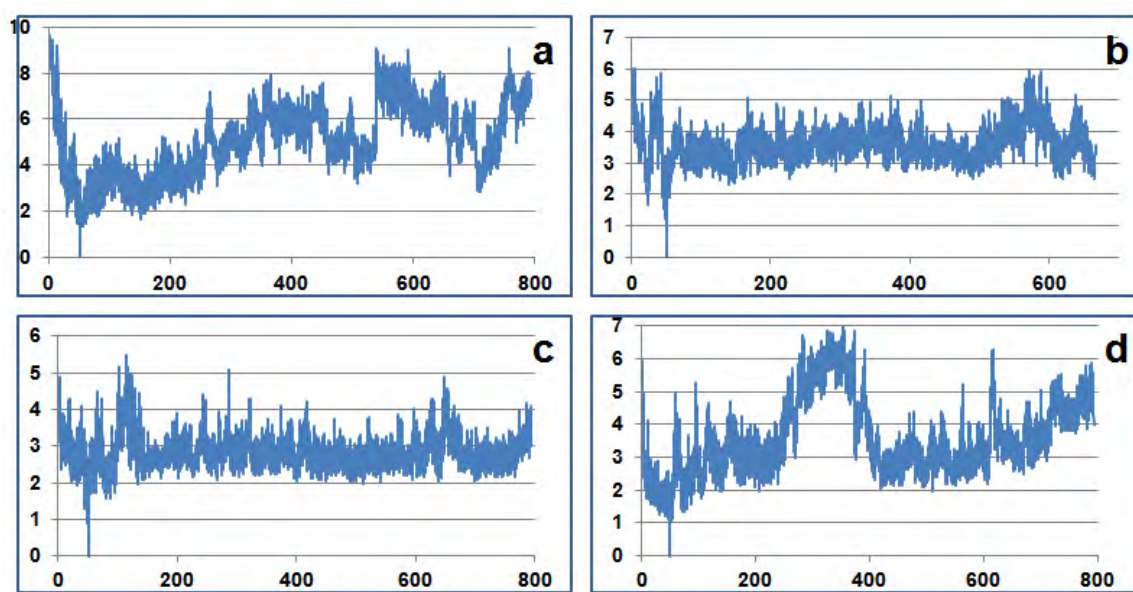


Figure 8.17. RMSD (Å) of TG2 backbone atoms during run 1 (a), 3 (b), 5 (c) and 4 (d).

To identify the mobile residues of TG2 when the potent inhibitors bound to the predicted allosteric site of the enzyme, differences between the RMSF values of the protein in run 1 and those in run 3, 4 and 5 were calculated (Figure 8.18). It is detectable that most of the residues of TG2 are more stable in run 3, 4 and 5 than in run 1. However, among the catalytic core domain residues (residues 147 to 460), residues 325 to 328 and residues 362 to 366 fluctuated more significantly when TG2 was under the binding of the potent inhibitors. These residues reside in two separated loops in front of the proposed acyl-acceptor entrance that were indicated to form strong and stable hydrogen bonds in run 1. In contrast to the behaviour of these loops in run 1, the hydrogen bonds between SER328 and two residues PRO361 and GLN362 were observed being broken early in the simulations in run 3, 4 and 5. Therefore, these loops became highly mobile.

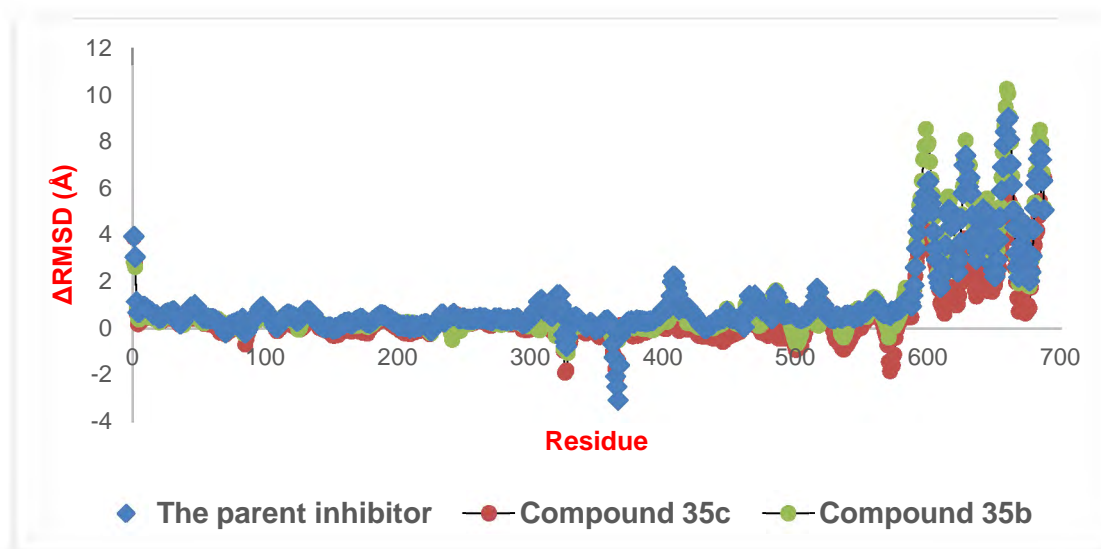


Figure 8.18. Differences between RMSF values of the empty TG2 and TG2 under the binding of the potent inhibitors **35b,c**.

The general results from the MD simulations of the potent inhibitors suggested that the binding of the potent inhibitors into the predicted allosteric site may lead to the breaking of the hydrogen bonds between SER328 and two residues PRO361 and GLN362 and consequently caused the separation of the loops containing them. These two loops also contain two important residues of the catalytic tunnel, TRP332 and THR360. The high fluctuation of these loops enlarged the entrance of the proposed acyl-acceptor binding site and may consequently weaken the binding of the substrates.

Among the three potent inhibitors, compound **35b** formed the most stable hydrogen bonds with the loop containing ALA399, ASP400. In its MD trajectory, the relevant hydrogen bonds between the ligand, the residues of the predicted binding site and the residues of the catalytic binding site were also observed as shown in Figure 8.19. Particularly, the backbone CO of residue SER328 formed hydrogen bonds with the side chain of residue ASP573. The backbone of ASP573 was held by hydrogen bonds with the backbone of ASP400 which formed strong and long-lasting hydrogen bonds with the ligand.

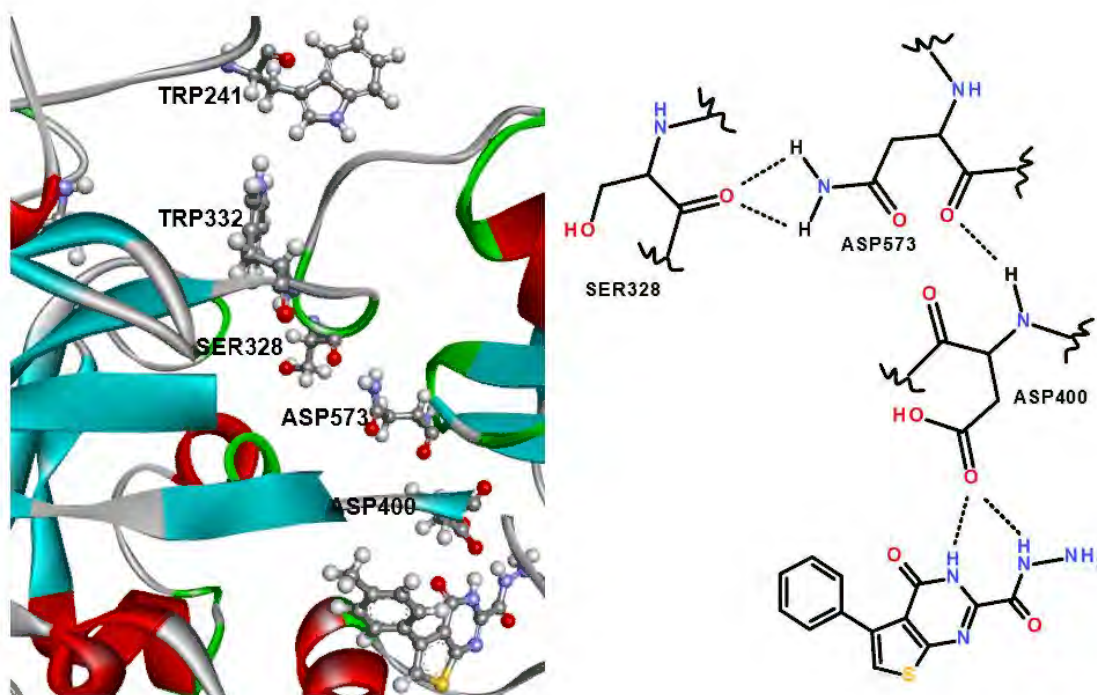


Figure 8.19. Relevant hydrogen bonds formed between the allosteric inhibitor **35b**, residue ASP400 of the predicted allosteric site, residue ASP573 and residue SER328 of the catalytic site.

The hydrogen bonds formed between SER328 and ASP573 pulled the loop containing residue TRP332 and gave more space for TRP241 to fluctuate. In addition, LYS327 moved towards the catalytic site, formed hydrogen bonds with GLU396, which resides in the same loop as ASP400, and also interrupted the hydrophobic interactions between TRP241 and TRP332. Therefore, TRP241 became significantly more mobile and moved towards the outside of the catalytic site. The distance between the nucleophilic sulphur of CYS277 and hydro (indole NH) of TRP241 during run 1 and run 5 (Figure 8.20) indicated a significant movement of the indole NH to the outside of the catalytic tunnel in run 5. The indole NH of TRP241 was proved to be essential for the transamidation activity of TG2 by stabilising the transition-state intermediates (Murthy et al., 2002; Iismaa et al., 2003; Pinkas et al., 2007). Specifically, the intermediate is stabilised by H-bonding both to the backbone NH of CYS277 and to the indole NH of TRP241. The hydrogen bonds formed between the intermediates and TRP241 that are critical for the stabilisation of the intermediate will disappear when the indole NH moves toward the outside of the catalytic tunnel. That will inhibit the catalytic activity of TG2.

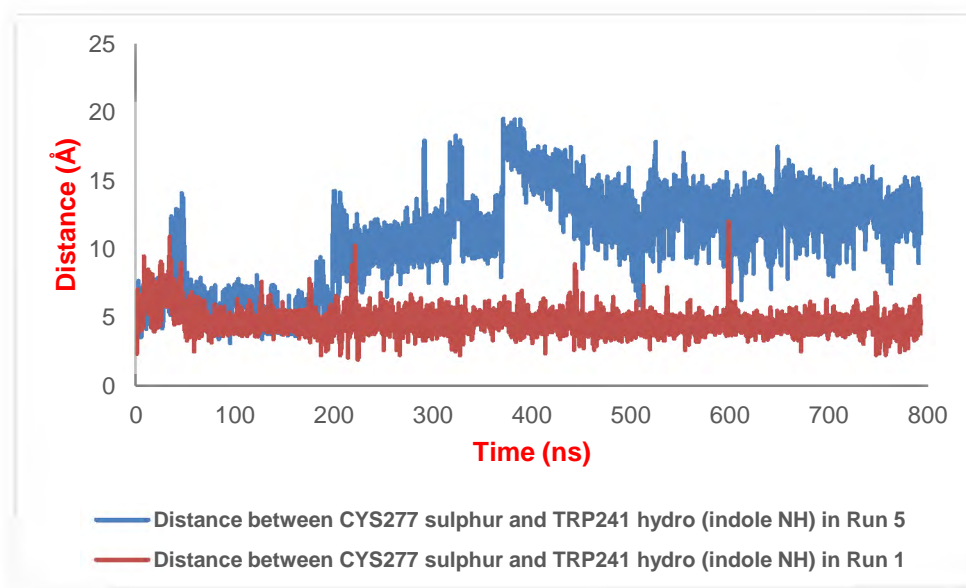


Figure 8.20. Distances between the sulphur atom of CYS277 and hydro (indole NH) of TRP241 during MD simulation of the empty TG2 (red) and TG2 under the binding of compound **35b** (blue).

8.2 Repeated long MD simulations

8.2.1 Repeated long MD simulation of compound **35b** – TG2 complex (run 6)

In order to confirm the effect of the binding of compound **35b** on the catalytic site when it bound into the predicted allosteric site, the MD simulation of this compound in chapter 3, in which TG2 structure was shortened to only two parts: the catalytic core domain and the first C terminal β barrel, was continued to 800 ns. The short structure of TG2 was used to reduce the cost of running MD simulation. Similar to the trajectory in run 5, the high occurrence hydrogen bonds were formed between the ligand and the loop residing nearby the catalytic core domain. However, the ligand mainly formed hydrogen bonds with two residues ASN398 and ASP399 (Figure 8.21) while in run 5 the hydrogen bond with ASP400 was dominant. The similar break of the hydrogen bonds formed between residue SER328 and two residues GLN362 and PRO361 following the separation of the loops containing these residues was observed. The high fluctuation of residues 325 to 328 and residues 362 to 366 are indicated in Figure 8.22. The hydrophobic interactions between the two tryptophans TRP241 and TRP332 were interrupted and the leaving of TRP241 from the catalytic binding site was observed but only for a short period (from 338 ns to 342 ns). Interestingly, the hydrogen bonds

NTA, Nguyen, PhD Thesis, Aston University 2020

formed between the ligand and ASP400 only occurred 2.64% the simulation time and was mainly formed during the period when TRP241 moved out from the catalytic tunnel. Figure 8.22 indicated that during the period the distance between the sulphur of CYS277 and the hydrogen of TRP241 indole NH was significantly increased from 4 to 10 Å, the distances between the ligand atoms relevant to the hydrogen bonds formed between the ligand and ASP400 fluctuated less than 3.0 Å.

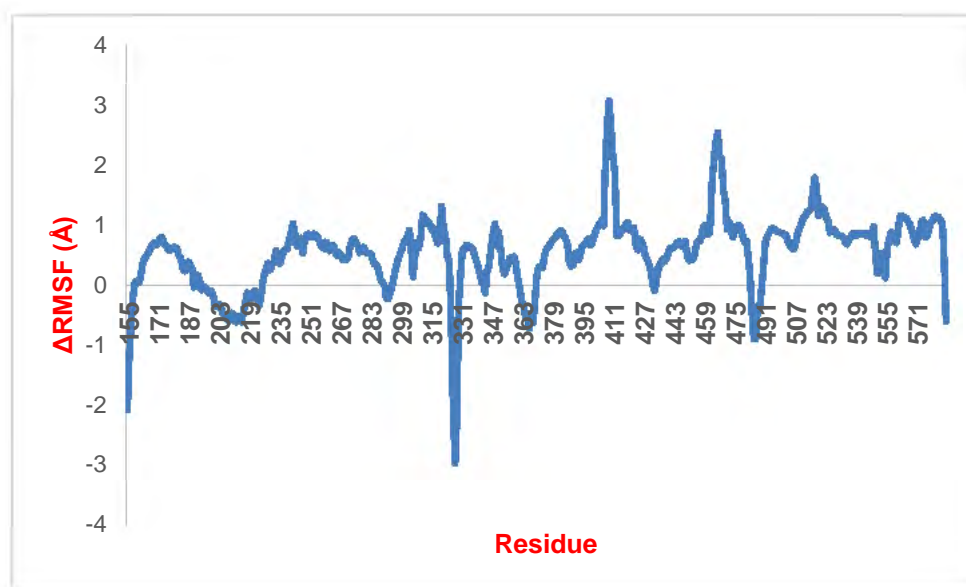


Figure 8.21. Differences between RMSF values of empty TG2 and TG2 under the binding of **35b** in the repeated MD simulation.

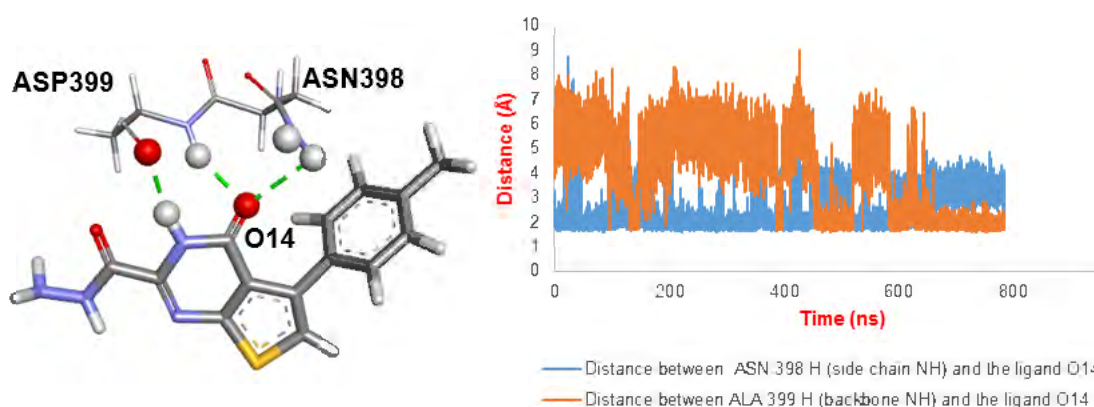


Figure 8.22. Hydrogen bonds between compound **35b** and two residues ASN398 and ASP399 and the distances between the relevant atoms during the repeated 800 ns MD simulation.

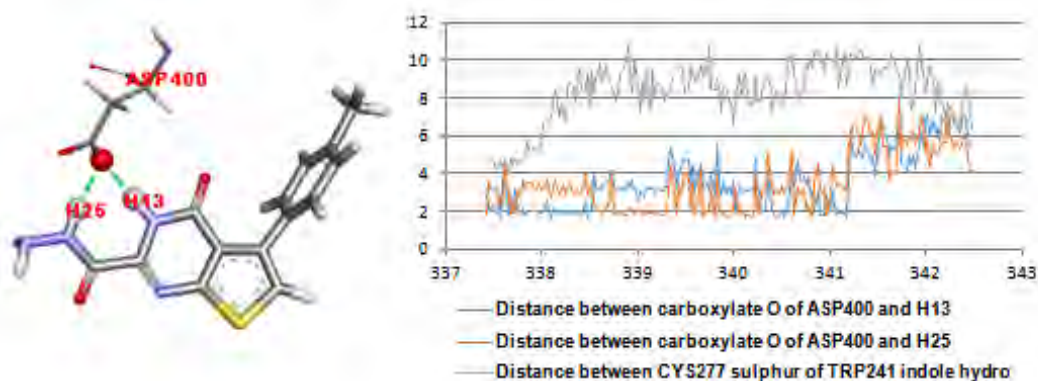


Figure 8.23. (a) Hydrogen bonds formed between compound **35b** and ASP400; (b) distance between CYS277 sulphur and TRP241 indole NH (H) and the distances between the atoms relevant to the hydrogen bonds formed between the ligand and ASP400 during the period TRP241 moved towards to the outside of the catalytic binding site.

8.2.2 Repeated long MD simulation of the compound having no inhibitory effect (run 7)

The MD simulation of compound **32a** in chapter 3, which indicated that the ligand stayed inside the predicted binding site during 400 ns simulation, was continued to 800 ns in order to identify the effect of its binding on the catalytic site. During the first 650 ns simulation, similar to the trajectory of the empty TG2, SER328 formed strong hydrogen bonds with two residues PRO361 and GLN362. However, after 650 ns these hydrogen bonds were broken, the hydrogen bonds between LYS327 backbone carbonyl and GLN362 side chain amine and between the side chain amine of LYS327 and the hydroxyl of THR360 were generated. That was pointed out by the distances between the relevant atoms as given in Figure 8.24. Due to the strong hydrogen bonds, these loops were held quite firmly and the entrance of the catalytic binding site was not be enlarged as in runs 3, 4 and 5. The differences of the RMSF values of the enzyme in run 1 and run 7 given in Figure 8.25 indicated the same fluctuation of the loop containing residue THR360, PRO361, GLN362 in these two MD simulations.

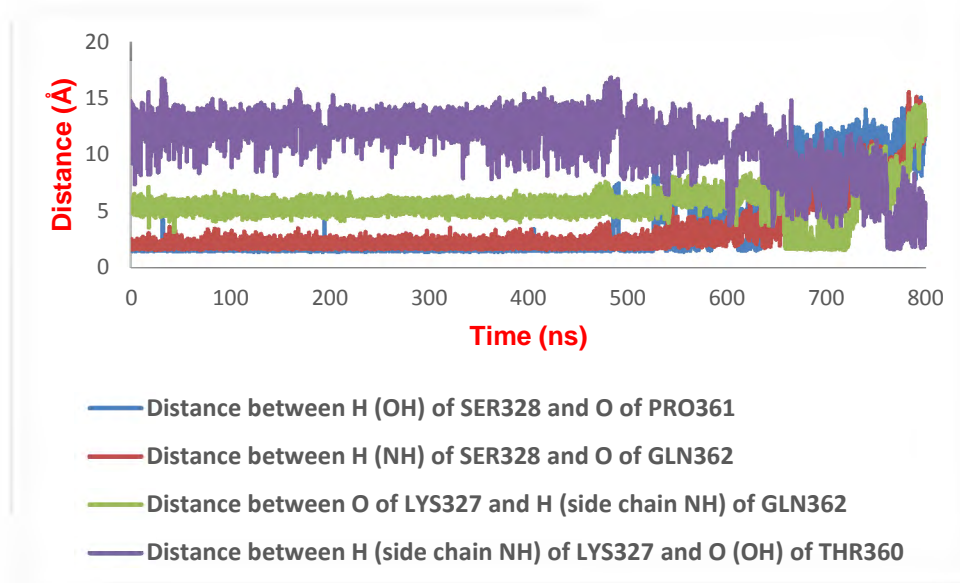


Figure 8.24. Distances between the relevant atoms of the hydrogen bonds formed between the two loops residing in front of the catalytic binding site during 800 ns MD simulation of compound **32a** – TG2 complex.

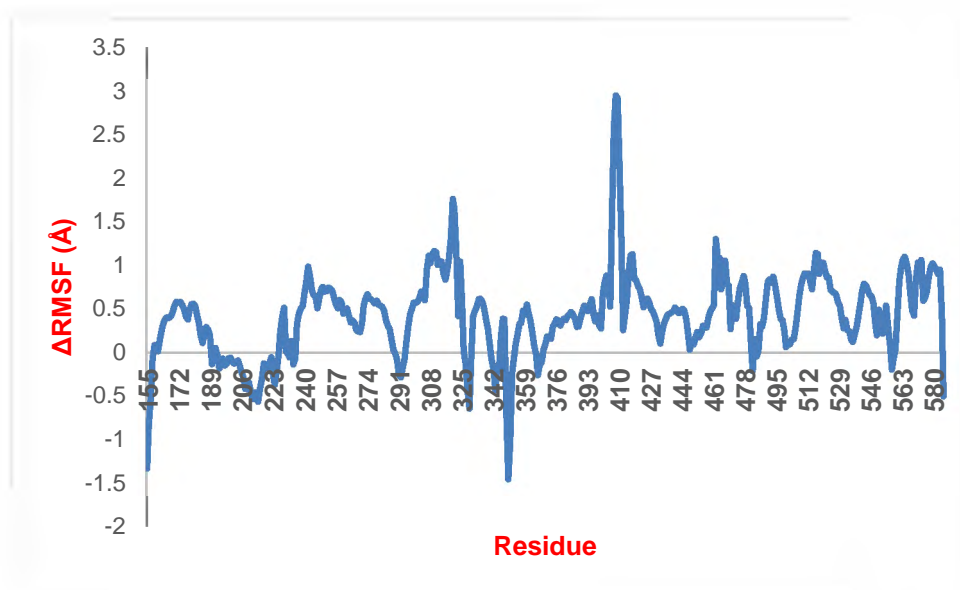


Figure 8.25. Differences between RMSF values of the empty TG2 and TG2 under the binding of **32a** in the repeated MD simulation.

In contrast to the potent inhibitors, compound **32a** did not form hydrogen bonds with the loop containing residues ASN398, ALA399 and ASP400. The ligand thieno[2,3-d]pyrimidine ring moved towards TYR445 and generated high occurrence hydrogen bonds with the backbone of TYR445 (Figure 8.26b). The loop containing TYR445 is located further towards the catalytic binding site as shown in Figure 8.26a. The

distances between the relevant atoms of these hydrogen bonds mostly fluctuated less than 3.0 Å as shown in Figure 8.27 and that indicated the strong and long-lasting hydrogen bonds. The moving towards the outside of the predicted allosteric site and the lack of hydrogen bonds with the loop located nearby the catalytic site may explain the fluctuations of the residues of the catalytic site were not affected by the binding of this ligand.

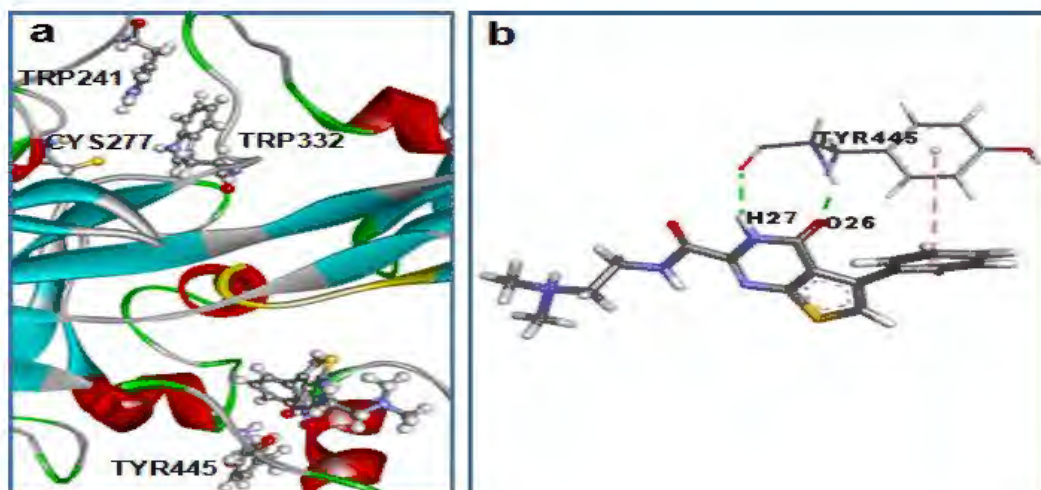


Figure 8.26. (a) Position of compound **32a** when it formed hydrogen bonds with TYR445 (the loop containing ASN398, ALA399 and ASP400 is coloured in yellow) (b) the hydrogen bonds between the ligand and TYR445.

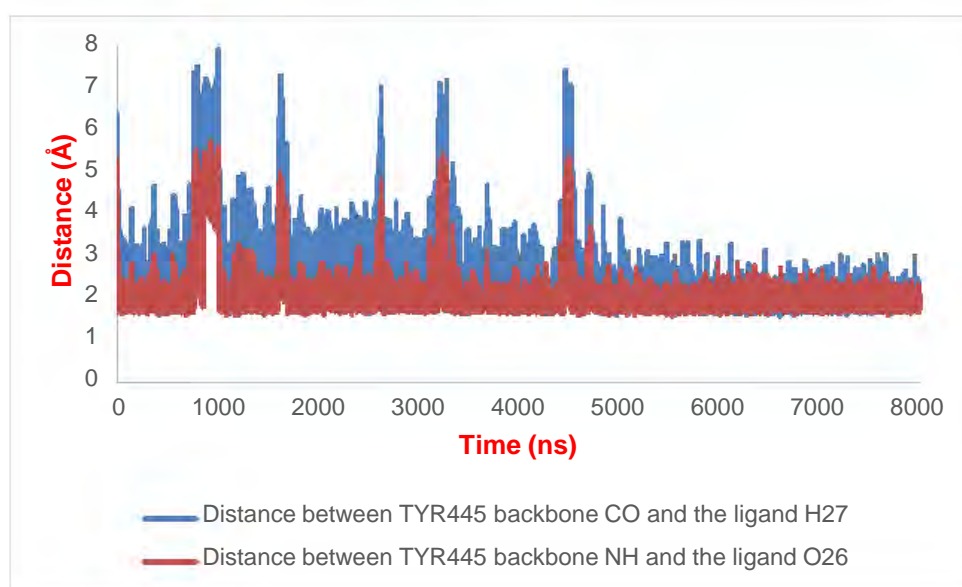


Figure 8.27. Distances between atoms related to the hydrogen bonds formed between compound **32a** and residue TYR445.

8.3 Discussion

During the long MD simulations of the whole structure of TG2 with and without the binding of a ligand, the potent inhibitors including compounds **6**, **35b** and **35c** were all maintained into the predicted allosteric site for 750 ns while the compound having no inhibitory effect had a transient binding. That predicts high affinities in the predicted allosteric site of the potent inhibitors and low affinity of the compound having no inhibitory effect.

It was also observed that the binding of the potent allosteric inhibitors stabilised the open conformation of TG2. The potent allosteric inhibitors all formed high occurrence hydrogen bonds with the loop located near the catalytic binding site. In contrast, the compound with no inhibitory effect did not generate hydrogen bonds with this loop but it formed high occurrence hydrogen bonds with the opposite loop located further from the catalytic site.

During long MD simulations of the empty TG2 or the complex of TG2 and the compound having no inhibitory effect, the loop containing TRP332 was held firmly by hydrogen bonds with the loop containing THR360. These two separate loops reside in front of the catalytic tunnel. However, under the binding of the potent inhibitors, the hydrogen bonds were broken and these loops fluctuated significantly. The entrance of the catalytic site was observed to be enlarged by the high fluctuation of these loops.

In the MD simulations of the most potent inhibitor, TRP241 was observed to move out of the catalytic binding site. The more significant fluctuation of this residue was observed in the trajectory where the hydrogens between the ligand and residue ASP400 were dominant. The movement happened when the hydrogen bonds between this inhibitor and ASP400 were generated. The leaving of TRP241 far away from CYS277 would prevent these residues from forming of the dual hydrogen bonds to stabilise the tetrahedral oxyanion intermediates and consequently TG2 activity would be inhibited.

The results from MD simulations contributed to the confirmation of the actual binding of the allosteric inhibitors into the predicted allosteric site. The catalytic activity of TG2 is inhibited when the allosteric inhibitors bind in the predicted allosteric site may be

explained in two proposed hypotheses. Firstly, the inhibitors bind to the allosteric site, form hydrogen bonds with residues ASN398, ALA399 and ASP400 and these hydrogen bonds indirectly cause high fluctuations of the residues located on the two loops of the catalytic binding site entrance and enlarge of formation of the entrance. Consequently, the binding of the substrates into the catalytic site is inhibited. Secondly, the strong hydrogen bonds with ASP400 may indirectly cause the leaving of TRP241 out of the catalytic site. As a result, the hydrogen bonds between the indole NH and the transition-state intermediates are interrupted and the cycle of transamidation reaction is inhibited.

9 General Discussion and Conclusions

9.1 Structure-activity relationship of the newly synthesised allosteric inhibitors of TG2

The significant mobility in the predicted allosteric site during the MD simulations of the amines (**32a,b,c** and **33a,b,c**), the esters (**36a,b,c**) and the carboxylic acids (**37a,b,c**) are in a good agreement with the low inhibitory effects of these compounds in the biological assays. The amides (**34a,b,c**) and the acylhydrazides (**35a,b,c**) were both stable in the predicted binding site during the MD simulations and but the amides showed a little inhibitory effect while the acylhydrazides were of the higher potency than the parent compound. That indicates the binding of the amides alone in the predicted allosteric site may not induce any effect on the catalytic site. The attachment of one methyl group at the para position of the acylhydrazide phenyl ring showed the improvement of the ligand stability during MD simulation and that is in consistency with the achieved biological potency.

The long MD simulations in chapter 8 gave information about the modification of the conformation of TG2 and the effect caused on the catalytic binding site when the ligands with or without an inhibitory effect bound into the predicted allosteric site. The open conformation of TG2 was indicated to be stabilised under the binding of the parent inhibitor and the two acylhydrazides (**35b,c**) whose IC_{50} values are half of the parent's. There are three key observations that support the actual binding of these potent inhibitors in the predicted allosteric site and the impacts of their binding on the catalytic site. Firstly, the maintaining of the potent inhibitors in the predicted allosteric site during the long MD simulations and the common hydrogen bonds formed between these ligands and the loop containing ASP400. Secondly, the extension of the entrance of the catalytic binding site was observed under the binding of all the potent inhibitors but was not seen when the ligand had no inhibitory effect. Thirdly, the leaving of TRP241, a key residue in stabilising the enzyme-thiol intermediates formed during the catalysis of the acyl-transfer reaction, from the catalytic binding site in the MD simulations of compound **35b**. The consistency between the leaving of TRP241 and the forming of the hydrogen bonds between the ligand **35b** and residue ASP400 suggests an

important connection between these hydrogen bonds and the potency of the allosteric inhibitors. This suggests further modelling that could be undertaken in which the hydrogen bonds between the ligand and residue ASP400 are restrained to identify the effect of these interactions on the catalytic binding site.

9.2 Structure-activity relationships of the newly synthesised irreversible inhibitors of TG2

In chapter 6, the compound with the propynamide warhead (compound **27a**) and the 4-pyridyl triazolyl acrylamide with a long side chain (compound **41b**) were predicted to have high affinity in the catalytic site due to their stability during the MD simulations and the short distances between the warhead electrophilic carbon and the nucleophilic sulphur of CYS277. Unfortunately, these compounds were not available for screening because of the failures in the attachment of the propionic warhead and in the lengthening the side chain. Compound **41a**, a derivative of compound **41b** having a shorter side chain, was synthesised and tested against rhTG2. The IC₅₀ value of this compound was $3.9 \pm 0.7 \mu\text{M}$ but is significantly lower than that of the parent compound. This is in agreement with the prediction from the MD simulation which indicated a transient stay in the catalytic tunnel of the ligand warhead and the long distance between the warhead electrophilic carbon and the nucleophilic sulphur of CYS277.

Except for the (Z)-isomer of compound **27b**, the compounds with the maleic form of warhead were all predicted to have low inhibition effects owing to the transient binding of their warheads into the catalytic tunnel together with the long distances between the warhead electrophilic carbon and the nucleophilic sulphur. The results from the screening test are in good agreement with the prediction. All the (2Z)-4-amino-4-oxo-2-butenic acid derivatives had no inhibitory effect against rhTG2. The inhibitory effect of the acrylamide warhead was halted by the attachment of a carboxyl group on the *cis*-position of the warhead. The synthesis the (E)-isomers of these compounds could not be achieved during the course of this research.

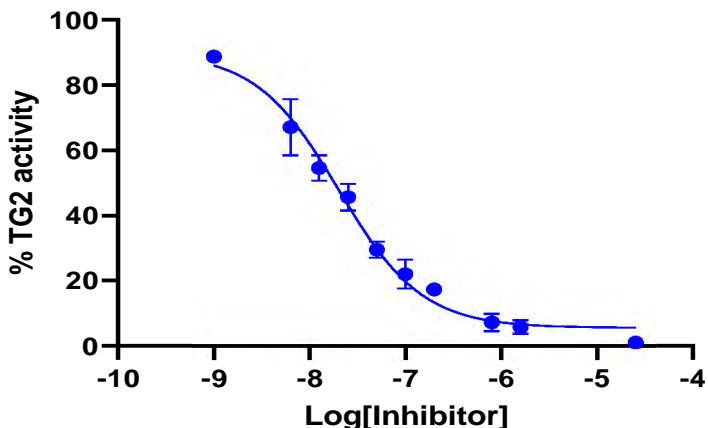
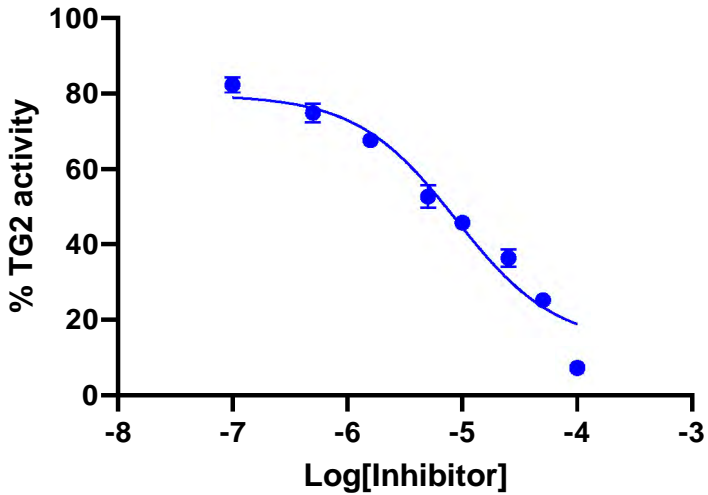
The compounds having a phenyl ring inserted between the piperazine ring and the acrylamide warhead (compound **26a** and **27g**) were expected to have higher potency

than the parent compounds due to the significant improvement in the stability of the warhead in the catalytic tunnel and the reduction in the distance between the warhead electrophilic carbon and the CYS277 sulphur atom during the MD simulations. Surprisingly, in the biological screening test the modified compounds were significantly less potent than the parent compounds. These unexpected results may be explained by the mechanism of inhibition TG2 by compounds with α,β -unsaturated carbonyl compounds. As pointed out in chapter 1, to inhibit TG2 activity, the Michael reaction must occur between the warhead electrophilic carbon of the inhibitor and the catalytic cystein sulphur. MD simulations predicted the affinity of the ligand in the catalytic binding site based on the stability of the ligand warhead in the catalytic tunnel. It also predicted the possibility of the attack between the warhead electrophilic carbon and the cystein nucleophilic sulphur based on their distance. However, the formation and cleavage of the covalent bonds in the Michael reaction depend on many factors that cannot be predicted by MD simulations. In addition, the rigid conformation of the ligand side chain may prevent the warhead electrophilic carbon from actual reaching to the nucleophilic sulphur atom needed for the Michael reaction to occur. Therefore, the inconsistency between the prediction of the MD simulations and the real biological inhibition effect is explainable. A quantum mechanical reaction profiling of the Michael reaction between the ligand acrylamide warhead and the catalytic CYS277 may give a better evaluation of the potency of the irreversible inhibitors.

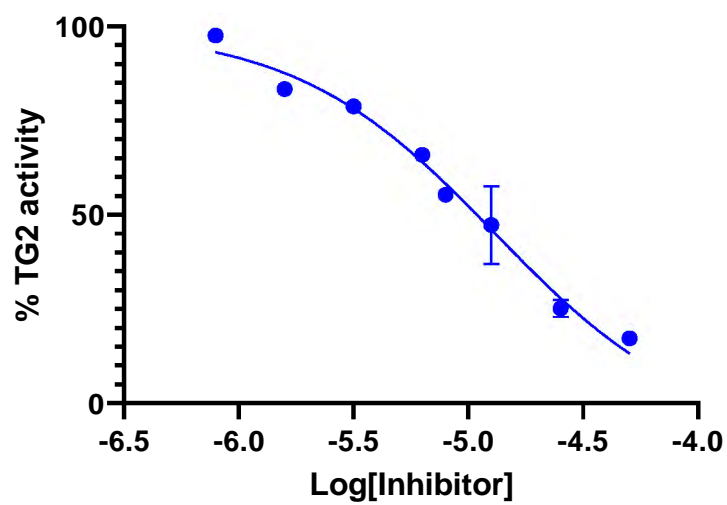
10 Appendix

The IC_{50} values of the inhibitors of TG2 shown in chapter 7 were calculated from the curves which indicate the relationship between \log [inhibitor] and %TG2 activity when TG2 was bound by the inhibitors as given in this appendix.

Table 10.1. \log [inhibitor] vs. %TG2 activity curves of irreversible inhibitors of TG2.

Name	Graph	IC_{50} (μM)
27		0.02 ± 0.003
27e		8.9 ± 1.6

27g

 13.5 ± 3.0 

41b

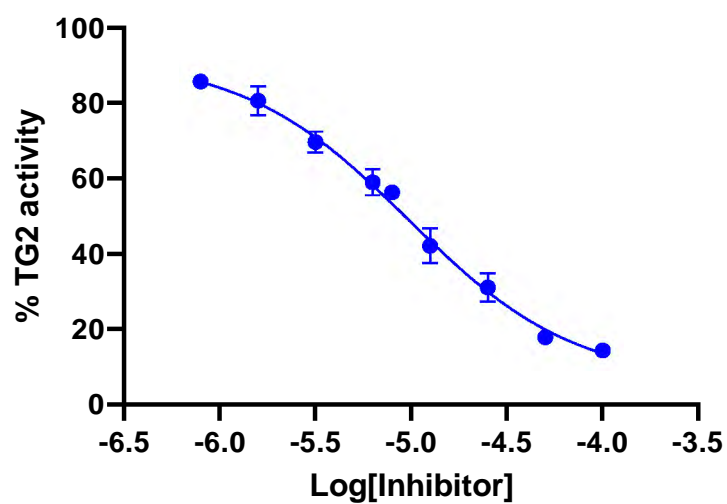
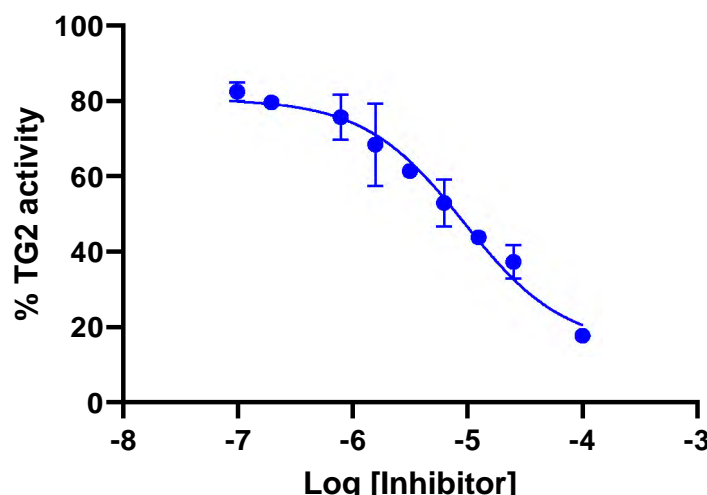
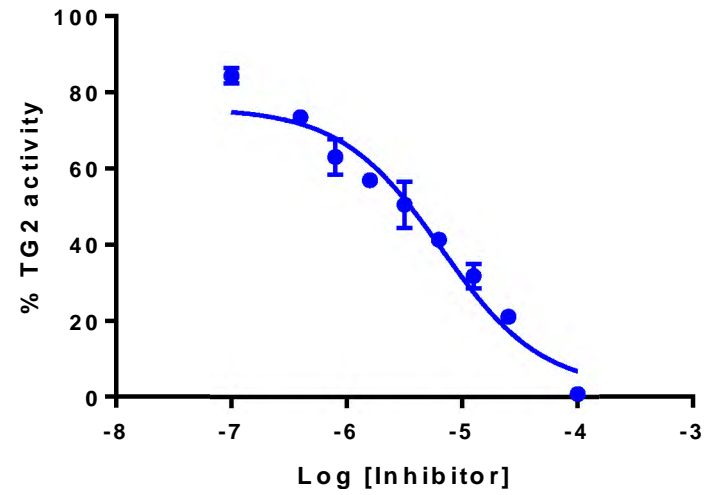
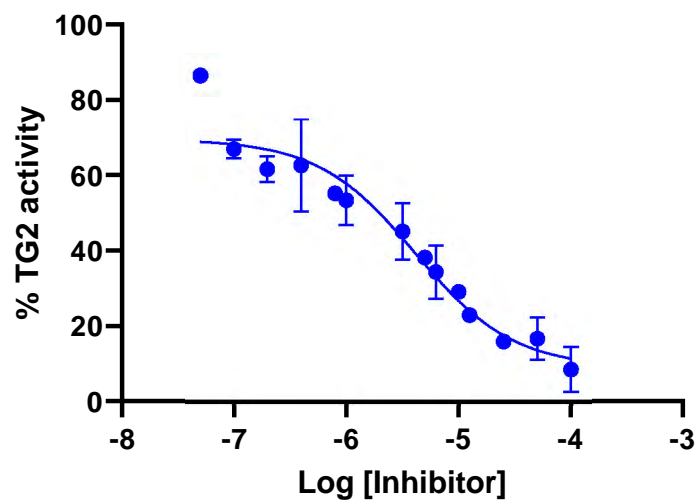
 3.9 ± 0.7 

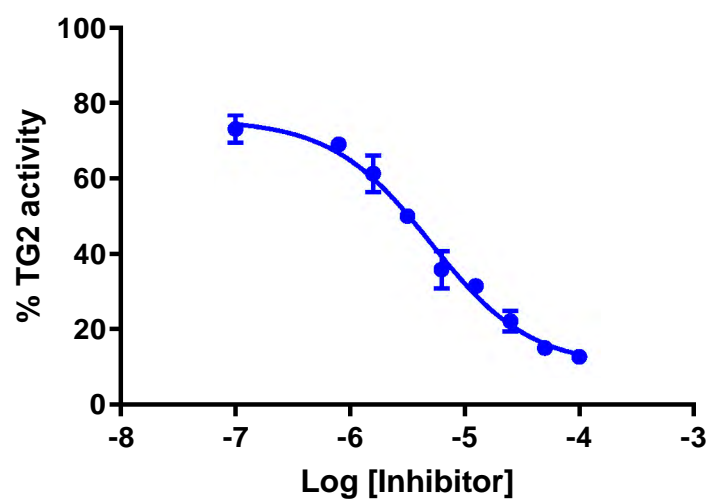
Table 10.2. Log [inhibitor] vs %TG2 activity curves of allosteric inhibitors of TG2

Name	Graph	IC ₅₀ (μM)																										
6	 <p>Dose-response curve for compound 6. The y-axis represents % TG2 activity (0 to 100) and the x-axis represents Log [Inhibitor] (-8 to -3). The curve is sigmoidal, starting at ~82% activity at Log [Inhibitor] = -7 and reaching ~18% activity at Log [Inhibitor] = -4. The IC₅₀ is 7.3 ± 0.8 μM.</p> <table><tr><th>Log [Inhibitor]</th><th>% TG2 activity</th></tr><tr><td>-7.0</td><td>82</td></tr><tr><td>-6.8</td><td>80</td></tr><tr><td>-6.2</td><td>75</td></tr><tr><td>-6.0</td><td>70</td></tr><tr><td>-5.8</td><td>65</td></tr><tr><td>-5.5</td><td>60</td></tr><tr><td>-5.2</td><td>55</td></tr><tr><td>-5.0</td><td>50</td></tr><tr><td>-4.8</td><td>45</td></tr><tr><td>-4.5</td><td>40</td></tr><tr><td>-4.2</td><td>35</td></tr><tr><td>-4.0</td><td>18</td></tr></table>	Log [Inhibitor]	% TG2 activity	-7.0	82	-6.8	80	-6.2	75	-6.0	70	-5.8	65	-5.5	60	-5.2	55	-5.0	50	-4.8	45	-4.5	40	-4.2	35	-4.0	18	7.3 ± 0.8
Log [Inhibitor]	% TG2 activity																											
-7.0	82																											
-6.8	80																											
-6.2	75																											
-6.0	70																											
-5.8	65																											
-5.5	60																											
-5.2	55																											
-5.0	50																											
-4.8	45																											
-4.5	40																											
-4.2	35																											
-4.0	18																											
35a	 <p>Dose-response curve for compound 35a. The y-axis represents % TG2 activity (0 to 100) and the x-axis represents Log [Inhibitor] (-8 to -3). The curve is sigmoidal, starting at ~85% activity at Log [Inhibitor] = -7 and reaching ~0% activity at Log [Inhibitor] = -4. The IC₅₀ is 6.0 ± 1.5 μM.</p> <table><tr><th>Log [Inhibitor]</th><th>% TG2 activity</th></tr><tr><td>-7.0</td><td>85</td></tr><tr><td>-6.8</td><td>80</td></tr><tr><td>-6.2</td><td>65</td></tr><tr><td>-6.0</td><td>60</td></tr><tr><td>-5.8</td><td>55</td></tr><tr><td>-5.5</td><td>50</td></tr><tr><td>-5.2</td><td>45</td></tr><tr><td>-5.0</td><td>40</td></tr><tr><td>-4.8</td><td>35</td></tr><tr><td>-4.5</td><td>30</td></tr><tr><td>-4.2</td><td>25</td></tr><tr><td>-4.0</td><td>0</td></tr></table>	Log [Inhibitor]	% TG2 activity	-7.0	85	-6.8	80	-6.2	65	-6.0	60	-5.8	55	-5.5	50	-5.2	45	-5.0	40	-4.8	35	-4.5	30	-4.2	25	-4.0	0	6.0 ± 1.5
Log [Inhibitor]	% TG2 activity																											
-7.0	85																											
-6.8	80																											
-6.2	65																											
-6.0	60																											
-5.8	55																											
-5.5	50																											
-5.2	45																											
-5.0	40																											
-4.8	35																											
-4.5	30																											
-4.2	25																											
-4.0	0																											

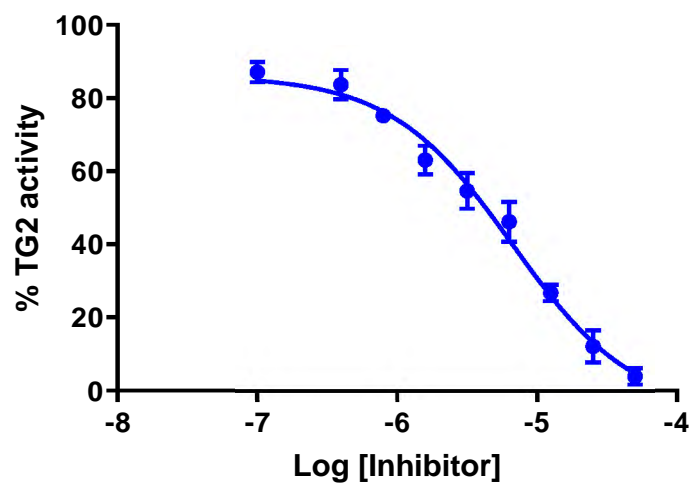
35b

 4.1 ± 0.7 

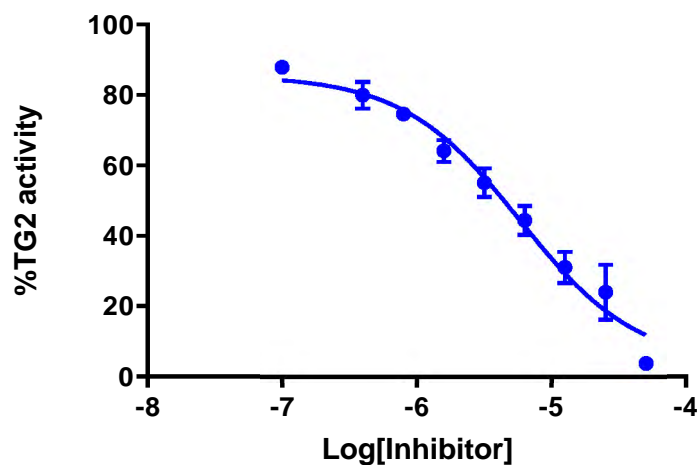
35c

 4.3 ± 0.6 

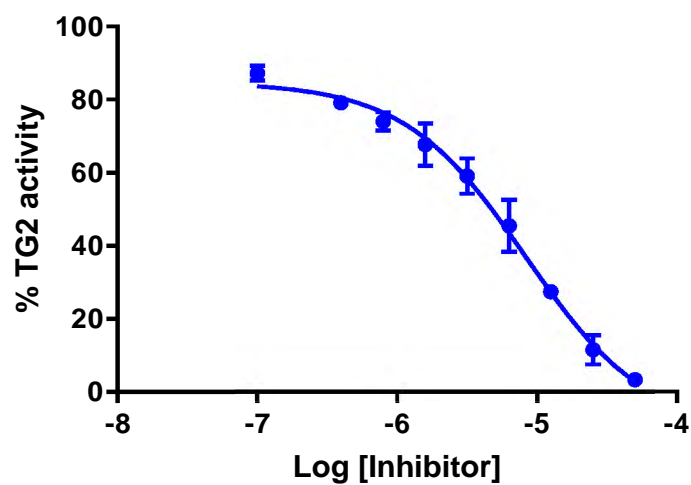
39a

 6.6 ± 1.0 

39b

 5.7 ± 1.0 

39c

 8.2 ± 1.0 

11 References

- ACTIS, M. L., AMBAYE, N. D., EVISON, B. J., SHAO, Y., VANAROTTI, M., INOUE, A., MCDONALD, E. T., KIKUCHI, S., HEATH, R., HARA, K., HASHIMOTO, H. & FUJII, N. 2016. Identification of the first small-molecule inhibitor of the REV7 DNA repair protein interaction. *Bioorganic & Medicinal Chemistry*, 24, 4339-46.
- AESCHLIMANN, D. & PAULSSON, M. 1994. Transglutaminases: protein cross-linking enzymes in tissues and body fluids. *Thromb Haemost*, 71, 402-15.
- AKBAR, A., MCNEIL, N. M. R., ALBERT, M. R., TA, V., ADHIKARY, G., BOURGEOIS, K., ECKERT, R. L. & KEILLOR, J. W. 2017. Structure-Activity Relationships of Potent, Targeted Covalent Inhibitors That Abolish Both the Transamidation and GTP Binding Activities of Human Tissue Transglutaminase. *Journal of Medicinal Chemistry*, 60, 7910-27.
- ALLEN, M. P. & TILDESLEY, D. J. 2017. *Computer Simulation of Liquids: Second Edition*, Oxford, Oxford University Press.
- APPERLEY, K. Y. P., ROY, I., SAUCIER, V., BRUNET-FILION, N., PISCOPO, S.-P., PARDIN, C., DE FRANCESCO, É., HAO, C. & KEILLOR, J. W. 2016. Development of new scaffolds as reversible tissue transglutaminase inhibitors, with improved potency or resistance to glutathione addition. *MedChemComm*, 8, 338-45.
- ARONIN, N. 1999. Hot papers - Huntington's disease - Aggregation of huntingtin in neuronal intranuclear inclusions and dystrophic neurites in brain by M. DiFiglia, E. Sapp, K.O. Chase, S.W. Davies, G. P. Bates, J.P. Vonsattel, N. Aronin - Comments. *Scientist*, 13, 16-+.
- BADARAU, E., MONGEOT, A., COLLIGHAN, R., RATHBONE, D. & GRIFFIN, M. 2013. Imidazolium-based warheads strongly influence activity of water-soluble peptidic transglutaminase inhibitors. *European Journal of Medicinal Chemistry*, 66, 526-30.
- BADARAU, E., WANG, Z., RATHBONE, D. L., COSTANZI, A., THIBAUT, T., MURDOCH, C. E., EL ALAOUI, S., BARTKEVICIUTE, M. & GRIFFIN, M. 2015. Development of Potent and Selective Tissue Transglutaminase Inhibitors: Their Effect on TG2 Function and Application in Pathological Conditions. *Chemistry & Biology*, 22, 1347-61.
- BANIK, B. K. & BECKER, F. F. 2001. Polycyclic aromatic compounds as anticancer agents: structure–activity relationships of chrysene and pyrene derivatives. *Bioorganic & Medicinal Chemistry*, 9, 593-605.
- BARSIGIAN, C., STERN, A. M. & MARTINEZ, J. 1991. Tissue (type II) transglutaminase covalently incorporates itself, fibrinogen, or fibronectin into high molecular weight complexes on the extracellular surface of isolated hepatocytes. Use of 2-[(2-oxopropyl)thio]imidazolium derivatives as cellular transglutaminase inactivators. *Journal of Biological Chemistry*, 266, 22501-9.

- BAXTER, C. A., MURRAY, C. W., CLARK, D. E., WESTHEAD, D. R. & ELDRIDGE, M. D. 1998. Flexible docking using Tabu search and an empirical estimate of binding affinity. *Proteins*, 33, 367-82.
- BEGG, G. E., CARRINGTON, L., STOKES, P. H., MATTHEWS, J. M., WOUTERS, M. A., HUSAIN, A., LORAND, L., IISMAA, S. E. & GRAHAM, R. M. 2006. Mechanism of allosteric regulation of transglutaminase 2 by GTP. *Proceedings of the National Academy of Sciences of the United States of America*, 103, 19683-8.
- BERENDSEN, H. J. C., VAN DER SPOEL, D. & VAN DRUNEN, R. 1995. GROMACS: A message-passing parallel molecular dynamics implementation. *Computer Physics Communications*, 91, 43-56.
- BERGAMINI, C. M. 1988. GTP modulates calcium binding and cation-induced conformational changes in erythrocyte transglutaminase. *FEBS Lett*, 239, 255-8.
- BERGAMINI, C. M. & SIGNORINI, M. 1993. Studies on tissue transglutaminases: interaction of erythrocyte type-2 transglutaminase with GTP. *The Biochemical journal*, 291 (Pt 1), 37-9.
- BIOVIA, D. S. 2013. Accelrys Discovery Studio Visualizer version 3.5.0.12158. *San Diego: Dassault Systèmes*.
- BROOKS, B. R., BROOKS, C. L., 3RD, MACKERELL, A. D., JR., NILSSON, L., PETRELLA, R. J., ROUX, B., WON, Y., ARCHONTIS, G., BARTELS, C., BORESCH, S., CAFLISCH, A., CAVES, L., CUI, Q., DINNER, A. R., FEIG, M., FISCHER, S., GAO, J., HODOSCEK, M., IM, W., KUCZERA, K., LAZARIDIS, T., MA, J., OVCHINNIKOV, V., PACI, E., PASTOR, R. W., POST, C. B., PU, J. Z., SCHAEFER, M., TIDOR, B., VENABLE, R. M., WOODCOCK, H. L., WU, X., YANG, W., YORK, D. M. & KARPLUS, M. 2009. CHARMM: the biomolecular simulation program. *Journal of computational chemistry*, 30, 1545-614.
- CARMI, C., LODOLA, A., RIVARA, S., VACONDIO, F., CAVAZZONI, A., ALFIERI, R. R., ARDIZZONI, A., PETRONINI, P. G. & MOR, M. 2011. Epidermal growth factor receptor irreversible inhibitors: chemical exploration of the cysteine-trap portion. *Mini-Reviews in Medicinal Chemistry*, 11, 1019-30.
- CASE, A., NI, J., YEH, L. A. & STEIN, R. L. 2005a. Development of a mechanism-based assay for tissue transglutaminase--results of a high-throughput screen and discovery of inhibitors. *Anal Biochem*, 338, 237-44.
- CASE, A. & STEIN, R. L. 2007. Kinetic Analysis of the Interaction of Tissue Transglutaminase with a Nonpeptidic Slow-Binding Inhibitor. *Biochemistry*, 46, 1106-15.
- CASE, D. A., BETZ, R. M., CERUTTI, D. S., CHEATHAM, T. E., DARDEN, T. A., DUKE, R. E., GIESE, T. J., GOHLKE, H., GOETZ, A. W., HOMEYER, N., IZADI, S., JANOWSKI, P., KAUS, J., KOVALENKO, A., LEE, T. S., LEGRAND, S., LI, P., LIN, C., LUCHKO, T., LUO, R., MADEJ, B., MERMELSTEIN, D., MERZ, K. M., MONARD, G., NGUYEN, H., NGUYEN, H. T., OMELIAN, I., ONUFRIEV, A., ROE, D. R., ROITBERG, A., SAGUI, C., SIMMERLING, C. L., BOTELLO-SMITH, W. M., SWAILS, J., WALKER, R. C., WANG, J., WOLF, R. M., WU, X., XIAO, L. & KOLLMAN, P. A. 2016. AMBER 16. *University of California, San Francisco*.

- CASE, D. A., CHEATHAM, T. E., 3RD, DARDEN, T., GOHLKE, H., LUO, R., MERZ, K. M., JR., ONUFRIEV, A., SIMMERLING, C., WANG, B. & WOODS, R. J. 2005b. The Amber biomolecular simulation programs. *Journal of computational chemistry*, 26, 1668-88.
- CASTELHANO, A. L., BILLEDEAU, R., PLIURA, D. H., BONAVENTURA, B. J. & KRANTZ, A. 1988. Synthesis, chemistry, and absolute configuration of novel transglutaminase inhibitors containing a 3-halo-4,5-dihydroisoxazole. *Bioorganic Chemistry*, 16, 335-40.
- CHICA, R. A., GAGNON, P., KEILLOR, J. W. & PELLETIER, J. N. 2004. Tissue transglutaminase acylation: Proposed role of conserved active site Tyr and Trp residues revealed by molecular modeling of peptide substrate binding. *Protein Science*, 13, 979-91.
- CHOI, K., SIEGEL, M., PIPER, J. L., YUAN, L., CHO, E., STRNAD, P., OMARY, B., RICH, K. M. & KHOSLA, C. 2005. Chemistry and biology of dihydroisoxazole derivatives: Selective inhibitors of human transglutaminase 2. *Chemistry & Biology*, 12, 469-75.
- CHRISTEN, M., HUNENBERGER, P. H., BAKOWIES, D., BARON, R., BURGI, R., GEERKE, D. P., HEINZ, T. N., KASTENHOLZ, M. A., KRAUTLER, V., OOSTENBRINK, C., PETER, C., TRZESNIAK, D. & VAN GUNSTEREN, W. F. 2005. The GROMOS software for biomolecular simulation: GROMOS05. *J Comput Chem*, 26, 1719-51.
- CORNELL, W. D., CIEPLAK, P., BAYLY, C. I., GOULD, I. R., MERZ, K. M., FERGUSON, D. M., SPELLMEYER, D. C., FOX, T., CALDWELL, J. W. & KOLLMAN, P. A. 1996. A Second Generation Force Field for the Simulation of Proteins, Nucleic Acids, and Organic Molecules. *J. Am. Chem. Soc.* 1995, 117, 5179-5197. *Journal of the American Chemical Society*, 118, 2309-.
- DANESHPOUR, N., GRIFFIN, M., COLLIGHAN, R. & PERRIE, Y. 2011. Targeted delivery of a novel group of site-directed transglutaminase inhibitors to the liver using liposomes: a new approach for the potential treatment of liver fibrosis. *Journal of Drug Targeting*, 19, 624-31.
- DAY, N. & KEILLOR, J. W. 1999. A continuous spectrophotometric linked enzyme assay for transglutaminase activity. *Anal Biochem*, 274, 141-4.
- DE MACEDO, P., MARRANO, C. & KEILLOR, J. W. 2000. A direct continuous spectrophotometric assay for transglutaminase activity. *Analytical Biochemistry*, 285, 16-20.
- DE MACÉDO, P., MARRANO, C. & KEILLOR, J. W. 2002. Synthesis of dipeptide-bound epoxides and α,β -unsaturated amides as potential irreversible transglutaminase inhibitors. *Bioorganic & Medicinal Chemistry*, 10, 355-60.
- DI SABATINO, A., VANOLI, A., GIUFFRIDA, P., LUINETTI, O., SOLCIA, E. & CORAZZA, G. R. 2012. The function of tissue transglutaminase in celiac disease. *Autoimmun Rev*, 11, 746-53.
- DURRANT, J. D. & MCCAMMON, J. A. 2011. Molecular dynamics simulations and drug discovery. *BMC Biology*, 9, 71.

- DUVAL, E., CASE, A., STEIN, R. L. & CUNY, G. D. 2005. Structure-activity relationship study of novel tissue transglutaminase inhibitors. *Bioorganic & Medicinal Chemistry Letters*, 15, 1885-9.
- ELDRIDGE, M. D., MURRAY, C. W., AUTON, T. R., PAOLINI, G. V. & MEE, R. P. 1997. Empirical scoring functions: I. The development of a fast empirical scoring function to estimate the binding affinity of ligands in receptor complexes. *Journal of Computer-Aided Molecular Design*, 11, 425-45.
- FOK, J. Y., EKMEKCIOGLU, S. & MEHTA, K. 2006. Implications of tissue transglutaminase expression in malignant melanoma. *Molecular Cancer Therapeutics*, 5, 1493-503.
- FOLK, J. E. & COLE, P. W. 1966. Identification of a functional cysteine essential for the activity of guinea pig liver transglutaminase. *Journal of Biological Chemistry*, 241, 3238-40.
- FOLK, J. E., COLE, P. W. & MULLOOLY, J. P. 1968. Mechanim of action of guinea pig liver transglutaminase. V. The hydrolysis reaction. *Journal of Biological Chemistry*, 243, 418-27.
- FRANZ, J. E. & DHINGRA, O. P. 1984. 4.25 - 1,2,4-Thiadiazoles. In: KATRITZKY, A. R. & REES, C. W. (eds.) *Comprehensive Heterocyclic Chemistry*. Oxford: Pergamon.
- FREUND, K. F., DOSHI, K. P., GAUL, S. L., CLAREMON, D. A., REMY, D. C., BALDWIN, J. J., PITZENBERGER, S. M. & STERN, A. M. 1994. Transglutaminase inhibition by 2-[(2-oxopropyl)thio]imidazolium derivatives: mechanism of factor XIIIa inactivation. *Biochemistry*, 33, 10109-19.
- GAUKROGER, K., HADFIELD, J. A., HEPWORTH, L. A., LAWRENCE, N. J. & MCGOWN, A. T. 2001. Novel Syntheses of Cis and Trans Isomers of Combretastatin A-4. *The Journal of Organic Chemistry*, 66, 8135-8.
- GILLET, S. M., PELLETIER, J. N. & KEILLOR, J. W. 2005. A direct fluorometric assay for tissue transglutaminase. *Analytical Biochemistry*, 347, 221-6.
- GNACCARINI, C., BEN-TAHAR, W., LUBELL, W. D., PELLETIER, J. N. & KEILLOR, J. W. 2009. Fluorometric assay for tissue transglutaminase-mediated transamidation activity. *Bioorganic & Medicinal Chemistry*, 17, 6354-9.
- GOLUB, A. G., BDZHOLA, V. G., BRIUKHOVETSKA, N. V., BALANDA, A. O., KUKHARENKO, O. P., KOTEY, I. M., OSTRYNSKA, O. V. & YARMOLUK, S. M. 2011. Synthesis and biological evaluation of substituted (thieno[2,3-d]pyrimidin-4-ylthio)carboxylic acids as inhibitors of human protein kinase CK2. *European Journal of Medicinal Chemistry*, 46, 870-6.
- GRIFFIN, M., CASADIO, R. & BERGAMINI, C. M. 2002. Transglutaminases: Nature's biological glues. *Biochemical Journal*, 368, 377-96.
- GRIFFIN, M., MONGEOT, A., COLLIGHAN, R., SAINT, R. E., JONES, R. A., COUTTS, I. G. & RATHBONE, D. L. 2008. Synthesis of potent water-soluble tissue transglutaminase inhibitors. *Bioorganic & Medicinal Chemistry Letters*, 18, 5559-62.

- GRIFFIN, M., RATHBONE, D. & BADARAU, E. 2014. *Acylpiperazines as inhibitors of transglutaminase and their use in medicine*. WO2013GB52631
- GUNTHEY, P. P. 2013. *Synthesis and screening of potential antimicrobial compounds*. Doctor of Philosophy, Aston University.
- HALIM, D., CARON, K. & KEILLOR, J. W. 2007. Synthesis and evaluation of peptidic maleimides as transglutaminase inhibitors. *Bioorganic & Medicinal Chemistry Letters*, 17, 305-8.
- HAN, A. L., KUMAR, S., FOK, J. Y., TYAGI, A. K. & MEHTA, K. 2014. Tissue transglutaminase expression promotes castration-resistant phenotype and transcriptional repression of androgen receptor. *European Journal of Cancer*, 50, 1685-96.
- HARTWIG, S., NGUYEN, M. M. & HECHT, S. 2010. Exponential growth of functional poly(glutamic acid)dendrimers with variable stereochemistry. *Polymer Chemistry*, 1, 69-71.
- HAUSCH, F., HALTTUNEN, T., MAKI, M. & KHOSLA, C. 2003. Design, synthesis, and evaluation of gluten peptide analogs as selective inhibitors of human tissue transglutaminase. *Chemistry & Biology*, 10, 225-31.
- HAYDEN, F. G., TURNER, R. B., GWALTNEY, J. M., CHI-BURRIS, K., GERSTEN, M., HSYU, P., PATICK, A. K., SMITH, G. J., 3RD & ZALMAN, L. S. 2003. Phase II, randomized, double-blind, placebo-controlled studies of rupintrivir nasal spray 2-percent suspension for prevention and treatment of experimentally induced rhinovirus colds in healthy volunteers. *Antimicrob Agents Chemother*, 47, 3907-16.
- HILL, P. J., ABIBI, A., ALBERT, R., ANDREWS, B., GAGNON, M. M., GAO, N., GREBE, T., HAJEC, L. I., HUANG, J., LIVCHAK, S., LAHIRI, S. D., MCKINNEY, D. C., THRESHER, J., WANG, H., OLIVIER, N. & BUURMAN, E. T. 2013. Selective Inhibitors of Bacterial t-RNA-(N1G37) Methyltransferase (TrmD) That Demonstrate Novel Ordering of the Lid Domain. *Journal of Medicinal Chemistry*, 56, 7278-88.
- HUANG, L., HAYLOR, J. L., HAU, Z., JONES, R. A., VICKERS, M. E., WAGNER, B., GRIFFIN, M., SAINT, R. E., COUTTS, I. G., EL NAHAS, A. M. & JOHNSON, T. S. 2009. Transglutaminase inhibition ameliorates experimental diabetic nephropathy. *Kidney Int*, 76, 383-94.
- HUMPHREY, W., DALKE, A. & SCHULTEN, K. 1996. VMD: visual molecular dynamics. *J Mol Graph*, 14, 33-8, 27-8.
- HWANG, J. Y., MANGALA, L. S., FOK, J. Y., LIN, Y. G., MERRITT, W. M., SPANNUTH, W. A., NICK, A. M., FITERMAN, D. J., VIVAS-MEJIA, P. E., DEAVERS, M. T., COLEMAN, R. L., LOPEZ-BERESTEIN, G., MEHTA, K. & SOOD, A. K. 2008. Clinical and biological significance of tissue transglutaminase in ovarian carcinoma. *Cancer Research*, 68, 5849-58.
- IISMAA, S. E., CHUNG, L., WU, M. J., TELLER, D. C., YEE, V. C. & GRAHAM, R. M. 1997. The core domain of the tissue transglutaminase Gh hydrolyzes GTP and ATP. *Biochemistry*, 36, 11655-64.

- IISMAA, S. E., HOLMAN, S., WOUTERS, M. A., LORAND, L., GRAHAM, R. M. & HUSAIN, A. 2003. Evolutionary specialization of a tryptophan indole group for transition-state stabilization by eukaryotic transglutaminases. *Proceedings of the National Academy of Sciences of the United States of America*, 100, 12636-41.
- JANG, T. H., LEE, D. S., CHOI, K., JEONG, E. M., KIM, I. G., KIM, Y. W., CHUN, J. N., JEON, J. H. & PARK, H. H. 2014. Crystal structure of transglutaminase 2 with GTP complex and amino acid sequence evidence of evolution of GTP binding site. *PLoS One*, 9, e107005.
- JASIM, M. H. 2016. *Computational investigation of small-molecule human tissue transglutaminase inhibitors*. PhD thesis, Aston University.
- JOHNSON, T. S., FISHER, M., HAYLOR, J. L., HAU, Z., SKILL, N. J., JONES, R., SAINT, R., COUTTS, I., VICKERS, M. E., EL NAHAS, A. M. & GRIFFIN, M. 2007. Transglutaminase inhibition reduces fibrosis and preserves function in experimental chronic kidney disease. *Journal of the American Society of Nephrology*, 18, 3078-88.
- JONES, G., WILLETT, P. & GLEN, R. C. 1995. Molecular recognition of receptor sites using a genetic algorithm with a description of desolvation. *Journal of Molecular Biology*, 245, 43-53.
- JONES, G., WILLETT, P., GLEN, R. C., LEACH, A. R. & TAYLOR, R. 1997. Development and validation of a genetic algorithm for flexible docking. *J Mol Biol*, 267, 727-48.
- KEILLOR, J. W., CHICA, R. A., CHABOT, N., VINCI, V., PARDIN, C., FORTIN, E., GILLET, S. M. F. G., NAKANO, Y., KAARTINEN, M. T., PELLETIER, J. N. & LUBELL, W. D. 2008. The bioorganic chemistry of transglutaminase — from mechanism to inhibition and engineering. *Canadian Journal of Chemistry*, 86, 271-6.
- KENNISTON, J. A., CONLEY, G. P., SEXTON, D. J. & NIXON, A. E. 2013. A homogeneous fluorescence anisotropy assay for measuring transglutaminase 2 activity. *Analytical Biochemistry*, 436, 13-5.
- KIM, N., KANG, J. H., LEE, W. K., KIM, S. G., LEE, J. S., LEE, S. H., PARK, J. B., KIM, K. H., GONG, Y. D., HWANG, K. Y. & KIM, S. Y. 2018. Allosteric inhibition site of transglutaminase 2 is unveiled in the N terminus. *Amino Acids*, 50, 1583-94.
- KIM, N., KWAK, S. H., LEE, S. H., JUVEKAR, V., LEE, B. I., AHN, H. C., KIM, S. Y. & GONG, Y. D. 2014. Novel 3-arylethynyl-substituted thieno[3,4-b]pyrazine derivatives as human transglutaminase 2 inhibitors. *Organic and Biomolecular Chemistry*, 12, 4932-40.
- KIM, S., LEE, J. I. & KIM, Y. C. 1985. A simple and mild esterification method for carboxylic acids using mixed carboxylic-carbonic anhydrides. *The Journal of Organic Chemistry*, 50, 560-5.
- KIM, S. Y., JEITNER, T. M. & STEINERT, P. M. 2002. Transglutaminases in disease. *Neurochemistry International*, 40, 85-103.
- KLÖCK, C., JIN, X., CHOI, K., KHOSLA, C., MADRID, P. B., SPENCER, A., RAIMUNDO, B. C., BOARDMAN, P., LANZA, G. & GRIFFIN, J. H. 2011. Acylideneoxoindoles: A new class of

- reversible inhibitors of human transglutaminase 2. *Bioorganic & Medicinal Chemistry Letters*, 21, 2692-6.
- KORB, O., STUTZLE, T. & EXNER, T. E. 2009. Empirical scoring functions for advanced protein-ligand docking with PLANTS. *Journal of Chemical Information and Modeling*, 49, 84-96.
- KRIPPENDORFF, B. F., NEUHAUS, R., LIENAU, P., REICHEL, A. & HUISINGA, W. 2009. Mechanism-based inhibition: deriving $K(I)$ and $k(inact)$ directly from time-dependent $IC(50)$ values. *Journal of Biomolecular Screening*, 14, 913-23.
- KU, B. M., KIM, S. J., KIM, N., HONG, D., CHOI, Y. B., LEE, S. H., GONG, Y. D. & KIM, S. Y. 2014. Transglutaminase 2 inhibitor abrogates renal cell carcinoma in xenograft models. *Journal of Cancer Research and Clinical Oncology*, 140, 757-67.
- KUMAR, A., HU, J., LAVOIE, H. A., WALSH, K. B., DIPETTE, D. J. & SINGH, U. S. 2014. Conformational changes and translocation of tissue-transglutaminase to the plasma membranes: role in cancer cell migration. *BMC Cancer*, 14, 256.
- LAI, T.-S., LIU, Y., LI, W. & GREENBERG, C. S. 2007. Identification of two GTP-independent alternatively spliced forms of tissue transglutaminase in human leukocytes, vascular smooth muscle, and endothelial cells. *Faseb Journal*, 21, 4131-43.
- LAI, T. S., SLAUGHTER, T. F., PEOPLES, K. A., HETTASCH, J. M. & GREENBERG, C. S. 1998. Regulation of human tissue transglutaminase function by magnesium-nucleotide complexes. Identification of distinct binding sites for Mg-GTP and Mg-ATP. *Journal of Biological Chemistry*, 273, 1776-81.
- LEE, S. H., KIM, N., KIM, S. J., SONG, J., GONG, Y. D. & KIM, S. Y. 2013. Anti-cancer effect of a quinoxaline derivative GK13 as a transglutaminase 2 inhibitor. *Journal of Cancer Research and Clinical Oncology*, 139, 1279-94.
- LINDAHL, E. 2015. Molecular Dynamics Simulations. In: KUKOL, A. (ed.) *Molecular Modeling of Proteins*. New York, NY: Springer New York.
- LIU, S., CERIONE, R. A. & CLARDY, J. 2002. Structural basis for the guanine nucleotide-binding activity of tissue transglutaminase and its regulation of transamidation activity. *Proceedings of the National Academy of Sciences of the United States of America*, 99, 2743-7.
- LORAND, L. & CONRAD, S. M. 1984. Transglutaminases. *Mol Cell Biochem*, 58, 9-35.
- LOVELL, S. C., WORD, J. M., RICHARDSON, J. S. & RICHARDSON, D. C. 2000. The penultimate rotamer library. *Proteins*, 40, 389-408.
- MAIER, J. A., MARTINEZ, C., KASAVAJHALA, K., WICKSTROM, L., HAUSER, K. E. & SIMMERLING, C. 2015. ff14SB: Improving the Accuracy of Protein Side Chain and Backbone Parameters from ff99SB. *J Chem Theory Comput*, 11, 3696-713.
- MANGALA, L. S., FOK, J. Y., ZORRILLA-CALANCHA, I. R., VERMA, A. & MEHTA, K. 2007. Tissue transglutaminase expression promotes cell attachment, invasion and survival in breast cancer cells. *Oncogene*, 26, 2459-70.
- NTA, Nguyen, PhD Thesis, Aston University 2020

- MARRANO, C., DE MACEDO, P. & KEILLOR, J. W. 2001. Evaluation of novel dipeptide-bound alpha,beta-unsaturated amides and epoxides as irreversible inhibitors of guinea pig liver transglutaminase. *Bioorganic & Medicinal Chemistry*, 9, 1923-8.
- MENG, X. Y., ZHANG, H. X., MEZEI, M. & CUI, M. 2011. Molecular docking: a powerful approach for structure-based drug discovery. *Curr Comput Aided Drug Des*, 7, 146-57.
- MOOIJ, W. T. & VERDONK, M. L. 2005. General and targeted statistical potentials for protein-ligand interactions. *Proteins*, 61, 272-87.
- MORRIS, G. M. & LIM-WILBY, M. 2008. Molecular Docking. In: KUKOL, A. (ed.) *Molecular Modeling of Proteins*. Totowa, NJ: Humana Press.
- MORTIER, J., RAKERS, C., BERMUDEZ, M., MURGUEITIO, M. S., RINIKER, S. & WOLBER, G. 2015. The impact of molecular dynamics on drug design: applications for the characterization of ligand-macromolecule complexes. *Drug Discovery Today*, 20, 686-702.
- MOTULSKY, H. J. 2019. Relative vs. absolute IC50. <https://www.graphpad.com/support/faqs/relative-vs-absolute-ic50/>.
- MURTHY, S. N., IISMAA, S., BEGG, G., FREYMAN, D. M., GRAHAM, R. M. & LORAND, L. 2002. Conserved tryptophan in the core domain of transglutaminase is essential for catalytic activity. *Proceedings of the National Academy of Sciences of the United States of America*, 99, 2738-42.
- NAKANE, M., REID, J. A., HAN, W. C., DAS, J., VU CHI, T., HASLANGER, M. F., GARBER, D., HARRIS, D. N. & HEDBERG, A. 1990. 7-Oxabicyclo[2.2.1]heptyl carboxylic acids as thromboxane A2 antagonists: aza .omega.-chain analogs. *Journal of Medicinal Chemistry*, 33, 2465-76.
- NARA, H., KAIEDA, A., SATO, K., NAITO, T., MOTOTANI, H., OKI, H., YAMAMOTO, Y., KUNO, H., SANTOU, T., KANZAKI, N., TERAUCHI, J., UCHIKAWA, O. & KORI, M. 2017. Discovery of Novel, Highly Potent, and Selective Matrix Metalloproteinase (MMP)-13 Inhibitors with a 1,2,4-Triazol-3-yl Moiety as a Zinc Binding Group Using a Structure-Based Design Approach. *Journal of Medicinal Chemistry*, 60, 608-26.
- ODIL, B. O. & COUSSONS, P. 2014. Biological functionalities of transglutaminase 2 and the possibility of its compensation by other members of the transglutaminase family. *ScientificWorldJournal*, 2014, 714561.
- OLSEN, K. C., EPA, A. P., KULKARNI, A. A., KOTTMANN, R. M., MCCARTHY, C. E., JOHNSON, G. V., THATCHER, T. H., PHIPPS, R. P. & SIME, P. J. 2014. Inhibition of Transglutaminase 2, a Novel Target for Pulmonary Fibrosis, by Two Small Electrophilic Molecules. *American Journal of Respiratory Cell and Molecular Biology*, 50, 737-47.
- OLSEN, K. C., SAPINORO, R. E., KOTTMANN, R. M., KULKARNI, A. A., IISMAA, S. E., JOHNSON, G. V. W., THATCHER, T. H., PHIPPS, R. P. & SIME, P. J. 2011. Transglutaminase 2 and Its Role in Pulmonary Fibrosis. *American Journal of Respiratory and Critical Care Medicine*, 184, 699-707.

- ONUFRIEV, A. 2008. Chapter 7 - Implicit Solvent Models in Molecular Dynamics Simulations: A Brief Overview. In: WHEELER, R. A. & SPELLMEYER, D. C. (eds.) *Annual Reports in Computational Chemistry*. Elsevier.
- PAQUET, E. & VIKTOR, H. L. 2015. Molecular Dynamics, Monte Carlo Simulations, and Langevin Dynamics: A Computational Review. *BioMed Research International*, 2015, 18.
- PARDIN, C., GILLET, S. M. & KEILLOR, J. W. 2006. Synthesis and evaluation of peptidic irreversible inhibitors of tissue transglutaminase. *Bioorganic & Medicinal Chemistry*, 14, 8379-85.
- PARDIN, C., PELLETIER, J. N., LUBELL, W. D. & KEILLOR, J. W. 2008a. Cinnamoyl Inhibitors of Tissue Transglutaminase. *The Journal of Organic Chemistry*, 73, 5766-75.
- PARDIN, C., ROY, I., LUBELL, W. D. & KEILLOR, J. W. 2008b. Reversible and Competitive Cinnamoyl Triazole Inhibitors of Tissue Transglutaminase. *Chemical Biology & Drug Design*, 72, 189-96.
- PHILLIPS, J. C., BRAUN, R., WANG, W., GUMBART, J., TAJKHORSHID, E., VILLA, E., CHIPOT, C., SKEEL, R. D., KALÉ, L. & SCHULTEN, K. 2005. Scalable molecular dynamics with NAMD. *Journal of Computational Chemistry*, 26, 1781-802.
- PINKAS, D. M., STROP, P., BRUNGER, A. T. & KHOSLA, C. 2007. Transglutaminase 2 undergoes a large conformational change upon activation. *PLoS Biol*, 5, e327.
- PITTA, E., ROGACKI, M. K., BALABON, O., HUSS, S., CUNNINGHAM, F., LOPEZ-ROMAN, E. M., JOOSSENS, J., AUGUSTYNS, K., BALLELL, L., BATES, R. H. & VAN DER VEKEN, P. 2016. Searching for New Leads for Tuberculosis: Design, Synthesis, and Biological Evaluation of Novel 2-Quinolin-4-yloxyacetamides. *Journal of Medicinal Chemistry*, 59, 6709-28.
- PLIURA, D. H., BONAVENTURA, B. J., PAULS, H. W., KILLACKEY, J. F. & KRANTZ, A. 1992. Irreversible inhibition of transglutaminases by sulfonium methylketones: optimization of specificity and potency with omega-aminoacyl spacers. *Journal of Enzyme Inhibition and Medicinal Chemistry*, 6, 181-94.
- POWERS, J. C., ASGIAN, J. L., EKICI, Ö. D. & JAMES, K. E. 2002. Irreversible Inhibitors of Serine, Cysteine, and Threonine Proteases. *Chemical Reviews*, 102, 4639-750.
- POWERS, J. P., PIPER, D. E., LI, Y., MAYORGA, V., ANZOLA, J., CHEN, J. M., JAEN, J. C., LEE, G., LIU, J., PETERSON, M. G., TONN, G. R., YE, Q., WALKER, N. P. & WANG, Z. 2006. SAR and mode of action of novel non-nucleoside inhibitors of hepatitis C NS5b RNA polymerase. *Journal of Medicinal Chemistry*, 49, 1034-46.
- PRIME, M. E., ANDERSEN, O. A., BARKER, J. J., BROOKS, M. A., CHENG, R. K., TOOGOOD-JOHNSON, I., COURTNEY, S. M., BROOKFIELD, F. A., YARNOLD, C. J., MARSTON, R. W., JOHNSON, P. D., JOHNSON, S. F., PALFREY, J. J., VAIDYA, D., ERFAN, S., ICHIHARA, O., FELICETTI, B., PALAN, S., PEDRET-DUNN, A., SCHAERTL, S., STERNBERGER, I., EBNETH, A., SCHEEL, A., WINKLER, D., TOLEDO-SHERMAN, L., BECONI, M., MACDONALD, D., MUNOZ-SANJUAN, I., DOMINGUEZ, C. & WITYAK, J. 2012a. Discovery and structure-

activity relationship of potent and selective covalent inhibitors of transglutaminase 2 for Huntington's disease. *Journal of Medicinal Chemistry*, 55, 1021-46.

PRIME, M. E., BROOKFIELD, F. A., COURTNEY, S. M., GAINES, S., MARSTON, R. W., ICHIHARA, O., LI, M., VAIDYA, D., WILLIAMS, H., PEDRET-DUNN, A., REED, L., SCHAERTL, S., TOLEDO-SHERMAN, L., BECONI, M., MACDONALD, D., MUNOZ-SANJUAN, I., DOMINGUEZ, C. & WITYAK, J. 2012b. Irreversible 4-Aminopiperidine Transglutaminase 2 Inhibitors for Huntington's Disease. *ACS Med Chem Lett*, 3, 731-5.

RAM, S. & EHRENKAUFER, R. E. 1988. Ammonium Formate in Organic Synthesis: A Versatile Agent in Catalytic Hydrogen Transfer Reductions. *Synthesis*, 1988, 91-5.

RATHBONE, D. L., PARKER, K. J., COLEMAN, M. D., LAMBERT, P. A. & BILLINGTON, D. C. 2006. Discovery of a potent phenolic N1-benzylidene-pyridinecarboxamidrazone selective against Gram-positive bacteria. *Bioorganic & Medicinal Chemistry Letters*, 16, 879-83.

RUAN, Q. & JOHNSON, G. V. 2007. Transglutaminase 2 in neurodegenerative disorders. *Frontiers in Bioscience*, 12, 891-904.

SASHUK, V., SCHOEPS, D. & PLENIO, H. 2009. Fluorophore tagged cross-coupling catalysts. *Chemical Communications*, 770-2.

SATPATHY, M., CAO, L., PINCHEIRA, R., EMERSON, R., BIGSBY, R., NAKSHATRI, H. & MATEI, D. 2007. Enhanced peritoneal ovarian tumor dissemination by tissue transglutaminase. *Cancer research*, 67, 7194-202.

SCARPELLINI, A., HUANG, L., BURHAN, I., SCHROEDER, N., FUNCK, M., JOHNSON, T. S. & VERDERIO, E. A. M. 2014. Syndecan-4 Knockout Leads to Reduced Extracellular Transglutaminase-2 and Protects against Tubulointerstitial Fibrosis. *Journal of the American Society of Nephrology*, 25, 1013-27.

SCHAERTL, S., PRIME, M., WITYAK, J., DOMINGUEZ, C., MUNOZ-SANJUAN, I., PACIFICI, R. E., COURTNEY, S., SCHEEL, A. & MACDONALD, D. 2010. A profiling platform for the characterization of transglutaminase 2 (TG2) inhibitors. *Journal of Biomolecular Screening*, 15, 478-87.

SHAW, E. 1994. [46] Peptidyl diazomethanes as inhibitors of cysteine and serine proteinases. *Methods in Enzymology*. Academic Press.

SHI, L., CHEN, L., CHEN, R. & CHEN, L. 2010. Synthesis of deuterium-labelled fosamprenavir calcium. *Journal of Labelled Compounds and Radiopharmaceuticals*, 53, 147-51.

SIEGEL, M., STRNAD, P., WATTS, R. E., CHOI, K., JABRI, B., OMARY, M. B. & KHOSLA, C. 2008. Extracellular transglutaminase 2 is catalytically inactive, but is transiently activated upon tissue injury. *PLoS One*, 3, e1861.

SIKDAR, S. 2010. *Design and synthesis of potential antimicrobial agents*. PhD thesis, Aston University.

SONG, M., HWANG, H., IM, C. Y. & KIM, S. Y. 2017. Recent Progress in the Development of Transglutaminase 2 (TGase2) Inhibitors. *Journal of Medicinal Chemistry*, 60, 554-67.

NTA, Nguyen, PhD Thesis, Aston University 2020

- STAMNAES, J., PINKAS, D. M., FLECKENSTEIN, B., KHOSLA, C. & SOLLID, L. M. 2010. Redox regulation of transglutaminase 2 activity. *Journal of Biological Chemistry*, 285, 25402-9.
- STOTE, R., DEJAEGERE, A., KUZNETSOV, D. & FALQUET, L. 1999. Setting up and running a molecular dynamics simulations. https://embnet.vital-it.ch/MD_tutorial/.
- STRELOW, J. M. 2017. A Perspective on the Kinetics of Covalent and Irreversible Inhibition. *SLAS Discovery*, 22, 3-20.
- TANG, S. Q., LEE, Y. Y., PACKIARAJ, D. S., HO, H. K. & CHAI, C. L. 2015. Systematic Evaluation of the Metabolism and Toxicity of Thiazolidinone and Imidazolidinone Heterocycles. *Chem Res Toxicol*, 28, 2019-33.
- VERMA, A., WANG, H., FOK, J. Y. & MEHTA, K. 2007. Increased expression of tissue transglutaminase in pancreatic ductal adenocarcinoma and its implications in drug resistance and metastasis. *Proceedings of the American Association for Cancer Research Annual Meeting*, 48, 1290.
- WANG, J., WOLF, R. M., CALDWELL, J. W., KOLLMAN, P. A. & CASE, D. A. 2004. Development and testing of a general amber force field. *Journal of computational chemistry*, 25, 1157-74.
- WANG, Z., STUCKEY, D. J., MURDOCH, C. E., CAMELLITI, P., LIP, G. Y. H. & GRIFFIN, M. 2018. Cardiac fibrosis can be attenuated by blocking the activity of transglutaminase 2 using a selective small-molecule inhibitor. *Cell Death & Disease*, 9, 613.
- WATTS, R. E., SIEGEL, M. & KHOSLA, C. 2006. Structure-activity relationship analysis of the selective inhibition of transglutaminase 2 by dihydroisoxazoles. *Journal of Medicinal Chemistry*, 49, 7493-501.
- WODTKE, R., SCHRAMM, G., PIETZSCH, J., PIETZSCH, M. & LÖSER, R. 2016. Synthesis and Kinetic Characterisation of Water-Soluble Fluorogenic Acyl Donors for Transglutaminase 2. *ChemBioChem*, 17, 1263-81.
- YU, J., GAUNT, M. J. & SPENCER, J. B. 2002. Convenient Preparation of trans-Arylalkenes via Palladium(II)-Catalyzed Isomerization of cis-Arylalkenes. *The Journal of Organic Chemistry*, 67, 4627-9.
- YUAN, L., SIEGEL, M., CHOI, K., KHOSLA, C., MILLER, C. R., JACKSON, E. N., PIWNICA-WORMS, D. & RICH, K. M. 2007. Transglutaminase 2 inhibitor, KCC009, disrupts fibronectin assembly in the extracellular matrix and sensitizes orthotopic glioblastomas to chemotherapy. *Oncogene*, 26, 2563-73.